

**SISSA**

Scuola  
Internazionale  
Superiore di  
Studi Avanzati

Physics Area - PhD course in  
Statistical Physics

# Non-equilibrium dynamics and localization in statistical quantum systems

Candidate:  
Carlo Vanoni

Advisors:  
Prof. Andrea Gambassi  
Prof. Antonello Scardicchio

Academic Year 2023-24









# Abstract

The study of non-equilibrium behaviors of quantum matter is one of the research directions at the frontiers of condensed matter physics and, in general, of theoretical and experimental physics. Understanding the mechanisms which prevent many quantum particles from reaching thermal equilibrium can ultimately shed light on the foundations of statistical physics and provide insight into the anomalous long-time collective behaviors observed in experiments. In this thesis, we present new theoretical developments in this direction.

In the first part of the thesis we discuss the non-equilibrium dynamics of the two-dimensional quantum Ising model, the prototypical model of magnetism. In particular, we investigate the dynamics of interfaces separating different spin domains. In some regimes, we can provide an exact description of their unitary time evolution, but we also discuss the robustness of our predictions away from the exactly-solvable limit. Moreover, we address the same problem in the presence of disorder and provide a hydrodynamic interpretation of our findings.

In the second part of the thesis, we investigate the localization properties of disordered quantum systems. In particular, we develop a renormalization-group picture of the Anderson localization transition in generic geometries. This provides a new framework to understand the phase diagram of such systems and their critical behavior beyond the usual finite-size scaling analysis. We also provide further insights on this topic both by studying resonances and their connection with observables and by employing unsupervised non-parametric learning techniques to probe disordered systems in an experimentally accessible form.

The results presented in this thesis constitute a step forward in understanding the non-equilibrium phases and regimes of quantum matter and they pave the way to interesting future developments.



# Contents

|   |           |
|---|-----------|
| <b>List of Publications</b>   | <b>ix</b> |
| <b>1 Introduction</b>   | <b>3</b>  |
| <b>I Interface dynamics in two-dimensional quantum systems and related problems</b>                   | <b>9</b>  |
| <b>2 Localization and melting in the two-dimensional quantum Ising model</b>                          | <b>11</b> |
| 2.1 Model . . . . .   | 13        |
| 2.2 Infinite-coupling dynamics for strips and smooth domain walls . . . . .                           | 17        |
| 2.3 Infinite-coupling dynamics for an infinite corner . . . . .                                       | 27        |
| 2.4 Mechanisms of integrability breaking . . . . .  | 38        |
| 2.5 Conclusions . . . . .   | 46        |
| <b>3 Melting of a disordered quantum crystal</b>  | <b>49</b> |
| 3.1 Model . . . . .   | 51        |
| 3.2 Mapping to Young diagrams and to lattice fermions . . . . .                                       | 53        |
| 3.3 Perturbation theory estimates . . . . .   | 56        |
| 3.4 Spectral statistics via exact diagonalization . . . . .   | 59        |
| 3.5 Dynamics . . . . .  | 62        |
| 3.6 Discussion . . . . .  | 66        |
| 3.7 Conclusions . . . . .   | 68        |
| <b>4 Hydrodynamic theory of Stark localization</b>  | <b>69</b> |
| 4.1 Generalized hydrodynamics of inhomogeneous systems . . . . .                                      | 70        |
| 4.2 Dynamics in the presence of a linear potential . . . . .  | 71        |
| 4.3 Stark localization in a generic potential . . . . .   | 81        |
| 4.4 Conclusions . . . . .   | 86        |
| <b>Appendix of Part I</b>   |           |
| <b>A Additional information - Melting and Localization in the two-dimensional quantum Ising model</b> | <b>91</b> |
| A.1 Magnetization in the linear strip . . . . .   | 91        |
| A.2 Useful properties of the Bessel functions . . . . .   | 92        |
| A.3 Two-point functions . . . . .   | 94        |
| A.4 Comparison with classical simple exclusion processes . . . . .                                    | 96        |
| A.5 Second order Schrieffer-Wolff and integrability breaking . . . . .                                | 97        |

|                            |  |            |
|----------------------------|--|------------|
| A.6                        | Participation ratio and localization length . . . . .  | 100        |
| <b>B</b>                   | <b>Additional information - Hydrodynamic theory of Stark localization</b>  | <b>103</b> |
| B.1                        | Derivation of the semi-classical Hamiltonian . . . . .   | 103        |
| B.2                        | Numerical method . . . . .   | 104        |
| <b>II</b>                  | <b>Renormalization group and finite size effects in disordered localized systems</b>   | <b>105</b> |
| <b>5</b>                   | <b>Renormalization group analysis of Anderson localization in finite dimensions</b>  | <b>107</b> |
| 5.1                        | Concepts and definitions . . . . .   | 108        |
| 5.2                        | Main results . . . . .   | 110        |
| 5.3                        | Anderson model and scaling theory for conductance . . . . .  | 111        |
| 5.4                        | $\beta$ -function for ‘modern’ observables . . . . .   | 112        |
| 5.5                        | $\beta$ -function in two dimensions . . . . .  | 115        |
| 5.6                        | $\beta$ -function for higher dimensions . . . . .  | 117        |
| 5.7                        | $\beta(D)$ in the $\epsilon$ -expansion and self-consistent theories . . . . .   | 120        |
| 5.8                        | The high-gradient operators in the non-linear $\sigma$ -model and the irrelevant exponent $y$                                    | 124        |
| 5.9                        | Approaching the critical point . . . . .   | 126        |
| 5.10                       | Increasing space dimensionality and the Random Regular Graph . . . . .   | 127        |
| 5.11                       | Conclusions . . . . .  | 128        |
| <b>6</b>                   | <b>Renormalization group analysis of Anderson localization in infinite dimensions and random graphs</b>                          | <b>129</b> |
| 6.1                        | Renormalization Group Equations . . . . .  | 130        |
| 6.2                        | The critical region . . . . .  | 134        |
| 6.3                        | Role of loops and correlations in infinite dimensions . . . . .  | 138        |
| 6.4                        | Conclusions . . . . .  | 139        |
| <b>7</b>                   | <b>Resonance counting and finite-size effects in random matrices</b>   | <b>141</b> |
| 7.1                        | Background and motivation . . . . .  | 143        |
| 7.2                        | Self-consistent resonance condition . . . . .  | 146        |
| 7.3                        | Analytical study of the Gaussian Rosenzweig-Porter model . . . . .   | 148        |
| 7.4                        | Resonance counting in other Rosenzweig-Porter models . . . . .   | 150        |
| 7.5                        | Microscopic approach to resonance criteria . . . . .   | 154        |
| 7.6                        | Conclusion . . . . .   | 162        |
| <b>8</b>                   | <b>Non-parametric unsupervised learning and localization transitions</b>   | <b>163</b> |
| 8.1                        | Wavefunction sampling and analysis . . . . .   | 165        |
| 8.2                        | Anderson model and results . . . . .   | 167        |
| 8.3                        | Study of many-body localization . . . . .  | 169        |
| 8.4                        | Conclusions . . . . .  | 169        |
| <b>Appendix of Part II</b> |  |            |
| <b>C</b>                   | <b>Additional information - Renormalization group analysis of Anderson localization in infinite dimensions and random graphs</b> | <b>173</b> |
| C.1                        | $\beta$ -function in the critical region . . . . .   | 175        |

|          |   |            |
|----------|---|------------|
| <b>D</b> | <b>Additional information - Resonance counting and finite-size effects in random matrices</b>     | <b>181</b> |
| D.1      | Exact entropy for the rotational-invariant random matrices . . . . .                              | 181        |
| D.2      | Another analytical approach to the Gaussian RP model . . . . .                                    | 182        |
| <b>E</b> | <b>Additional information - Non-parametric unsupervised learning and localization transitions</b> | <b>185</b> |
| E.1      | PCA entropy analysis . . . . .  | 185        |
| <b>9</b> | <b>Final remarks</b>  | <b>191</b> |



# List of Publications

*The results presented in this thesis are based on the following research papers published during the Ph.D.*

- [1] F. Balducci, A. Gambassi, A. Lerose, A. Scardicchio and **C. Vanoni**  
*Localization and melting of interfaces in the two-dimensional quantum Ising model*  
Phys. Rev. Lett. **129**, 120601, 120601 (2022)
- [2] F. Balducci, A. Gambassi, A. Lerose, A. Scardicchio and **C. Vanoni**  
*Interface dynamics in the two-dimensional quantum Ising model*  
Phys. Rev. B **107**, 024306 (2023)
- [3] F. Balducci, A. Scardicchio and **C. Vanoni**  
*Slow melting of a disordered quantum crystal*  
Phys. Rev. B **107**, 024201 (2023)
- [4] L. Capizzi, **C. Vanoni**, P. Calabrese and A. Gambassi  
*A hydrodynamic approach to Stark localization*  
J. Stat. Mech.: Theor. Exp. **2023**, 073104 (2023)
- [5] **C. Vanoni**, B. L. Altshuler, V. E. Kravtsov and A. Scardicchio  
*Renormalization group analysis of the Anderson model on random regular graphs*  
Preprint arXiv:2306.14965 (2023) - Accepted on PNAS
- [6] B. L. Altshuler, V. E. Kravtsov, A. Scardicchio, P. Sierant, and **C. Vanoni**  
*Renormalization group for Anderson localization on high-dimensional lattices*  
Preprint arXiv:2403.01974 (2024)
- [7] A. Kutlin and **C. Vanoni**  
*Investigating finite-size effects in random matrices by counting resonances*  
Preprint arXiv:2402.10271 (2024)
- [8] **C. Vanoni** and V. Vitale  
*An analysis of localization transitions using non-parametric unsupervised learning*  
Preprint arXiv:2311.16050 (2023)



# Chapter 1

## Introduction

As indicated on the title page, this thesis constitutes the final point of the Ph.D. studies in statistical physics. Accordingly, it is prudent to succinctly contextualize within the broader framework of Statistical Mechanics the topics we have explored and which will be subsequently discussed.

Until the XVIII century, physicists mainly studied systems consisting of few degrees of freedom, whose individual time evolution could be described precisely. Such a level of precision became out of reach when the study of gases took off: in a physical system with  $O(10^{23})$  degrees of freedom (e.g., the molecules constituting the gas under analysis) it is impossible to describe the motion of every single constituent. Moreover, even if such control was possible, it is not needed and would be an overkill: the interesting quantities are few (such as temperature and pressure) and it is not even trivial to determine them from the precise knowledge of the particles' positions and velocities. As a consequence, thermodynamics developed, and the founding fathers of statistical physics (Ludwig Boltzmann, James C. Maxwell, Josiah W. Gibbs, etc.) understood that the success of the newly born theory was rooted in the possibility of describing probabilistically the long-time behavior of the dynamics of many-particle systems. In particular, the ergodic hypothesis states that the long-time behavior of physical observables at equilibrium can be determined as a statistical ensemble average and does not depend on the specific initial state, but only on the conserved quantities of the system. In practice, assuming that the ergodic hypothesis applies, all equilibrium properties of many-particle systems can be successfully derived.

It is widely believed that the ergodic hypothesis holds for the vast majority of physical systems, but it can actually be proven only for a few of them. It is thus interesting to address those physical systems or models for which the ergodic hypothesis does not apply, as they host counter-intuitive phenomena. Let me briefly mention three examples in the realm of classical physics.

- Classically integrable systems are, by construction, expected not to reach equilibrium and thus do not thermalize: the presence of an extensive number of conserved quantities constrains the dynamics to a submanifold of much smaller dimensionality of the total phase space. The closed-form solution of such systems can be extremely complicated and it constitutes a research field on its own [9].
- A related set of systems that do not thermalize as expected is that of nonlinear lattice systems. Everything started with the seminal work of E. Fermi, J. Pasta, S. Ulam, and M. Tsingou (FPUT) [10], where a surprisingly long quasi-periodic behavior in a chain of non-linear oscillators was observed, in contrast to the expected thermalization after a short

transient. Since that first work, the study of nonlinear systems has grown quickly [11, 12]. Among the models belonging to this class, there is the discrete nonlinear Schrödinger equation [13], describing a set of nonlinear oscillators and obtained as a discretization of an integrable, continuous model. Formulating the problem on a lattice makes it non-integrable, but still, ergodicity is not restored for all possible choices of the initial conditions [14–20].

- As a final example, let us mention the field of disordered classical systems, and in particular spin-glasses. In such systems, introduced in Refs. [21, 22], below the freezing temperature a novel non-ergodic phase emerges, named the “spin glass phase”, which is particularly interesting both at equilibrium and out of equilibrium. In this regime, the energy landscape of the system displays many local and deep minima, separated by large energy barriers. The equilibrium properties of (a class of) spin glasses can be determined using the replica symmetry-breaking (RSB) theory proposed by G. Parisi, which led to the exact solution of the Sherrington-Kirkpatrick model [23]. Also the dynamical properties of spin glasses show striking effects. It turns out that the relaxation time of glassy systems becomes exceedingly long at low temperatures (albeit larger than the freezing temperature), so long that glassy systems are never seen at equilibrium on physically relevant time-scales [24–26]. A surprising experimental consequence of this non-equilibrium property consists in the phenomenon of aging, meaning that the ability of the system to “forget” the initial condition decreases with its age [27]. Let me also mention that the techniques and methods developed for spin-glass systems have found a large variety of applications [28, 29], ranging from biology and chemistry [30] to machine learning [31] and combinatorial optimization [32–34].

The situation remains interesting and, possibly, becomes more complicated when the basic degrees of freedom obey the laws of quantum mechanics. This is the case because quantum evolution is unitary and, thus, even a proper definition of ergodicity is not straightforward, as it is not possible to track a “quantum” trajectory in phase space and verify the classical ergodic hypothesis [35, 36]. This can also be seen by observing that the probability of finding the state at time  $t$  in a specific eigenstate of the Hamiltonian does not depend on  $t$  and on the Hamiltonian, but only on the initial state. A different definition of thermalization is thus needed to distinguish thermal from non-thermal states in quantum systems.

The main idea behind the eigenstate thermalization hypothesis (ETH) [37, 38] is that of considering the expectation values of *local* operators, being the physically relevant observables, and requiring that the expectation value of such operators attains a thermal value. This implies that the information contained in the initial state  $|\psi(0)\rangle$  is effectively erased during the dynamics, as it is transferred to highly non-local and inaccessible correlations. Concretely, ETH is an ansatz for both diagonal and off-diagonal matrix elements of local observables in the eigenbasis of the Hamiltonian [38]. Importantly, using the ETH expression for the matrix elements it is easy to show that the equilibrium, long-time value of the corresponding local observable is equal to the average over a microcanonical ensemble of states in a narrow energy shell [39]. This yields the notion of quantum ergodicity, in that all eigenstates of the Hamiltonian within the energy shell contribute equally to the long-time average of the observable under analysis. Notice that ETH is a sufficient condition for the onset of thermalization, but whether it is also a necessary condition is still an open question.

In analogy to the classical case, also in studying quantum thermalization, it is natural to ask in which cases such a phenomenon can be circumvented in order to attain genuine non-equilibrium phases of matter. The answer, once again in analogy to the classical situation, is not easy, but rather there are multiple examples of systems that violate ETH and are believed to not thermalize.

We will now present the main classes of such quantum systems, as an introduction to a more detailed discussion of some specific cases in the rest of this thesis:

- Similarly to the classical case, a quantum integrable model is characterized by an extensive number of operators commuting with the Hamiltonian and among themselves, and thus an extensive number of conservation laws. The small subset of  $1 + 1$  (one spacial and one temporal) dimensional quantum many-body systems that turn out to be integrable has the advantage of being amenable to analytical solutions [40, 41]. In fact, the presence of extensively many conserved quantities allows to determine each eigenstate of the system and characterize it by a set of quantum numbers, that are ultimately related to a quasi-particle description of the model.

The basic ingredient responsible for the analytical solution of integrable models is the factorizability of any scattering event in a product of two-body scattering processes [42]. Such property is the basic assumption of the Bethe Ansatz [43], the main theoretical tool for solving integrable models [40].

Because of the presence of an extensive number of conservation laws, it has been shown that the stationary states of integrable systems are actually described by a generalized Gibbs ensemble (GGE) [44–47]. As the name suggests, a GGE is a generalization of the standard Gibbs ensemble which does not enforce only energy conservation, but also the conservation of the other integrals of motion responsible for the model’s integrability. A systematic theoretical approach to investigate the dynamics of inhomogeneous integrable systems, including in particular free theories, has been recently formulated in the form of a generalized hydrodynamics (GHD) [48, 49]. This approach extends standard hydrodynamics by accounting for the additional conservation laws enforced by integrability. GHD turned out to be a versatile and predictive method in a large variety of contexts, including transport phenomena in spin-chains [50–62], inhomogeneous quantum gases both in and out of equilibrium [63–72], quantum and diffusion effects [73–81], as reviewed in Refs. [81–83]. Its theoretical predictions have also been confirmed in recent experiments [84, 85].

- The discovery of systems weakly violating ETH (in the sense explained further below) is very recent, and it was first observed in an experiment in 2018 using Rydberg atoms [86]. Although certain initial states showed the relaxation to thermal ensembles which is expected in an ergodic system, other states exhibited periodic revivals. The surprise was due to the fact that the systems did not have conserved quantities other than the total energy and that there was no disorder, ruling out integrability and localization. The theoretical investigations [87] that followed have shown that the measured revivals were due to the presence of anomalous non-thermal eigenstates in the highly excited energy spectrum of the system. The presence of such anomalous eigenstates is what is typically referred to as a weak violation of ETH. Notice that the number of such eigenstates comprises only a vanishing fraction of the full Hilbert space and, in analogy to what happens in chaotic stadium billiards [88], such states have been dubbed “quantum many-body scars” [87, 89].

Different mechanisms leading to many-body scarring have been found [90], and we will not review them here. We want to briefly mention the PXP models, as they are relevant for the discussion in the first part of the thesis and they explain the experimental observations. In essence, in PXP models a constraint on the allowed configurations of the system is enforced [91]; to reproduce the Rydberg atom experiment, the constraint to be imposed is that of having a Rydberg blockade, namely preventing neighboring atoms from being simultaneously excited. The resulting model is interacting and non-integrable [87], but it presents

some atypical eigenstates, i.e., quantum scars, with anomalously low entanglement entropy. The study of PXP and other models displaying weak ergodicity breaking has been very intense in the last few years [92–95], and a complete understanding of the mechanism has to be reached.

- Since the seminal work of Phil W. Anderson [96], it has been known that the presence of disorder in quantum systems can lead to the absence of transport, and localization. This phenomenon occurs because of a combination of disorder and quantum interference: accordingly, one can see that it has no classical analog. Disorder-induced localization in non-interacting systems (known as “Anderson localization”) has been extensively analyzed during the second half of the last century [97–102]. However, a significant revival in the field occurred in the last two decades after the first studies of localization phenomena in disordered *interacting* quantum systems by D. Basko, I. Aleiner and B. Altshuler [103], and V. Oganesyan and D. Huse [104], who suggested the possibility of the occurrence of many-body localization (MBL) (see Ref. [105] for a recent review).

While the conditions for the occurrence of Anderson localization (i.e., in non-interacting systems) are well understood [100], the situation is way less settled for interacting systems. The original work of Basko, Aleiner, and Altshuler shows that, at fixed interaction strength, there is a critical temperature below which the conductivity vanishes. The validity of their calculations in perturbation theory relies on the possibility of neglecting some diagrammatic contributions in the expansion. It is known that, if the same approximations are performed on a non-interacting system, the result of the perturbation theory provides an upper bound to the critical disorder [106, 107], thus implying that for sure the system is localized for higher values of the disorder strength. Yet, it is not clear if the same upper bound is obtained when performing such an approximation to interacting systems, thus leaving the stability of MBL an open question.

Subsequent works, starting from Ref. [104], focused almost exclusively on one-dimensional lattice spin models at infinite temperature. There it has been argued, based primarily on numerical results on rather small systems (the best ones available), that MBL is a phase of matter at strong enough disorder, i.e., the system does not thermalize and ergodicity is broken [108]. It has been shown that a perturbation theory similar to the one of Ref. [103], when applied to lattice spin models, leads to the existence of local integrals of motion (LIOMs) [109, 110], and algorithms for finding the LIOMs have also been proposed [111]. Accordingly, such models are believed to pass from the usual diffusive dynamics at small disorder, to subdiffusive transport [112–115], and then finally to a localized regime [96], becoming effectively integrable systems. Moreover, a mathematical proof of the stability of MBL for one-dimensional spin chains has been proposed [116, 117].

Recently, however, there have been serious objections to the statement that MBL is a genuine phase of matter, starting from Ref. [118, 119], where it has been argued that the observed data could be interpreted also in terms of a drastic slow-down in the dynamics, but still without violating ETH. An intense debate surged from those works [120, 121] and other concerns have been raised, ultimately leading to the conclusion that it is not clear whether MBL is a true phase of matter [122], and the notion of MBL regime has been proposed to pertain the observed phenomena at finite size and short time scales. Let me also mention that non-perturbative effects possibly able to destabilize the MBL phase have been recently discussed, such as quantum avalanches [123, 124] and many-body resonances [125]. So far, the outcome of such models has been that of moving the critical value of the disorder to higher values (about one order of magnitude) than those obtained numerically from exact

diagonalization [125, 126].

The interest in disordered interacting systems generated also a revival in Anderson localization on tree-like graphs [107, 127–138]. This occurred for at two reasons. On the one hand, when turning on the interaction on a system that is localized in the one-electron approximation, the perturbation theory presented in Ref. [103] has many features that resemble the spreading of a quantum particle on an infinite-dimensional graph [139], which can locally be approximated by a tree. On the other hand, Anderson localization of tree-like graphs, in particular random regular graphs (RRG), displays finite-size effects that are very reminiscent of those of MBL [130, 140]. However, it is well known where the localization transition is on RRGs and the model is non-interacting, so genuinely different from a many-body system.

The topics presented in this thesis are based on the research works we performed during the Ph.D. and concern the properties of quantum systems that break ergodicity. Despite the investigation of non-equilibrium properties of quantum systems is the *fil rouge* connecting all the topics discussed, we chose to split the thesis into two main parts, where the subjects are more easily connected. Moreover, both parts deal, at least in part, with properties of disordered quantum systems and their localization transition properties.

Let me present here more in detail the content of the following Chapters.

**Part I.** In the first part of the thesis, we will discuss the non-equilibrium dynamics in the two-dimensional Ising model, as well as some problems strictly related to it. More specifically:

- In Chapter 2, we will discuss the dynamics of interfaces in the two-dimensional quantum Ising model. We will show how to solve exactly the problem in the strong coupling limit for a class of initial states and how to perturbatively address the dynamics at long time scales away from the strong coupling regime.
- In Chapter 3, we consider the same problem in the presence of a disordered external field. While the dynamics remains confined when the field is homogeneous, we show that there is no localization when the field is random. Nevertheless, the dynamics is much slower than expected.
- In Chapter 4, we use the generalized hydrodynamics technique to study the entanglement properties of the Stark localized free fermions. The interest in the model originates from what is discussed in Chapter 2, in that the exact solution of the two-dimensional model is obtained via the solution of a Stark localized free fermionic chain.

**Part II.** In the second part of the thesis, instead, we focus on studying the localization phenomena in disordered quantum systems. In particular:

- In Chapter 5, we present a renormalization group study of the Anderson model on finite-dimensional lattices. We show how to use spectral properties, easily accessible numerically, to build the complete  $\beta$ -function of the model, for different space dimensionalities. We also discuss the large dimension limit, that connects to the subject of Chapter 6.
- In Chapter 6, we apply the technique presented in the previous Chapter to tackle the Anderson model on random regular graphs, and we show that its properties match those expected in the infinite-dimensional limit. In particular, we discuss how the one-parameter scaling becomes a two-parameter scaling at the critical point.

- In Chapter 7, we investigate the role of resonances in the localization transition in disordered quantum systems. In particular, we present a criterion for identifying resonances that is easily related to physically relevant observables, allowing us to compute eigenstates' participation entropy and fractal dimension for some random matrix models.
- In Chapter 8, we propose an alternative approach for addressing the localization properties of quantum systems using unsupervised machine learning. The method we present is agnostic about the nature of the system under analysis, but it is nevertheless able to predict known properties with high accuracy. Moreover, the technique is easily applicable experimentally.

Each chapter of this thesis will contain an abstract, and specific introduction and conclusion. At the end of the thesis, in Chapter 9, we will give a brief summary of the results obtained and future promising perspectives stemming from the results presented here.

## Part I

# Interface dynamics in two-dimensional quantum systems and related problems



## Chapter 2

# Localization and melting in the two-dimensional quantum Ising model

*In this Chapter, we study the domain-wall dynamics in the two-dimensional quantum Ising model in the strong coupling limit. In the case of a wedge, we will show how to solve exactly the problem in the infinite coupling limit using a holographic mapping to a one-dimensional free fermionic chain in a field. We will then relax the infinite coupling constraint and discuss the connection between the problem presented and the measure concentration on random partitions. This Chapter is based on Refs. [1, 2].*

THE Ising model, which will be the main character of Part I of this Thesis, is the prototypical model for studying magnetic properties in materials since its introduction in Ref. [141]. Here we will focus on the non-equilibrium dynamics of the quantum Ising model in two spatial dimensions. The motivation for the research interest in this topic is at least twofold and has different origins.

On the one hand, as discussed in the Introduction, strongly interacting quantum many-body systems evolving out of equilibrium are generically expected to locally relax to thermodynamic equilibrium after a short transient [39, 142]. In several cases, however, microscopic interactions support long-lived dynamical stages away from equilibrium. These anomalous nonequilibrium states attract much interest, as they facilitate the realization of unconventional phases of matter.

Much insight into non-ergodic behavior is gained, however, from one-dimensional ( $1d$ ) systems, for which advanced analytical [143, 144] and numerical [145] techniques are available. The nonequilibrium and possibly non-ergodic evolution of higher-dimensional quantum systems, instead, is largely uncharted territory. While the development of theoretical tools to analyze their dynamics stands as a formidable challenge, recent experimental advances allow an unprecedented degree of engineering and control of two-dimensional ( $2d$ ) arrays of two-level systems [146–150], exhibiting forms of ergodicity breaking [151]. Moreover, it was recently suggested that pseudorandom disorder may stabilize many-body localization in  $2d$  systems [124, 152, 153].

On the other hand, the dynamical nucleation of a region of true vacuum in a sea of false vacuum is a classic problem in statistical mechanics [154–156]. Most of the progress, however, has been achieved in the context of stochastic dynamics so far, since the unitary quantum dynamics constitutes a significant challenge. Stochastic dynamics often provides an adequate description of equilibrium condensed matter systems, such as magnets or crystal-liquid mixtures, due to the

continuous influence of noisy environmental degrees of freedom, which act like a bath at a well-defined temperature. Nevertheless, there are situations in which one cannot neglect the unitary nature of the quantum dynamical evolution from a pure initial state. This is the case, for instance, in a cosmological setting: the problem was studied long ago by Kobzarev, Okun and Voloshin [157], and then by Coleman and Callan [158–160], finding also applications in inflationary models of the universe [161]. In addition, unitary evolution plays a crucial role in recent experiments with ultracold matter, which make it possible to investigate analogous false-vacuum-decay phenomena in coherent quantum many-body systems, where the nucleation is driven by quantum rather than thermal fluctuations (see, e.g. Ref. [162] for a recent experiment in this direction). Finally, there are quantum optimization algorithms [163–165], which are designed to find the ground state of a classical Ising model (a computationally NP-hard task in the case of an Ising spin glass in dimension larger than three or in two dimensions with a magnetic field [166]), but can incur several dynamical drawbacks associated with classical or quantum effects [167–169]. One can only expect that, in the near future, quantum simulators will allow finely controlled explorations of this physics using table-top experiments, allowing the observation of more counter-intuitive effects of coherent quantum dynamics.

With these motivations in mind, here we set to study the unitary evolution of nucleated vacuum bubbles in the two-dimensional ( $2d$ ) ferromagnetic quantum Ising model with longitudinal and transverse fields of strengths  $h$  and  $g$ , respectively. These vacuum bubbles correspond, to a first approximation, to regions on the lattice with a certain spin orientation, surrounded by a sea of spins with opposite orientation. We find that the limit of large Ising coupling  $J \gg |h|, |g|$  is amenable to several simplifications: this is due to the emergence of a constraint on the length of the interface, which separates the regions of opposite spin alignment in the initial state.

In this context, we address the issue of Hilbert space fragmentation, recently investigated in Refs. [170, 171], and elaborate on the effective Hamiltonian governing the dynamics. Such effective Hamiltonian further simplifies, and becomes amenable to analytical treatment, when restricted to two classes of initial states. The first is defined by the presence of a strip of aligned consecutive spins, running along one of the principal axes of the square lattice; the second, by an infinitely long “smooth” interface separating regions with oppositely aligned spins. The dynamics of the latter can be mapped onto a one-dimensional chain of fermions, which becomes integrable for  $J \rightarrow \infty$ . The integrability of this effective model is responsible for ergodicity breaking: we will show, for example, that the corner of a large bubble melts and reconstructs itself periodically in time, with period  $\propto 1/|h|$ . The same periodic dynamics generically characterizes an initially smooth profile, the evolution of which turns out to take a particularly simple form in a suitable continuum limit, which we discuss in detail. The proposed mapping on the fermionic chain allows us to study also interface fluctuations and the evolution of the entanglement entropy for an infinitely extended right-angled corner. In addition, we will also unveil surprising connections with classic mathematical results, concerning the limiting shape of random Young diagrams, as well as with similar problems in classical statistical physics.

Based on the mapping, we can trace back the observed ergodicity breaking in the dynamics of the interface in  $2d$  to the Wannier-Stark localization of the single-particle eigenstates of the dual fermionic theory. Surprisingly, we find that, even moving away from the limit  $J \rightarrow \infty$  in a perturbation theory in  $g/J \ll 1$ , the emerging many-particle eigenstates of the resulting perturbative Hamiltonian are *Stark many-body localized* (MBL) [172, 173]: thus, they display the typical MBL phenomenology [103, 108, 110, 174, 175], which carries over to the  $2d$  quantum Ising model. As several works have questioned the existence of MBL in more than one spatial dimension [176, 177] (even in the disordered version of the model studied in Chapter 3), the present case provides a valuable example of a mechanism by which the non-ergodic dynamics of a

one-dimensional model renders the dynamics of the dual two-dimensional model non-ergodic. The phenomenology observed here is reminiscent of the confinement that takes place in  $1d$  [178, 179].

Moreover, our mapping from  $2d$  Ising to  $1d$  confined fermions can also be interpreted as a toy model of duality between a theory of string (the domain wall) in  $2+1$  dimensions, and a theory of particles in one less dimension [180–182], which becomes integrable in the limit of infinite string tension; in our case, the confinement of the fermions is not due to their interaction but to an external potential. Finally, the dynamics at the corners of large bubbles in a  $2d$  quantum ferromagnet turns out to be related to a measure concentration phenomenon for random Young diagrams, a well-known result to the mathematical community [183–187].

It is interesting to remark also that the  $2d$  quantum Ising model displays strong stability of magnetic domains even when, in the absence of external fields, a Floquet dynamics is considered, characterized by imperfect stroboscopic single-spin kicks [188]. Therefore, the interest in this model is renewed also by the possibility of probing different mechanisms for the breakdown of ergodicity, even if disorder-induced MBL is not present, as we will discuss in Chapter 3.

The rest of the Chapter is organized as follows. In Sec. 2.1 we briefly introduce the Ising model, discussing how it reduces to a so-called “PXP” model in the limit of strong coupling (Sec. 2.1.1), for which Hilbert space fragmentation is expected to occur (Sec. 2.1.2). In Sec. 2.2 we focus on the dynamics of the model in the infinite-coupling limit. In particular, in Sec. 2.2.1 we study strip-like initial configurations, while in Sec. 2.2.2 we consider more generic initial states, characterized by the presence of a smooth and infinite interface separating spins with opposite orientation. In Sec. 2.2.3 we describe the continuum limit of the latter, and the connections with a semiclassical limit for the single-particle dynamics. In Sec. 2.3 we focus on a subset of initial configurations belonging to the general class discussed in Sec. 2.2.2, i.e. a corner-shaped interface: in Sec. 2.3.1 we determine the average shape of such interface during the dynamics, while in Sec. 2.3.2 we study its fluctuations. In Sec. 2.3.3 we focus on the time evolution of the entanglement, discussing the computation of the entanglement entropy. In Sec. 2.3.4 we show the connection between the unitary dynamics of the interface of a corner and some known results concerning the phenomenon of Plancherel measure concentration in random Young diagrams. Moving to Sec. 2.4, we discuss how the emergent integrability can be broken, either in a domain of finite size (Sec. 2.4.1) or when the ferromagnetic coupling is no longer assumed to be infinitely large (Sec. 2.4.2 and 2.4.3), giving also a comparison between the lattice and the field-theoretic dynamics of false vacuum bubbles (Sec. 2.4.4). Finally, in Sec. 2.5 we present our conclusions and outlook.

## 2.1 Model

As anticipated in the Introduction, we are interested in the dynamics of the quantum Ising model on a two-dimensional square lattice. The Hamiltonian reads

$$H_{\text{Is}} = -J \sum_{\langle ij \rangle} \sigma_i^z \sigma_j^z - g \sum_i \sigma_i^x - h \sum_i \sigma_i^z, \quad (2.1.1)$$

where  $\sigma_i^{x,y,z}$  are Pauli matrices acting on a lattice site  $i \in \mathbb{Z}^2$ ,  $\langle ij \rangle$  indicates the restriction of the sum to nearest neighbors,  $g$  and  $h$  are the strength of the transverse and longitudinal magnetic fields, respectively, and  $J > 0$  is the ferromagnetic coupling. We set  $g > 0$ , while we let  $h$  take both positive and negative values: the sign of  $h$ , indeed, will be relevant in Sec. 2.4.2.

In thermal equilibrium at temperature  $T$ , this model displays a quantum phase transition at  $T = 0$  and  $h = 0$ , belonging to the universality class of the classical  $3d$  Ising model: upon decreasing  $g$  below a critical value  $g_c$ , it passes from a quantum paramagnet to a quantum ferromagnet,

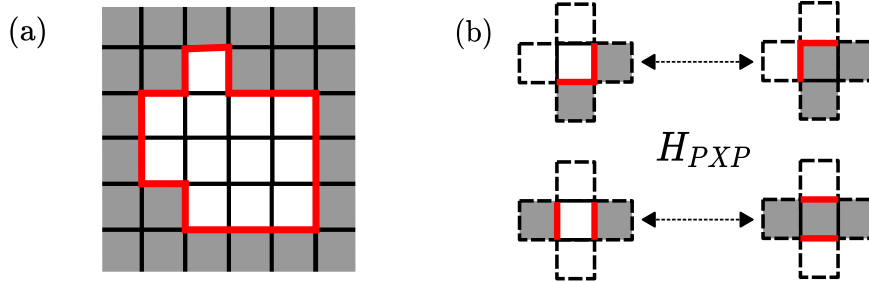


Figure 2.1: (a) Example of a “convex” (in the sense defined in Sec. 2.4.1) bubble of “down” spins ( $\downarrow = \square$ ) in a sea of “up” spins ( $\uparrow = \blacksquare$ ). Here each spin is represented by the surrounding square plaquette in the dual lattice. The side of a plaquette separating neighboring spins with the same or opposite orientation is marked in black or red, respectively, the latter corresponding to a portion of a domain wall. (b) Example of transitions allowed at the leading order in the coupling  $J$ , i.e. due to the term  $\propto g$  in  $H_{PXP}$ , see Eq. (2.1.7). Flipping the central spin makes the part highlighted in red of the domain wall move, in the corresponding plaquette, as represented in the figure. The remaining possible moves (not displayed) are obtained by considering all the configurations of the central spin and its neighbors, with the constraint that two neighbors are up and two down.

characterized by two degenerate, magnetized ground states spontaneously breaking the  $\mathbb{Z}_2$  symmetry. Upon increasing  $T$ , the ferromagnetic phase survives up to a finite critical temperature  $T_c$  (depending on  $g$  and  $J$ ), since the energetic cost of creating domains with reversed magnetization increases upon increasing their perimeter. At  $g = 0$ , the model becomes the  $2d$  classical Ising model, therefore displaying the corresponding critical properties. These critical properties also characterize the transition occurring on the line of thermal critical points, which joins the classical model at  $g = 0$  to the quantum critical point at  $T = 0$ . The longitudinal field  $h \neq 0$  breaks explicitly the  $\mathbb{Z}_2$  symmetry of the two possible ground states, lifting their degeneracy. Accordingly, the model at  $T = 0$  and  $g < g_c$  undergoes a first-order quantum phase transition as  $h$  crosses 0. As discussed in the Introduction, one expects that highly non-equilibrium false vacuum states exhibit a slow decay, through the nucleation of bubbles of characteristic size related to the inverse decay rate. With this background motivation in mind, below we will be interested in the fate of such bubbles, and more generally of interfaces, under the subsequent, coherent unitary evolution.

Studying the dynamics of  $2d$  interacting models constitutes *a priori* a formidable task: numerical methods are limited to very small system sizes or very short times. In addition, analytical tools are restricted to near-equilibrium conditions, or generally involve uncontrolled approximations, such as dynamical mean-field theory [189] or kinetic equations [190]. Despite these shortcomings, insight can be obtained from suitable limits. While the extreme paramagnetic regime  $J \ll |h|, g$  reduces to a set of weakly interacting “magnonic” excitations, the strongly-coupled ferromagnetic regime  $J \gg |h|, g$  retains a great part of the interacting nature of the problem. It is our purpose to show that, in such strong coupling limit, there exists a relevant class of highly excited, non-thermal initial states, the dynamics of which is amenable to analytical treatment. In particular, in the next Sections we show that the formal limit  $J \rightarrow \infty$  of infinitely strong ferromagnetic coupling actually renders a highly non-trivial constrained dynamical problem, characterized by a fragmented Hilbert space.

### 2.1.1 Constrained dynamics in the strong-coupling limit

Starting from this Section, and throughout this Chapter, we will consider the strong-coupling limit  $J \gg |h|, g$ . In practice, we start by formally taking  $J = +\infty$ , while later on in Sec. 2.4.2 we will

relax this assumption. In this limit, it is particularly convenient to study the problem in the basis of the eigenstates  $\otimes_i |\uparrow/\downarrow\rangle_i$  of  $\sigma_i^z$  at each lattice site  $i$ , with  $\sigma_i^z |\uparrow\rangle_i = |\uparrow\rangle_i$  and  $\sigma_i^z |\downarrow\rangle_i = -|\downarrow\rangle_i$ . At the leading order in  $J$ , the model is actually diagonal (i.e., classical) in this basis and, up to a constant, the energy of each of these eigenstates is given by  $2Jl$ , where  $l$  is the number of distinct pairs of neighboring spins with opposite orientation. Accordingly, the Hilbert space  $\mathcal{H}$  at infinite coupling is fragmented into dynamically independent sectors with  $\mathcal{H} = \bigoplus_l \mathcal{H}_l$ , each sector  $\mathcal{H}_l$  being identified by  $l$  [1, 170]. Being  $J = +\infty$ , in fact, no transitions are actually allowed from a state in  $\mathcal{H}_l$  to one in  $\mathcal{H}_{l'}$ , unless  $l = l'$ , since the energy difference between them would be infinite. Note that, equivalently,  $l$  measures the total length of the domain walls that are present on the lattice, separating the regions with spins  $\sigma_i^z = +1$  from those with  $\sigma_i^z = -1$ . Accordingly, in the limit  $J \rightarrow \infty$ , *dynamical constraints* emerge, in the form of a *perimeter constraint* on the bubbles of spins aligned along the same direction. Stated more formally, the domain-wall length operator

$$\mathcal{L} = \frac{1}{2} \sum_{\langle i,j \rangle} (1 - \sigma_i^z \sigma_j^z), \quad (2.1.2)$$

is exactly conserved by  $H_{\text{Is}}$  in the  $J \rightarrow \infty$  limit.

As a consequence of the perimeter constraint, the dynamics of the model can be effectively studied by focusing on each sector  $\mathcal{H}_l$  separately, thereby reducing significantly the complexity of the problem. Let us start by determining the reduced Hamiltonian in  $\mathcal{H}_l$  by elementary reasoning. Since the total domain-wall length must be conserved, the only spins that can be flipped by the term  $\propto g$  in Eq. (2.1.1) are those that just displace an existing domain wall. In practice, these spins are characterized by having two neighbors up ( $\uparrow$ ) and two neighbors down ( $\downarrow$ ), such that their flipping does not change the number of distinct pairs of neighboring spins with opposite orientation, i.e., the length of the domain wall in the associated plaquettes. Considering the  $(4 \times 3)/2$  possible configurations of the four spins  $L_i/R_i/U_i/D_i$  which satisfy this constraint and are, respectively, left/right/above/below a site  $i \in \mathbb{Z}^2$  with a certain spin orientation, one easily gets convinced that the only allowed transitions are those generated by the following reduced Hamiltonian:

$$\begin{aligned} H_{\text{PXP}} = & -h \sum_i \sigma_i^z - g \sum_i (P_{L_i}^\uparrow P_{D_i}^\uparrow \sigma_i^x P_{R_i}^\downarrow P_{U_i}^\downarrow + P_{L_i}^\uparrow P_{D_i}^\downarrow \sigma_i^x P_{R_i}^\downarrow P_{U_i}^\uparrow \\ & + P_{L_i}^\downarrow P_{D_i}^\downarrow \sigma_i^x P_{R_i}^\uparrow P_{U_i}^\uparrow + P_{L_i}^\downarrow P_{D_i}^\uparrow \sigma_i^x P_{R_i}^\uparrow P_{U_i}^\downarrow + P_{L_i}^\uparrow P_{D_i}^\downarrow \sigma_i^x P_{R_i}^\uparrow P_{U_i}^\downarrow + P_{L_i}^\downarrow P_{D_i}^\uparrow \sigma_i^x P_{R_i}^\downarrow P_{U_i}^\uparrow), \end{aligned} \quad (2.1.3)$$

where we introduced the projectors

$$P_i^\uparrow := \frac{1 + \sigma_i^z}{2} = |\uparrow\rangle_{ii}\langle\uparrow|, \quad P_i^\downarrow := \frac{1 - \sigma_i^z}{2} = |\downarrow\rangle_{ii}\langle\downarrow|. \quad (2.1.4)$$

The term  $\propto h$  in Eq. (2.1.1), being diagonal in  $\sigma_i^z$ , is instead unaffected. One can recognize that Eq. (2.1.3) has the structure of a so-called PXP Hamiltonian [92].

The elementary procedure outlined above can be viewed as the first step of a systematic elimination, from a Hamiltonian with large energy gaps, of highly non-resonant transitions (i.e., involving states distant in energy). This is formally implemented by a perturbative unitary transformation known as Schrieffer-Wolff transformation [191]. In Sec. 2.4.2 we will be concerned with the possible additional contributions to Eq. (2.1.3) due to higher-order corrections  $O(J^{-1})$ .

We stress here that the constrained Hamiltonian in Eq. (2.1.3) is actually similar to the one describing strongly interacting Rydberg atom arrays [149, 192]. In this case, each spin-1/2 describes a trapped neutral atom, which can be in either its ground state ( $\downarrow$ ) or in a highly excited Rydberg

state ( $\uparrow$ ). The basic model Hamiltonian that describes a lattice of such strongly interacting atoms reads [192]

$$H_{\text{Ryd}} = \Delta \sum_i n_i + \Omega \sum_i \sigma_i^x + \sum_{i,j} V_{ij} n_i n_j \quad (2.1.5)$$

where  $n_i = (1 + \sigma_i^z)/2$  counts the local number of atoms excited to the Rydberg state while the interaction  $V_{ij}$  is very strong for neighboring sites and it decays rapidly as the distance  $|i - j|$  increases. Upon rearranging the various terms, Eq. (2.1.5) may be viewed as a  $2d$  quantum Ising model; the strong coupling  $V_{ij}$ , however, couples here to the operator  $n_i n_j$  rather than to  $\sigma_i^z \sigma_j^z$ . When this nearest-neighbor interaction becomes larger than all the other energy scales— as it happens in the so-called regime of Rydberg blockade—its dynamics is described by an effective constrained Hamiltonian,

$$H_{\text{Ryd}}^0 = \frac{\Delta}{2} \sum_i \sigma_i^z + \Omega \sum_i P_{Li}^\dagger P_{Di}^\dagger \sigma_i^x P_{Ri}^\dagger P_{Ui}^\dagger. \quad (2.1.6)$$

which is obtained from Eq. (2.1.5) by setting  $V_{ij} \rightarrow \infty$  for neighboring atoms  $\langle ij \rangle$  and  $V_{ij} = 0$  otherwise. In this case, pairs of neighboring excited atoms are completely frozen, and an atom can flip only if all its four neighbors are in the ground state, which is expressed by the last term in Eq. (2.1.6). The Hamiltonian in Eq. (2.1.3), instead, imposes a different form of the constraint, which implements the local perimeter-conserving motion of domain walls. It is interesting to note, however, that the two constraints differ only by a strong longitudinal field term, which can be adjusted to transform one into the other. Specifically, by identifying  $V \equiv -4J$ , it is sufficient to take a single-atom energy level detuning  $\Delta \equiv 2J + h$  to obtain the Ising model (2.1.1) and hence, in the regime of Rydberg-blockade, the effective Hamiltonian in Eq. (2.1.3)<sup>1</sup>.

The Hamiltonian in Eq. (2.1.3) can be alternatively written via a shorthand notation, which describes graphically the transitions induced on the part of domain wall (in red) existing in the square plaquette surrounding a spin (i.e. the dual lattice), due to its allowed flipping (see also Fig. 2.1):

$$H_{\text{PXP}} = -h \sum_i \sigma_i^z - g \sum_i \left( |\ulcorner\rangle_{ii} \langle \llcorner| + |\lrcorner\rangle_{ii} \langle \urcorner| + |\sqsupset\rangle_{ii} \langle \sqsubset| + \text{H.c.} \right). \quad (2.1.7)$$

Here, the transitions due to the coupling  $g$  are apparent: either a domain wall corner is moved across the diagonal of a plaquette ( $\ulcorner \leftrightarrow \llcorner$  or  $\lrcorner \leftrightarrow \urcorner$ ), or two parallel segments of the domain wall are recombined across opposite sides of the plaquette ( $\sqsupset \leftrightarrow \sqsubset$ ). These moves guarantee the conservation of the domain wall length.

## 2.1.2 Hilbert space fragmentation

The convenient notation of Eq. (2.1.7) makes it possible to analyze the fate of the dynamics of large portions of the  $2d$  lattice in various cases. For instance, consider multiple, distant spins oriented up, i.e. with  $\sigma^z = +1$ , embedded in a sea of oppositely aligned spins, with  $\sigma^z = -1$ . This configuration is fully frozen, as no allowed transition can shift any of the domain walls. Thus, all of these states are eigenstates of the constrained Hamiltonian (2.1.7). This simple example—easily generalizable to many others [170]—shows that individual sectors  $\mathcal{H}_l$  are, in general, further heavily fragmented. More formally, one can introduce the notion of *Krylov subspace* of a state  $|\psi_0\rangle$ : by definition, it is the subspace of  $\mathcal{H}$  spanned by the set of vectors  $\{|\psi_0\rangle, H|\psi_0\rangle, H^2|\psi_0\rangle, \dots\}$ , where

<sup>1</sup>We note, however, that this might be problematic at an experimental level, as the Rydberg interactions are very sensitive to the precise position of the trapped atoms, resulting in unwanted noisy fluctuations of the longitudinal field. We thank Hannes Pichler for this clarification (private communication).

$H$  is the Hamiltonian of the system. With this definition, one recognizes that the Krylov sector of a state  $|\psi\rangle \in \mathcal{H}_l$  may not coincide with the full  $\mathcal{H}_l$ , but instead represent a finer shattering. A detailed study of the Krylov sectors of the model under consideration was presented in Ref. [171]; here, instead, we will be concerned mainly with the *dynamical effects* of the fragmentation on some physically relevant states. This is what we set out to study in the next Section.

## 2.2 Infinite-coupling dynamics for strips and smooth domain walls

In the previous Section we have argued that, in the limit of large  $J$ , the dynamics of the  $2d$  quantum Ising model simplifies significantly, because of the presence of emergent constraints. Here, we show that this simplification is really substantial in some particular cases, as it leads to simple *one-dimensional effective models*.

From Eq. (2.1.7), one can see that the first two terms ( $|\ulcorner\rangle_{ii}\langle\llcorner| + \text{H.c.}$  and  $|\lrcorner\rangle_{ii}\langle\urcorner| + \text{H.c.}$ ) correspond to the translation of a domain wall, while the last one ( $|\blacksquare\rangle_{ii}\langle\blacksquare| + \text{H.c.}$ ) cuts two nearby portions of domain wall into two halves and recombines those belonging to different portions. If the initial condition has a geometry that allows only one of the two types of transitions, then it is possible to gain further analytical control of the dynamics. In particular, we show in Sec. 2.2.1 that initial conditions consisting of a thin, pseudo- $1d$  domain are only affected by interface-recombining moves. This allows us to make a connection with  $1d$  PXP and confining Ising models. In Sec. 2.2.2, instead, we show that if the  $2d$  lattice is cut by a single, Lipschitz-continuous interface (this notion will be clarified further below), then its dynamics can be studied via an effective  $1d$  model of non-interacting fermions in a linear potential. Its emergent integrability allows us to predict the  $2d$  evolution exactly, and to describe precisely how ergodicity is broken.

### 2.2.1 Strip-like configurations

In this Section, we consider a class of initial configurations that are essentially one-dimensional, as the one depicted in Fig. 2.2. As it was also pointed out in Ref. [170], for this type of states it is possible to establish an explicit connection with  $1d$  PXP models. We show here that, when the initial configuration  $|\Psi_0\rangle$  has no overlap with scarred states<sup>2</sup>, it is possible to calculate the asymptotic magnetization of the bubble.

We focus on an initial condition consisting of a linear strip of  $L$  consecutive down spins ( $\downarrow$ ), along one of the principal lattice axes, surrounded by up spins ( $\uparrow$ ). In the Krylov sector of this configuration (see Sec. 2.1.2 above), and in the absence of longitudinal magnetic field (i.e. for  $h = 0$ ), the PXP Hamiltonian (2.1.3) reduces to the one-dimensional PXP Hamiltonian familiar from tilted bosonic traps [193], one-dimensional Rydberg-blockaded arrays [194], or dimer models [195]. Indeed, due to the perimeter constraint, neither the spins outside the initial strip nor those at its two ends can be flipped by  $H_{\text{PXP}}$ ; accordingly, the only dynamical degrees of freedom are the internal spins initially set to be down. This reduces the full,  $2d$  dynamics to an effectively  $1d$  dynamics.

For convenience, we label the accessible basis states by the corresponding  $1d$  configuration of the spins in the strip; the initial state  $|\Psi_0\rangle$  is therefore denoted by  $|\Psi_0\rangle = |\downarrow\downarrow\dots\downarrow\rangle$ . Assuming for

---

<sup>2</sup>Quantum many-body scars denote special eigenstates of the spectrum that does not satisfy the eigenstate thermalization hypothesis. This means that the expectation values of observables evaluated on such states do not attain the thermal value, even if their energy density corresponds to infinite temperature states.

the moment  $h = 0$ , the Hamiltonian (2.1.3) reduces to

$$H_{\text{PXP},1d} = -g \sum_{j=2}^{L-1} P_{j-1}^\downarrow \sigma_j^x P_{j+1}^\downarrow, \quad (2.2.1)$$

as the spins above and below the strip are fixed to be up. Above, we are also taking into account that the first and last spin of the strip cannot be flipped.

Because of the constraints, not all  $1d$  configurations are dynamically accessible: for example, those containing two or more consecutive spins up are not. This implies that the spins adjacent to a spin up are down, and that completely fragmented configurations consist of singlets or pairs of spins down, separated by single spins up, see Fig. 2.2a. Denoting by  $l$  the number of spins that are reversed compared to the initial configuration, the number  $C(L, l)$  of accessible basis states in the strip of length  $L$  satisfies the recursion relation (see also App. A.1)

$$C(L, l) = C(L - 1, l) + C(L - 2, l - 1), \quad (2.2.2)$$

which has solution

$$C(L, l) = \binom{L - l - 1}{l}, \quad (2.2.3)$$

once the initial condition  $C(L, 0) = 1$  for all  $L$  is enforced. The maximum number  $l_{\text{max}}$  of spins that can be flipped satisfying the perimeter constraint is

$$l_{\text{max}} = \left\lceil \frac{L - 2}{2} \right\rceil, \quad (2.2.4)$$

and the total number of accessible configurations is therefore given by

$$F_L = \sum_{l=0}^{l_{\text{max}}} C(L, l), \quad (2.2.5)$$

i.e. by the  $L$ -th Fibonacci number [196].

It is worth recalling that PXP Hamiltonians exhibit quantum many-body scars [92], i.e. particular eigenstates that violate the eigenstate thermalization hypothesis [37, 38]. The number of such eigenstates increases only algebraically upon increasing the system size, making them very rare in the many-body spectrum. However, they profoundly affect the dynamical properties of particular initial configurations: for instance, the Néel state  $|\mathbb{Z}_2\rangle = |\downarrow\uparrow\downarrow\uparrow\dots\rangle$  exhibits remarkable long-lived revivals, as discovered in early experimental explorations [87]. While it has become clear that these non-thermal eigenstates slowly disappear in the large-size limit of the PXP model, their ultimate origin is presently unclear, despite significant research efforts, and is the subject of an active ongoing debate [90]. On the other hand, the initial state  $|\Psi_0\rangle$  we consider here is not significantly affected by quantum many-body scars [90, 92]. Accordingly, it is expected that the magnetization profile along the chain at long times is compatible with an assumption of ergodicity, i.e. that all allowed configurations (having the same expectation value of the energy) will be occupied with uniform probability. Under this assumption, the long-time average magnetization  $\langle m_L(j) \rangle$  at position  $j = 1, \dots, L$  along the strip of length  $L$  is expected to be given by

$$\langle m_L(j) \rangle = 2 \frac{F_{L-j} F_{j-1}}{F_L} - 1, \quad (2.2.6)$$

as detailed in App. A.1. The explicit expression of the Fibonacci numbers [196],

$$F_n = \frac{\phi^n - (-\phi)^{-n}}{2\phi - 1} \quad (2.2.7)$$

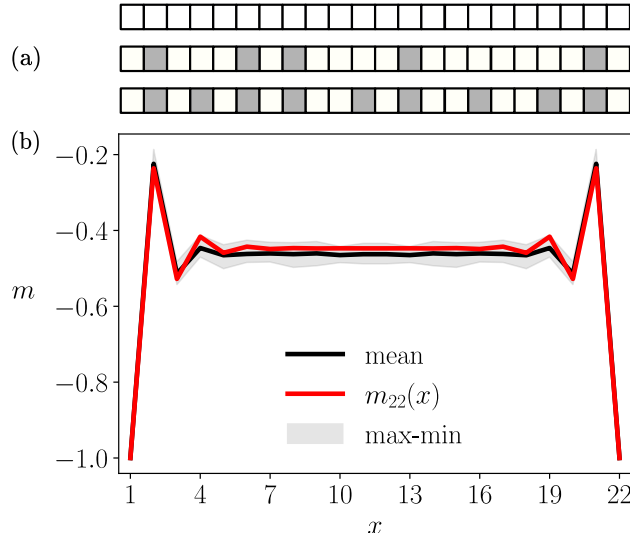


Figure 2.2: (a) The top row represents the initial state of the strip  $|\Psi_0\rangle$ ; the middle row shows an example of a configuration which can be dynamically reached from  $|\Psi_0\rangle$ ; the bottom row displays a completely fragmented configuration. (b) Magnetization along the strip of panel (a) at long times. The comparison between the analytical prediction ( $m_{22}(x) = \langle m_L(x) \rangle$ ), in red, corresponding to Eq. (2.2.6) and the numerical results for the magnetization is reported. The numerical analysis is performed by unitarily evolving the initial state. The plot shows the minimum and maximum magnetization for  $5000 < t < 10000$  (shaded gray area) and the magnetization for  $t = 10000$  (black). One can see a good agreement between the numerical simulations and the analytical prediction, showing that the classical sampling introduced in the text is effective in describing infinite-temperature magnetization.

in terms of the golden ratio  $\phi = (1 + \sqrt{5})/2$ , allows us to determine the resulting magnetization profile  $\langle m_L(j) \rangle$ . We compare it with numerical simulations for short strips in Fig. 2.2, showing fairly good agreement with the assumption of ergodicity. The magnetization, as expected, is fixed at the boundaries of the strip, due to the fact that fluctuations cannot occur there, while its absolute value decreases upon moving away from the boundaries. In particular, the value  $\langle m_{\infty, \text{bulk}} \rangle$  of the magnetization  $\langle m_L(j) \rangle$  in the middle of an infinitely long strip can be easily obtained by taking first the limit  $L \rightarrow \infty$  and then  $j \rightarrow \infty$  in Eq. (2.2.6), finding (see App. A.1)

$$\langle m_{\infty, \text{bulk}} \rangle = \frac{2}{(2\phi - 1)\phi} - 1 = -\frac{1}{\sqrt{5}}, \quad (2.2.8)$$

where we used Eq. (2.2.7). The (alternating-sign) approach of  $\langle m_{\infty}(j) \rangle$  to  $\langle m_{\infty, \text{bulk}} \rangle$  upon increasing  $j$  turns out to be exponential, with a rather short characteristic length  $\xi_b = -1/\ln|1 - \phi^{-1}| \simeq 1.04$ . The derivation of this fact is provided again in App. A.1, see Eq. (A.1.2).

The solution presented above applies to the case of a single strip of reversed spins running along one of the principle lattice axes. In the presence of more than one strip (possibly having different orientations), the same results apply to each strip separately as long as the spins belonging to two different strips do not have a common nearest neighbour. In fact, in case they have one, a change of its orientation might cause the interfaces of the two strips to merge and, due to the resulting shape, the term  $|\ulcorner\rangle_{ii}\langle \llcorner| + |\llcorner\rangle_{ii}\langle \urcorner| + \text{H.c.}$  in the effective Hamiltonian (2.1.7) would contribute to the dynamics as well. In particular, it is easy to realize that the initial condition  $|\Psi_0\rangle$  discussed above is dynamically connected with the configuration consisting of the largest rectangular “envelope”, which contains all initial strips with at least one common nearest-neighbor. While the dynamics

in this case turns out to be highly non-trivial, in Sec. 2.3 we will focus on what happens to one of the corners of this rectangular envelope when it is sufficiently extended.

We conclude this Section by noting that what we have done, essentially, was to compute local observables in the infinite-temperature ensemble within the Krylov sector of the initial configuration  $|\Psi_0\rangle$ , instead of computing the expectation values on  $|\Psi_0(t)\rangle$ . The two procedures are equivalent, since the initial state  $|\Psi_0\rangle$  lies in the middle of the spectrum (and thus is an infinite-temperature state<sup>3</sup>)<sup>4</sup>, and the  $1d$  PXP model is ergodic [90, 92].

### 2.2.2 Smooth domain walls on the lattice

In the previous Section, we considered strip-like initial configurations, the dynamics of which involved only the operators  $|\dashv\rangle\langle\vdash| + \text{H.c.}$  of Eq. (2.1.7), i.e. only domain-wall-breaking transitions. We now turn to a different family of initial states for which, instead, the only involved operators are  $|\llcorner\rangle\langle\lrcorner| + \text{H.c.}$  or  $|\ulcorner\rangle\langle\llcorner| + \text{H.c.}$ : thus, solely domain-wall-moving transitions are generated.

Being the systems ergodic, this assumption might seem not allowed. In fact, the dynamics can be pictured as a quantum walk on the graph of the exponentially many possible configurations of the domain wall of length  $\ell$ . At long times, the domain wall may be naively expected to explore all the dynamically accessible configurations and, in particular for  $h = 0$ , to dissolve into  $O(\ell)$  small bubbles—the most entropic macrostate. At short times, however, the dynamics generates local quantum fluctuations of the interface starting from its corners, as neither inner/outer spins, nor spins adjacent to a flat portion of the interface can flip. It is thus meaningful to focus the attention on smooth portions of the interface.

For later convenience, let us rotate by a  $\pi/4$  angle with respect to the vertical and horizontal directions of the square lattice on which the model is defined, such that the lattice axes are oriented along the diagonals of the quadrants of the standard coordinate system, as shown in Fig. 2.3. Then, let us consider an interface separating a domain of spins up ( $\uparrow = \blacksquare$ ) from one of spins down ( $\downarrow = \blacklozenge$ ), highlighted in red in Fig. 2.3. We require that such an interface varies only slowly, so that it can be thought of as the graph of a function in the rotated frame, see Fig. 2.3. More precisely, the interface profile  $\mu(x)$  should be described by a quantum superposition of functions  $\mu_0 : \mathbb{Z} \rightarrow \mathbb{Z}$  which are *Lipschitz-continuous* on the lattice, i.e.

$$|\mu_0(x) - \mu_0(y)| \leq |x - y|, \quad \forall x, y \in \mathbb{Z}. \quad (2.2.9)$$

Let us remark that, since only the operators  $|\llcorner\rangle\langle\lrcorner| + \text{H.c.}$  or  $|\ulcorner\rangle\langle\llcorner| + \text{H.c.}$  of the Hamiltonian in Eq. (2.1.7) act on these configurations, the Krylov sector of a Lipschitz state contains only Lipschitz states. Accordingly, the unitary dynamics starting from such configurations involves only Lipschitz states and their superpositions, and cannot generate kinks or overhangs of the interface. Two-dimensional initial states of this type, other than being rather generic in the context of interface dynamics, are interesting because they can be alternatively described as states of a corresponding *one-dimensional* system. The mapping simply consists of associating to each downward segment of the interface an empty site on the  $1d$  chain, and to each upward segment a site occupied by a particle (see Fig. 2.3), following the interface line from left to right. In practice, this mapping amounts to a differentiation: in fact, one associates an empty (resp. occupied) site if the domain-wall derivative is negative (resp. positive). As a consequence, the interface profile  $\mu(x)$  can be

<sup>3</sup>In the middle of the spectrum, the density of states is typically maximal (in the cases we consider), which means that the maximum of the microcanonical entropy is peaked around the middle of the spectrum, leading to infinite temperature.

<sup>4</sup>That  $|\Psi_0\rangle$  lies in the middle of the spectrum follows from the fact that, first, it holds  $\langle\Psi_0|H|\Psi_0\rangle = 0$ ; and second, that the spectrum is symmetric around zero ( $H_{\text{PXP},1d}$  commutes with the space reflection operator  $I$ , and anti-commutes with the spectral reflection operator  $C = \prod_j \sigma_j^z$  [197]).

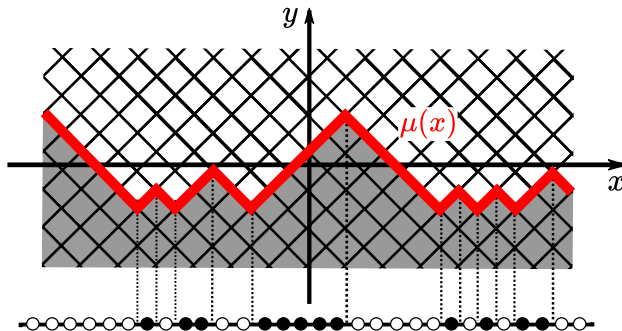


Figure 2.3: Graphical representation of the mapping from the  $2d$  Lipschitz interface to the  $1d$  fermionic chain. Moving from left to right, each downward segment corresponds to an empty site on the chain, while an occupied site is associated to each upward line. For completeness notice that, in doing the projection, the lattice spacing on the chain is reduced by a factor  $\sqrt{2}$  compared to the original one on the  $2d$  lattice.

reconstructed by “integrating” the density profile  $n(x)$  on the chain [198–201]:

$$\mu(x) = \sum_{y \leq x} [2n(y) - 1] + \text{const.} \quad (2.2.10)$$

The mapping described above works also in a classical setting, where a fluctuating interface induces on the  $1d$  particles an effective dynamics, as the simple exclusion processes [202–204] (more on this at the beginning of Sec. 2.3). In the quantum setting, the statistics of the particles plays a fundamental role. For the case under consideration—i.e. the  $2d$  quantum Ising model—these particles have to be hard-core bosons, because at most one particle can be present at a lattice site, and those at different sites commute. Applying a Jordan-Wigner transformation, these hard-core bosons can be equivalently represented as fermions. From now on we will adopt this more convenient representation.

Having set up the mapping between the accessible basis states of the two systems, we can proceed to determine the  $1d$  Hamiltonian on the chain, corresponding to the  $2d$  PXP Hamiltonian (2.1.7). With a bit of reasoning, one notices that each allowed spin flip in  $2d$  (which induces one of the transitions  $\checkmark \rightleftharpoons \wedge$  in the interface of Fig. 2.3) corresponds to a fermion hop along the chain. At the same time, in the presence of the longitudinal magnetic field  $h \neq 0$ , each spin flip in  $2d$  contributes with a  $\mp 2h$  energy difference depending on the corresponding upward/downward direction of the domain-wall transition  $\checkmark \rightleftharpoons \wedge$ , and therefore every fermion hop must be accompanied by the same energy change. This is achieved by introducing a linear potential in the  $1d$  Hamiltonian such that a particle jumping to the right (resp. left) gains (resp. loses) an energy  $2h$ . The same procedure applied to off-diagonal elements fixes the hopping term of the chain, leading to the fermionic Hamiltonian

$$H_F = -g \sum_x \left( \psi_x^\dagger \psi_{x+1} + \text{H.c.} \right) + 2h \sum_x x \psi_x^\dagger \psi_x, \quad (2.2.11)$$

defined up to a constant related to the choice of the origin of  $x$ .

Equation (2.2.11) is the well-known Wannier-Stark Hamiltonian [205]. It is diagonalized by the unitary transformation

$$b_m = \sum_{x \in \mathbb{Z}} J_{x-m}(\gamma) \psi_x, \quad (2.2.12)$$

where  $\gamma := g/h$  and  $J_\nu(z)$  is the Bessel function of the first kind, yielding

$$H_{\text{F,diag}} = 2h \sum_{m \in \mathbb{Z}} m b_m^\dagger b_m. \quad (2.2.13)$$

The energy spectrum is thus given by a set of equally spaced levels  $E_m = 2hm$ , insensitive to  $g$ . We anticipate that this feature will be important in the discussion about non-ergodicity, further below in Secs. 2.4.2–2.4.3.

In terms of the functions introduced above we are now able to predict the dynamics of any Lipschitz initial state  $|\Psi_0\rangle$ . In fact, such a state can be expressed as

$$|\Psi_0\rangle = \prod_k \psi_{x_k}^\dagger |0\rangle \quad (2.2.14)$$

on the chain, where the sequence  $\{x_k\}_{k \in \mathbb{Z}}$  contains the sites occupied at  $t = 0$  and  $|0\rangle$  is the vacuum of the  $1d$  chain. The time evolution of the operators  $b_m$  is simply given by  $b_m(t) = b_m(0)e^{-2ihmt}$ , and thus

$$\psi_x(t) = \sum_{m,y} J_{x-m}(\gamma) J_{y-m}(\gamma) e^{-2ihmt} \psi_y(0) = \sum_y e^{-i(x+y)ht} J_{x-y}(\omega_t) \psi_y(0), \quad (2.2.15)$$

where we introduced

$$\omega_t := 2|\gamma \sin(ht)| = 2 \left| \frac{g}{h} \sin(ht) \right|, \quad (2.2.16)$$

and used the completeness relation of the Bessel functions, Eq. (A.2.8). Similarly, by using the previous expression and by calculating some Wick contractions, one can determine the evolution of the average of the density  $n(x, t) = \psi_x^\dagger(t) \psi_x(t)$ , i.e.

$$\langle n(x, t) \rangle = \sum_{y,z} \sum_k J_{x_k-y}(\gamma) J_{x_k-z}(\gamma) J_{x-y}(\gamma) J_{x-z}(\gamma) e^{-2iht(z-y)} = \sum_k J_{x_k-x}^2(\omega_t), \quad (2.2.17)$$

where we used the property in Eq. (A.2.4), and defined the averages over the initial state

$$\langle \cdots \rangle := \langle \Psi_0 | \cdots | \Psi_0 \rangle. \quad (2.2.18)$$

As discussed above,  $\langle n(x, t) \rangle$  corresponds to the average slope of the quantum-fluctuating interface in the original  $2d$  system, and therefore describes its evolution<sup>5</sup>. Moreover, the expression for  $\langle n(x, t) \rangle$  in Eq. (2.2.17) clearly shows that the dynamics in the cases  $h = 0$  and  $h \neq 0$  are simply connected by the minimal substitution  $2g|t| \rightarrow \omega_t$  (and that the latter, in particular, is independent of the sign of  $h$ ).

Equation (2.2.17), and its dependence on time via  $\omega_t$  (Eq. (2.2.16)), imply that the dynamics on the chain—and therefore the full  $2d$  dynamics—is periodic with period  $\pi/|h|$ : this is due to the *Bloch oscillations* [205], which localize each fermion near its initial position  $x_k$ . In fact,  $J_{x_k-x}^2(\omega_t)$  in Eq. (2.2.17) decays exponentially fast upon increasing  $|x - x_k|$  beyond  $\omega_t$ , and therefore each fermion, during the evolution, explores a region of space of amplitude (in units of the lattice spacing)

$$\ell \simeq |g/h|. \quad (2.2.19)$$

This perfect localization is a feature of the  $J = +\infty$  limit, and of the presence of a nonzero longitudinal field  $h$  which makes  $\omega_t$  a periodic function of time. If, instead,  $h \rightarrow 0$ , one finds

<sup>5</sup>It is interesting to note that, by time-reversal symmetry, Eq. (2.2.17) can also be interpreted as the total probability of finding a single particle starting at  $x$  at time 0, in the subset of positions  $\{x_k\}$  at time  $t$ .

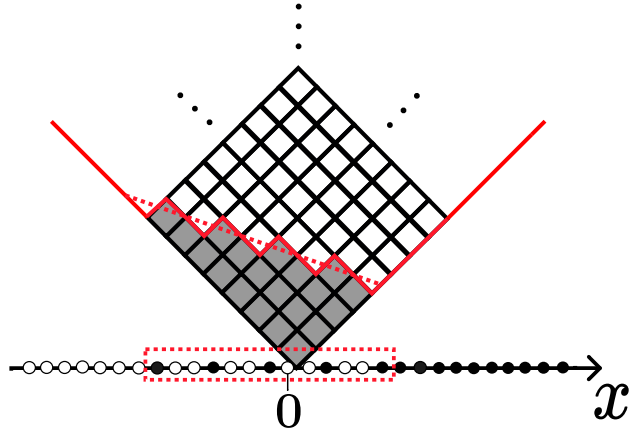


Figure 2.4: Initial configuration with a sequence of fermions alternated by  $s - 1 = 2$  empty lattice sites. As indicated by the dashed line, this corresponds to a flat tilted interface in the equivalent  $2d$  problem.

that  $\omega_t = 2g|t|$ . Accordingly, the dynamics of the  $1d$  system becomes ballistic, as the underlying fermionic excitations are free to move. Note that the presence of  $h$  induces periodicity in the time evolution already at the level of Eq. (2.2.15), which is the solution of the Heisenberg equation for  $\psi_x$ . We emphasize again that such periodicity is both due to the external field  $h$  and the presence of the lattice. In Secs. 2.4.2 and 2.4.3 we will investigate the extent to which the localization is preserved at finite but large  $J$ , and nonzero  $h$ .

In general,  $\langle n(x, t) \rangle$  cannot be calculated in closed form from Eq. (2.2.17) for an arbitrary initial condition  $\langle n(x, t = 0) \rangle = \sum_k \delta_{x_k, x}$ . However, in some special cases, this can be done. As an example, consider an initial state consisting of a sequence of fermions alternated by  $s - 1$  empty lattice sites, with  $x_k = sk$  for some  $s \in \mathbb{N}$  with  $s \geq 1$ . This corresponds to a domain wall in the  $2d$  lattice which is almost flat, with an approximate slope  $-(s - 2)/s$  (see Fig. 2.4 for a visual representation). With this initial state, the average profile  $\mu(x, t)$  can be determined from the average number density  $\langle n(x, t) \rangle$  on the chain (see Eq. (2.2.17)):

$$\langle n(x, t) \rangle = \sum_k J_{sk-x}^2(\omega_t) = \frac{1}{s} \sum_{0 \leq n < s} e^{2ixn\pi/s} J_0\left(2\omega_t \sin \frac{n\pi}{s}\right), \quad (2.2.20)$$

where the last equality follows from the integral representation of the Bessel functions, Eq. (A.2.12). At spatial scales much larger than the (unit) lattice spacing, i.e. for  $|x| \gg 1$ , the expression above implies

$$\langle n(x, t) \rangle \simeq 1/s, \quad (2.2.21)$$

because only the term with  $n = 0$  contributes to the sum for large  $|x|$ , due to the oscillating exponentials of the remaining terms. This result is expected, as the value  $1/s$  actually corresponds to the average occupation along the chain in the initial condition which, up to lattice effects, does not evolve in time. After summing Eq. (2.2.20) over space, as prescribed by Eq. (2.2.10), one obtains the average shape of the interface. In the limit  $|x| \gg 1$  this corresponds to  $\langle \mu(x, t) \rangle \simeq x(2/s - 1) + \text{const.}$ , i.e. to a time-independent flat interface, with the slope fixed by the initial condition. Accordingly, up to lattice effects, flat interfaces in the  $2d$  system do not evolve, independently of the underlying lattice: this actually suggests that a proper continuum limit of this lattice dynamics might emerge, as we discuss in more detail in the next Section.

### 2.2.3 Smooth domain walls on the continuum and the semi-classical limit

We now explore how to modify the parameters of the fermionic model discussed above in a way such that, after reinstating the lattice spacing  $a$ , a non-trivial continuum limit of the dynamics of the particle density, or of the corresponding (Lipschitz) interface, is obtained as  $a \rightarrow 0$ . In particular, in Sec. 2.2.3 we derive the dynamics of the fermion density and of the Lipschitz interfaces on the continuum, while in Sec. 2.2.3 we provide a physical interpretation of this dynamics in terms of a semiclassical picture.

#### Dynamics on the continuum

We begin by noting that Eq. (2.2.17) can also be rewritten in an integral form as

$$\langle n(x, t) \rangle = \int dy \rho(y) J_{y-x}^2(\omega_t), \quad (2.2.22)$$

where we introduced the initial density

$$\rho(y) = \sum_k \delta(y - x_k). \quad (2.2.23)$$

To discuss the continuum limit of these expressions, it is convenient to introduce an absolute value in the index of the Bessel function in Eq. (2.2.22), owing the symmetry in Eq. (A.2.3):  $J_{y-x}^2 \rightarrow J_{|y-x|}^2$ . The above expressions are valid in full generality, for any Lipschitz initial state on the lattice, completely specified by  $\rho(y)$ . In taking the continuum limit as we will describe below, this comb-like function eventually turns into a smooth function, which is obtained by properly rescaling the coordinates with the lattice spacing.

The continuum limit is expected to provide accurate predictions at large distances and long times if, correspondingly, the typical amplitude  $\ell$  of the Bloch oscillations given by Eq. (2.2.19) (in units of the lattice spacing  $a$ ) becomes large on the lattice scale, but attains a finite value when measured in actual units, i.e. if  $\ell a$  is finite as the formal continuum limit  $a \rightarrow 0$  is taken. According to Eq. (2.2.19), this is obtained by assuming  $h \sim a$  and therefore  $\gamma \sim a^{-1}$ , see the definition of  $\gamma$  after Eq. (2.2.12). Equivalently, the same goal can be achieved by requiring that  $g \sim a^{-1}$ . Moreover, as the dependence of the relevant quantities such as  $\langle n(x, t) \rangle$  and  $\langle \mu(x, t) \rangle$  on time  $t$  is only via  $\omega_t$  (Eq. (2.2.16)), which involves the product  $ht$ , a non-trivial limit is obtained by considering long times, with  $t \sim a^{-1}$  as  $a \rightarrow 0$ , but such that  $ht$  remains constant. In turn, this implies that  $\omega_t \rightarrow \omega_t/a$  in Eq. (2.2.22), see also Eq. (2.2.16). The scaling  $h \sim a$  actually corresponds to effectively diminishing the strength of  $h$  with respect to  $g$ , making it easier for fermions to move. In practice, it can be obtained by introducing a factor  $a$  in front of the linear potential in the Hamiltonian (2.2.11). This can be understood, in an equivalent manner, as the requirement that the external potential generated by a (finite) constant field  $E$  must be proportional to the physical position  $X := xa$  in the continuum: if  $V(X) = -EX = -Eax$ , where  $x \in \mathbb{Z}$  labels the lattice site, then one readily recognizes that  $h = Ea \propto a$ .

Quite generically, it is possible to infer the continuum limit of the density of fermions starting from Eqs. (2.2.22) and (2.2.23). In fact, after reinstating the lattice spacing  $a$  and introducing the actual coordinate  $X$  as above (and analogously  $Y := ay$ ), one can write

$$\langle n(X, t) \rangle = \int \frac{dY}{a} \hat{\rho}(Y) J_{|X-Y|/a}^2(\omega_t/a), \quad (2.2.24)$$

Above, with a slight abuse of notation, we use the same notation for the density on the continuum  $\langle n(X = ax, t) \rangle$  and on the lattice  $\langle n(x, t) \rangle$ . Moreover, we introduced

$$\hat{\rho}(Y) := a \sum_k \delta(Y - ax_k) = \rho(Y/a) \quad (2.2.25)$$

it is the initial density of fermions in the actual coordinates. As  $a \rightarrow 0$ , the comb-like function  $\hat{\rho}(Y)$  attains a more regular dependence on  $Y$ —with  $0 \leq \hat{\rho}(Y) \leq 1$  due to the fermionic nature of the particles on the chain—, and we can use Eq. (A.2.17) to determine the continuum limit of the kernel  $J_{|y-x|}^2$ . Then, Eq. (2.2.24) in the limit  $a \rightarrow 0$  can be written as

$$\begin{aligned} \langle n(X, t) \rangle &\xrightarrow{a \rightarrow 0} \int_{-\infty}^{+\infty} dY \hat{\rho}(Y) \frac{\theta(\omega_t - |X - Y|)}{\pi \omega_t \sqrt{1 - |X - Y|^2 / \omega_t^2}} \\ &= \int_{-1}^1 dz \frac{\hat{\rho}(z\omega_t + X)}{\pi \sqrt{1 - z^2}}, \end{aligned} \quad (2.2.26)$$

where  $\theta(x)$  is the Heaviside step function:  $\theta(x \geq 0) = 1$  and  $\theta(x < 0) = 0$ . In Sec. 2.2.3 below we provide an interpretation of this expression in terms of the semiclassical limit of the fermion dynamics.

It is worth noticing that the kernel  $1/(\pi\sqrt{1 - z^2})$ , which appears in the previous equation, is normalized to 1 in the interval  $|z| \leq 1$  in such a way that, for  $t = 0$ , one recovers  $\langle n(X, t = 0) \rangle \rightarrow \hat{\rho}(X)$ . From this expression, it is also apparent that any initial condition of the fermions on the lattice, which translates into a space-independent  $\hat{\rho}$  on the continuum, does not actually evolve in the continuum limit. This is the case, for example, of the initial condition considered at the end of Sec. 2.2.2, with  $x_k = sk$  and  $s = 1, 2, \dots$ , for which (see Eq. (2.2.25))

$$\hat{\rho}(Y) = a \sum_{k \in \mathbb{Z}} \delta(Y - ask). \quad (2.2.27)$$

In the continuum limit, the sum above turns into an integral, i.e.  $\sum_{k \in \mathbb{Z}} f(ask) \xrightarrow{a \rightarrow 0} a^{-1} \int d\xi f(\xi)$  and therefore

$$\hat{\rho}(Y) \xrightarrow{a \rightarrow 0} \int_{-\infty}^{+\infty} d\xi \delta(Y - s\xi) = \frac{1}{s}. \quad (2.2.28)$$

By inserting this density on the continuum in Eq. (2.2.26), one readily finds Eq. (2.2.21). Note that, while on the lattice we considered integer values of  $s$ , in the continuum limit  $s$  can take any value  $s \geq 1$ , which corresponds to having an initial average density  $1/s$  of fermions on the lattice.

The linear and translationally-invariant structure of the relationship between the initial fermion density  $\langle n(X, t = 0) \rangle = \hat{\rho}(X)$  and its value  $\langle n(X, t) \rangle$  at a later time carries over to the corresponding average positions  $\langle \mu(X, t) \rangle$  of the interface, given that  $d\langle \mu(X, t) \rangle / dX = 2\langle n(X, t) \rangle - 1$ . This can be seen via integration by parts after having expressed  $\langle n(X, t) \rangle$  as the derivative of  $\langle \mu(X, t) \rangle$  on both sides of Eq. (2.2.26). Accordingly, in the continuum

$$\langle \mu(X, t) \rangle = \int_{-1}^1 dz \frac{\mu_0(z\omega_t + X)}{\pi \sqrt{1 - z^2}}, \quad (2.2.29)$$

where  $\mu_0(X)$  stands for the initial condition. Note that the fermionic constraint on the possible values of  $\hat{\rho}$  translates into the request that  $|d\langle \mu_0(X) \rangle / dX| \leq 1$ , as it is for a Lipschitz function on the continuum. On the lattice, on the other hand, even if there is a clear relation between the initial configuration of the chain and of the interface (given by the mapping), the linearity is not

present because of the fermionic nature of the particles. Indeed, while in the continuum one can multiply the particle density by a constant  $\kappa$  as long as  $0 \leq \rho_0$ ,  $\kappa\rho_0 \leq 1$ , the same cannot be done *locally* on the lattice.

Due to the positivity of the kernel, it is also rather straightforward to show that if the initial condition  $\mu_0(X)$  is a Lipschitz function with a certain constant, then the same applies to the evolved function  $\langle\mu(X, t)\rangle$ . As anticipated above, Eq. (2.2.29) clearly shows that any flat initial profile  $\mu_0(X) = \alpha X + X_0$  does not evolve in time (with possible dynamics occurring solely at the lattice scale).

More generally, if the variation of the initial interface  $\mu_0$  occurs on a length scale  $\ell_0$  much larger than  $\omega_t$ , the function  $\mu_0(Y = z\omega_t + X)$  on the r. h. s. of Eq. (2.2.29), can be expanded around  $Y = X$  (recall that  $|z| \leq 1$ ) and one finds that

$$\langle\mu(X, t)\rangle = \mu_0(X) + \frac{\omega_t^2}{4}\mu_0''(X) + \frac{3}{8}\frac{\omega_t^4}{4!}\mu_0^{(4)}(X) + O((\omega_t/\ell_0)^6). \quad (2.2.30)$$

This implies, inter alia, that a locally quadratic portion of the profile is simply shifted upward or downward depending on the sign of its curvature.

As an explicit application of Eq. (2.2.29), consider the case in which the initial interface is described on the continuum by  $\mu_0(X) = A\sin(\kappa X)$ , with  $|\kappa A| \leq 1$  for the Lipschitz condition to hold. From Eq. (2.2.29), one readily infers that  $\langle\mu(X, t)\rangle = AJ_0(\kappa\omega_t)\sin(\kappa X)$ , i.e. the shape of the boundary is not affected by the dynamics but its amplitude is periodically modulated. Generalizing this result, the linearity of the relationship between  $\mu_0$  and  $\mu$  allows us to conclude that if the initial profile has a spatial Fourier transform  $\tilde{\mu}_0(k)$  on the continuum, then  $\mu(X, t)$  has  $\tilde{\mu}(k, t) = J_0(k\omega_t)\tilde{\mu}_0(k)$  as its Fourier transform in  $X$ . This means that if the spatial average of the interface height is initially finite, i.e.  $\tilde{\mu}_0(k=0)$  is finite, then this average is not affected by the dynamics because  $\tilde{\mu}(k=0, t) = \tilde{\mu}_0(k=0)$ .

### Semiclassical limit

Equation (2.2.26) allows one to predict on the continuum the average fermion density  $\langle n(x, t) \rangle$  in terms of its initial value  $\langle n(x, t=0) \rangle = \hat{\rho}(X)$  for  $a \rightarrow 0$ . Interestingly enough, the same expression can be derived starting directly from a semiclassical model for the evolution of the effective excitations at the interface.

To see this more explicitly, consider the case of a single fermion evolving with Eq. (2.2.11) and take the classical limit of its Hamiltonian, which is given by (see e.g. Ref. [206])

$$\mathcal{H}(p, q) = -2g \cos p + 2hq, \quad (2.2.31)$$

in the phase space  $(q, p) \in \mathbb{R} \times [0, 2\pi)$ , with  $q$  the coordinate of the particle and  $p$  the conjugated momentum. Consequently, the equations of motion are

$$\dot{q}(t) = \partial_p \mathcal{H} = 2g \sin p(t), \quad (2.2.32)$$

$$\dot{p}(t) = -\partial_q \mathcal{H} = -2h, \quad (2.2.33)$$

that lead to

$$p(t) = (-2ht + p_0) \bmod 2\pi, \quad (2.2.34)$$

$$q(t) = q_0 - \frac{2g}{h} \sin(ht) \sin(ht - p_0), \quad (2.2.35)$$

where  $q_0$  and  $p_0$  indicate the initial values of  $q(t)$  and  $p(t)$ , respectively.

Since we are dealing with non-interacting fermions, in the classical analog we can consider a single particle located at a certain position  $q_0$  at time  $t = 0$ . As a consequence of the uncertainty principle, the momentum  $p_0$  of the particle will be distributed uniformly over the interval  $[0, 2\pi)$ , with a uniform probability density:  $P(p_0) = 1/(2\pi)$ . Accordingly, at a certain time  $t$  the position  $q(t)$  of the particle will have a distribution centered around  $q_0$ , with an amplitude  $|2g \sin(ht)/h| = \omega_t$ . The resulting distribution  $P(q(t))$  is obtained by inverting Eq. (2.2.35), yielding

$$P(q(t)) = \frac{\theta(\omega_t - |q(t) - q_0|)}{\pi\omega_t \sqrt{1 - [q(t) - q_0]^2/\omega_t^2}}. \quad (2.2.36)$$

This is exactly the same kernel of Eq. (2.2.26), with the identification  $q_0 \rightarrow Y$  and  $q(t) \rightarrow X$ . The procedure just outlined is very reminiscent of the hydrodynamics approach to free fermions [56] which, however, uses the Wigner function to extract the quantities of interest. Let us mention here (see Sec 2.3 for more details) that a genuine classical dynamics on the fermions, i.e. not obtained via a semiclassical limit, would give a distribution different from Eq. (2.2.36) and different limit shapes.

### 2.3 Infinite-coupling dynamics for an infinite corner

In the previous Section we have studied two particular cases—the strip-like configuration and a Lipschitz interface—for which the dynamical constraints emerging at infinite  $J$  significantly simplify the evolution of the interface, which then can be described in terms of an equivalent 1d model. In this Section, we specialize the generic case discussed in Sec. 2.2.2, by considering an interface shaped as in Fig. 2.5a, which is composed of two straight lines (parallel to the lattice directions) and a single, right-angled corner. This interface is Lipschitz-continuous in the sense of Eq. (2.2.9), and therefore the approach outlined in Sec. 2.2.2 can be applied.

The case of a corner-shaped interface is particularly instructive, because of several connections to other fields of physics and mathematics:

1. Its evolution can be thought of as the quantum counterpart of *corner growth models* studied in classical, non-equilibrium statistical mechanics [202, 207–210]. These models describe the process of erosion of crystals; the case considered here extends the investigation of the melting phenomenon to *quantum* crystals [211, 212]. In fact, while a flat interface (of the type considered in Sec. 2.2.2) can only fluctuate around its initial position, the corner configuration can be eroded indefinitely—if no other localization mechanism is present, as we will discuss below (see also Chapter 3). However, in comparing the quantum to the classical case one should bear in mind that, for the quantum model under consideration, the addition/removal of a block from the corner (i.e. a spin flip) is always a *coherent* process, while in the classical problems the removed blocks “dephase” in the liquid state before being possibly reattached to the solid.

It is also interesting to notice the following feature. According to the stochastic dynamics, which is usually implemented for the *classical* Ising model (corresponding to Eq. (2.1.1) with  $g = 0$ ), the possible transitions between different spin configurations occur with a rate which is biased by  $\exp(-\Delta E/T)$  (in a specific way that depends on the algorithm), where  $\Delta E$  is the energy difference between the final and the initial configuration and  $T$  the temperature of the bath. This implies, as expected on physical ground, that at zero temperature  $T = 0$  the possible transitions are those with  $\Delta E \leq 0$ . Assuming that the stochastic dynamics proceeds via randomly flipping single spins (as the coupling  $\propto g$  does in the quantum case), this implies that the allowed classical spin moves can be represented analogously to Eq. (2.1.7) as

- (a)  $\ulcorner \leftrightarrow \llcorner$ ,  $\llcorner \leftrightarrow \lrcorner$  and  $\lrcorner \leftrightarrow \urcorner$  for the fully reversible transitions with  $\Delta E = 0$  (or, more generally,  $\Delta E = o(J)$  for  $h = 0$ ). These are the moves contained in Eq. (2.1.7).
- (b)  $\sqsupset \rightarrow \lrcorner$ , its spatial  $\pi/2$  rotations, and  $\square \rightarrow \cdot$ . These moves, occurring as indicated by the arrows, are not reversible and correspond to  $\Delta E < 0$ , with  $\Delta E = O(J)$ .

Moves of type (b) are not present in Eq. (2.1.7). However, it is easy to realize that, when considering an initial state with an interface in the form of a corner or, more generally of a Lipschitz function, these moves as well as the third type of moves in (a) are inconsequential, making the classical and the quantum dynamics actually explore the same set of configurations. In a heuristics sense, they share the same Krylov space of configurations in the  $\sigma^z$ -basis. As a consequence, the mapping discussed in Sec. 2.2.2 and in Fig. 2.3 for the quantum interface can be applied also to the classical interface. This was done, e.g., in Refs. [187, 210, 213, 214]. The corresponding *classical* model is characterized by the classical equivalent of the fermionic statistics, i.e. by the constraint of exclusion in the occupation number of each lattice site which can be at most one, making it belong to the general class of *simple exclusion processes* (SEPs) [202, 203, 209]. In the absence of the external field  $h = 0$ , the only allowed transitions starting from a corner (see Fig. 2.5a for the conventions) are  $\blacktriangledown \rightarrow \blacktriangle$  and its reversed  $\blacktriangle \rightarrow \blacktriangledown$ , corresponding to flipping a spin inside a corner from its two possible initial states. Such moves have the same rate, and therefore each classical particle in 1d attempts jumps to the left or to the right empty neighboring sites with the same rate, resulting in the so-called *symmetric simple exclusion process* (SSEP). Due to the intrinsic (unbiased) diffusive nature of their dynamics, the growth of the interface turns out to be diffusive, while it is ballistic in the quantum case, as discussed further below. For  $h \neq 0$ , on the other hand, the transition  $\blacktriangledown \rightarrow \blacktriangle$  and its reversed  $\blacktriangle \rightarrow \blacktriangledown$  occur with different rates, depending on the sign and magnitude of  $h/T$ . In particular, for  $T = 0$  it turns out that the only allowed moves are  $\blacktriangle \rightarrow \blacktriangledown$  for  $h < 0$  and  $\blacktriangledown \rightarrow \blacktriangle$  for  $h > 0$ . This corresponds to the classical particle jumping only towards the empty neighboring site to the left or to the right depending on having  $h > 0$  or  $h < 0$ , i.e. to the so-called *totally asymmetric simple exclusion process* (TASEP). This model turns out to display generically a ballistic growth (see, e.g. Ref. [210]), while the quantum dynamics is actually localized for  $h \neq 0$ . In addition, also the resulting limit shape is different: we discuss this aspect in more detail further below in this Section.

2. Each configuration that is dynamically connected to the corner corresponds to a *Young diagram*, as detailed in Sec. 2.3.4. In particular, we will show an interesting connection between two seemingly unrelated measures on Young diagrams: the probability density of the quantum-fluctuating interface, which naturally emerges in the context of the  $2d$  Ising model, and the Plancherel measure, commonly studied in representation theory [183–186, 215–217].
3. Lastly, it is worth mentioning that in the case of a Lipschitz interface, and in particular of a corner, the mapping to free fermions points to an explicit form of *holography*: a two-dimensional quantum problem in strong-coupling limit is mapped to a free, simpler problem in one less spatial dimension. This is reminiscent of the AdS/CFT duality [180–182]: the interface in the Ising model is the string in two spatial dimensions (plus time as an additional coordinate), while the non-interacting fermions on the chain are the dual field theory. When the string tension  $J$  is large, the corresponding field theory is free. When the string tension decreases, the field theory becomes interacting and, in our case, no longer integrable.

However, in order to discuss the melting of a bubble and not of a simple corner, one has

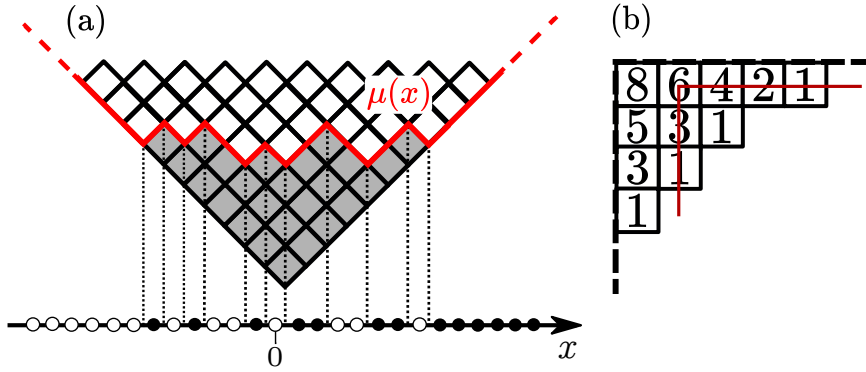


Figure 2.5: (a) Visual representation of the mapping introduced Sec. 2.2.2, applied to the corner configuration. The squares highlighted in gray correspond to the “eroded area”, i.e. to spins belonging to the corner which have been flipped from  $\downarrow = \square$  to  $\uparrow = \blacksquare$  due to the dynamics, forming a Young diagram. The interface  $\mu(x)$  is highlighted in red. (b) An example of Young diagram with the hook  $\mathfrak{h}(\square)$  indicated for each of its elements  $\square$ . The hook of a box  $\square$  is obtained by summing the number of boxes below it and to its right (highlighted in red for a specific box in the figure), plus one (corresponding to the box itself).

necessarily to introduce a more complicated theory of fermions, possibly with many species. It is worth noticing that going back further in time, one finds other connections between the Ising model and string theory, for instance the conjecture that the  $3d$  Ising model should be dual to a weakly-coupled string theory [218, 219] (for a recent discussion see Ref. [220]), although that is supposed to hold only at the critical point.

Before passing on, we finally notice that the initial condition for the  $2d$  Ising model discussed in this Section actually corresponds to a single domain wall on the fermionic chain, which separates the filled part of the chain from the empty one. Let us emphasize that, for  $h \neq 0$ , this initial configuration is close to the boundary of the spectrum of the Hamiltonian within the Krylov sector it belongs to. Indeed, such configuration maximizes (or minimizes, depending on the sign of  $h$ ) the expectation value of the Hamiltonian, being the state of maximal area of its Krylov sector. While in the limit  $J = \infty$  this observation is marginal, as the system is integrable (thus any initial configuration leads to a non-ergodic behavior), it becomes relevant at finite  $J$ , where the behavior of states at the middle of the spectrum can be also qualitatively different from the ones at the edges. This observation will be relevant in Secs. 2.4.2–2.4.3 when discussing the finite- $J$  corrections.

### 2.3.1 Average of the interface and its continuum limit

In the language of Sec. 2.2.2, the corner-shaped initial state corresponds on the fermionic chain to

$$|\Psi_0\rangle = \prod_{x>0} \psi_x^\dagger |0\rangle, \quad (2.3.1)$$

with a domain wall separating the empty half-chain for  $x \leq 0$  from the completely filled one at  $x \geq 1$ . In the language of electronics, this would be called a “maximum voltage bias” Fermi Sea. By applying the approach previously illustrated (in particular Eq. (2.2.17)), one easily finds that the average density profile on the chain is given by

$$\langle n(x, t) \rangle = \sum_{y<x} J_y^2(\omega_t). \quad (2.3.2)$$

Summing over space (see Eq. (2.2.10)), one obtains the average interface profile

$$\langle \mu(x, t) \rangle = 2 \sum_{y \leq x} (x - y) J_y^2(\omega_t) - x, \quad (2.3.3)$$

which, as anticipated, displays periodic oscillations with period  $\pi/|h|$  at each position  $x$ .

As discussed in Sec. 2.2.3, in order to determine the continuum limit of Eqs. (2.3.2) and (2.3.3) it is then sufficient to replace  $\gamma$  by  $\gamma/a$  and therefore  $\omega_t$  by  $\omega_t/a$  in Eqs. (2.3.2)–(2.3.3), after reinstating the lattice spacing  $a$ . Then the limit  $a \rightarrow 0$  can be determined as explained in Sec. 2.2.3. Alternatively, one can specialize the general prediction in Eq. (2.2.26) to the corner considered above, which corresponds to having, in the continuum,

$$\hat{\rho}(Y) = a \sum_{k=0}^{+\infty} \delta(Y - ak) \xrightarrow{a \rightarrow 0} \int_0^{+\infty} d\xi \delta(Y - \xi) = \theta(Y), \quad (2.3.4)$$

i.e. a homogeneous spatial density of fermions equal to 1 for  $Y \geq 0$  and an empty lattice for  $Y < 0$ . A straightforward integration leads to

$$\langle n(X, t) \rangle = \begin{cases} 0 & \text{for } X \leq -\omega_t, \\ \frac{1}{2} + \frac{1}{\pi} \arcsin(X/\omega_t) & \text{for } |X| < \omega_t, \\ 1 & \text{for } X \geq \omega_t, \end{cases} \quad (2.3.5)$$

which, for  $h = 0$ , agrees with the prediction of Ref. [221] for free fermions. Integrating over  $X$ , one finds

$$\langle \mu(X, t) \rangle = \omega_t \Omega(X/\omega_t), \quad (2.3.6)$$

with

$$\Omega(v) = \begin{cases} |v| & \text{for } |v| \geq 1, \\ \frac{2}{\pi} \left( \sqrt{1 - v^2} + v \arcsin v \right) & \text{for } |v| < 1. \end{cases} \quad (2.3.7)$$

Alternatively, this expression can be derived directly from Eq. (2.2.29), by using  $\mu_0(X) = [2\theta(X) - 1]X$  as the initial condition. In the right corner of Fig. 2.6 we report the exact interface evolution expressed by Eq. 2.3.6; the inset shows the corresponding evolution of the fermionic density Eq. 2.3.5.

Equations (2.3.6) and (2.3.7) can be easily generalized to the case of a Lipschitz corner in which, however, the slopes of the interface in its two sides are not the same. On the lattice, this corresponds to having a certain average density of fermions on the left of the origin and a different one on its right. In fact, consider an initial profile that is linear for both  $X < 0$  and  $X > 0$ , but with two different slopes  $\alpha_-$  and  $\alpha_+$ , respectively, and that fulfills  $\mu_0(X = 0) = 0$ . Such a profile must take the form

$$\mu_0(X) = [\alpha_- \theta(-X) + \alpha_+ \theta(X)]X. \quad (2.3.8)$$

The right-angled corner considered above corresponds to  $\alpha_{\pm} = \pm 1$ . With this  $\mu_0(X)$ , Eq. (2.2.29) implies that

$$\langle \mu(X, t) \rangle = \frac{\alpha_+ + \alpha_-}{2} X + \frac{\alpha_+ - \alpha_-}{2} \omega_t \Omega(X/\omega_t), \quad (2.3.9)$$

where  $\Omega(v)$  is given by Eq. (2.3.7). In fact, this expression simply follows from the linearity of the equation and from the result reported above for the right-angled corner.

Remarkably, the function  $\Omega(v)$  in Eq. (2.3.7) first appeared in the context of random Young diagrams [183–185]; we will elaborate more on this point in Sec. 2.3.4. Here, instead, we comment

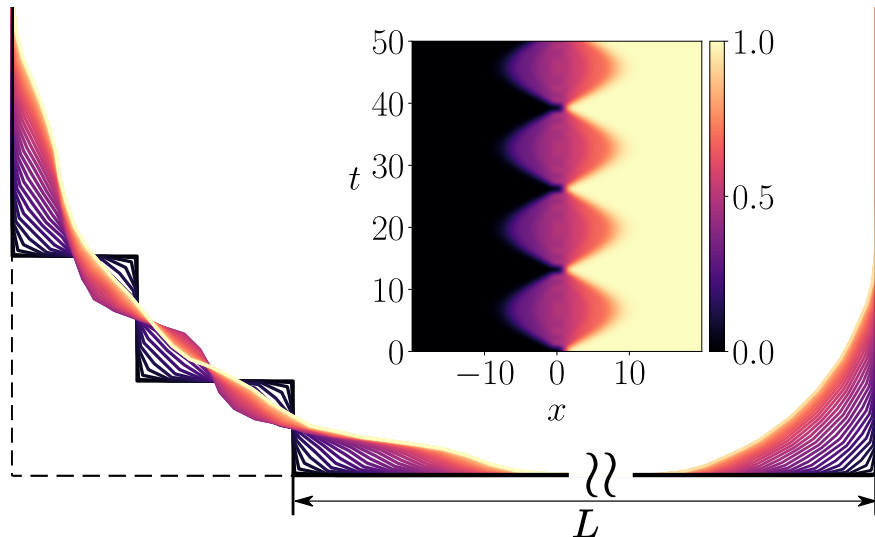


Figure 2.6: Snapshots of the time evolution of two corners separated by a large distance  $L$ , for  $g = 1$ ,  $h = 0.24$ . The black initial profile evolves periodically as indicated by the various colors, reaching the yellow line at half period  $t = \pi/(2|h|)$  before receding towards the initial condition. (Inset) Time evolution of the density profile  $\langle \psi_x^\dagger(t) \psi_x(t) \rangle$  of the fermionic chain, starting from the state  $|\Psi_0\rangle$  corresponding to the right corner of the main figure.

on the connection between the dynamics studied above and the *classical* melting processes which were mentioned at point 1. of the introduction to this Section. In fact, in the cases of the SSEP or the TASEP, the stochastic dynamics starting from a completely filled half-line—corresponding to the dynamics at zero temperature of a corner in the Ising model—can be solved, obtaining the large-time behaviour of the density of particles (briefly reported in App. A.4). As anticipated at the beginning of this Section, the SSEP is, in a sense, the classical analog of the quantum dynamics with  $h = 0$ , while the TASEP of the dynamics with  $h \neq 0$ . It turns out, however, that the scaling functions describing the erosion of the corner (which occurs diffusively for SSEP and ballistically for TASEP), via the same mapping described in Sec. 2.2.2, have a different functional form compared to  $\Omega$  of Eq. (2.3.7) (see App. A.4). This fact highlights how the quantum and classical dynamics turn out to be quantitatively and qualitatively different in spite of their many similarities. In Sec. 2.3.4 we will discuss how this difference emerges also in terms of *concentration of probability measures*, showing that a simple entropic argument concerning the accessible configurations is not sufficient for explaining the limiting shapes of the interfaces, but that, as expected, also the classical or quantum nature of the underlying microscopic dynamics matters.

### 2.3.2 Fluctuations of the interface

The approach described in the previous Section allows one to determine not only the average position of the quantum-fluctuating interface, but also its fluctuations. While presenting the complete calculation in App. A.3, we report here the final result for the connected two-point function of the density:

$$\langle n(x, t) n(y, t) \rangle_C = \delta_{xy} \sum_{i>0} J_{i-x}^2(\omega_t) - \mathcal{B}^2(x, y; \omega_t), \quad (2.3.10)$$

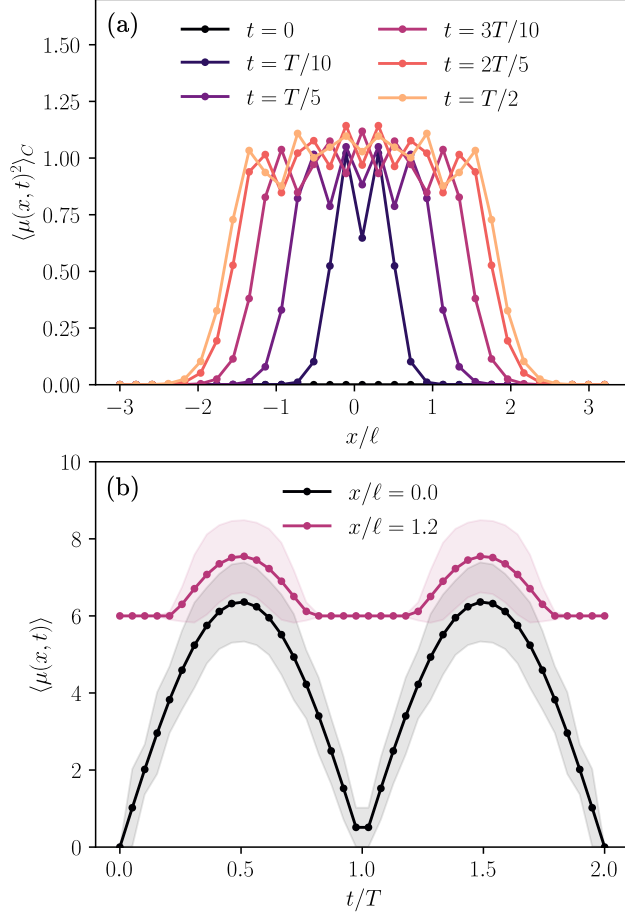


Figure 2.7: Fluctuations of the interface profile, quantified via  $\langle \mu^2(x, t) \rangle_C$ , starting from the infinite corner at  $t = 0$ . (a) Space dependence of  $\langle \mu^2(x, t) \rangle_C$  for various values of the time  $t$  within a half period. Because of the presence of the linear external potential also the fluctuations of the interface periodically return to the original value. (b) Time dependence of the average interface position  $\langle \mu(x, t) \rangle$  (solid line) and of the corresponding fluctuations (shaded area), for two different values of the position.

where we introduced the *Bessel kernel*

$$\mathcal{B}(x, y; \omega) := \omega \frac{J_{x-1}(\omega) J_y(\omega) - J_x(\omega) J_{y-1}(\omega)}{2(x-y)}. \quad (2.3.11)$$

Note that, for  $x = y$ , Eq. (2.3.10) straightforwardly reduces to

$$\langle n^2(x, t) \rangle_C = \langle n(x, t) \rangle [1 - \langle n(x, t) \rangle], \quad (2.3.12)$$

which is actually expected for fermionic particles. Summing over  $x$  and  $y$  in Eq. (2.3.10)—thus applying the prescription of Eq. (2.2.10)—leads to the connected 2-point function of the interface profile  $\langle \mu(x, t) \mu(y, t) \rangle_C$  (Eq. (A.3.9)). In Fig. 2.7 we show the fluctuations of the interface profile: in panel (a) we present the value of  $\langle \mu^2(x, t) \rangle_C$  as a function of position for different times, while in panel (b) we plot, for two values of  $x$  along the chain, the average position of the interface with the corresponding fluctuations, over two periods of oscillation.

It is instructive to discuss the continuum limit also for the fluctuations of the shape  $\mu$ . As they involve the Bessel kernel in Eq. (2.3.11), they are related to the universal fluctuations found e.g.

in Laguerre and Jacobi ensembles of random matrices [222] (see also Ref. [223]), and of random representations of the symmetric group [215]. In particular, the presence of the Bessel functions implies a *light-cone structure* for the correlations, see Fig. 2.8a: if either  $|x| \gg \omega_t$  or  $|y| \gg \omega_t$ , the correlations are exponentially suppressed (as follows from the large-index asymptotic behavior of the Bessel function discussed in Eq. (A.2.13)). If, instead, both  $x, y \ll \omega_t$ , then by virtue of the large-argument asymptotics of the Bessel functions presented in Eq. (A.2.14), the kernel reduces to the *sine kernel*

$$\mathcal{S}(x, y) = \frac{\sin(\pi(x - y)/2)}{\pi(x - y)}. \quad (2.3.13)$$

The sine kernel is found in numerous contexts in physics and mathematics, among which Gaussian ensembles of random matrices [224], and free fermionic chains *without* a linear potential [225]. Notice that, in passing from the Bessel kernel to the sine kernel, the explicit dependence on  $\omega_t$  has been lost in the expression for the correlations, while it remains implicit in the maximum value attained by  $x$  or  $y$  (i.e. the border of the light cone), see Fig. 2.8b. Finally, let us mention that a less trivial limit emerges in a region of order  $\omega_t^{1/3}$  around the light cone, where by means of a uniform expansion (Eqs. (A.2.15)–(A.2.16)) the Bessel kernel reduces to the celebrated Airy kernel [226, 227].

Despite all the connections mentioned above, we need to emphasize that in this quantum setting the fluctuations are given by the *square* of the Bessel kernel, see Eq. (2.3.10): accordingly, they are quantitatively different from the cases mentioned above, which involve the kernels at their linear order.

### 2.3.3 Entanglement dynamics

The “holographic” description of the interface in terms of an integrable  $1d$  model (i.e. non-interacting fermions in a linear potential) allows one to extract much more information beyond averages and correlations, using the vast amount of analytical techniques developed in recent years [143, 144, 228, 229]. For instance, one can compute the so-called *full counting statistics*, i.e. the probability distribution of the fermions, with the techniques of Ref. [230]. In fact, it turns out that the predictions of Ref. [230] for the case  $h = 0$  carry over to our case  $h \neq 0$  just by replacing  $t \rightarrow \omega_t/(2g)$ ; this “minimal” substitution is motivated by the fact that in the analytical expressions discussed in Sec. 2.2.2 the time dependence occurred only via  $\omega_t$  defined in Eq. (2.2.16), which encompasses both cases. Similarly, the growth of the entanglement across a bipartition of the lattice can be studied by using the results available for the  $1d$  problem [231]. In particular, one has to partition the  $2d$  lattice in two halves by means of a “vertical” line (e.g. through the corner, corresponding to the time axis in Fig. 2.8a), so that, on the chain, one has well-defined subsystems. At this point, the entanglement of the  $2d$  and the  $1d$  problems are equal, as there is a one-to-one mapping linking all possible states in the two settings. The entanglement between the two subsystems can be computed as detailed in Ref. [231]: from the eigenvalues  $\zeta_l(t)$  of the correlation matrix  $\mathcal{C}_{xy}(t) := \langle \psi_x^\dagger(t) \psi_y(t) \rangle$ , the entanglement entropy is obtained as

$$S_{\text{ent}}(t) = - \sum_{l=0}^{\infty} \left[ \zeta_l \ln \zeta_l + (1 - \zeta_l) \ln(1 - \zeta_l) \right]. \quad (2.3.14)$$

The correlation matrix can be calculated explicitly, by using the properties of the Bessel functions which were used for calculating the average magnetization, with the result that

$$\mathcal{C}_{xy}(t) = e^{i(\frac{\pi}{2} + ht)(y-x)} \mathcal{B}(x, y; \omega_t), \quad (2.3.15)$$

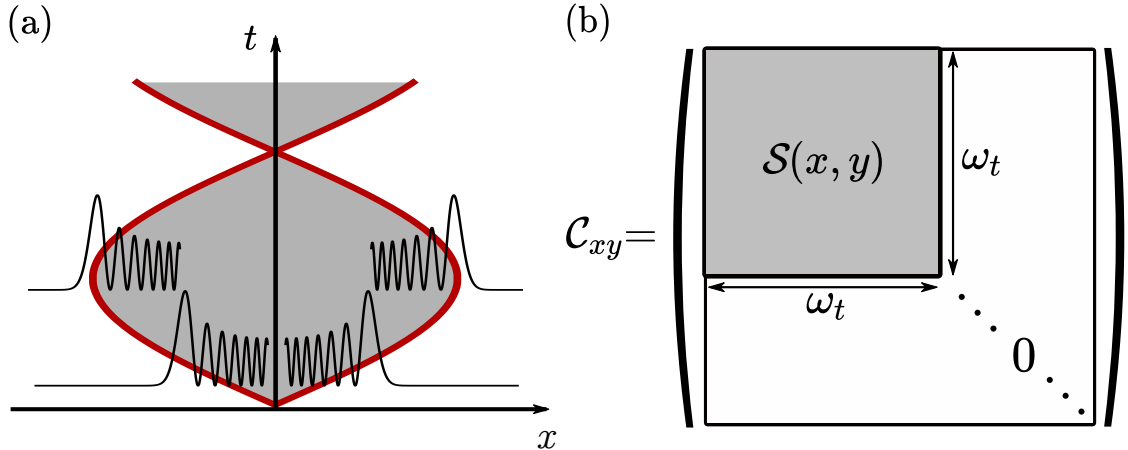


Figure 2.8: (a) Light-cone structure induced by the presence of the Bessel kernel, see Eqs. (2.3.10) and (2.3.11). The red line represents the position of the light cone  $x = |\omega_t|$ . Inside the light cone, the Bessel functions oscillate with a non-zero average value. It is within this region, in the continuum limit, that the Bessel kernel reduces to the sine kernel of Eq. (2.3.13). Outside the light cone, instead, the Bessel functions decay exponentially upon moving away from it, and in the continuum limit they approximately vanish. Therefore, if both  $x$  and  $y$  are inside the light cone, i.e. in the gray area, the Bessel kernel has a non-vanishing value. If at least one of the two points is outside the light cone, the Bessel kernel approximately vanishes. (b) Correlation matrix (see Eq. (2.3.15)) in the continuum limit. As discussed in the text, in this regime  $\mathcal{C}_{x,y}$  can be set to zero outside the light cone, while inside the light cone the Bessel kernel  $\mathcal{B}(x, y; \omega_t)$  can be replaced by the sine kernel  $\mathcal{S}(x, y)$ .

$\mathcal{B}$  being the Bessel kernel of Eq. (2.3.11). If one computes the entanglement entropy between two subsystems  $A$  and  $B$ , separated by a vertical line in the  $2d$  problem, the indices of the correlation matrix  $\mathcal{C}_{xy}$  are such that  $x, y \in A$  (or  $B$  equivalently). For a bipartition located in  $0$ , one has  $x, y > 0$ . Let us notice that the phase factor in the last equation does not affect the entanglement entropy; in fact, it can be removed via a unitary transformation. Accordingly, it is clear that the correlation matrix  $\mathcal{C}_{xy}(t)$  (and thus  $S_{\text{ent}}(t)$ ) is a periodic function of time with period  $|h|/\pi$ , as its time dependence is only through  $\omega_t$ . Even if, to our knowledge, the eigenvalues of the correlation matrix of Eq. (2.3.15) cannot be obtained analytically, some analytical progress can be made in the continuum limit [232, 233]. Let us introduce the entanglement Hamiltonian  $\mathcal{H}_A$  such that

$$\rho_A = \mathcal{K}_A e^{-\mathcal{H}_A}, \quad (2.3.16)$$

being  $\rho_A$  the reduced density matrix of a subsystem  $A$ , and  $\mathcal{K}_A$  a normalization constant. With this definition, one finds [232, 234, 235]

$$\mathcal{H}_A = \ln \left( \frac{1 - \mathcal{C}_A}{\mathcal{C}_A} \right), \quad (2.3.17)$$

where  $\mathcal{C}_A$  is here the correlation matrix restricted to positions belonging to the considered subsystem  $A$ . This means that  $\mathcal{H}_A$  and  $\mathcal{C}_A$  are diagonal in the same basis, and the corresponding eigenvalues satisfy the relation in Eq. (2.3.17).

As discussed also in Sec. 2.3.2, the Bessel kernel reduces to the sine kernel in the continuum limit inside the light cone. In this regime one can thus approximate the correlation matrix  $\mathcal{C}_{xy}$  by setting to zero the entries with  $x, y \gtrsim \omega_t$ , and therefore one is left with an effective matrix of size

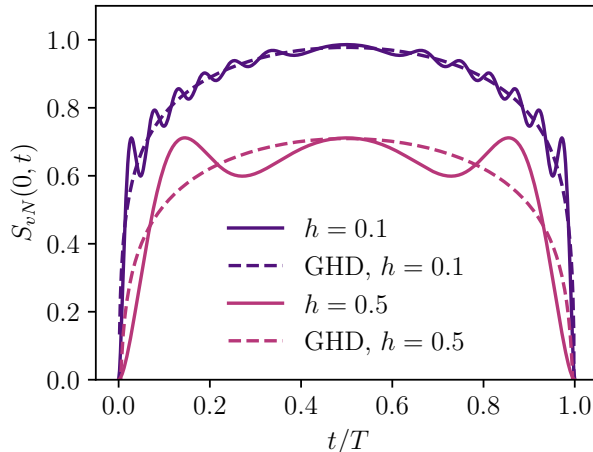


Figure 2.9: The plot shows the time dependence of the entanglement entropy for two different values of the external field  $h$ , over one period  $T = \pi/h$ , with  $g = 1$ . The solid lines represent the entanglement entropy computed via diagonalization of the correlation matrix, according to Eq. (2.3.14). In both cases, the diagonalization has been performed on a chain of length  $L = 100 \gg \ell = g/h$ . The dashed lines represent the prediction given by GHD, reported in Eq. (2.3.20). One can clearly see that, for smaller values of  $h$ , i.e. closer to the continuum limit, the agreement between numerical diagonalization and GHD improves.

$\omega_t \times \omega_t$ , as depicted in Fig. 2.8b. Thanks to this approximation, one can obtain the eigenvalues  $\epsilon_k$  of  $\mathcal{H}_A$  as [225, 232]

$$\epsilon_k(t) = \pm \frac{\pi^2}{2 \ln \omega_t} (2k + 1), \quad (2.3.18)$$

with  $k = 0, 1, 2, \dots$ . Denoting by  $\zeta_k$  the eigenvalues of  $\mathcal{C}_A$ , one has from Eq. (2.3.17)

$$\zeta_k = \frac{1}{e^{\epsilon_k} + 1}. \quad (2.3.19)$$

Note, however, that the asymptotic value Eq. (2.3.18) needs a very large  $\omega_t$  to be accurate. For smaller values of  $\omega_t$ , the eigenvalues vary as  $1/(\ln \omega_t + b_k)$  rather than  $1/\ln \omega_t$ , where  $b_k$  are constants depending on the specific eigenvalue [232]. The evolution of the entanglement entropy can now be determined by using Eqs. (2.3.19) and (2.3.18) in Eq. (2.3.14). In Fig. 2.9 we show the numerical evaluation of the time evolution of the entanglement entropy, according to Eq. (2.3.14), for various values of  $h$ . The presence of a non-vanishing external field implies that also the entanglement entropy is periodic in time.

We have shown how the mapping of the original  $2d$  problem onto a  $1d$  chain can be used in order to calculate the half-system entanglement entropy. However, the computation was possible only because of a convenient choice of the bipartition of the  $2d$  lattice (i.e. a vertical one in the rotated frame): more general bipartitions of the  $2d$  lattice would instead map non-locally on the chain. It seems that computing the entanglement of the  $2d$  system using the mapping into  $1d$  is viable as long as the cut along which the entanglement is computed is parallel to the projection performed in the mapping itself.

As a final point of this Section, it is worth noticing that the above results, valid in general on the lattice for arbitrary values of the couplings  $g$  and  $h$ , reduce, in the continuum limit  $h \ll g$ , to the predictions of conformal field theory in curved space [236, 237] or quantum generalized

hydrodynamics (GHD) [56]. The entanglement entropy is in fact given by

$$S(x, t) = \frac{1}{6} \ln \left[ \omega_t \left( 1 - \frac{x^2}{\omega_t^2} \right)^{3/2} \right] + c, \quad (2.3.20)$$

where  $c \simeq 0.475$  and  $x$  is the position of the bipartition. Equation (2.3.20) is clearly valid for  $|x| \leq \omega_t$ ; otherwise, the entanglement entropy is zero because of the light-cone structure. In Fig. 2.9 we also compare the prediction given by Eq. (2.3.20) with the results of the exact diagonalization on the lattice, showing that a good agreement is attained for small values of  $h$ , as expected. This relation was derived in Ref. [56] for  $h = 0$ ; the general case is obtained by means of the minimal substitution  $2g|t| \rightarrow \omega_t$ , coming from Eq. (2.2.16). In passing we mention that the GHD formalism allows one to predict the dynamics of one-dimensional integrable quantum systems directly in the continuum limit, even when the system is interacting; this is the reason why one needs the limit  $h \ll g$  to match the GHD prediction. A more extensive discussion of the GHD analysis of the Stark localized chain can be found in Chapter 4.

### 2.3.4 Connection with the asymptotics of the Plancherel measure

As pointed out at the beginning of Sec. 2.3, the states in the Krylov sector connected with the infinite corner are in one-to-one correspondence with *Young diagrams* (also known as *Ferrers diagrams*). By definition, a Young diagram is a collection of boxes, arranged in a sequence of left-justified rows of non-increasing length [238]. Young diagrams are a graphical tool commonly used to represent integer partitions, to compute dimensions of group representations, and for many other mathematical purposes [238].

In order to discuss the connection with the results presented here, let us recall here some basic facts concerning Young diagrams. A partition  $\lambda = (\lambda_1 \geq \lambda_2 \geq \dots \geq \lambda_n \geq 0)$  of an integer  $N$  indicates a possible decomposition of  $N$  as a sum of  $n$  positive integers, i.e.

$$|\lambda| := \sum_{k=1}^n \lambda_k = N. \quad (2.3.21)$$

Representing each integer  $\lambda_k$  as a string of  $\lambda_k$  adjacent boxes  $\square \square \dots \square$ , one can easily see that a partition corresponds to a Young diagram, obtained by stacking all the  $n$  strings, starting from the first. A theorem [238] states that the irreducible representations of the symmetric group  $S_N$  of degree  $N$  are labelled by the possible partitions  $\lambda$  of size  $|\lambda| = N$ . Moreover, the dimension of the representation corresponding to a certain  $\lambda$  can be obtained via the *hook length formula*

$$\dim(\lambda) = \frac{|\lambda|!}{\prod_{\square \in \lambda} \mathfrak{h}(\square)}, \quad (2.3.22)$$

where  $\mathfrak{h}(\square)$  is the so-called *hook* of the square  $\square$  [238], an integer number determined as explained in Fig. 2.5b.

For our purposes, the most interesting interpretation of  $\dim(\lambda)$  resides in the fact that it gives the number of ways in which the diagram  $\lambda$  can be constructed, starting from the empty diagram, by adding one square at a time in such a way that at each step one still has a partition [239]. In the mathematical literature, it is common to define the *Plancherel measure* on the set of partitions as [183–186, 215]

$$\mu_{\text{P}}(\lambda) := \frac{[\dim(\lambda)]^2}{|\lambda|!}, \quad (2.3.23)$$

which is proved to be a normalized measure, i.e. a probability [240].

An important result of combinatorics is that the Plancherel measure  $\mu_P$  *concentrates* at large  $N$ , i.e. it becomes a delta function on a particular set of diagrams [183–186, 215]. The diagrams belonging to this set have approximately the same shape; more precisely, after a  $3\pi/4$  counter-clockwise rotation of the diagrams (such that they are finally arranged as in Fig. 2.5a) their shape is actually described by the function  $\sqrt{N}\Omega(x/\sqrt{N})$  with  $\Omega(v)$  given in Eq. (2.3.7). It is thus quite surprising to find another, completely different growth process that leads to the same limiting shape as the one induced by the quantum dynamics of the  $2d$  Ising model.

While we could not devise a mathematically rigorous proof, we heuristically understand the above correspondence as follows. Recalling that  $\dim(\lambda)$  gives the number of paths that reach the diagram  $\lambda$  from the empty one, always remaining within the set of Young diagrams, we notice that the Plancherel measure  $\mu_P$  weights each diagram with the *square* of the number of paths. On the other hand, one can consider the Green's function

$$G(\lambda', \lambda; E) = \langle \lambda' | \frac{1}{E - H_g} | \lambda \rangle, \quad (2.3.24)$$

where we denoted with  $H_g$  the Hamiltonian  $H_{PXP}$  in Eq. (2.1.7), making explicit the dependence on  $g$ , and  $\lambda$  and  $\lambda'$  are two Young diagrams. Performing the locator expansion of the resolvent [3, 106, 241, 242]

$$G(\lambda, \lambda'; E) = \frac{\delta_{\lambda\lambda'}}{E - E_{\lambda'}} + \frac{1}{E - E_{\lambda'}} \sum_{p \in P(\lambda', \lambda)} \prod_{k=1}^{|p|} \frac{g}{E - E_{p_k}}, \quad (2.3.25)$$

where  $P(\lambda', \lambda)$  denotes the set of paths in configuration space from  $\lambda'$  to  $\lambda$ ,  $|p|$  is the length of the path  $p$  and we introduced the notation  $H_{g=0} |\lambda'\rangle = E_{\lambda'} |\lambda'\rangle$ , i.e.  $E_{\lambda}$  denotes the energy of  $|\lambda\rangle$  in the absence of hopping ( $g = 0$ ). In the spirit of the forward approximation [3, 106, 242], one can approximate the sum in Eq. (2.3.25) by reducing  $P(\lambda', \lambda)$  to  $SP(\lambda', \lambda)$ , i.e. the set of *shortest* paths from  $\lambda'$  to  $\lambda$ . This corresponds to work at the lowest order in the hopping  $g$ . Under this assumption, the argument of the sum does no longer depend on the specific path, but only on its length  $d(\lambda', \lambda)$ , because all the diagrams with a fixed number of blocks, viz. at the same distance from the empty diagram, have the same energy  $E_{\lambda} = -h|\lambda|$ , see Eq. (2.1.7). This means that the sum gives the number of shortest paths from  $\lambda'$  to  $\lambda$  (with  $\lambda \neq \lambda'$ , otherwise it gives zero). Specializing Eq. (2.3.25) to the case of the path from the empty diagram  $\lambda' = 0$  (with  $E_{\lambda'=0} = 0$ ) to  $\lambda$  ( $\neq 0$ ), one finds

$$G(\lambda, 0; E) = \frac{\dim(\lambda)}{E} \prod_{k=1}^{d(0, \lambda)} \frac{g}{E + hk} = \frac{\dim(\lambda)}{E} \left(\frac{g}{h}\right)^{|\lambda|} \frac{\Gamma(1 + E/h)}{\Gamma(1 + E/h + |\lambda|)}, \quad (2.3.26)$$

where, in the second line, we used the fact that  $d(0, \lambda) = |\lambda|$ . Taking the residue of this propagator at  $E = 0$ , one finds the expression of the corresponding eigenfunction

$$\psi_{E=0}(\lambda) = \frac{\dim(\lambda)}{|\lambda|!} \left(\frac{g}{h}\right)^{|\lambda|}. \quad (2.3.27)$$

Accordingly, the probability  $|\psi_{E=0}(\lambda)|^2$  of being in the state  $|\lambda\rangle$  turns out to be proportional to  $[\dim(\lambda)]^2$ —i.e. to the square of the number of paths leading to it, according to the interpretation of  $\dim(\lambda)$ —and therefore to the Plancherel measure  $\mu_P(\lambda)$  in Eq. (2.3.23). This motivates the connection between the quantum dynamics and the Plancherel measure concentration.

Before passing to the next Section, it is interesting to note that the forward approximation also gives the correct result for the decay of the eigenfunctions upon increasing  $|\lambda|$ . To see this,

one must plug in Eq. (2.3.27) the value of  $\dim(\lambda)$ , which clearly depends on the specific form of the diagram associated with the state  $|\lambda\rangle$ . Referring for details to Ref. [185], we just say here that it is possible to provide an upper (resp. lower) bound to the maximal (resp. typical) value of  $\dim(\lambda)$ : in both cases, the leading term scales as  $\sqrt{|\lambda|!}$ . Using Eq. (2.3.27), one gets that the eigenfunctions approach zero faster than exponentially upon increasing  $|\lambda|$ , because of the overall factor  $1/\sqrt{|\lambda|!}$ . This estimate is in agreement with the exact result of Eq. (2.2.12), since the Bessel functions decay as the inverse factorial of the (large) index, see Eq. (A.2.13).

## 2.4 Mechanisms of integrability breaking

In the previous sections we showed that the Hilbert space of the  $2d$  Ising model in the infinite-coupling limit  $J \rightarrow \infty$  shatters in many disconnected Krylov sectors. Among these sectors, those corresponding to the wide class of interfaces discussed in Sec. 2.2.2 can be mapped onto a  $1d$  model which turns out to be integrable. In this Section we discuss the dynamics of the interface beyond integrability and the robustness of the qualitative features of the exact solution.

In Sec. 2.4.1 we argue that the interfaces which do not satisfy the Lipschitz condition of Eq. (2.2.9) may have a very different dynamical behavior compared to the one described so far, because they can break into disconnected pieces. This is done by considering the case of an interface which is *locally* Lipschitz, but which it is not the graph of a function  $\mu$  at a larger scale. In Sec. 2.4.2 we consider, instead, another possible source of integrability breaking: the presence of a finite, albeit still large, coupling  $J$ . Specifically, we will discuss the  $O(J^{-1})$  corrections to the infinite-coupling Hamiltonian (2.1.3) and address the ergodicity of the resulting model. In Sec. 2.4.3 we discuss, using both analytical and numerical techniques, why the  $O(J^{-1})$  corrections to the infinite-coupling Hamiltonian lead to a localization phenomenon, named Stark MBL, induced by the presence of the longitudinal field  $h$ . Finally, in Sec. 2.4.4 we compare our results for the time evolution of a domain on the lattice with the equivalent problem in the continuum, studied in the context of the false vacuum decay scenario, highlighting qualitative differences.

### 2.4.1 Finite bubbles

Throughout Secs. 2.2.2 to 2.3.4 we assumed the presence of a single interface, separating the  $2d$  lattice in two infinitely extended domains. It is then natural to investigate the extent to which the predictions derived therein carry over to finite domains. The easiest and most natural case to be considered is that of a single, large bubble of “down” spins, surrounded by “up” spins (or vice-versa). Let us also introduce the notion of convexity on the lattice: we will say that a domain is *convex* if any line *parallel to the lattice axes* joining two points in the domain lies entirely within the domain itself. As already noted in Refs. [1, 171], all convex bubbles are dynamically connected with the minimal rectangle (with sides parallel to the lattice axes) that contains them, i.e. they belong to the Krylov sector generated by this rectangle. Moreover, because of the perimeter constraint, the domain-wall dynamics is always confined within such a rectangle. Accordingly, we can directly assume that the shape of the bubble at the initial time  $t = 0$  is a rectangle, as all the other cases will follow from this one.

The early-stage dynamics of such a rectangular bubble can be predicted on the basis of the previous analysis. In fact, the sides of the bubble are immobile, since no spin can be flipped without modifying the perimeter, while the corners start to be eroded, as discussed in Sec. 2.3. However, the evolution will deviate from that of an infinite and isolated corner as soon as two adjacent corners start “feeling” the presence of the other. The timescale at which this happens can be bounded from below by computing, in the fermionic language, the probability of finding

two fermions, each coming from a different isolated corner, halfway along the flat portion of the interface that connects these two corners.

Let us denote by  $L$  the length of the shortest side of the rectangular, finite bubble (see also Fig. 2.6). There are now two possible cases. If the longitudinal field  $h = 0$  or, more generally,  $h$  is small enough for the Bloch oscillations to have an amplitude  $\ell \simeq |g/h|$  (Eq. (2.2.19)) larger than the distance  $L/2$ , then the excitations propagate ballistically on the chain with speed  $2g$  (Eq. (2.3.6)), and they meet at  $L/2$  after a time

$$T_{\text{corner}}(h = 0) \sim \frac{L}{4g}. \quad (2.4.1)$$

If, instead,  $h$  is nonzero and large enough to confine the dynamics in a region *smaller* than  $L/2$ , one can estimate the probability  $P(x, t)$  of having a fermion at a distance  $x < 0$  from the corner (equivalently, a hole at distance  $x > 0$ ) with  $P(x, t) = 1 - \langle n(x, t) \rangle$ . On the maxima of the oscillations of the corresponding interface<sup>6</sup>, attained at times  $t^*$  such that  $\omega_{t^*} = 2\gamma$  (Eqs. (2.2.16) and (2.3.6)), one finds  $\langle n(x, t^*) \rangle = \sum_{y < x} J_y^2(2\gamma)$ , cf. Eq. (2.3.2), and consequently

$$P(L/2, t^*) = \sum_{y \geq L/2} J_y^2(2\gamma). \quad (2.4.2)$$

Recalling that the Bessel functions of large order decay exponentially fast to zero, one can approximate (see also Eq. (A.2.13))

$$P(L/2, t^*) \approx J_{L/2}^2(2\gamma) \approx \frac{1}{\pi L} \left( \frac{2eg}{Lh} \right)^L. \quad (2.4.3)$$

With this result, the typical time after which two fermions, coming from different corners, interact can be estimated as  $T_{\text{corner}}(h \neq 0) \sim 1/P^2(L/2, t^*)$  or, more explicitly<sup>7</sup>,

$$T_{\text{corner}}(h \neq 0) \sim \frac{1}{g} e^{2L \ln L - 2L \ln(2eg/h)}. \quad (2.4.4)$$

One can see that, in the case  $h \neq 0$ , a time that is more than exponentially large in the bubble size  $L$  must pass, before integrability breaking starts to be manifest.

It is natural to wonder what happens to the bubble after this timescale. Based on elementary reasoning, one can argue that two kinds of processes may take place: (a) the excitations coming from one corner may start to affect the dynamics of adjacent corners, transferring energy between corners and deteriorating the perfect coherence of the single-corner oscillations; (b) the interface may break because of the detachment of isolated bubbles of flipped spins caused by the interface-splitting transitions  $|\square\rangle\langle \square| + \text{H.c.}$  of Eq. (2.1.7). We note, however, that these detached parts can move away from the parent interface only via  $g^2/J$  processes. A detailed study of this challenging problem is left for future investigations.

We conclude by emphasizing that the case of two adjacent corners we have considered here actually applies to any very large bubble, provided that its boundaries are “smooth” enough—i.e., that the Lipschitz condition is locally satisfied while the points responsible for its global violation are very dilute. If, instead, the initial interface is rather corrugated, i.e. it is not the graph of a function  $\mu(x)$  even locally, then we expect a really complicated time evolution, during which all accessible configurations may be explored, and the single-interface description is no longer possible.

<sup>6</sup>A very similar result is obtained if taking the average over a period, rather than the maximum of the oscillations.

<sup>7</sup>This result can be obtained using Fermi Golden Rule. In particular, the interaction rate for two fermions coming from different corners is proportional to the probability of having both fermions at half chain. Being fermions of different species, they interact only at the scattering point and therefore such probability is the product of the single fermion probability of being at a distance  $L/2$  from the corner. Consequently, taking the inverse of the rate, one obtains  $T_{\text{corner}}$ .

## 2.4.2 Finite coupling

We now relax the assumption that  $J$  is strictly infinite, considering the effects of the corrections  $\propto 1/J$ , but still under the assumption that  $J \gg |h|, g$ .

A large but finite  $J$  still imposes an *effective* dynamical constraint, valid up to a timescale which becomes exponentially long upon increasing  $J$ : this follows from the rigorous prethermalization bounds of Ref. [243]. Specifically, the perturbatively “dressed” version of the domain-wall length operator  $\mathcal{L}$  (defined in Eq. (2.1.2)), arising from the Schrieffer-Wolff transformation, is accurately conserved for a long time that scales (at least) exponentially:

$$T_{\text{preth}} \geq T_{\text{preth}}^0 \equiv \frac{C}{g} \exp \left[ \frac{cJ}{\max(g, |h|)} \right] \quad (2.4.5)$$

(here  $c$  and  $C$  are numerical constants independent of  $J$ ,  $g$ , and  $h$ ). This is because the Schrieffer-Wolff effective Hamiltonian  $H_{\text{eff}} = H_{\text{PXP}} + (1/J)(\dots) + (1/J^2)(\dots) + \dots$ , computed up to a suitable optimal perturbative order, commutes with  $\mathcal{L}$  in Eq. (2.1.2) up to an exponentially small error [243]. In addition, the evolution of all local observables is well approximated by  $H_{\text{eff}}$  for  $t \leq T_{\text{preth}}$  [243].

As anticipated above, the zeroth order of the Schrieffer-Wolff effective Hamiltonian  $H_{\text{eff}}$  was already determined in Sec. 2.1.2 and is given by Eq. (2.1.3). Computing higher-order corrections to  $H_{\text{eff}}$  becomes rapidly very complex, as the number of terms increases more than exponentially. In App. A.5.1 we sketch the computation of the first-order corrections in  $1/J$ , while in App. A.5.2 we specialize it to the dynamical sector of a smooth interface, of the type defined in Sec. 2.2.2. In this sector, the perturbative corrections take a simpler form. The construction above can be translated into the fermionic representation. The Schrieffer-Wolff effective Hamiltonian

$$H_{\text{eff}} = H_F^{(0)} + H_F^{(1)} + O(J^{-2}), \quad (2.4.6)$$

has the zeroth-order contribution  $H_F^{(0)}$  given by Eq. (2.2.11), while the first-order corrections turn out to be

$$H_F^{(1)} = -\frac{g^2}{4J} \sum_x \left( \psi_x^\dagger \psi_{x+2} + \text{H.c.} \right) + \frac{g^2}{4J} \sum_x \left( 2\psi_x^\dagger \psi_{x+1}^\dagger \psi_{x+1} \psi_{x+2} + \text{H.c.} - 3\psi_x^\dagger \psi_x \psi_{x+1}^\dagger \psi_{x+1} \right). \quad (2.4.7)$$

One may recognize that they entail next-nearest-neighbour hoppings and density-density interactions. One can notice also that the density-density interactions, which are diagonal in the occupation number basis, do not depend on  $h$ . Consequently, the addition of the first-order corrections breaks the  $h \rightarrow -h$  symmetry: changing the sign of  $h$  modifies the expectation value of the energy. The terms in  $H_F^{(1)}$  are rather generic, and therefore one naturally expects them to break the integrability of the model, and make it thermalize rather quickly. However, if  $h$  is sufficiently large the perturbation is not able to restore ergodicity. In the next Section, we describe this phenomenon in detail.

Let us briefly mention that, upon including the  $O(J^{-1})$  corrections, an isolated flipped spin can spread in the  $2d$  lattice with a hopping amplitude  $\propto g^2/J$ . This means that it is no longer possible to provide an effective  $1d$  description even for initial configurations of the strip-like form, discussed in Sec. 2.2.1 for  $J = \infty$ .

Before continuing, it is important to emphasize a fundamental issue with the Schrieffer-Wolff transformation. For large but finite  $J$ , the dynamics of the initial product states considered so far in the form of the classical configurations will exhibit vacuum fluctuations even away from the existing domain walls. This is due to the perturbative dressing of the bare ferromagnetic state by

virtual spin excitations. In practice, this arises from the application of the Schrieffer-Wolff unitary transformation  $\exp(iS_1)$ , c.f. Eq. (A.5.8), to the fully polarized initial product state. Accordingly, for such initial states, one should think of the ferromagnetic vacua (i.e. those on the two sides of an infinite interface or the inner and outer regions of a bubble) as *superpositions* of dilute spin-flip excitations, of spatial density  $\sim (g/J)^2$ . Such excitations can be described as magnons, hopping on the  $2d$  lattice with amplitude  $\propto g^2/J$ . In principle, this dilute magnon gas contributes to the dynamics of the interface, but in the following we will ignore this fact, leaving its discussion to future investigations. This choice actually corresponds to taking as the initial state an interface in the *the Schrieffer-Wolff transformed basis*, rather than in the classical one discussed so far.

### 2.4.3 Arguments in favor of Stark many-body localization

The goal of this Section is to study the evolution induced by the Hamiltonian (2.4.6). The first term in Eq. (2.4.6) is the Hamiltonian  $H_F$  considered already in Secs. 2.2.2 and 2.3: it represents a chain of Stark-Wannier-localized, non-interacting fermions. The second term, i.e.  $H_F^{(1)}$  of Eq. (2.4.7), is a small perturbation containing both next-nearest-neighbor hoppings and two-body interactions. Accordingly, there is a competition between the localized nature of the dynamics induced by  $H_F^{(0)}$  and the interactions in  $H_F^{(1)}$ , which are generally expected to drive the system towards a thermal phase. Previous works [172, 173, 244] have shown that, for interacting Hamiltonians very similar to Eq. (2.4.6), an extended non-thermal phase is present for sufficiently strong field  $h$ , partly in analogy to what happens in the disorder-induced many-body localization (MBL). Indeed, the phenomenon has been dubbed *Stark MBL*.

In order to quantify the competition between interactions and the linear potential responsible for the localization, we developed an analytical argument à la Basko-Aleiner-Altshuler (BAA) [103] which goes as follows. Start from the integrable limit  $J = +\infty$ : the eigenfunctions are expressed in terms of the single-particle orbitals of Eq. (2.2.12) and are all spatially localized. Their localization length  $\xi$  can be quantified by the participation ratio: using Eq. (2.2.12) and Neumann's addition theorem (see App. A.2),

$$\xi^{-1} = \sum_x J_x^4(\gamma) = \frac{1}{\pi} \int_0^\pi d\theta J_0^2\left(\gamma\sqrt{2-2\cos\theta}\right), \quad (2.4.8)$$

where  $\gamma$  is given after Eq. (2.2.12). An approximate form of this relation is derived in App. A.6, where we perform the asymptotic expansion of the above integral for large values of  $\gamma$  through the method of the Mellin transform, determining

$$\xi^{-1} = \frac{\ln(\gamma C)}{\pi^2 \gamma} + O\left(\frac{\ln \gamma}{\gamma^3}\right), \quad (2.4.9)$$

where  $C = 2^5 e^{\gamma_E} \simeq 56$  and  $\gamma_E = 0.5772 \dots$  is the Euler-Mascheroni constant. Such approximation is clearly accurate for  $\gamma \gg 1$ , i.e. for small  $h$ .

We now assume that one can partition the system into boxes (“quantum dots”) of size  $\xi$ , as sketched in Fig. 2.10. Within each of them, the number of states is clearly  $N_\xi = 2^\xi$  (there are  $\xi$  sites that can be either empty or occupied), whereas the maximum energy difference between two many-particle states is  $\Delta_{\max} \approx |h|\xi^2$ . To understand this latter estimate, assume  $h > 0$ : then, the minimum energy is attained when no particle is present ( $E_{\min} = 0$ ), while the maximum when all sites are occupied (and thus  $E_{\max} = \sum_{x=0}^{\xi} hx \approx h\xi^2$ ). With the same reasoning, with  $h < 0$  one gets  $\Delta_{\max} \approx |h|\xi^2$ , thus confirming the estimate.

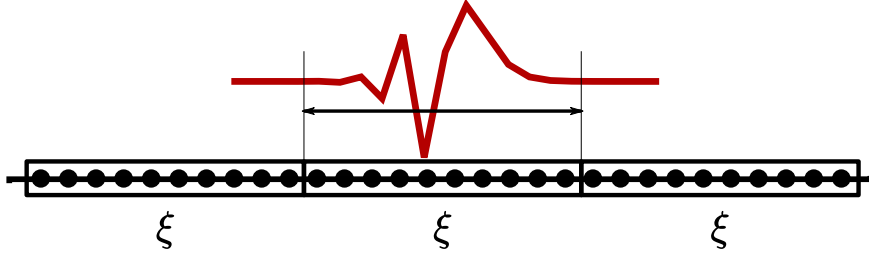


Figure 2.10: Graphical representation of adjacent regions (“quantum dots”) of size  $\xi$  along the chain, each corresponding to one localization length, as represented by the eigenfunction (red, solid line). As described in the text, focusing on one of these intervals, one can derive an estimate for the critical value of  $h$ , above which the system is not ergodic even in the presence of a finite  $J$ .

Following BAA (and thus also building on Ref. [139]), we say that interactions should not be able to restore ergodicity (at least perturbatively) if their strength  $\lambda \sim g^2/J$  is smaller than the average local level spacing:

$$\delta_\xi \approx \frac{\Delta_{\max}}{N_\xi} \approx \frac{|h|\xi^2}{2\xi}, \quad (2.4.10)$$

i.e. when  $\lambda < \delta_\xi$ . This is equivalent to requiring

$$\frac{g^2}{J} < \frac{|h|\xi^2}{2\xi}, \quad (2.4.11)$$

which is always satisfied for  $0 \leq |\gamma| \lesssim 1$ , i.e. for sufficiently large  $|h|$ . It is interesting to note that the regime of validity of the heuristic criterion (2.4.11) depends only weakly on  $J$ . In Fig. 2.11 we show, upon varying  $J$  and  $h$ , the regions of validity of the inequality (2.4.11), where  $\xi = \xi(h/g)$  is given by Eq. (2.4.8). One can observe how, for fixed  $J$ , the criterion is satisfied for sufficiently large  $h$ ; moreover, for  $J/g \gtrsim 1$ , the condition in Eq. (2.4.11) holds for  $h/g \gtrsim 1$ .

As a check for the above estimate, we performed numerical simulations, focusing in particular on the “generalized imbalance”, a witness of ergodicity breaking. Given a generic initial state  $|\Psi_0\rangle$ , the time-evolved generalized imbalance for a system of length  $L$  is

$$I_L(t) = \sum_{x=-L/2+1}^{L/2} \frac{1}{L} \langle \Psi_0 | m(x,t)m(x,0) | \Psi_0 \rangle, \quad (2.4.12)$$

where we defined  $m(x,t) := 2n(x,t) - 1$ . If the initial state  $|\Psi_0\rangle$  is a Néel state, then the generalized imbalance reduces to the standard imbalance between the occupation number of odd and even sites, used both in numerical simulations and cold-atom experiments. Taking the infinite-size limit and averaging over time, one obtains

$$I = \lim_{L,T \rightarrow \infty} \frac{1}{T} \int_0^T dt I_L(t), \quad (2.4.13)$$

which is zero in generic thermalizing systems. Accordingly,  $I \neq 0$  is a sufficient condition for the system to be non-ergodic (even if it is not necessary). The infinite-time limit in the definition of  $I$  can be obtained also by using the diagonal ensemble: assuming  $|\Psi_0\rangle$  to be given as in Eq. (2.2.14), one finds

$$I = \lim_{L \rightarrow \infty} \frac{1}{L} \sum_{x=-L/2+1}^{L/2} \langle m(x,0) \rangle \sum_a \langle E_a | m(x,0) | E_a \rangle |\langle \Psi_0 | E_a \rangle|^2, \quad (2.4.14)$$

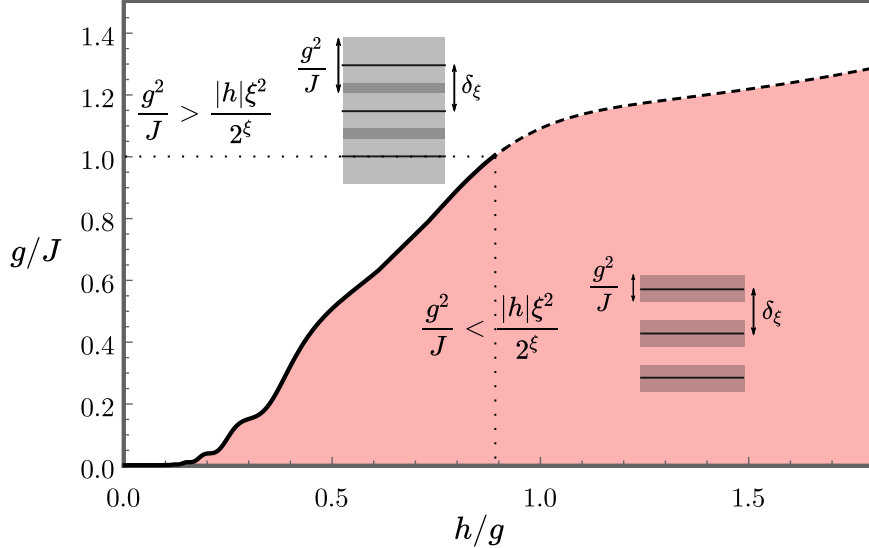


Figure 2.11: Region of the  $(h/g, g/J)$ -plane within which the condition of localization in Eq. (2.4.11) is valid (color), and region where delocalization is expected (white). For each region, a sketch is provided of the comparison between the unperturbed level spacings (solid black line) and the strength of the interactions (shaded gray area). We note that, for fixed  $J$ , the condition is satisfied for sufficiently large  $h$ . For  $J/g \gtrsim 1$  (dashed line), the predicted boundary between the two regions is no longer reliable because the higher-order corrections neglected here become dominant.

with the average  $\langle \dots \rangle$  defined in Eq. (2.2.18), and  $|E_a\rangle$  the eigenbasis of the Hamiltonian Eq. (2.2.11).

The ergodicity test based on the value of  $I$  should in principle be done for every initial configuration. However, there are states  $|\Psi_0\rangle$  that will trivially give a non-ergodic result  $I > 0$ . For example, states near the ground state will remain non-ergodic also in the presence of the  $1/J$  corrections, just because they lie at the edges of the spectrum: we checked numerically that this is the case, for instance, for the domain-wall state of Eq. (2.3.1) (data not shown). A non-trivial test, instead, is provided by generic states which lie in the middle of the spectrum: for our purposes, the Néel state  $|\mathbb{Z}_2\rangle = \prod_k \psi_{2k}^\dagger |0\rangle$ , for which  $\langle m(x, 0) \rangle = (-1)^x$ , will suffice.

In Fig. 2.12 we compare the numerical values of  $I$  at finite  $J$ , with the analytical prediction  $\tilde{I}$  at  $J = +\infty$ : using the definition in Eq. (2.4.12) and Eq. (A.2.4) one finds

$$\begin{aligned}
\tilde{I}_\infty(t) &= \lim_{L \rightarrow \infty} \sum_{x=-L/2+1}^{L/2} \frac{1}{L} \langle \mathbb{Z}_2 | m(x, t) m(x, 0) | \mathbb{Z}_2 \rangle \\
&= \lim_{L \rightarrow \infty} \frac{2}{L} \sum_{x=-L/2+1}^{L/2} \sum_{y=-\lceil L/4 \rceil + 1}^{\lceil L/4 \rceil} (-1)^x J_{2y-x}^2(2\gamma \sin(ht)) \\
&= J_0(4\gamma \sin(ht)).
\end{aligned} \tag{2.4.15}$$

In the long-time limit, the temporal average  $\bar{I}_\infty$  of  $\tilde{I}_\infty(t)$  is given by

$$\bar{I}_\infty = \lim_{T \rightarrow \infty} \frac{1}{T} \int_0^T dt J_0(4\gamma \sin(ht)) = J_0^2(2\gamma), \tag{2.4.16}$$

where the last step is a known property of the Bessel functions [245], see Eq. (A.2.22).

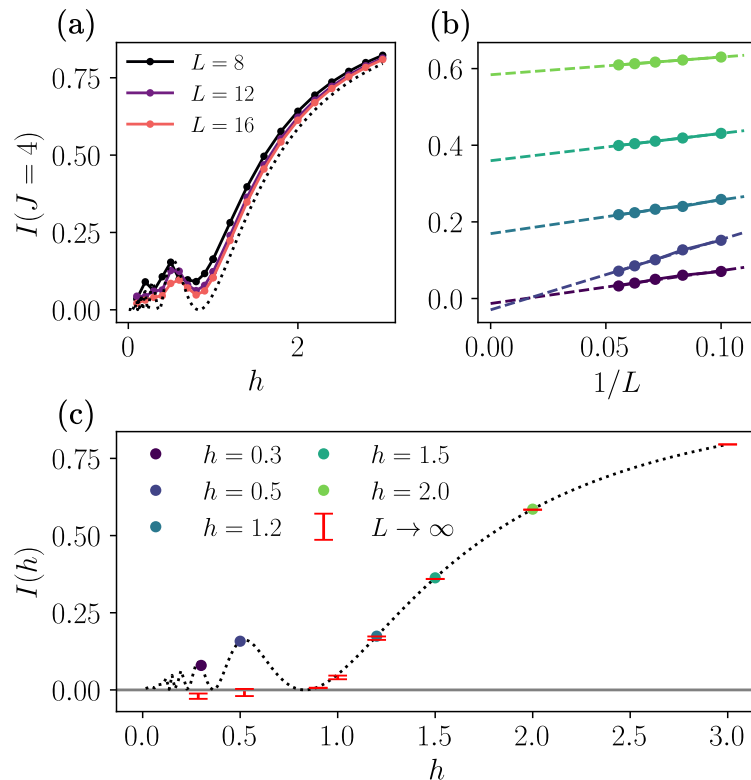


Figure 2.12: (a) Numerical values of the generalized imbalance  $I$  obtained in the diagonal ensemble at  $J = 4$ ,  $g = 1$ . In order to improve the readability, only the data for  $L = 8, 12, 16$  are reported. The dotted line represents the analytical prediction  $\tilde{I}_\infty$  for  $J = \infty$  and  $L = \infty$  given in Eq. (2.4.16). (b) Extrapolation to  $L = \infty$  of the size-dependent generalized imbalance  $I(L)$  obtained numerically, and reported in panel (a). The extrapolation is done using the ansatz  $I(L) = I_\infty + A/L$ . Different colors correspond to different values of  $h$  (see panel (c) for the legend). (c) The colored dots correspond to the values of  $h$  for which we reported the extrapolation in panel (b). The red error bars are the results of the extrapolation, with the error coming from the fit. The two points with the smaller values of  $h$  are in correspondence of the local maxima of  $I_\infty$  at  $J = \infty$  and their extrapolations are compatible with zero within the error bars. At larger values of  $h$ , instead, the extrapolation provides values of the generalized imbalance which turn out to be compatible with those at  $J = \infty$ .

The curve  $\tilde{I}_\infty$  is represented, for  $g = 1$ , by the dashed lines in Figs. 2.12a and 2.12c. For finite values of  $J$ , instead, one is able to compute the generalized imbalance only numerically and for finite  $L$ . Accordingly, the estimate for  $L \rightarrow \infty$  has to be obtained via extrapolation, which we perform in Fig. 2.12b. The numerical values of the generalized imbalance show a linear dependence on  $1/L$ , allowing for a reliable extrapolation to  $L = \infty$  (see the caption of Fig. 2.12 for more details). The final results are reported in Fig. 2.12c: while for  $h \lesssim 1$  the generalized imbalance is compatible with 0, for  $h > 1$  the results at finite  $J$  are perfectly compatible with the analytic prediction at  $J = \infty$ . These data provide numerical support to the argument à la BAA that we discussed above. In addition, we performed also numerical simulations for the time evolution of the generalized imbalance (which we do not report here), and we noticed that the relaxation time to the diagonal ensemble value depends on  $J$  (the larger  $J$ , the longer the time needed), whereas the asymptotic value does not, again in agreement with the argument à la BAA.

#### 2.4.4 Implication for the dynamics of finite bubbles and the decay of false vacuum

As mentioned in the Introduction, the problem addressed in the previous Sections is reminiscent of the false vacuum decay process, that received much attention in the field theory context, in particular starting from the works by Coleman [158–160]. In our case, we started directly from the situation in which a true vacuum bubble is already present in the false vacuum (or false vacuum in the true vacuum, which is equivalent in our setting). Therefore, we will not discuss here the timescale needed to create a bubble out of a uniform configuration (for the  $1d$  quantum Ising model this issue has been addressed in Refs. [246, 247]). Here we will limit ourselves to compare the evolution of such domains on the lattice and in the continuum, the latter problem being solved in Ref. [158].

Let us start by reminding the reader that a false vacuum, i.e. the state in which the spins are uniformly aligned in opposite direction to the longitudinal field, is a highly-excited state with finite energy density, which is expected to decay to configurations with equal total energy but larger entropy. Coleman identified and described this kind of decay process occurring in a field theory as the generation of a resonant true-vacuum bubble(s), the critical linear size  $L_*$  of which is determined by the balance between the energetic cost for creating its interface ( $\sim +8JL_*$  in our setup), and the bulk energy gain in having a bubble of true vacuum (in our setup, this comes from the spin alignment, with gain  $\sim -2hL_*^2$ ). The value of the critical linear size of the bubble is easily found:  $L_* \sim J/h$ .

In continuous space-time, the timescale associated with the formation of the bubble above can be calculated in the framework of relativistic quantum field theory using instantons. The total potential energy change  $\Delta V \sim JL_* - 2hL_*^2$ , which vanishes at the moment of the formation of the bubble, starts *decreasing* to large negative values when the bubble increases its dimension and accelerates quickly to swallow the remaining false vacuum, transforming the gained potential energy in kinetic energy  $\Delta T$  so that the total energy  $E$  does not change, i.e.,  $\Delta E = \Delta T + \Delta V = 0$ . However, there are considerable differences between our lattice setting and what happens in a field theory on the continuum. First of all, in the limit  $J \rightarrow \infty$  it is easily seen that  $L_* \rightarrow \infty$  and therefore the bubble is not formed at all. But, for finite  $J$ , if one waits a time exponentially large in  $J/h$  (using the result from Coleman’s continuum calculations), the bubble will eventually form. The walls are now expected to accelerate, expanding the bubble indefinitely, and accumulating excess potential energy in a way that conserves the total energy. This expansion and acceleration, however, cannot occur on the lattice: as it can be seen from the dual fermionic description, the kinetic energy of the domain wall is actually bounded on the lattice by the value of  $g$ , and this prevents an expansion to sizes larger than  $g/h$ . This is the reason why the bubble starts oscillating.

We have proven that these oscillations survive the perturbative introduction of a finite  $1/J$ , because the mechanism of Stark MBL confines the holographic fermions. With finite  $J$ ,  $h$ , and  $g$ , instead, Coleman’s results for the expansion and the acceleration must proceed on timescales which are exponentially large (non-perturbative) in  $J$ . Our best attempt at calculating this rate is in Sec. 2.4. In the simpler case of  $1d$  spin chains, in fact, it was found that Bloch oscillations also inhibit the expansion of the true vacuum bubble [178, 179, 248]. Accordingly, the post-vacuum-decay scenario ought to be profoundly different from that described by Coleman.

## 2.5 Conclusions

In this Chapter, we have shown how to describe the dynamics of interfaces in the two-dimensional quantum Ising model with strong ferromagnetic coupling  $J$ . As a first step, we discussed the *infinite*-coupling limit  $J = \infty$ , focusing both on the equilibrium properties of  $1d$  linear spin domains embedded in the  $2d$  lattice, and on the dynamics of infinite interfaces described by Lipschitz-continuous functions. In the first case, we have shown that the model reduces to a  $1d$  PXP Hamiltonian, for which one can calculate exactly the equilibrium magnetization, assuming that the initial state has negligible overlap with quantum many-body scars. The interest in the second case, instead, has a twofold motivation: first, the corresponding configurations effectively describe smooth interfaces and, second, given the impossibility of breaking the domain wall (ensured by the Lipschitz condition which is conserved by the dynamics), an effective  $1d$  description can be provided in terms of fermionic particles subject to a linear potential, which is amenable to an exact solution. We also discussed how to take the continuum limit of the dynamics, to predict the behavior of the quantum-fluctuating interface at scales much larger than the lattice spacing. A semiclassical interpretation of the resulting formula naturally emerged, and we will discuss it more in Chapter 4.

Then, we moved to the case of an interface shaped like an infinite corner. In particular, we discussed the properties of the average limiting shape, both on the lattice and in the continuum, and its relationship with classical corner growth models. We predicted the dynamics of the entanglement entropy between the two halves of the corner, and unveiled a deep connection between the quantum problem and the asymptotics of the Plancherel measure on random Young diagrams.

We finally relaxed the assumption of infinite strength of the Ising coupling  $J$ , making use of a Schrieffer-Wolff transformation to calculate the  $O(1/J)$  corrections. The first-order corrections break the integrability of the model with  $J = \infty$  but, remarkably, ergodicity is not restored. In fact, the presence of the longitudinal magnetic field in  $2d$ , which translates into a linear potential in  $1d$ , causes the emergence of Stark MBL, that we characterized both numerically, computing the generalized imbalance, and analytically, providing an argument for its validity. Even if a recent work provided analytical evidence against Stark MBL [249], their results apply only to the infinite-time limit, where our perturbation theory in  $1/J$  is no longer reliable. We expect therefore that, on the timescales we considered, the phenomenology of localization is quite robust.

In order to understand the temporal range of validity of our predictions, we investigated the relevant timescales controlling the dynamics of the system in generic conditions. In particular, we identified in  $T_{\text{preth}}$  the *prethermal* timescale, after which the description in terms of Schrieffer-Wolff expansion is no longer valid: it turned out that  $T_{\text{preth}}$  becomes (at least) exponentially long upon increasing  $J$ . Moreover, the possibility of utilizing a  $1d$  chain to describe interfaces in  $2d$  is justified as long as the effects of possibly having a finite bubble size are negligible. Accordingly, we estimated the timescale  $T_{\text{corner}}$  below which this is a reliable assumption, and  $T_{\text{corner}}$  turned out to increase more than exponentially upon increasing the linear size of the domain. Both these timescales ensure that the results presented here, which were derived in the infinite-coupling or

infinite-size limits, actually carry over to the case with finite but “large” coupling and sizes, up to very long times.

The approach presented here is expected to allow one to tackle even more generic questions concerning the dynamics of quantum interfaces in lattice models. For example, an intriguing issue is the ultimate “evaporation” of a bubble, driven by the exploration of disconnected configurations due to quantum fluctuations. Moreover, “holographic” mappings of the kind introduced here may inspire experimental applications in which  $2d$  degrees of freedom are used to engineer  $1d$  Hamiltonians with interesting dynamical properties, or vice-versa.

Another intriguing question is about the dynamical effects arising at times longer than  $T_{\text{preth}}$  and  $T_{\text{corner}}$ . While we leave this problem to future work, we can argue that the description given here is no longer valid, as the interface-splitting moves start playing a major role, and even the conservation of the interface length is no longer strictly guaranteed. As a consequence, the possibility of employing a  $1d$  chain to describe the dynamics of a *generic*  $2d$  domain will likely be lost. However, for some initial configurations or at least in some regimes, we expect that it will still be possible to give a description in terms of a  $1d$  effective problem, which we hope to address in future work. In the general case, however, the full  $2d$  nature of the problem will emerge in the long-time limit, or for generic couplings. In these regimes, no  $1d$  description will be reliable, and new techniques will be needed. Ultimately, it is natural to expect that a complete solution of the  $2d$  quantum Ising model is at least as hard as the solution of the  $3d$  classical Ising model.

Let us conclude by saying that “holographic” mappings similar to the one used in this Chapter to connect the  $2d$  to an equivalent  $1d$  system are also possible in higher dimensions, once the strong coupling limit is enforced. In  $3d$ , the dynamics of the quantum Ising model is still equivalent to the evolution of  $3d$  partitions, which have been shown to be equivalent to a dimer problem on a hexagonal lattice (see e.g. Refs. [211, 217]). An analytical treatment of this model currently seems to be out of reach, but still, the limit shape under the quantum dynamics is expected to be the same one provided by the analog of the Plancherel measure for  $3d$  partitions. However, in the mathematical community, a different generalization of the Plancherel measure has been considered, leading to a different limit shape. Therefore more work is needed in this direction to have analytical control of the  $3d$  problem.



## Chapter 3

# Melting of a disordered quantum crystal

*In this Chapter, we generalize the model discussed in the previous Chapter by considering a random longitudinal field. The emergent integrability at strong coupling is not present anymore, but we address the localization properties of the dynamics as it is customary in disordered quantum systems, like Anderson localization (discussed in Chapters 5, 6) and many-body localization (MBL). We find that the model does not display MBL, but the dynamics is slower than diffusive. The results presented in this Chapter are based on the publication [3].*

IN the previous Chapter, we studied the dynamics of interfaces in the two-dimensional Ising model, also in the presence of a longitudinal magnetic field, where we found that the time-evolved wave function remains localized in space because of Stark localization. In this Chapter, we consider instead the process of melting of the corner of an imperfect, two-dimensional quantum crystal. The process of melting of *classical* crystals is a wide-studied phenomenon in statistical mechanics [154, 155] and mathematical physics [250, 251], with connections ranging from the theory of random integer partitions [186, 216, 239] to determinantal point processes [209, 252–255], and even to Calabi-Yau manifolds [217, 256]. To tackle the quantum version of the problem, alongside the discussion in Chapter 2, we model the melting process by the strong-coupling limit of the  $2d$  quantum Ising model in both transverse and longitudinal magnetic fields. In particular, via a Schrieffer-Wolff transformation [191] one can obtain an effective Hamiltonian, that is particularly suitable for interpreting the process in terms of the motion of the “crystal-liquid” interface. Such Hamiltonian is in the same family of constrained PXP models [95, 193, 257], arising in the context of ultracold Rydberg atoms [258]. In the presence of disorder, PXP models show resilience towards localization already in  $1d$  [259]. The explanation relies on the fact that the local disorder *before* the constraints are applied maps to *non-local* terms in the Hamiltonian, which escape in this way the usual arguments leading to localization in the perturbative limit. This is a first clue that makes us suspect that crystal melting cannot be stopped by disorder, no matter how strong the latter can be. In this Chapter, we will exactly prove this working hypothesis: the dynamics of the crystal-melting gets only slowed down—albeit quite dramatically—never stopping at any finite value of disorder.

To prove our claim, we proceed as follows. After having introduced the model, which is the quantum Ising model in two spatial dimensions, we consider the evolution of a particular type of

initial condition, under the approximation that the Ising coupling  $J$  be the largest scale in the problem, the other two being the longitudinal ( $h$ ) and transverse ( $g$ ) magnetic fields. Within this approximation, the states of the Hilbert space can be put in one-to-one correspondence with Young diagrams, thereby reducing considerably the growth of the Krylov subspaces for the evolution. This allows us to go to relatively large system sizes, and explore the dynamical and eigenstate properties as the amount of disorder is increased. We find that, for any given system size, the eigenstate properties show some signs of localization, at least for sufficiently large disorder. However, the disorder strength for which localization is seen grows with the system size in a way that seems to indicate that no transition to MBL is present in the thermodynamic limit. Because of this, the delocalized phase emerging in such limit is rather peculiar in nature, as the dynamics is extremely slow: for example, the expected number of spin flips at time  $t$  grows like  $\sim \ln(gt)$ , irrespective of the value of disorder. This is in contrast with other situations in which the delocalized side shows transport dictated by continuously changing exponents, which are functions of the disorder strength (see for example Refs. [114, 115, 122]). We support these numerical findings with an analytical argument, employing the forward approximation in the locator expansion of the resolvent.

Our findings are relevant for several reasons. First, they show that when the process of melting of a crystal is quantum-coherent, then it cannot be stopped even by the presence of arbitrarily strong quenched disorder. Second, our work shows that generic PXP models do not likely present any stable MBL phase in two dimensions, despite this feature being very difficult to infer from the dynamical evolution alone. Indeed, the delocalized phase suffers of a severe dynamical slowdown, which could be easily misinterpreted for localization if considered alone (e.g. in an experimental setting, where eigenstate properties are difficult to access). Third, our findings hint at the conclusion that quenched disorder *and* dynamical constraints, when combined, prevent the occurrence of a stable MBL phase in two dimensions. While our results do not constitute a real proof of this latter statement, they nevertheless provide solid evidence. In this respect, our work is one of the very few numerical studies (others that we are aware of are Refs. [260, 261]) that is able to explore two-dimensional system sizes, which are not too small to draw any possible conclusion on the thermodynamic limit. In fact, as we discussed in the Introduction, the pieces of evidence for an MBL phase have been investigated mostly in one-dimensional spin chains, where still many doubts about the true existence of the MBL phase are present because of the limited available sizes, that might not be able to capture non-perturbative effects. In two and higher dimensions, the existence of MBL beyond the original paper [103] and a few others [262–266] is even more questionable.

The rest of the Chapter is organized as follows. In Sec. 3.1.1 we introduce the model and in Sec. 3.1.2 we specialize it to the strong coupling limit. In Sec. 3.2.1 we discuss the connection between the dynamics of a corner interface and the growth of Young diagrams, while in Sec. 3.2.2 we show how to describe the corner evolution using a  $1d$  fermionic chain. Subsequently, in Sec. 3.3 we move to discuss the forward approximation for the model under consideration, presenting in Sec. 3.3.1 the analytic treatment and in Sec. 3.3.2 the comparison with numerical results. Then, we move to a detailed presentation of the numerical results both for the spectrum, in Sec. 3.4, and for the dynamics, in Sec. 3.5.3. Finally, in Sec. 3.6 we discuss the limits of validity of the results presented when the strong coupling limit is relaxed (Sec. 3.6.1) and the comparison with corresponding classical models (Sec. 3.6.2), giving some final considerations in Sec. 3.7.

## 3.1 Model

### 3.1.1 A disordered quantum solid undergoing melting

As anticipated, we are interested in the dynamics of melting of a two-dimensional, disordered quantum crystal. As done commonly in the literature [209, 216, 250, 251], we consider the melting process starting from the tip of an infinite, right-angled wedge, see Fig. 3.1. More general finite- and infinite-size initial configurations could be treated with similar tools, see for more details Refs. [1, 2] and Chapter 2. We describe the solid, non-melted part of the crystal via “up” Ising spins  $\sigma_i^z = +1$ ,  $i \in \mathbb{Z}^2$ , and the melted part via “down” spins  $\sigma_i^z = -1$  ( $\sigma^{x,y,z}$  are Pauli matrices). The Hamiltonian is that of the two-dimensional Ising model on a square lattice (the same as in Eq. (2.1.1)), with a constant transverse field  $g$  and, now, a *random* longitudinal field  $h_i$ :

$$H_{\text{Ising}} = -J \sum_{\langle ij \rangle} \sigma_i^z \sigma_j^z + \sum_i h_i \sigma_i^z + g \sum_i \sigma_i^x. \quad (3.1.1)$$

The physical interpretation of the terms appearing in the Hamiltonian is rather straightforward. The  $g$  term lets the spins flip freely between  $+1$  and  $-1$ , thus neither the melted phase nor the crystal is preferred at this level (we stress that we want to describe the *quantum-coherent* process of melting *in real time*, thus we need time reversibility). The presence of the ferromagnetic coupling term ( $J > 0$  throughout the Chapter), however, favors the formation of bubbles of aligned spins, contrasting to a certain extent the action of the  $g$  flips. Finally, we introduce disorder in the form of a random longitudinal field  $h_i \in [-W/2, W/2]$ , with a uniform distribution: this models the presence of impurities by assigning a different energy cost for the addition/removal of a particle at each site  $i \in \mathbb{Z}^2$ . Notice that our choice of the Hamiltonian (3.1.1) implies that particles in the liquid state *do not lose phase coherence*, as they are represented, in a rather simplistic way, by immobile “down” spins, that do not wander around and interact with one another. This choice is made so to boost the quantum coherence of the model, which otherwise should be described as an open quantum system.

### 3.1.2 Strong-coupling limit and effective PXP description

In this Section, we recall some concepts already described in Chapter 2, in particular in Sec. 2.1.1, therefore it can be skipped by the reader familiar with the notions of Chapter 2.

We will assume here that the strong-coupling limit  $J \gg g \sim W$  holds. This assumption is necessary to make sense of a *quantum-fluctuating interface*, that clearly separates the solid and melted phases; otherwise, one could not speak of a melting process altogether.

When the coupling  $J$  is very strong, as in the clean case, the Hilbert space of the model effectively decomposes into sectors identified by the length of the domain walls, i.e. the number of violated Ising bonds [1, 2, 170, 171]. The operator  $\mathcal{L}$ , introduced in Eq. (2.1.2), is the combined length of the strings/domain walls, and it is a conserved quantity in the limit  $J \rightarrow \infty$ . Indeed,  $\mathcal{L}$  is very closely related to the interaction energy in the original model, and by unitarity, it must be conserved: the excess energy cannot be compensated by other means.

When instead  $J$  is large but finite,  $\mathcal{L}$  is only approximately conserved. However, while for the ordered case with field  $h$  this is a singular limit (since the energy of a string of length  $\ell$  is  $J\ell$  and the volume energy contribution  $\sim h\ell^2$  is always dominant), for our disordered model with average field  $\langle h \rangle = 0$ , the volume energy contribution is, typically, of order  $\langle h^2 \rangle^{1/2} \ell$ . Thus, in the limit  $J \gg h$  the string length can be conserved to high accuracy.

As just described, through the operator  $\mathcal{L}$  the Hilbert space is split into sectors of equal domain-wall length and, if the initial condition is supported within only one of those sectors, the dynamics

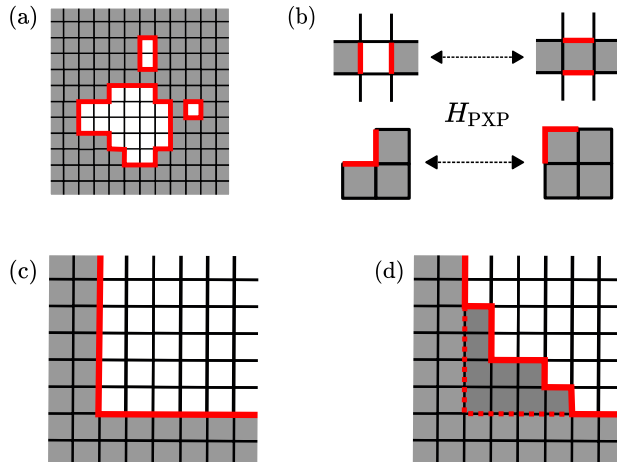


Figure 3.1: (a) Generic configuration diagonal in the  $\sigma^z$  basis, made of 3 disconnected bubbles of “down” spins (in white) surrounded by “up” spins (in gray). (b) Visual representation of the hopping terms of the Hamiltonian Eq. (3.1.2). The top row represents moves that break a bubble into two pieces (or join them), and will not be considered in our discussions. The bottom row represents moves that give dynamics to the corner, allowing it to melt: we will focus our attention on these ones. (c) The initial configuration we will consider: an infinite, right-angled wedge. (d) One of the possible configurations reached from the wedge in the melting process.

will be confined in it for all times. In Refs. [170, 171] the fragmentation of the Hilbert space of the clean version of the model (3.1.1) was studied in great detail, showing in particular that the *Krylov subspaces* represent an even finer scale wrt. the eigenspaces of  $\mathcal{L}$ .

The Hilbert space fragmentation in the strong-coupling limit can be formally described through a Schrieffer-Wolff (SW) transformation [191], which accounts for the Ising interaction in a perturbative way. In terms of the operator  $\mathcal{L}$ , the Hamiltonian  $H_{\text{eff}}$  generated by the SW transformation, order by order in  $J^{-1}$ , will be such that  $[H_{\text{eff}}, \mathcal{L}] = 0$ . To lowest order, the effective Hamiltonian one finds in any Krylov subspace is of the PXP form [1, 2]:

$$H_{\text{PXP}} = \sum_i h_i \sigma_i^z + g \sum_i \left( |\Uparrow\rangle\langle\Downarrow| + |\Lrcorner\rangle\langle\Uparrow| + |\Downarrow\rangle\langle\Uparrow| + \text{h.c.} \right). \quad (3.1.2)$$

Above, we have introduced a convenient graphical notation to indicate spin flips. Indeed, one can easily get convinced that spin flips can take place only next to an up/down spin border, as in Fig. 3.1a, and are only of the form indicated by the shapes in Eq. (3.1.2) and Fig. 3.1b.

The next order in the SW transformation encompasses the first  $O(1/J)$  corrections. However, the resulting SW Hamiltonian is rather complicated, and probably of little practical use in general situations. We derived such Hamiltonian in Chapter 2 for the class physically relevant Krylov sectors, which comprise the one investigated here. While we could study also in this Chapter the effects of a finite  $J$ , we believe that such effects would entail just a *quantitative* modification of the results presented, while leaving the physical picture unchanged. Therefore, in the following, we will always neglect the  $O(1/J)$  corrections, while leaving to Sec. 3.6.1 a brief informal discussion of their possible implications.

So far, we have argued that one can pass from the Hamiltonian of the full  $2d$  quantum Ising model, Eq. (3.1.1), to the effective Hamiltonian, Eq. (3.1.2), capturing the dynamics of domain walls in the original model, when the strong coupling limit is considered. Before moving on, let us remind that PXP Hamiltonians in  $1d$  have shown some form of slow dynamics in either

numerics or experiments [89, 92, 194, 267, 268], and presence of “scars” in the spectrum, i.e. atypical eigenstates (e.g. with atypically low entanglement entropy). At the same time, for PXP models both the spectrum as a whole and the dynamics at finite energy density, are ergodic. Such ergodicity is resistant also to the introduction of quenched disorder [259]: this is a consequence of the fact that the disorder maps, in an *unconstrained* basis of states, to generic, non-local interaction terms. This feature will be present also in the  $2d$  model under consideration, thus we refer to Sec. 3.2 for a detailed discussion.

## 3.2 Mapping to Young diagrams and to lattice fermions

As stated in the Introduction, we are interested in the dynamics of melting generated by the Hamiltonian (3.1.1) (or equivalently Eq. (3.1.2)), starting from a particular type of initial condition: a corner made of “up” spins, in a sea of otherwise “down” spins, see Fig. 3.1c. This configuration is physically relevant, as it is one of the simplest crystal shapes whose melting can be studied. In this Section, we discuss two mappings of the Krylov subspace containing such corner-shaped interface: a mapping to Young diagrams in Sec. 3.2.1, and one to lattice fermions in Sec. 3.2.2. The usefulness of such mappings will become clear as we proceed.

### 3.2.1 Young diagrams

The fragmentation into Krylov subspaces, briefly outlined in the previous Section, represents a huge source of simplification for the full,  $2d$  problem. A particularly neat example is given by the initial state whose evolution we aim at describing, viz. a right-angled, infinite corner (see Fig. 3.1c). For this case in particular, only the moves ( $|\uparrow\rangle\langle\downarrow| + \text{h.c.}$ ) and ( $|\downarrow\rangle\langle\uparrow| + \text{h.c.}$ ) in Eq. (3.1.2) are allowed, and all the states in the Krylov subspace are in one-to-one correspondence with *Young diagrams*. Let us recall that, by definition, a Young diagram is a collection of boxes, arranged in left-justified rows, and stacked in non-increasing order of length [238]. The mapping to Young diagrams is quite transparent; a detailed explanation can be found in Chapter 2 (or equivalently Refs. [1, 2]). We also recall *en passant* that the Young diagrams of size  $N$  are in one-to-one correspondence with the integer partitions of  $N$ .

Thanks to the mapping, the quantum dynamics which makes the crystal wedge melt can be described equivalently by the hopping on the space of Young diagrams  $\mathcal{D}$ , see Fig. 3.2. The initial state, viz. the full wedge, is the empty Young diagram  $D = \emptyset$ . Then, the energy of a diagram  $D \in \mathcal{D}$  is given by the sum of the longitudinal fields on the “blocks” composing the diagram:

$$E_D = \sum_{i \in D} h_i. \quad (3.2.1)$$

The rate of hopping between two Young diagrams  $D, D'$  is  $g$  if they are connected by a single block addition or deletion (neighbouring diagrams), or zero otherwise. Therefore, the adjacency matrix of the Young lattice has non-zero elements only between the set of diagrams of size  $N$ , call it  $\mathcal{D}_N$ , and that of size  $N - 1$  ( $\mathcal{D}_{N-1}$ ) or  $N + 1$  ( $\mathcal{D}_{N+1}$ ); see Fig. 3.2b for a sketch.

In the end, one is left with a Hamiltonian operator, acting on the Hilbert space  $\mathcal{H}_{\mathcal{D}}$  built on the set of diagrams  $\mathcal{D}$ , i.e. the Krylov subsector of the original Ising model that contains the infinite wedge:

$$H_{\mathcal{D}} = g \sum_{\langle D, D' \rangle} |D\rangle\langle D'| + \sum_D E_D |D\rangle\langle D|. \quad (3.2.2)$$

The net gain is that the dimension of  $\mathcal{H}_{\mathcal{D}}$  is much smaller than that of the full Hilbert space of all the spins configurations  $\{\sigma_i\}$  on the plane. Indeed, let us denote the dimension of the

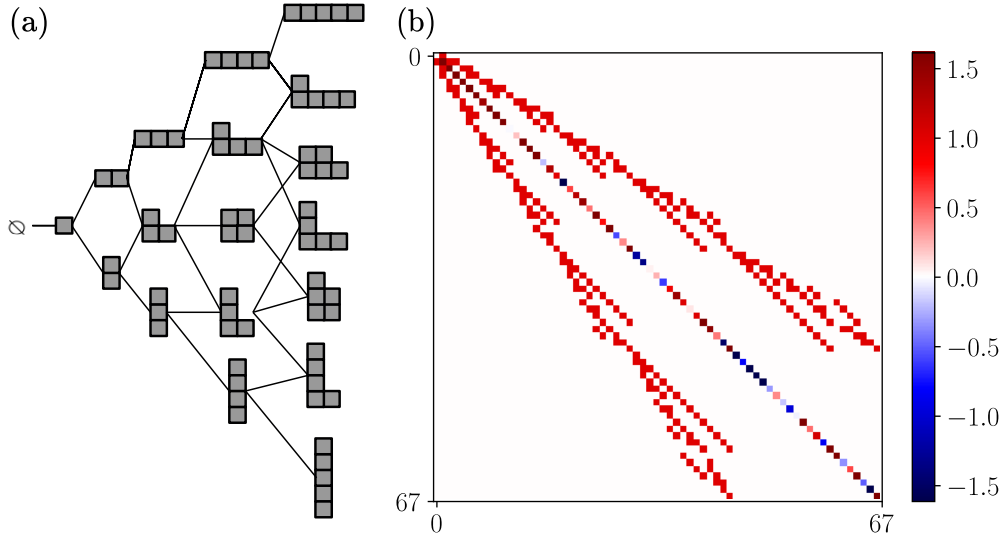


Figure 3.2: (a) Young lattice, i.e. the set of Young diagrams where two of them are connected if differing by a single box. In figure the lattice up to  $N = 5$  is represented. (b) Matrix plot of the Hamiltonian Eq. (3.2.2) up to  $N = 8$ , corresponding to a Hilbert space of dimension 67. The off-diagonal elements correspond to the adjacency matrix of the Young lattice, and are all set to  $g \equiv 1$ , while the diagonal part is determined by the disordered magnetic field as detailed in Sec. 3.2.1.

Hilbert subspace, made of diagrams composed of exactly  $N$  squares, as  $d_N := \dim \mathcal{H}_{\mathcal{D}_N}$ . It follows that, for the diagrams made up at most of  $N$  squares, one has to compute the cumulative  $\bar{d}_N := \sum_{k=0}^N d_k$ . Thus, from the Hardy-Ramanujan asymptotic formula for partitions, one finds  $\bar{d}_N \simeq \exp\left\{\left(\pi\sqrt{2N/3}\right)\right\}/\sqrt{8\pi^2N}$ : the mild, stretched-exponential growth of such numbers will enable us to reach system sizes of up to  $N = 36$  spins. Notice that such dimensions correspond to a *vanishing entropy density* in the original model, since  $s = \ln(\bar{d}_N)/N \sim N^{-1/2}$ . In other constrained models (including the  $2d$  dimer models of Refs. [260, 261]) the growth of Krylov sectors is instead exponential, with a finite entropy density.

Before moving on, let us remark that the approach outlined above, i.e. passing from the original interacting model to an hopping problem on the Hilbert space graph, is a common practice in the field of many-body physics, and in particular of MBL [106]. For more standard quantum spin chains with particle number conservation, one usually restricts to the half-filling sector, thus obtaining the subset of the hypercube with an equal number of positive and negative vertices as graph—eventually with a disordered, correlated chemical potential if the original model is disordered itself. In the case under consideration, instead, the graph obtained is the Young diagrams lattice of Fig. 3.2, another subset of the hypercube but with very different connectivity properties wrt. the former: this can be already guessed from the scaling with  $N$  of the number of vertices and edges [269]. Let us also mention that this hopping problem is very different from XXZ-type models *on random graphs themselves* [270], since one has already got rid of interactions by passing to the graph.

### 3.2.2 Lattice fermions

It is a classic result of combinatorics that Young diagrams can be mapped to a spin-1/2 chain [202] or, equivalently, to a fermionic chain via a Jordan-Wigner transformation, see also Fig. 3.3. This

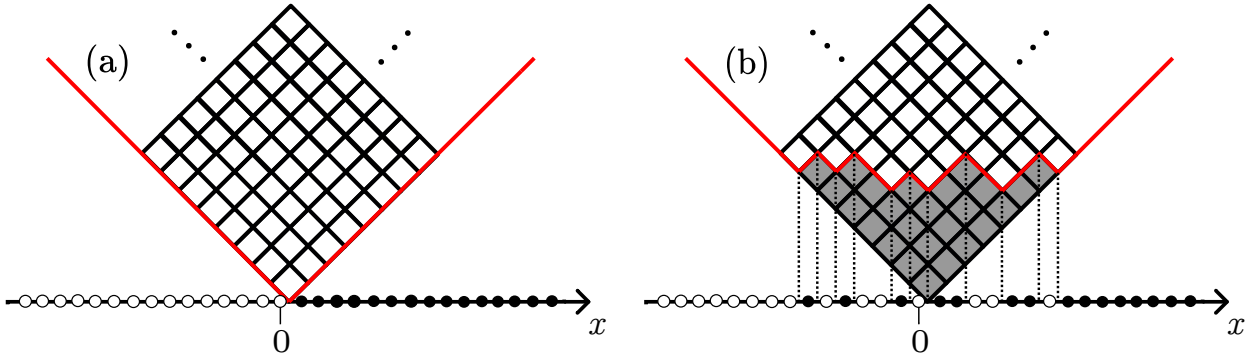


Figure 3.3: Mapping of  $2d$  configurations dynamically connected to the corner, and thus of Young diagrams, to fermions. (a) The initial configuration, i.e. an infinite wedge, is mapped to the domain wall state  $|\cdots 000111 \cdots\rangle$  on the chain. (b) A generic state (in this case, the Young diagram corresponding to the partition  $\{7, 6, 4, 3, 3, 1, 1\}$ ) is mapped to a fermion configuration according to the procedure described in the main text.

has allowed for an analytic solution for the limiting shape of the crystal wedge presented in Chapter 2 (for a clean system), and unveiled connections to the mathematics of random integer partitions [186, 217, 239]. In the case of a clean system, in particular, the Hamiltonian (3.1.1) maps to free fermions on the chain. In the disordered case we are now studying, instead, the integrability will be lost but the mapping, which is a form of *holography* between a  $2d$  problem and a  $1d$  problem, retains its usefulness in simplifying the description of the problem, both for a numerical and an analytical treatment. Therefore, we will briefly describe it here.

Let us start with the null Young diagram  $D = \emptyset$ : as shown in Fig. 3.3a, it is associated to a domain wall centered in 0 on the chain. Then, by moving on the line particles to the left, or holes to the right, to each and every  $1d$  fermion configuration at half filling there corresponds a Young diagram, as in Fig. 3.3b.

For what concerns the Hamiltonian, the hopping term becomes associated to simple nearest-neighbour hoppings on the chain (whose fermionic operators we represent as  $\psi_x$ ,  $x \in \mathbb{Z}$ )

$$g \sum_{\langle D, D' \rangle} |D\rangle \langle D'| \longleftrightarrow g \sum_x \left( \psi_x^\dagger \psi_{x+1} + \text{h.c.} \right). \quad (3.2.3)$$

The energy  $E_D |D\rangle \langle D|$ , on the other hand, has no simple interpretation as a local term. Instead, it is a generic operator which involves all the fermions, through their number operator  $n_x = \psi_x^\dagger \psi_x$ :

$$E_D |D\rangle \langle D| \longleftrightarrow E(n_x, n_y, \dots) \quad (3.2.4)$$

where  $x, y, \dots$  are the indices of the sites “touched” by the diagram  $D$ . This non-locality of the disordered potential terms, already anticipated in the Introduction, is typical of PXP models [259], and it comes from the interplay of dynamical constraints and local fluctuations in the potential energy. In one spatial dimension, it was proven to be the cause of the absence of a MBL phase [259]: indeed, the presence of non-local interactions on the chain makes the model evade all the arguments in favor of ergodicity breaking. We believe that the same happens in our  $2d$  setting, since the perturbative arguments supporting MBL work equally in any dimension, while the non-perturbative effects that destabilize MBL are stronger.

In view of the above, it is quite surprising to remark that, on the contrary, in the clean case  $h_i \equiv h$  the mapping simplifies to

$$\sum_D E_D |D\rangle \langle D| \longleftrightarrow -2h \sum_x x \psi_x^\dagger \psi_x. \quad (3.2.5)$$

Therefore, for a uniform field  $h \neq 0$  the melting dynamics will be Stark-localized, as found in Chapter 2. Moreover, for  $h \gtrsim 1$  the finite- $J$  corrections are likely incapable of thermalizing the system, which therefore enters a Stark-MBL phase. We see therefore that the presence of disorder is *assisting* the thermalization, since it breaks the integrability (in the sense of free fermions) of the model, while it is not able to make the model athermal by itself, due to its non-local nature.

To conclude this Section, we remark that the mapping of the  $2d$  dynamics onto a line of fermions is interesting for several reasons. First, as said above it constitutes a great simplification of the problem, as it enables a  $1d$  effective description, amenable of much more analytical control. Second, the  $2d$  dynamics induces on the fermions a rather particular type of dynamics, interesting by itself, which we set up to investigate in the next Sections. Third, as remarked also in the previous Chapter, the mapping is a form of *holography* [180], which surely deserves a better investigation, in view of the intense interest of the last years on such phenomena, especially in presence of quenched disorder [271–273].

### 3.3 Perturbation theory estimates

It is becoming clear, as the discussion unfolds, that the melting of an infinite quantum crystal wedge does not undergo a localization phenomenon, even if it may be severely slowed down by disorder. Therefore, as a first thing we perform a perturbative estimate for the critical disorder strength  $W_c$  of a putative MBL transition, showing that such  $W_c$  flows to infinity as the thermodynamic limit is approached. To do so, we employ the so-called *forward approximation* (FA) [96, 102, 106, 242], which consists in calculating the Green's functions to lowest order in the hopping among localized orbitals. For the sake of being self-contained, we review briefly the main ideas of the FA in Sec. 3.3.1, and then discuss the implications for our system in Sec. 3.3.2.

#### 3.3.1 Brief description of the forward approximation

In the FA, one starts from the locator expansion of the resolvent [241]:

$$G(b, a; E) = \langle b | \frac{1}{E - H} | a \rangle = \frac{\delta_{ab}}{E - E_a} + \frac{1}{E - E_a} \sum_{p \in P(a, b)} \prod_{k=1}^{|p|} \frac{g}{E - E_{p_k}} \quad (3.3.1)$$

where  $P(a, b)$  denotes the set of paths from  $a$  to  $b$ . Notice that in our case the labels  $a, b, \dots$  will represent Young diagrams, and the graph will be defined by the adjacency matrix  $\sum_{\langle D, D' \rangle} |D\rangle \langle D'|$  (see  $H_{\mathcal{D}}$  in Eq. (3.2.2)). As customary, one can pass from the random walks  $P(a, b)$  to the self-avoiding walks  $\text{SAW}(a, b)$  at the cost of introducing a self energy term:

$$G(b, a; E) = G(a, a; E) \times \sum_{p \in \text{SAW}(a, b)} \prod_{k=1}^{|p|} \frac{g}{E - E_{p_k} - \Sigma_{p_k}^{\{p_0, p_1, \dots, p_{k-1}\}}(E)}, \quad (3.3.2)$$

where indeed  $\Sigma_a^{\{b, c, \dots\}}(E)$  is the self-energy at site  $a$  obtained removing from the lattice the sites  $b, c, \dots$ . From the *exact* representation of Eq. (3.3.2) one can in principle obtain also the (many-body) amplitude  $\Psi_\alpha(b)$  of the system to be found in configuration  $b$ , while being in the eigenstate  $\alpha$  localized around configuration  $a$ :

$$\Psi_\alpha(b) = \frac{1}{\Psi_\alpha(a)} \lim_{E \rightarrow E_\alpha} (E - E_\alpha) G(b, a; E). \quad (3.3.3)$$

Notice that this reduces to  $\delta_{ab}$  in the limit  $g \rightarrow 0$ . Finally, performing the approximation of summing only on the *shortest paths* (or *directed polymers*)  $\text{SP}(a, b)$  from  $a$  to  $b$ , and thus working to lowest order in  $g$ , one finds

$$\Psi_\alpha(b) \approx \sum_{p \in \text{SP}(a,b)} \prod_{k=1}^{|p|} \frac{g}{E_a - E_{p_k}} = \left(\frac{g}{W}\right)^{d(a,b)} \sum_{p \in \text{SP}(a,b)} \prod_{k=1}^{|p|} \frac{1}{E'_a - E'_{p_k}}. \quad (3.3.4)$$

Above, we have introduced the distance  $d(a, b)$ , and the rescaled diagonal elements of the Hamiltonian  $E'_a := E_a/W$ .

At this point, the criterion for localization is given by the requirement that, with probability 1 over the disorder realizations, the probability of finding a particle at distance  $O(L)$  from the localization center of the state goes to zero for  $L \gg 1$  [106, 242]. More formally, defining

$$\Psi_r := \max_{b: d(a,b)=r} |\Psi_\alpha(b)| \quad (3.3.5)$$

the system is considered to be localized if  $Z_r := \frac{1}{r} \ln |\Psi_r|$  satisfies

$$P\left(Z_r \leq -\frac{1}{\xi}\right) \rightarrow 1 \quad \text{for } r \rightarrow \infty \quad (3.3.6)$$

for some finite  $\xi > 0$ . The other way round, if the system is delocalized we expect

$$P(Z_r \geq -\epsilon) \rightarrow 1 \quad \text{for } r \rightarrow \infty \quad (3.3.7)$$

for any arbitrarily small  $\epsilon > 0$ . The critical value of the disorder can be estimated from the average value  $\langle Z_\infty \rangle = \lim_{r \rightarrow \infty} \langle Z_r \rangle$  using the condition

$$\langle Z_\infty(W_c) \rangle = -\ln |g|. \quad (3.3.8)$$

The possibility of passing from the statements in probability, Eqs. (3.3.6)–(3.3.7), to the one in terms of the average value, Eq. (3.3.8), is possible because of probability concentration as  $r \rightarrow \infty$  [106].

### 3.3.2 Application to the melting process

The numerical results, obtained by using the empty diagram  $D = \emptyset$  as starting point (“ $a$ ” in the formulae above), are reported in Fig. 3.4. It is sufficient to plot a value of  $W$  only, in virtue of Eq. (3.3.4). As  $r$  is increased,  $\langle Z_r \rangle$  diverges, being fitted reasonably well both by  $\sim \sqrt{r}$  or  $\ln r$  (more on this below). This proves the absence of a finite critical value  $W_c$ , which instead can be present only if  $\langle Z_r \rangle$  saturates to a finite constant.

We now explain why both the square-root and the logarithmic fits are reasonable for the data in Fig. 3.4 (larger system sizes are needed to discriminate between the two). Starting from the former, one can see that it traces back to the dimension of the Hilbert space as follows. In Eq. (3.3.4), the dominant contribution to the term  $(E'_a - E'_{p_k})^{-1}$  is of order  $\sim d_{|p_k|}$ , being  $d_k$  the number of states at distance  $k$  from the initial configuration (cf. Sec. 3.2.1): indeed, one can take the average level spacing to be  $\delta E'_{p_k} \approx 2k/d_{|p_k|}$ , and take only the dominant (exponential) contribution. The initial configuration being empty, the diagrams at distance  $k$  are all made of  $k$  blocks, thus they belong to the subspace  $\mathcal{H}_{\mathcal{D}_k} \subset \mathcal{H}_{\mathcal{D}}$ . At this point, one can evaluate the product over  $k$  in Eq. (3.3.4):

$$\prod_{k=1}^r \frac{1}{E'_a - E'_{p_k}} \sim \prod_{k=1}^r d_k \sim \exp \left[ \sum_{k=1}^r \pi \sqrt{\frac{2k}{3}} \right] \sim \exp \left[ \pi \left(\frac{2}{3}\right)^{3/2} r^{3/2} \right], \quad (3.3.9)$$

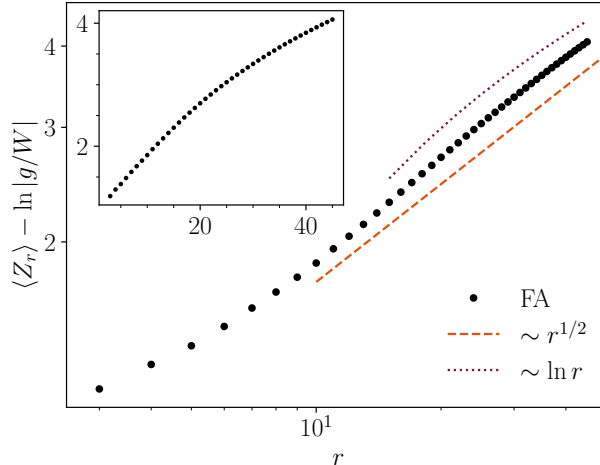


Figure 3.4: Plot of  $\langle Z_r \rangle$  vs  $r$  as described in the main text: in the main panel it is shown in log-log scale, while in the inset in linear scale. The dots are the numerical results of the FA up to  $r = 45$ . Their growth should be compared either with a square-root (dashed orange line), or a logarithm (dotted purple line). Fitting a square-root behaviour compares reasonably well with the mean-field-like estimate of the main text: the fit (not shown) gives  $Z_r \approx 0.57r^{0.52}$ , while the analytical prediction was  $Z_r \approx \pi(2/3)^{3/2}\sqrt{r} \approx 1.71\sqrt{r}$ . The numerical data was averaged over 3000 disorder realizations. The inset contains the same data plotted in linear scale.

where there was used the Hardy-Ramanujan formula  $\dim \mathcal{H}_{\mathcal{D}_k} = d_k \sim \exp(\pi\sqrt{2k/3})$ , and the asymptotic expansion of the harmonic numbers of order  $1/2$ <sup>1</sup>. Notice that one can set, according to the convention of Eq. (3.3.5),  $|p| = r$  and  $|p_k| = k$ .

The further sum over the SP in Eq. (3.3.4) does not alter the behavior of the estimate for large  $|p|$ , as one can check by giving an upper bound to the number of SP: for example, one can bound it by making all diagrams of size  $k$  connected to all diagrams of size  $k+1$ , for all  $k$ . In this case, also the number of SP is  $\prod_{k=1}^r d_k$ , thus giving the same asymptotic behavior (see also the discussion below).

Putting the pieces together, one gets

$$Z_r = \frac{1}{r} \ln |\Psi_r| \sim \sqrt{r}. \quad (3.3.10)$$

This estimate gives a good prediction for  $Z_r$ , as shown in Fig. 3.4, but it relies on the assumption that, at each step of the optimal path, it is feasible to remain as close as possible to the resonant energy. Therefore, we understand that this is a *optimistic* estimate for  $Z_r$ , yielding a scaling that we can consider to be a sort of upper bound for it.

The assumption of remaining on resonance at each step is not valid for general geometries: it is false, for instance, on the Bethe lattice—which usually constitutes a good approximation of many-body Fock spaces. On the other hand, it is surely valid in the case in which each configuration  $D \in \mathcal{D}_r$  is connected to any other configuration  $D' \in \mathcal{D}_{r+1}$ , in a mean-field-like setting (this same mean-field approximation was used above to bound the number of SP). We argue that the Young lattice of Fig. 3.2, i.e. the graph obtained by joining two Young diagrams iff they differ by just one square, has indeed properties much closer to the mean-field case rather than to the Bethe lattice.

<sup>1</sup>The summation can be performed using the Euler–Maclaurin formula. For the present case, it gives  $\sum_{k=1}^n \sqrt{k} = \frac{2}{3}n^{3/2} + \frac{\sqrt{n}}{2} + \zeta(-\frac{1}{2}) + O(n^{-1/2})$ , therefore yielding the leading contribution reported in Eq. (3.3.9).

Let us consider the number of shortest paths connecting the empty diagram  $\emptyset$  to a configuration made of  $r$  blocks, call it  $D \in \mathcal{D}_r$ . For the Bethe lattice, by definition, the number of paths going between any two configurations is one, as there are no loops. On the other hand, considering the mean-field Young lattice in which any configuration in  $\mathcal{D}_r$  is connected to any configuration in  $\mathcal{D}_{r+1}$ , we already showed that the number of shortest paths connecting the empty diagram with any diagram at level  $r$  is  $\prod_{k=1}^r d_k \sim \exp(Cr^{3/2})$ . For the true Young lattice, one can take advantage of the fact that the number of shortest paths leading to a Young diagram  $D$  coincides with the so-called dimension  $\dim(D)$ , computed according to the hook length formula [239]. Such number  $\dim(D)$  corresponds also to the dimension of the representation of the symmetric group identified by the diagram  $D$  [238]. At this point, the typical dimension of a diagram  $D$  made of  $r$  squares is found to be  $\dim(D) \sim \sqrt{r!}$  [185], so the typical number of SP will scale like  $\sqrt{r!}$  as well. Therefore, even if the SP are less than in the mean-field case, they are more than exponentially many in the distance from the starting configuration. In conclusion, one obtains a growth

$$\langle Z_r \rangle \sim \ln r. \quad (3.3.11)$$

The true behaviour of the curve in Fig. 3.4 will likely be something in between a square root and a logarithm. For the system sizes accessible to present-day computers, and given the slow growth of both curves, it is not possible to discern between the two hypotheses. Nevertheless, for our purposes the results shown are sufficient to claim that there is no finite-disorder localization transition, at least at the lowest order of perturbation theory.

### 3.4 Spectral statistics via exact diagonalization

In this Section, we support the conclusions found in perturbation theory by performing an extensive numerical study of the model through exact diagonalization. The numerics was performed by constructing explicitly the Hilbert space of the model, i.e. the Young lattice of Fig. 3.2a, with ad-hoc methods. An example of the Hamiltonian matrix, truncated to a finite  $N$ , is shown in Fig. 3.2b <sup>2</sup>.

To distinguish between the MBL and ETH regimes of a system, one can consider various indicators, each with well-defined, and different behaviors in the two cases. Here, we consider mainly spectral indicators. Let us start from the results for the statistics of the energy levels  $E_n$ , summarized in Figs. 3.5 and 3.6. In the inset of Fig. 3.5 we show how, at finite system size  $N$ , there is a crossover from Wigner's surmise (viz. GOE, at small  $W$ ) to the Poisson gap distribution (at large  $W$ ) for the normalized level spacings  $s_n = (E_{n+1} - E_n) / \langle E_{n+1} - E_n \rangle$ , taken at the center of the spectrum. To argue that such crossover builds up into a sharp transition in the thermodynamic limit, one may look at the spectral gap ratio parameter

$$r = \left\langle \frac{\min(s_{n+1}, s_n)}{\max(s_{n+1}, s_n)} \right\rangle, \quad (3.4.1)$$

which needs not be normalized. In the main panel of Fig. 3.5, one can see that the crossover from  $r_{\text{GOE}} \simeq 0.5307$  to  $r_{\text{Pois}} \simeq 0.3863$  gets slightly steeper as  $N$  increases, but it also moves to larger values of  $W$ . To perform a reliable finite-size scaling analysis, we decided to look at the

---

<sup>2</sup>Another possible way of simulating the system is with the fermionic chain representation. However, we chose not to do so for two reasons. First, the Fock space of a chain of length  $L$  at half filling does not contain only the Young diagrams made at most of  $L/2$  squares, but also Young diagrams with more squares: consider e.g. the state in which  $L/2$  fermions are on the left half of the chain, and the right half is empty, that corresponds to a Young diagram made of  $(L/2)^2$  squares. Second, and more importantly, the disorder maps to non-local interactions on the chain, which are more difficult to handle.

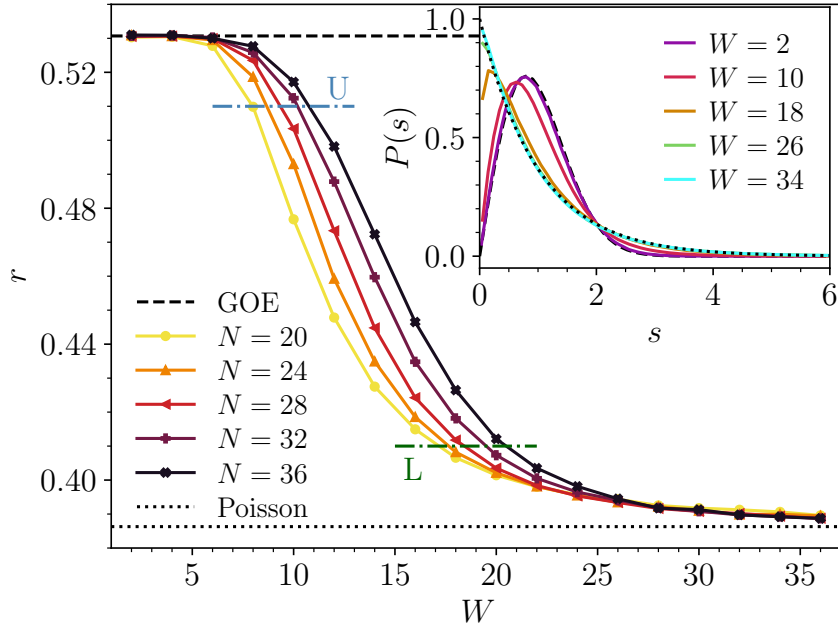


Figure 3.5:  $r$  parameter as a function of the disorder strength  $W$  (in units of  $g \equiv 1$ ), and for increasing system sizes. The  $r$  value flows from the GOE prediction at small disorder, to the Poisson one at large disorder for any considered system size. However, no real sign of the build-up of a transition is found; rather, the crossover from GOE to Poisson simply seems to shift to larger values of  $W$  as the thermodynamic limit is approached. This feature is analyzed by means of the upper (U) and lower (L) cuts, represented by the dashed-dotted lines; see the main text for more details. The number of disorder realizations used ranges from 10000 (smallest system size) to 17000 (largest system size). (Inset) Histogram of the normalized level spacings  $s$ , for  $N = 32$  and 3000 disorder realizations. Also here one can see flow from GOE (dashed black line) to Poisson (dotted black line).

disorder strengths  $W_U$  and  $W_L$ , for which the  $r$  parameter becomes smaller than 0.51 and 0.41, respectively<sup>3</sup>. Reliable estimates for  $W_U$  and  $W_L$  were obtained by fitting locally the values of  $r(W)$  with a polynomial function, and solving for the intersection. In the inset of Fig. 3.6, it is shown how the values found for  $W_U$  and  $W_L$  seem to diverge linearly with system size, but with two different slopes. In particular, the faster divergence of  $W_L$  indicates that no transition is being built up; instead, the crossover from GOE to Poisson seems to become smoother at larger system sizes. Notice that this last fact also prevents one to perform a scaling collapse of the data: it is impossible to accommodate the scalings of both  $r > 0.51$  and  $r < 0.41$  with only one function, since the two parts of the curve  $r(W)$  are flowing towards larger values of  $W$  with different speeds. In addition to the previous observations, both  $W_U$  and  $W_L$  seem to represent *lower bounds* (see how the curves  $r(W)$  change with system size in Fig. 3.5) for the critical disorder strength  $W_c$ , at which a putative MBL transition may take place: therefore, we believe that such transition does *not* take place at all in the thermodynamic limit, being pushed to infinite disorder strength.

A more refined analysis is shown in the main panel of Fig. 3.6. There, we try to extrapolate to  $N = \infty$  with two different fits. The dashed line represents the same fit of the inset, i.e. a linear one:  $W = a + bN$ . The dotted line, instead, is a fit of the form  $W = a' + b'/N + c'/N^2$ , which extrapolates

<sup>3</sup>The values of 0.51 and 0.41 are of no special importance; any other values near to  $r_{\text{GOE}} \simeq 0.5307$  and  $r_{\text{Pois}} \simeq 0.3863$  yield the same results.

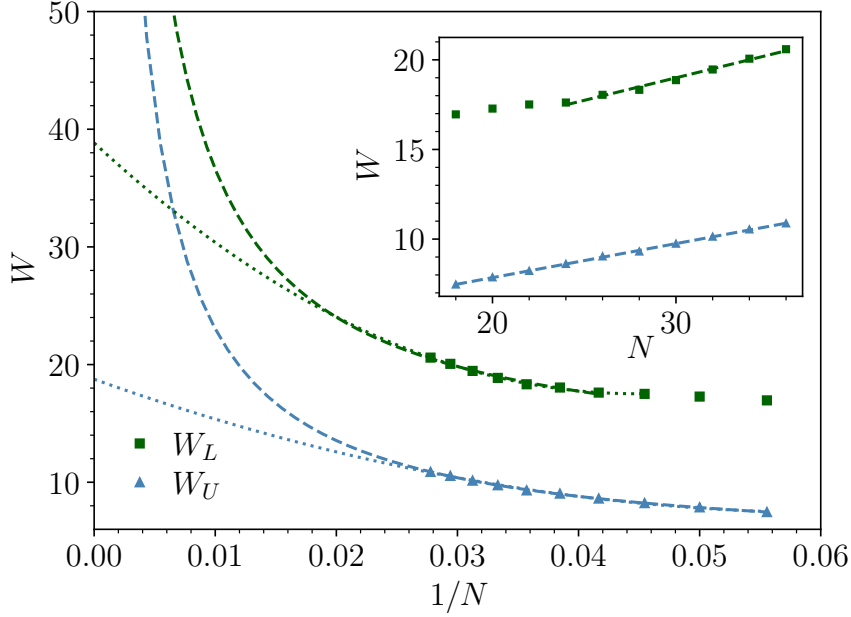


Figure 3.6: Finite-size scaling analysis of the disorder strengths for which the  $r$  parameter becomes smaller than 0.51 ( $W_U$ ) and 0.41 ( $W_L$ ). In the inset, it is shown how they seem to diverge linearly with system size, but with two different slopes. In the main panel, two different possible fits are performed: a linear one  $W = a + bN$  (dashed line), and one of the form  $W = a' + b'/N + c'/N^2$  (dotted line). Further implications are discussed in the main text.

to a finite value at  $N = \infty$ . Nevertheless, one can notice that the values extrapolated from  $W_U$  and  $W_L$  are far apart, indicating that either the fitting region is severely pre-asymptotic, or there is no single transition point, but a slow crossover even in the thermodynamic limit. Moreover, one can recognize that, to truly distinguish between the two fitting functions, one would need to go to system sizes  $N \gtrsim 60$  (at least for  $W_L$ , which is the most sensitive to delocalization). Such a system size corresponds to an Hilbert space dimension of more than  $\sim 6 \times 10^6$ , which is beyond reach for present-day computers and algorithms.

It is interesting to compare our Fig. 3.5 with the equivalents of Refs. [274, 275], where instead the data indicates the existence of a transition in the thermodynamic limit. The two plots are substantially different in the scaling as  $N \rightarrow \infty$ . In our case the curves  $r(W)$  seem to emanate from a common asymptote as  $W \rightarrow \infty$ , and simply shift towards larger values of  $W$  as  $N$  is increased. On the contrary, in Refs. [274, 275] such curves become steeper already at small system sizes, and in particular the lower part of the curves *moves towards smaller values of  $W$* . Therefore, in those works it was possible to analyze another reliable indicator of the MBL transition, namely  $W_*$ , the point at which the curves for  $N$  and  $N + 1$  intersect. Here, we could not extract a sensible  $W_*$  from the data of Fig. 3.5 being it ill-defined: the curves  $r(W)$  are almost superposed at large  $W$ .

As a last thing, we remark that all the above results apply to the center of the spectrum, i.e. to *generic* states of the model under consideration. However, as stated before, we are interested in the dynamics *starting from a particular state*, i.e. the empty Young diagram. Such state has zero expected energy, but for the system under consideration there is no symmetry that forces the spectrum symmetric wrt. zero, thus making the corner an infinite-temperature state. We checked explicitly, however, that the corner state on average lies at the center of the spectrum, and that it has a vanishing probability of being very close to the ground state (or the most excited state).

## 3.5 Dynamics

In the previous Section, we have looked at spectral indicators of ergodicity, and the emerging picture is that there is no *bona fide* MBL phase in the thermodynamic limit for the model under consideration. The absence of a truly localized phase does not immediately imply that, even in the thermodynamic limit, the dynamics of the model should be the same of a standard, ergodic and diffusive system [112–114]. We will now show, in fact, that the  $2d$  quantum Ising model induces on the “holographic” chain a peculiar type of dynamics. We will relate the properties on the chain to the ones in  $2d$ : in particular, the speed of the erosion of the corner will be mapped to the particle current on the chain in Sec. 3.5.1. The entanglement entropy arising from a bipartition of the  $1d$  chain, instead, will correspond again to the entanglement entropy of a bipartition of the  $2d$  model, that we will describe in Sec. 3.5.2. Finally, in Sec. 3.5.3 we present the numerical results both for transport and entanglement growth.

### 3.5.1 Transport on the chain

As a first step we find, in the  $\psi_x$  picture, the number of blocks a Young diagram is composed of. This is done by counting every fermion at distance  $x$  to the left from the domain wall, and every hole at distance  $x$  to the right, each weighted with the distance from the origin:

$$N = \sum_{x>0} x(1 - n_x) + \sum_{x\leq 0} |x| n_x, \quad (3.5.1)$$

where  $n_x = \psi_x^\dagger \psi_x$  is the fermion number at site  $x$ . Taking into account that the configurations are definitively  $n_x \equiv 1$  as  $x \rightarrow +\infty$ , and  $n_x \equiv -1$  as  $x \rightarrow -\infty$ , the sum converges. Then, let us take a derivative wrt. time in Eq. (3.5.1):

$$\dot{N}(t) = - \sum_x x \dot{n}_x(t). \quad (3.5.2)$$

Using the fermion number conservation  $\dot{n}_x(t) + \partial_x J(x, t) = 0$ , where  $\partial_x$  is the discrete space derivative, we can rewrite the total block number (after an integration by parts) as

$$N(t) = - \int_0^t dt' \sum_x J(x, t'). \quad (3.5.3)$$

This should be intended as an operator identity.

In the case of the clean crystal with  $h_i \equiv 0$ , it can be shown that, in the limit  $|x|, t \rightarrow \infty$  with  $|x/gt|$  held finite [1, 2], it holds

$$\langle n_x(t) \rangle \simeq \frac{1}{2} + \begin{cases} \frac{1}{\pi} \arcsin\left(\frac{x}{2|g|t}\right) & \text{if } |x| < 2|g|t \\ \frac{1}{2} \text{sgn}(x) & \text{if } |x| > 2|g|t. \end{cases} \quad (3.5.4)$$

Here, we are using the shorthand notation  $\langle A \rangle := \langle \emptyset | A | \emptyset \rangle$  for the averages starting from the empty Young diagram initial state. Using this result, in the continuum limit

$$\langle \dot{N}(t) \rangle \simeq 2g^2 t, \quad (3.5.5)$$

and it follows

$$\langle N(t) \rangle \simeq (gt)^2. \quad (3.5.6)$$

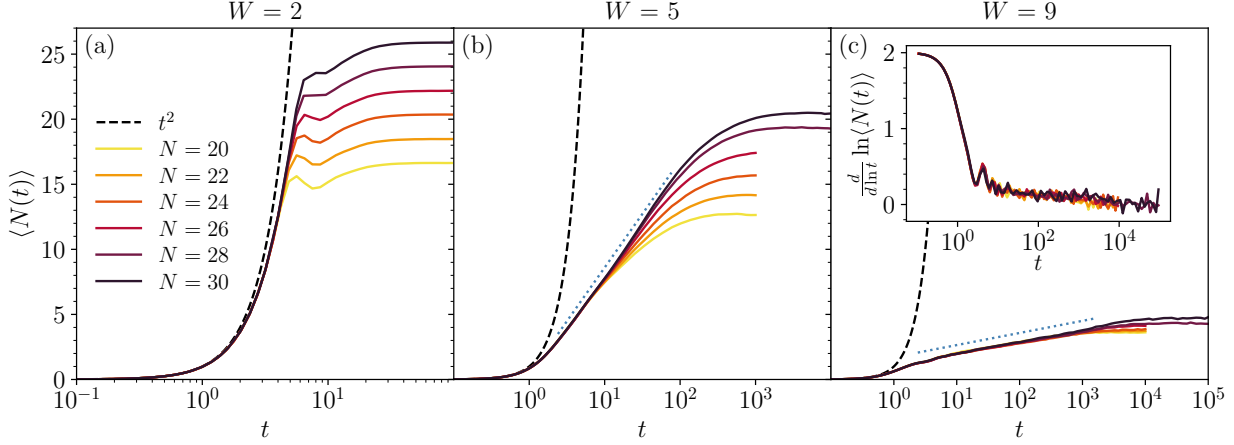


Figure 3.7: Time evolution generated by the Hamiltonian (3.1.2), starting from the corner state. The average number  $\langle N(t) \rangle$  of fermions hops is plotted for various system sizes, and for three values of the disorder strength  $W$  (here we set  $g \equiv 1$ , fixing the energy scale). One can see that at small disorder (i.e.  $W = 2$ , panel (a)) the curves do not behave much differently from the prediction for  $W = 0$ , Eq. (3.5.6), increasing almost as  $g^2 t^2$  (dashed line) before saturating. Already at  $W = 5$  (panel (b)), instead, the growth of  $\langle N(t) \rangle$  has been severely hindered, insomuch that it is compatible with a logarithm (dotted blue line):  $\langle N(t) \rangle \sim \eta_N \ln t$ . Finally, at  $W = 9$  (panel (c)) the logarithmic behaviour of  $\langle N(t) \rangle$  becomes manifest, as shown also by the inset: the logarithmic derivative keeps decreasing towards 0, indicating that  $\langle N(t) \rangle$  must be slower than a power law. All the values of  $\eta_N$ , extracted from fits, are displayed in Fig. 3.8. All the numerical data are averaged over at least 1600 disorder realizations.

This power-law scaling can be traced back to the fact that for the ballistic propagation of free fermions

$$\langle J(x, t) \rangle \simeq \begin{cases} |g|/2 & \text{if } |x| < 2|g|t \\ 0 & \text{if } |x| > 2|g|t, \end{cases} \quad (3.5.7)$$

so

$$\langle N(t) \rangle \simeq 2g^2 \int_0^t dt' t' = (gt)^2. \quad (3.5.8)$$

Now consider, instead, the case of diffusive motion of the excitations in the fermionic chain. One has  $J = -D\partial_x n_x$  for a diffusivity coefficient  $D$ , so

$$\int dx \langle J(x, t) \rangle = -D \langle n_{+\infty}(t) \rangle + D \langle n_{-\infty}(t) \rangle = -D \quad (3.5.9)$$

and

$$\langle N(t) \rangle \simeq Dt. \quad (3.5.10)$$

In a more general setting, the exponent of the growth of  $\langle N(t) \rangle$  in the Young blocks is related to the nature of transport for the excitations of the  $\psi$  chain ( $x(t)$  is the semiclassical trajectory of the excitation):

$$\langle N(t) \rangle \sim t^{2\beta} \quad \longleftrightarrow \quad x \sim t^\beta. \quad (3.5.11)$$

As just shown above, in the ballistic case  $\beta = 1$  and in the diffusive case  $\beta = 1/2$ . In Refs. [113, 276, 277] it is discussed at length how the exponent  $\beta$  dictates the decay of the correlation functions of the current, of the number  $n$ , and the non-equilibrium steady state current  $J_{\text{ness}}$  in a driven set-up:

|                        |              |                                  |                                |                         |
|------------------------|--------------|----------------------------------|--------------------------------|-------------------------|
| $\langle N(t) \rangle$ | $x^2$        | $\langle J(0, t)J(0, 0) \rangle$ | $\langle n_x(t)n_x(0) \rangle$ | $J_{\text{ness}}$       |
| $t^{2\beta}$           | $t^{2\beta}$ | $t^{-2+2\beta}$                  | $t^{-\beta}$                   | $L^{1-\frac{1}{\beta}}$ |

The extreme case in which  $\beta \rightarrow 0$  is expected when entering a MBL phase:  $\beta(W) \sim (W_c - W)^\alpha$ , although the critical exponent  $\alpha$  is currently unknown. In particular, for MBL systems it is possible to show that  $N(t)$  saturate to a constant in the long-time limit [108–110]. As we will show numerically in Sec. 3.5.3, for the model under consideration  $\beta \simeq 0$ , but the absence of true MBL will manifest in the slow growth  $\langle N(t) \rangle \sim \ln(|g|t)$ . This implies that the total current decays as  $\sim 1/t$ , which is indeed an extremely slow decay. We will comment in Sec. 3.6.2 how these features cannot be understood on the basis of simple semiclassical pictures, and instead are due to the quantum nature of the problem.

### 3.5.2 Entanglement growth

Let us turn now to entanglement spreading. One of the most direct ways of quantifying entanglement growth is to bipartite the system, and consider the entanglement entropy  $S_E$  relative to the bipartition. For the setting under consideration, the most natural bipartition is the one that cuts the fermion chain in half through the origin: on the  $2d$  lattice, it corresponds to a cut through the vertex of the corner, namely its bisectrix.

In the clean case ( $W = 0$ ), being the fermions free it is possible to compute exactly the entanglement growth. The computation was originally carried out in Ref. [231], and it briefly goes as follows. By definition,  $S_E = -\text{Tr}[\rho_A \ln \rho_A]$ ,  $\rho_A$  being the reduced density matrix of subsystem  $A$ . Both  $S$  and  $\rho_A$  descend from the correlation matrix  $\mathcal{C}_{xy} = \langle \psi_x^\dagger \psi_y \rangle$ ,  $x, y \in A$ . Therefore,  $S_E$  can be computed from the eigenvalues  $\lambda_i$  of  $\mathcal{C}$  as

$$S = - \sum_{i=0}^{\infty} [\lambda_i \ln \lambda_i + (1 - \lambda_i) \ln(1 - \lambda_i)]. \quad (3.5.12)$$

The computation of the eigenvalues turns out to be very complicated in general, and is usually performed numerically. In the continuum limit, however, the situation is simpler as the correlation matrix reduces to the Sine kernel (see Chapter 2), and a light cone structure emerges, so that  $\mathcal{C}$  has non-vanishing elements only inside the light cone. Using such simplifications, one obtains  $\lambda_k = 1/(e^{\epsilon_k} + 1)$ , with  $\epsilon_k(t) = \pm\pi^2(k + 1/2)/\ln|2|g|\sin(ht)/h|$ .

Turning on the disorder ( $W \neq 0$ ), the picture changes significantly. First, as anticipated above the number of particles that hop across the bipartition is severely reduced from  $\langle N(t) \rangle \sim (gt)^2$  to  $\langle N(t) \rangle \sim \ln(|g|t)$ : therefore, one should expect  $S_E(t)$  to grow at most like  $\sim \ln(|g|t)$  as well. Below, we will show the exact growth of  $S_E$  obtained numerically, and comment it in detail.

### 3.5.3 Numerical results

Here we summarize the results of a numerical investigation for the dynamics generated by the Hamiltonian (3.1.2). Time evolution was performed through full (for  $N \leq 26$ ) and sparse (for  $N \geq 28$ ) matrix exponentiation with SciPy, having constructed the Hamiltonian matrix incorporating both the hopping and the on-site disorder as in Sec. 3.4. The code is made available on GitHub [278].

We start by showing in Fig. 3.7 the time evolution for the average number of fermions  $\langle N(t) \rangle$  that have hopped. Equivalently,  $\langle N(t) \rangle$  is the average number of squares the state is composed of, in the language of Young diagrams. One can see that the growth is ballistic—i.e.  $\langle N(t) \rangle \sim (gt)^2$ —both at short times for all disorder strengths, and at all times for small disorder: for this latter

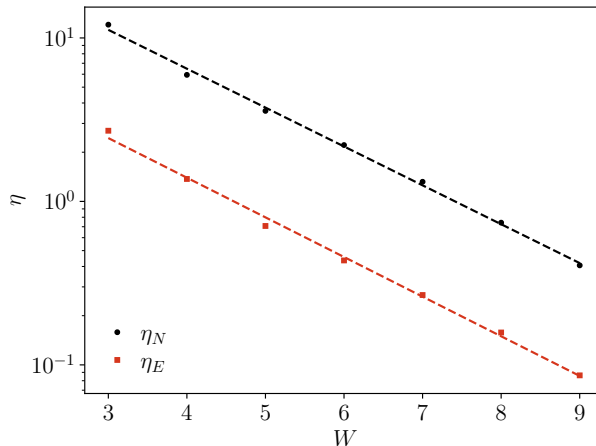


Figure 3.8: For both the average number  $\langle N(t) \rangle$  and the entanglement entropy  $S_E(t)$  we performed logarithmic fits  $\eta \ln t + c$ . Here, we display the dependence of the coefficients  $\eta_N$  and  $\eta_E$  on the disorder strength  $W$ . We find both of them compatible with an exponential decay  $\eta = \eta_0 e^{-W/W_0}$ , with  $W_0 \simeq 1.8$  (the dashed lines show the fits).

statement, see the case of  $W = 2$  (in units of  $g$ ) in Fig. 3.7a. Then, as the disorder is increased slightly, the growth of  $\langle N(t) \rangle$  slows down considerably: it acquires a logarithmic behaviour that lasts for three decades already at  $W = 5$  (Fig. 3.7b), and for four decades at  $W = 9$  (Fig. 3.7c), for the largest system sizes considered, before saturating to a finite-system value<sup>4</sup>. The growth of  $\langle N(t) \rangle$  is more consistent with a logarithm than with a very small power law: in the inset of Fig. 3.7c we show how the logarithmic derivative  $d \ln \langle N(t) \rangle / d \ln t$  keeps decreasing towards 0 also for the largest times reached—though some fluctuations are present. Large fluctuations are present also at the level of  $\langle N(t) \rangle$ : we found the fluctuation of  $N(t)$  to be of the same order of magnitude of  $\langle N(t) \rangle$  for the strongest disorders considered (i.e.  $W \gtrsim 8$ ).

The remarkable feature of the results of Fig. 3.7 is that, for the same values of the disorder strength  $W$ , the spectral indicators predict the presence of a *thermal* phase, where it is natural to expect  $\langle N(t) \rangle \sim t$  (i.e. diffusion), or at most  $\langle N(t) \rangle \sim t^{2\beta}$ ,  $\beta < 1/2$  (i.e. subdiffusion). We find, instead, a severe impediment to transport, that pushes down  $\langle N(t) \rangle$  to a logarithm. In Fig. 3.8 we show the results of fits  $\langle N(t) \rangle = \eta_N \ln t + c_N$ : we find the scaling  $\eta_N(W) = \eta_{0,N} e^{-W/W_0}$  with  $W_0 \simeq 1.8$ .

In Fig. 3.9 we analyze instead the behavior of  $N(t)$  at earlier times. To this end, we define the timescale  $\tau(W)$  that quantifies when the curve  $\langle N(t) \rangle$  departs from the ballistic growth  $g^2 t^2$ , e.g. when  $|\ln \langle N(t) \rangle - 2 \ln(|g|t)| > \varepsilon$  for some fixed threshold value  $\varepsilon$ . From the results of Fig. 3.7 we expect that  $\tau(W)$  suffers of little finite-size effects. Moreover, it is natural to expect  $\tau(W)$  to be a decreasing function of  $W$ , as for strong disorder, the departure from the ballistic motion is supposed to occur sooner. Also, one would guess  $\tau(W) \rightarrow 0$  for  $W \rightarrow \infty$ , i.e. for every finite disorder strength there is a ballistic regime at small times. Indeed, one can see, in the inset of Fig. 3.9, that  $\tau(W) \sim W^{-1}$ .

Let us finally move to the entanglement growth. In Fig. 3.10 we consider the entanglement entropy, relative to the bipartition along the bisectrix of the corner (and, consequently, that cuts the fermionic chain at the origin). Several comments are in order. First, despite the ballistic spreading of *particles*, at  $W = 0$  the entanglement growth is only *logarithmic* in time (dashed black line in

<sup>4</sup>Due to the extremely slow dynamics, system sizes larger than  $N = 30$  were not considered. We believe nonetheless that the system sizes analyzed in this Chapter represent good evidence supporting our claims.

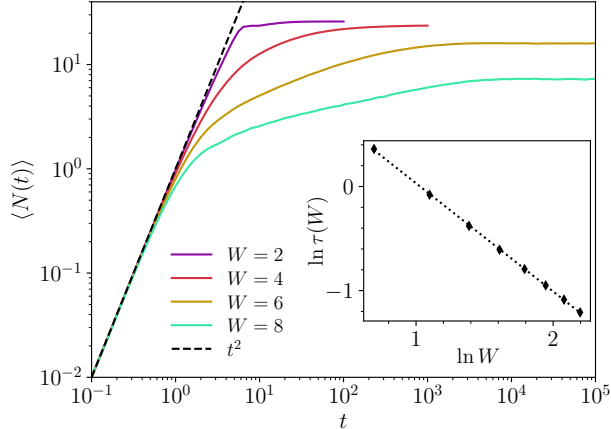


Figure 3.9: Average number of fermion hops  $\langle N(t) \rangle$ , for various disorder strengths, with system size  $N = 30$ . The log-log scale makes manifest the behaviour  $\langle N(t) \rangle \sim (gt)^2$  at small times ( $g \equiv 1$  for numerical purposes), from which  $\langle N(t) \rangle$  departs at the time  $\tau(W)$ . (Inset) Estimates of  $\tau(W)$ , using a threshold  $\varepsilon = 0.05$  (see main text). The fit entails  $\tau(W) \sim W^{-\gamma}$  with  $\gamma = 1.0$ .

Fig. 3.10), because of integrability. To see this, one can employ the so-called *quasiparticle picture*, or the conformal field theory description in the continuum [279]: in both cases, the slow growth of entanglement is traced back to excluded volume effects among the fermions. It should not worry, then, that  $S_E(t)$  grows faster if  $W > 0$ , but small: indeed, a small amount of disorder helps the system in thermalizing, and the entanglement entropy raises linearly in time, essentially because of chaos propagation [280–282].

Second, in Fig. 3.8 we show the results of fits  $S_E(t) = \eta_E \ln t + c_E$ , as was done for the number growth. We find the scaling  $\eta_E(W) = \eta_{0,E} e^{-W/W_0}$  with the same  $W_0 \simeq 1.8$ . Such agreement does not come unexpected: if transport is blocked, and no long-range dephasing interactions are present (contrary to the l-bit model of MBL [108–110]), then entanglement cannot spread beyond the melted part of the corner. Indeed, for each particle that hops across the origin, the entanglement entropy between the left and right halves of the chain increases fast, well before the next hop, because of non-local interactions entailed by the disordered potential. But such non-local interactions act only on the melted part of the corner, and thus particle spreading functions as a bottleneck for the entanglement growth.

## 3.6 Discussion

In this Section, we take the chance to describe the limits of validity of the approximations used (Sec. 3.6.1), and to draw a comparison with *classical* corner growth models, that have been extensively studied in the literature (Sec. 3.6.2). Finally, we present some concluding considerations in Sec. 3.7.

### 3.6.1 Limits of validity of the approximations

So far, we have been discussing the dynamics of melting of a  $2d$  disordered quantum crystal, by modeling it through the strong-coupling limit of the  $2d$  quantum Ising model, in presence of a random longitudinal field. However, the coupling  $J$  was *effectively taken to be infinite* or, equivalently, the  $O(1/J)$  corrections were considered always negligible. On the other hand, in Chapter 2 the  $O(1/J)$  corrections were studied in depth, showing that they lead to interesting

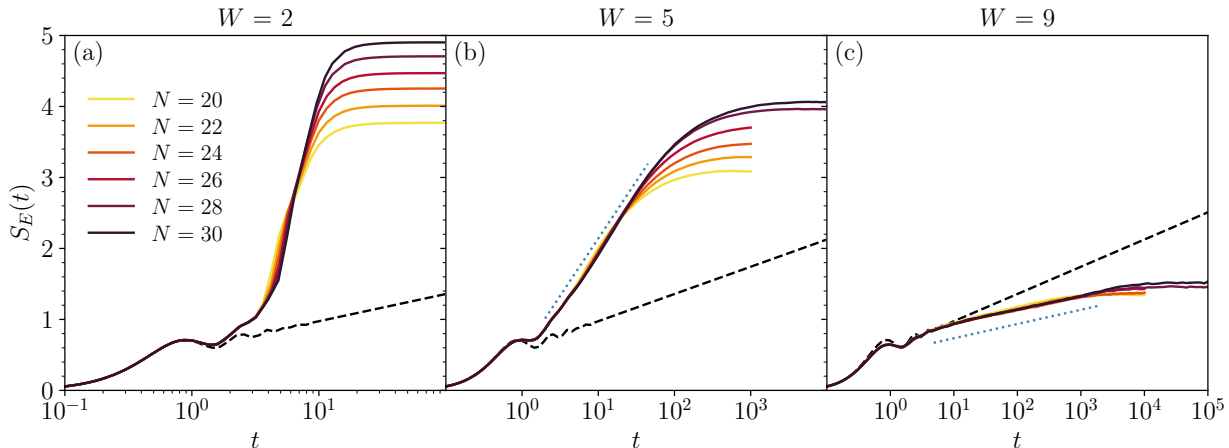


Figure 3.10: Time evolution of the half-system entanglement entropy  $S_E$ , for various system sizes, and three different disorder strengths. At small disorder ( $W = 2$ , panel (a)), the growth of entanglement is fast, probably a power law (even if larger system sizes are needed to extract a reliable scaling). Already at moderate disorder ( $W = 5$ , panel (b)), however, the growth of entanglement slows down to a logarithm (the dotted blue line serves as a guide to the eye), being impeded by a logarithmic transport (as described in the main text). When the disorder is ramped up ( $W = 9$ , panel (c)), the logarithmic behavior  $S_E(t) \sim \eta_E \ln t$  remains, but with a smaller coefficient  $\eta_E$  in front. The coefficients  $\eta_E$  extracted from fits are reported in Fig. 3.8. The dashed lines represent the entanglement growth in absence of disorder, i.e.  $W = 0$ , which is logarithmic because of integrability. All the numerical data are averaged over at least 1600 disorder realizations.

phenomena as Stark MBL. The rationale behind the choice of neglecting the corrections in this Chapter was the following: while in the clean system ( $W = 0$ ) the introduction of interactions leads to integrability breaking, for  $W \neq 0$  it would lead to just minor *quantitative* modifications in the dynamical behaviour. While we refer to Refs. [1, 2] and the previous Chapter for the precise form of such  $O(1/J)$  corrections, here we just remark that they are (parametrically small) four-body interactions on the fermionic chain: therefore, they become negligible in comparison with the strong, non-local interactions arising from the disorder. In particular, the sum appearing in Eq. (3.2.1) (and therefore in Eq. (3.2.4)) makes the disordered interactions of order  $\sqrt{N}W$ , when acting on Young diagrams of size  $N$ . Consequently, they become stronger as time passes by, and the Hilbert space of larger Young diagrams is explored, making the  $O(1/J)$  corrections even less relevant.

Of course, we expect the picture presented to break down at small values of  $J$ : there, also the mapping to fermions ceases to be valid, since it becomes possible for any  $2d$  spin to flip with non-vanishing probability, and the interface is no more well defined. How the dynamics changes in such limit is however a very interesting question, that we hope may be the object of future studies.

### 3.6.2 Comparison with classical corner growth models

The slow growth of the average number of squares in the Young diagrams  $\langle N(t) \rangle$ , observed in the quantum dynamics (Sec. 3.5.3), turns out to be anomalous also from the perspective of similar, classical models. Indeed, using the same mapping to a chain detailed in Sec. 3.2.2, one can describe a classical corner growth model in terms of simple exclusion processes on the line [283, 284]. In the absence of disorder, it is natural to associate the quantum process to the totally anti-

symmetric simple exclusion process (TASEP), that turns out to have ballistic dynamics [285], but a different limiting shape for the eroded part [2]. When disorder is added instead, one might hope to reproduce the quantum dynamics with an exclusion process in which particles are subject to a strongly inhomogeneous waiting time before moving, according to some probability distribution. It turns out that, even when a fat-tailed probability distribution for the waiting times is chosen (this also makes the process non-Markovian), the growth of the eroded corner is power-law [286, 287], never attaining a logarithmic behavior as the one observed in the quantum regime. In particular, a logarithmic growth can be obtained only if the waiting-time distribution behaves like  $p(\tau) \sim \tau^{-1}$  for large  $\tau$ , i.e. it is non-normalizable. This is an indication of the purely quantum nature of the problem we have discussed, that cannot be reproduced by classical means.

Another interesting question is about the comparison of the average limiting shapes, between classical and quantum melting processes. While the clean case was presented in the previous Chapter, the disordered case is more intriguing, and difficult to analyze: we plan to discuss this issue in a future work.

### 3.7 Conclusions

In this Chapter, we extended the discussion presented in Chapter 2 by addressing the spectral and dynamical properties of a disordered two-dimensional quantum crystal. In particular, we studied the quantum Ising model on a square lattice and studied the melting of an infinite, corner-shaped interface. While the same problem turned out to display ergodicity breaking in the absence of disorder, as discussed in Chapter 2 and Refs. [1, 2], in this Chapter we presented both analytical and numerical evidence supporting the *absence* of a many-body localized phase when disorder is added. We established, through an analytical argument based on the forward approximation, and numerical results for spectral properties, that the model is ergodic for any finite  $W$  in the thermodynamic limit. However, we also showed that the dynamics turns out to be extremely slow: we found, through an extensive numerical analysis, that the growth of the average number of melted squares,  $\langle N(t) \rangle$ , passes from ballistic to logarithmic in time already for small disorder, and we characterized the crossover between these two regimes with various indicators. Also, the entanglement entropy  $S_E(t)$  shows a similar behavior, that traces back to the growth of  $\langle N(t) \rangle$ .

While the results presented in this Chapter support the common belief that MBL does not survive in dimensions higher than one, we presented strong evidence for the onset of slow dynamics, namely slower than subdiffusive. Surprisingly, such behavior is already present at small disorder strength, when the system, at finite size, is fully ergodic according to the spectral indicators.

## Chapter 4

# Hydrodynamic theory of Stark localization

*In this Chapter, we present a hydrodynamic study of the Stark localized free fermionic chain, that appeared in Chapter 2. We show that, in the limit of a weak external field, it is possible to recover the exact lattice results within the hydrodynamic theory. Moreover, the quantum generalized hydrodynamics allows us to compute the entanglement entropy of the model. We also present some considerations for more generic potentials. The results presented in this Chapter are based on the publication [4].*

WE have shown in Chapter 2 that the dynamics of wedge interfaces in the two-dimensional Ising model can be equivalently formulated in terms of a free fermionic chain subject to a linear external potential. An early counter-intuitive discovery concerning the dynamics of non-interacting quantum particles on a lattice (described by the tight-binding model) [205] and subject to a constant force was the presence of Bloch oscillations [288]. Indeed, contrary to what one may heuristically expect, it was shown (as we also discussed in Chapter 2) that these particles display a periodic motion [205, 289–291] instead of drifting forever. The occurrence of this phenomenon, nowadays known as Stark localization, is not limited to tight-binding non-interacting models, but is believed to occur also in interacting systems. For example, this has been recently demonstrated experimentally in a 5-qubit superconducting processor [292]. In addition, it has been argued that Stark localization is robust against the presence of interaction, leading to the notion of Stark many-body localization [172, 173, 293] which has been observed in an experiment with a trapped-ion quantum simulator [244]. Similarly, the effective dynamics of quantum collective excitations may feature Stark localization, leading to confinement [178, 179]. Despite the pieces of evidence mentioned above, a general theoretical framework for understanding Stark localization beyond the cases of simple analytically solvable models and approximated descriptions [54, 206] seems still to be missing.

In this Chapter, we make use of the so-called Generalized Hydrodynamics (GHD) approach to bridge the gap. GHD is a recently formulated [48, 49] systematic theoretical approach to investigate the dynamics of inhomogeneous integrable systems, including in particular free theories. This approach extends standard hydrodynamics by accounting for the additional conservation laws enforced by integrability. GHD turned out to be a versatile and predictive method in a large variety of contexts, including transport phenomena in spin-chains [50–62], inhomogeneous quantum gases

both in and out of equilibrium [63–72], quantum and diffusion effects [73–81], as reviewed in Refs. [81–83]. Its theoretical predictions have also been confirmed in recent experiments [84, 85].

The rest of the presentation is organized as follows. In Sec. 4.1 we briefly review the GHD approach, with particular emphasis on lattice Fermi gases. In Sec. 4.2 we focus on the dynamics of a domain-wall initial state in the presence of a linear potential, providing analytical predictions for the particle density and current. In addition, by employing the recently proposed *quantum* GHD [81], we investigate the evolution of the entanglement entropy and the full-counting statistics. In Sec. 4.3 we consider the case of generic external potentials, in order to understand which ingredients are important for the occurrence of Stark localization. We summarize our findings in Sec. 4.4, listing some open questions.

## 4.1 Generalized hydrodynamics of inhomogeneous systems

In this Section, we briefly review the generalized hydrodynamics, setting the stage for our investigation of the problem of Stark localization. We consider a lattice Fermi gas with nearest-neighbor hopping, subject to an external potential  $V(x)$ . The corresponding Hamiltonian is

$$H = -\frac{1}{2} \sum_{x \in \mathbb{Z}} (\psi_x^\dagger \psi_{x+1} + \psi_{x+1}^\dagger \psi_x) + \sum_{x \in \mathbb{Z}} V(x) \psi_x^\dagger \psi_x, \quad (4.1.1)$$

where  $\psi_x$  and  $\psi_x^\dagger$  are the annihilation/creation fermionic operators satisfying the canonical anti-commutation relations

$$\{\psi_x, \psi_{x'}^\dagger\} = \delta_{xx'} \quad \text{and} \quad \{\psi_x, \psi_{x'}\} = 0. \quad (4.1.2)$$

Given an initial state  $|\Psi_0\rangle$  and an observable  $\mathcal{O}$ , one is usually interested in investigating the time evolution of the expectation value of  $\mathcal{O}$ , i.e., of

$$\langle \mathcal{O}(t) \rangle \equiv \langle \Psi_0 | e^{iHt} \mathcal{O} e^{-iHt} | \Psi_0 \rangle. \quad (4.1.3)$$

Remarkably, for the large class of Gaussian initial states, one can reconstruct the evolution of any observable  $\mathcal{O}$  on the basis of the two-point function only, namely

$$C(x, x'; t) \equiv \langle \psi_x^\dagger(t) \psi_{x'}(t) \rangle; \quad (4.1.4)$$

this allows a drastic simplification of the treatment of the microscopic dynamics. More generally, predicting the time evolution of the system requires the exact determination of the single-particle spectrum, which might be hard to calculate explicitly. However, it has been demonstrated that a somehow simpler hydrodynamic regime (known as inhomogeneous GHD [67]) emerges at large scales. For instance, if the potential  $V(x)$  is a sufficiently smooth function of  $x$  and the multi-point correlations in the initial state decay rapidly upon increasing their distances [294], a viable semi-classical description of the dynamics can be done in terms of a local Fermi occupation function  $n(x, k; t)$  defined as [295, 296]

$$n(x, k; t) \equiv \int dy \langle \psi_{x+y/2}^\dagger(t) \psi_{x-y/2}(t) \rangle e^{iky}. \quad (4.1.5)$$

This description amounts to studying the Liouville evolution to lowest order in  $\partial_x$  and  $\partial_k$ , given by [50, 59, 65]

$$\partial_t n(x, k; t) + v(k) \partial_x n(x, k; t) = V'(x) \partial_k n(x, k; t) \quad \text{where} \quad v(k) = \sin k. \quad (4.1.6)$$

Here,  $n(x, k; t)$  can be interpreted as a semi-classical probability distribution in the phase-space  $(x, k) \in \mathbb{R} \times \mathbb{R} \bmod 2\pi$  associated to the classical Hamiltonian

$$\mathcal{H}(x, k) = -\cos k + V(x), \quad (4.1.7)$$

which results in the following equations of motion:

$$\begin{cases} \dot{x} = \frac{\partial \mathcal{H}}{\partial k} = \sin k, \\ \dot{k} = -\frac{\partial \mathcal{H}}{\partial x} = -V'(x). \end{cases} \quad (4.1.8)$$

Let us mention that Eq. (4.1.6) comes from the requirement that the semi-classical probability  $n(x, k; t)$  is conserved (see also Eq. (4.2.9)). Within this approach, some local observables can be directly expressed and computed in terms of  $n(x, k; t)$  alone. In particular, the density of fermions takes the form

$$\rho(x, t) \equiv \langle \psi_x^\dagger(t) \psi_x(t) \rangle = \int_{-\pi}^{\pi} \frac{dk}{2\pi} n(x, k; t), \quad (4.1.9)$$

and the particle current

$$j(x, t) \equiv \frac{i}{2} \langle \psi_{x+1}^\dagger(t) \psi_x(t) - \psi_x^\dagger(t) \psi_{x+1}(t) \rangle = \int_{-\pi}^{\pi} \frac{dk}{2\pi} n(x, k; t) v(k). \quad (4.1.10)$$

Note the following crucial point: while the hydrodynamic approach is expected to be predictive at spatial and temporal scales much larger than the microscopic ones, the presence of a lattice makes the momentum  $k$  a compact variable, which is defined up to  $k \rightarrow k + 2\pi$ . Accordingly, the lattice strongly affects the resulting dispersion relation, i.e., the form of  $v(k)$  in Eq. (4.1.6) or, equivalently, the kinetic term in Eq. (4.1.7). In fact, after reinstating the lattice spacing  $a$  in the definition of  $v(k)$ , one readily realizes that for  $k$  smaller than  $a^{-1}$  it is legitimate to approximate

$$v(k) = a^{-1} \sin(ak) \simeq k, \quad (4.1.11)$$

retrieving the usual Galilean dispersion. However, this is no longer the case for generic values of  $k$  and the fact that  $v(k)$  is a periodic function of  $k$  plays a crucial role. As anticipated, this effect of the lattice is precisely the origin of Stark localization, as we shall demonstrate in the following sections.

## 4.2 Dynamics in the presence of a linear potential

In this section, we analyze in detail the dynamics of the standard setup in which Stark localization occurs [205], i.e., a tight-binding model of a lattice Fermi gas in the presence of a linear potential

$$V(x) = -hx, \quad (4.2.1)$$

where, without loss of generality, we assume  $h > 0$ . The single-particle spectrum of the microscopic model has been determined exactly in Refs. [290, 291, 297] and it features a Wannier-Stark ladder of energy levels and exponentially localized wave functions. Moreover, as discussed in Chapter 2 and Refs. [1, 2], a large-scale limit of this dynamics turns out to exist for a generic initial state and in the presence of weak field  $h$ , i.e., with

$$h \ll 1, \quad (4.2.2)$$

(in lattice spacing units). Correspondingly, Bloch oscillations for the density and the current starting from a domain-wall state were established analytically. In fact, as dimensional analysis suggests,  $1/h$  is a length (which turns out to be a localization length, see, c.f., Eq. (4.2.15)) and a semi-classical regime is expected to emerge when this length is much larger than the lattice spacing. While these previous results were derived on the basis of an explicit solution of the microscopic model, as far as we know, GHD has never been applied to this problem, which is precisely the goal of this Chapter.

Before presenting the calculation of the exact semi-classical dynamics, it is worth giving a simple physical description of the system. Let us consider a (classical) particle with the Hamiltonian (4.1.7) and the potential (4.2.1), i.e., with

$$\mathcal{H}(x, k) = -\cos k - hx, \quad (4.2.3)$$

(see also Appendix B.1) initially localized at  $x(0) = 0$  and  $k(0) = 0$ . At short times, the particle is accelerated to the right and thus its momentum  $k$  increases linearly, as one would expect in the continuum limit where the lattice is absent and the “kinetic term”  $-\cos k \simeq k^2/2 + \text{const.}$  reproduces the usual one. However, the velocity  $\dot{x}$  [see Eq. (4.1.8)] does not grow indefinitely (being bounded by  $|\dot{x}| \leq 1$ ) and the lattice provides negative feedback, slowing down the particle until it stops at position  $x_1$ , corresponding to the inversion point. Then, the particle is accelerated again towards the left and eventually reaches the initial position. This process is then repeated, leading to an oscillatory motion between two extreme points  $x = 0$  and  $x = x_1$ . The value of  $x_1$  is easily determined by energy conservation, requiring that the velocity at that point vanishes, finding

$$x_1 = 2/h. \quad (4.2.4)$$

The classical trajectory in phase space  $(x, k) \in \mathbb{R} \times \mathbb{R} \bmod 2\pi$  can be calculated by solving the equations of motion (4.1.8) for the linear potential (4.2.1), which read

$$\begin{cases} \dot{x} = \sin k, \\ \dot{k} = h, \end{cases} \quad (4.2.5)$$

for a generic initial condition  $(x(0), k(0))$ . The corresponding solution is (see, e.g., Ref. [2])

$$\begin{cases} k(t) = k(0) + ht, \\ x(t) = x(0) + \int_0^t dt' \sin(k(0) + ht') = x(0) + \frac{2}{h} \sin\left(k(0) + \frac{ht}{2}\right) \sin\left(\frac{ht}{2}\right). \end{cases} \quad (4.2.6)$$

Notice that for small  $k(0)$  and  $t$ , i.e.,  $k(0) \ll 1$  and  $t \ll 1/h$  one gets

$$x(t) \simeq x(0) + k(0)t + \frac{ht^2}{2}, \quad (4.2.7)$$

which, as expected, is the motion of a uniformly accelerated classical particle. Still, at longer times Eq. (4.2.6) implies that one always observes oscillatory motion in  $x \in [x(0) - 2/h, x(0) + 2/h]$ , no matter how small  $h \neq 0$  is. Correspondingly,  $k(t)$  periodically encircles the first Brillouin zone with a period given by

$$T = \frac{2\pi}{h}. \quad (4.2.8)$$

Figure 4.1 shows the foliation of the phase space  $(x, k)$  provided by the trajectories of  $\mathcal{H}(x, k)$  in Eq. (4.2.6).

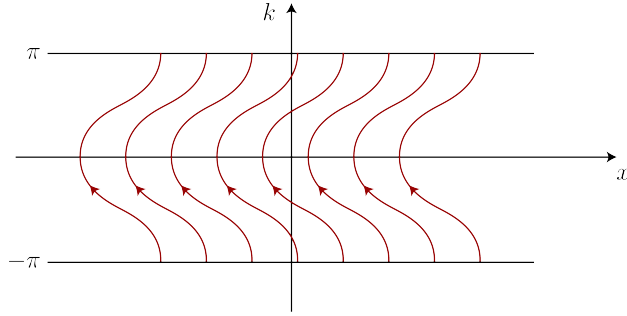


Figure 4.1: Classical trajectories of a particle with Hamiltonian (4.1.7) in the presence of a linear potential  $V(x) = -hx$ , given by Eq. (4.2.6). Each trajectory encircles the first Brillouin zone in a period  $T = 2\pi/h$ .

For the sake of completeness, we finally write the explicit expression of the dynamics of the probability distribution  $n(x, k; t)$  in phase space for a given initial distribution  $n(x, k; t = 0)$  of the non-interacting particles. In order to do so, it is sufficient to rewrite the equation of motion (4.1.6) as the conservation of the probability along the flow in phase space induced by the Hamiltonian (4.2.3), i.e.,

$$\frac{d}{dt}n(x(t), k(t); t) = 0. \quad (4.2.9)$$

In other words, by evolving backward in time the trajectory starting from  $(x, k)$  one easily gets the local occupation at time  $t$  from the initial one. Using Eqs. (4.2.6) we conclude that

$$n(x, k; t) = n\left(x - \frac{2}{h} \sin\left(k - \frac{ht}{2}\right) \sin\left(\frac{ht}{2}\right), k - ht; 0\right), \quad (4.2.10)$$

which satisfies Eq. (4.1.6) as one can easily check.

#### 4.2.1 Domain-wall initial state

Considering now the dynamics of the quantum system, we focus on an initial state with a single domain wall, which has been the subject of many studies [56, 83, 221, 298, 299], and we aim at characterizing its evolution. To do so, let us first introduce the empty or vacuum state  $|0\rangle$  defined by

$$\psi_x |0\rangle = 0, \quad \forall x \in \mathbb{Z}. \quad (4.2.11)$$

In terms of  $|0\rangle$ , the domain-wall state  $|\Psi_0\rangle$  can be expressed as

$$|\Psi_0\rangle = \prod_{x \leq 0} \psi_x^\dagger |0\rangle, \quad (4.2.12)$$

and corresponds to having all lattice sites filled by one fermion for  $x \leq 0$  and empty for  $x > 0$ . As shown, e.g., in Ref. [56], the state  $|\Psi_0\rangle$  admits a semi-classical description with local occupation given by

$$n(x, k; 0) = \begin{cases} 1 & \text{for } x \leq 0 \text{ and } k \in [-\pi, \pi], \\ 0 & \text{otherwise.} \end{cases} \quad (4.2.13)$$

In particular, a Fermi contour at  $x = 0$  separates the phase space into an empty region and a filled one. We now study the dynamics of  $|\Psi_0\rangle$ . A convenient way to express  $n(x, k; t)$ , which

overcomes the possible issues due to its discontinuities as a function of  $x$  and  $k$ , is via its Fermi contour (see also Ref. [56]). For instance, the set of points  $\{(x = 0, k = k_0)\}$  of the initial Fermi surface, parameterized by the initial momentum  $k_0 \in [-\pi, \pi)$ , evolves in a time  $t$  to the set

$$\left\{ (x_t, k_t) \mid x_t = \frac{2}{h} \sin\left(\frac{ht}{2}\right) \sin\left(k_t - \frac{ht}{2}\right) \quad \text{with} \quad k_t \in [-\pi, \pi) \right\}. \quad (4.2.14)$$

For the sake of convenience, we introduce the time-dependent length

$$l(t) \equiv \left| \frac{2}{h} \sin\left(\frac{ht}{2}\right) \right|, \quad (4.2.15)$$

which, as we shall see below, characterizes the dynamics of the system and is responsible for its localization for  $h \neq 0$  within a typical distance

$$l_{\text{loc}} = \max_t l(t) = 2/|h|. \quad (4.2.16)$$

It is easy to show that, for any given value of  $x$  such that  $|x| \leq l(t)$ , one can determine two generically distinct values  $k_F^-(x, t)$  and  $k_F^+(x, t) \geq k_F^-(x, t)$  of  $k$  on the Fermi contour at time  $t$  corresponding to  $x$ , given by

$$\begin{cases} k_F^-(x, t) = ht/2 - \phi(t) + \arcsin(x/l(t)), \\ k_F^+(x, t) = ht/2 - \phi(t) + \pi - \arcsin(x/l(t)), \end{cases} \quad (4.2.17)$$

where the phase  $\phi(t)$  is defined such that

$$\phi(t) = \begin{cases} 0 & \text{for} \quad \sin(ht/2) > 0, \\ \pi & \text{for} \quad \sin(ht/2) < 0. \end{cases} \quad (4.2.18)$$

The expressions in Eq. (4.2.17) follow from inverting Eq. (4.2.14) which defines the Fermi surface, suitably rewritten in the form  $x_t = l(t) \sin(k_t - ht/2 + \phi(t))$ . Note that these values  $k_F^\pm(x, t)$  play the role of local Fermi points, as explained in Ref. [66], and they have been carefully chosen here such that the vertical line  $(x, k)$  in phase space with  $k \in [k_F^-(x, t), k_F^+(x, t)]$  belongs to the region with  $n(x, k; t) = 1$ . For  $|x| > l(t)$ , instead, there are no such solutions  $k_F^\pm(x, t)$ , and for  $x < -l(t)$  or  $x > l(t)$  the system behaves locally as a completely filled or empty Fermi sea, respectively. The construction above is illustrated in Fig. 4.2, which provides a plot of the local occupation in phase space.

As a first application of this approach, we determine the particle density  $\rho(x, t)$  and the current  $j(x, t)$  from Eqs. (4.1.9) and (4.1.10), respectively. For  $|x| \leq l(t)$  we get

$$\rho(x, t) = \int_{k_F^-(x, t)}^{k_F^+(x, t)} \frac{dk}{2\pi} = \frac{k_F^+(x, t) - k_F^-(x, t)}{2\pi} = \frac{1}{\pi} \arccos\left(\frac{x}{l(t)}\right), \quad (4.2.19)$$

$$\begin{aligned} j(x, t) &= \int_{k_F^-(x, t)}^{k_F^+(x, t)} \frac{dk}{2\pi} \sin k = \frac{\cos k_F^-(x, t) - \cos k_F^+(x, t)}{2\pi} = \frac{1}{\pi} \sqrt{1 - \frac{x^2}{l^2(t)}} \cos\left(\frac{ht}{2} - \phi(t)\right) \\ &= \frac{1}{2\pi} \sqrt{1 - \frac{x^2}{l^2(t)}} \frac{\sin(ht)}{|\sin(ht/2)|}. \end{aligned} \quad (4.2.20)$$

Note that  $j(x, t)$  displays a discontinuity for  $t = t_k = kT$  (with  $T$  given in Eq. (4.2.8)) because  $j(x, t \rightarrow t_k^-) = -j(x, t \rightarrow t_k^+)$ , i.e., the (non-vanishing) current changes direction at the beginning

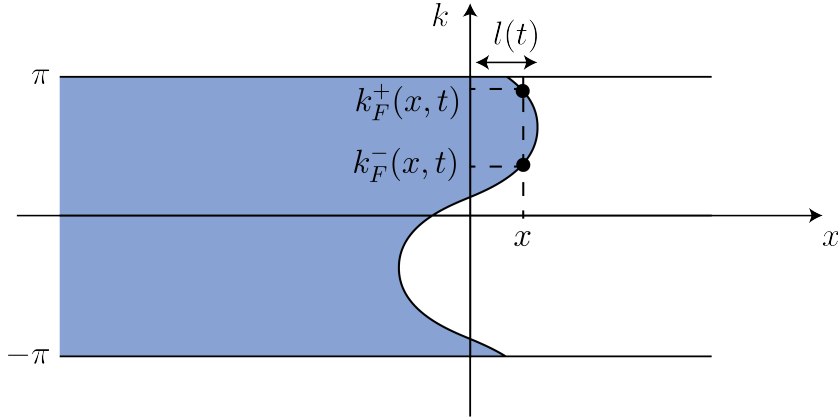


Figure 4.2: Local occupation  $n(x, k; t)$  in phase space at given time  $t > 0$ :  $n(x, k; t) = 1$  in the blue region and  $n(x, k; t) = 0$  in the complementary white one. For  $|x| < l(t)$  there is a pair of Fermi points, denoted by  $k_F^\pm(x, t)$ . In the region  $x > l_{\text{loc}}$  ( $x < -l_{\text{loc}}$ ), with  $l_{\text{loc}}$  given in Eq. (4.2.16), no local evolution occurs and the system is locally described by a completely empty (filled) Fermi sea.

of each period of oscillation. For  $|x| > l(t)$ , instead, the system does not evolve locally and a straightforward computation gives

$$\rho(x, t) = \begin{cases} 1 & \text{for } x < -l(t), \\ 0 & \text{for } x > l(t), \end{cases} \quad \text{and } j(x, t) = 0. \quad (4.2.21)$$

Note that all the previous expressions for  $\rho(x, t)$  and  $j(x, t)$  are periodic in time with the period  $T$  given by Eq. (4.2.8) in spite of the fact that some intermediate steps of the calculation involve separately  $\sin(ht/2)$  and  $\cos(ht/2)$ .

In Figs. 4.3 and 4.4 we plot the curves corresponding to Eqs. (4.2.19) and (4.2.20), respectively, and we compare them with the result of numerical calculations on the lattice in the hydrodynamic regime. The numerical data for the density profile have been obtained by computing the time evolution of the correlation matrix in Eq. (4.1.4) and then by considering its diagonal elements, as explained in Appendix B.2. For the current, instead, we used the analytical result on the lattice reported in, c.f., Eq. (A.3.14) of Appendix A.3.

The expressions derived above can be used also to investigate the limit  $h \rightarrow 0$ , — corresponding to the melting of a domain wall in a homogeneous chain, — which was studied in Refs. [56, 67, 221, 300]. In that case,  $l(t) = t$  [see Eq. (4.2.15)], the oscillations disappear, and Eq. (4.2.20) for  $|x| < t$  gives

$$\begin{cases} \rho(x, t) = (2/\pi) \arccos(x/t), \\ j(x, t) = (1/\pi) \sqrt{1 - x^2/t^2}, \end{cases} \quad (4.2.22)$$

which coincides with the results of Ref. [56] for a single domain wall. As pointed out in Chapter 2, it is worth noticing that, for a given  $x$ , the value of  $\rho(x, t)$  at  $h \neq 0$  [see Eq. (4.2.19)] can be easily obtained from its value at  $h = 0$  in Eq. (4.2.22), via the substitution

$$t \rightarrow l(t). \quad (4.2.23)$$

However, this does not hold for the current  $j(x, t)$ . To better understand the origin of these facts, it is sufficient to compare the Fermi contour for  $h \neq 0$  with that for  $h = 0$ . In particular, we

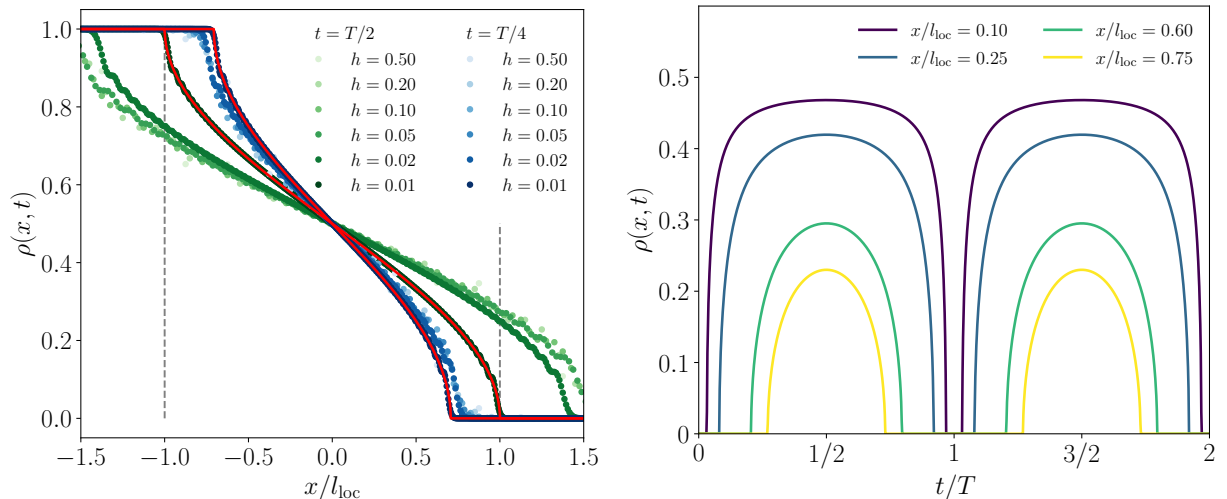


Figure 4.3: Particle density  $\rho(x, t)$  as a function of (left)  $x$  for  $t = T/2$  and  $t = T/4$  or (right)  $t$  for various values of  $x$  along the chain. In both panels, the solid lines correspond to the GHD prediction in Eq. (4.2.19). The dots in the left panel are the values obtained from the numerical computations with the lattice Hamiltonian, on a chain of length  $L = 600$  sites. By plotting these numerical data as functions of  $x/l_{\text{loc}}$  with  $l_{\text{loc}}$  given in Eq. (4.2.16) one observes their convergence towards the GHD prediction as the value  $h$  of the field decreases towards zero. Note, however, that there are rather large deviations from the GHD prediction for large values of  $h$ , which are anyhow expected due to the highly fluctuating Bessel functions involved in the exact analytic prediction on the lattice, especially for  $t \simeq T/2$ . As expected, for small values of  $h$ , the dynamics occurs only within the region  $|x| < l_{\text{loc}}$ , delimited by the vertical dashed lines. In the right panel,  $\rho(x, t)$  displays the periodicity due to the Stark localization, with  $\rho(x, t) = 0$  at all times if  $x/l_{\text{loc}} > 1$  or  $\rho(x, t) = 1$  if  $x/l_{\text{loc}} < -1$ .

observe that the former, given by

$$\left\{ (x, k) \mid x = l(t) \sin \left( k - \frac{ht}{2} + \phi(t) \right) \quad \text{and} \quad k \in [-\pi, \pi) \right\}, \quad (4.2.24)$$

[see the parameterization of Eq. (4.2.14) introduced after the definition of  $\phi(t)$  in Eq. (4.2.18)] is recovered from the latter, i.e.,

$$\{(x, k) \mid x = t \sin k \quad \text{and} \quad k \in [-\pi, \pi)\}, \quad (4.2.25)$$

via a reparameterization of time  $t \rightarrow l(t)$ , followed by a shift of the momentum  $k \rightarrow k - ht/2 + \phi(t)$ . Since the density  $\rho(x, t)$  does not depend on momenta [see its semi-classical expression in Eq. (4.1.9)], it is not sensitive to such a shift, and therefore the overall effect on  $\rho(x, t)$  of having a linear potential simply amounts at a reparameterization of time, as observed in Chapter 2. However, this does not apply to the current  $j(x, t)$  because its expression in Eq. (4.1.10) is not invariant under such a momentum shift.

## 4.2.2 Quantum GHD: Entanglement entropy and full counting statistics

We proceed further with the analysis of the domain-wall dynamics, and we aim at characterizing the entanglement among complementary spatial regions. While the entanglement in the presence of Stark localization has been studied, so far, numerically [231, 301], by using CFT in curved

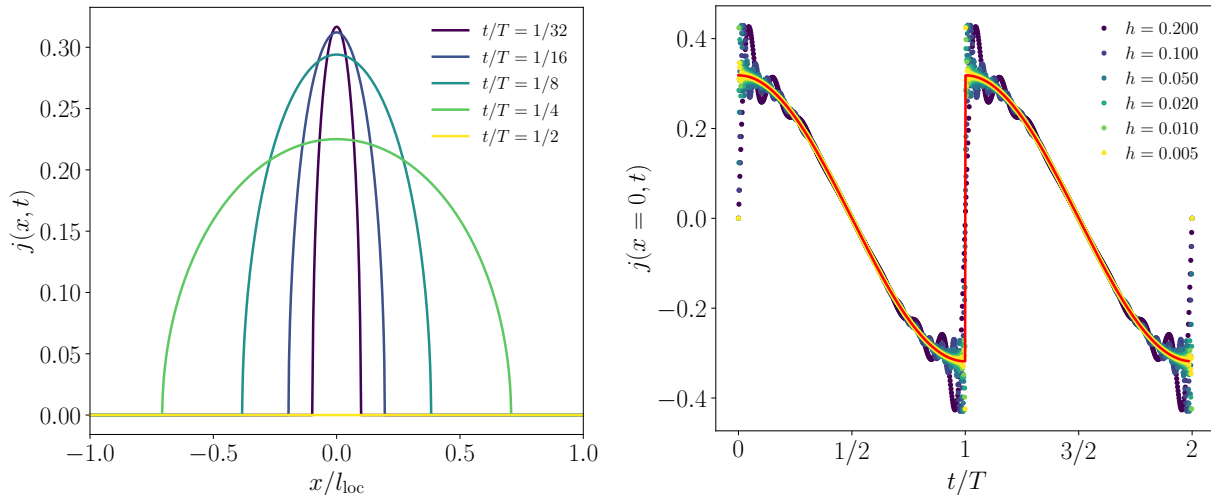


Figure 4.4: Particle current  $j(x, t)$  as a function of (left)  $x$  for various values of  $t/T$  within a half-period of oscillation or (right)  $t$  for  $x = 0$  and various values of  $h$ . In both panels, the solid lines correspond to the GHD prediction in Eq. (4.2.20). The coordinates  $x$  and  $t$  are rescaled by the natural  $h$ -dependent scales  $l_{\text{loc}}$  and  $T$  [see Eqs. (4.2.15) and (4.2.8)], respectively, so that their shapes in the hydrodynamic limit are actually independent of  $h$ . In the right panel, symbols correspond to the values derived from the exact solution of the lattice model (see, c.f., Eq. (A.3.14)). Upon reducing the strength of the external field  $h$  and upon rescaling  $t \rightarrow t/T$ , the results on the lattice approach the curve predicted by GHD.

space-time [236, 302, 303] or by exploiting the substitution  $t \rightarrow l(t)$  [2], here we derive analytically its dynamics on the basis of a quantized version of GHD [66, 81].

Let us consider a bipartition  $A \cup \bar{A}$  of the lattice in two extended and complementary subsystems  $A$  and  $\bar{A}$ . Given the reduced density matrix of  $A$

$$\rho_A(t) \equiv \text{Tr}_{\bar{A}} (e^{-iHt} |\Psi_0\rangle \langle \Psi_0| e^{iHt}), \quad (4.2.26)$$

a good entanglement measure between  $A$  and  $\bar{A}$  is provided by the von Neumann entropy (also known as entanglement entropy), given by

$$S(t) \equiv -\text{Tr} (\rho_A(t) \log \rho_A(t)). \quad (4.2.27)$$

Being this quantity highly non-local in space, one may ask whether it is possible to determine it via the local description provided by hydrodynamics. It turns out that, for states with short-range correlations, the semi-classical Yang-Yang entropy [304] is able to capture the leading contribution to the entanglement entropy [52], and therefore one gets

$$S(t) \simeq - \int_{-\pi}^{\pi} \frac{dk}{2\pi} \int_A dx [n \log n + (1-n) \log(1-n)]_{n=n(x,k;t)}. \quad (4.2.28)$$

However, the local occupation number  $n(x, k; t)$  is either 0 or 1 in the system under consideration here and therefore the semi-classical expression above vanishes, while the entanglement entropy does not. A solution to this apparent contradiction has been put forward in Refs. [66, 67, 236] by generalizing the standard GHD to what has been dubbed quantum GHD, which accounts for quantum effects beyond the semi-classical approximation. Indeed, while the Yang-Yang entropy

predicts the extensive contribution to  $S(t)$ , which vanishes, the dominant sub-extensive contribution is correctly predicted by quantum GHD.

This approach is well established for the domain-wall state in the absence of the external potential (i.e., for  $h = 0$ ), where the dynamics of the entanglement entropy, as well as other entanglement measures (e.g., Rényi entropies, full counting statistics, charged moments), have been studied [53, 56, 63]. Our goal here is to generalize that method in the presence of a linear potential, thus characterizing analytically the Bloch oscillation of the entanglement entropy. We anticipate here that the evolution of  $S(t)$  for  $h \neq 0$  can be recovered from the one at  $h = 0$  via the substitution in Eq. (4.2.23), as discussed in Sec. 4.2. While this might be expected, as the measures of spatial entanglement considered here should be insensitive to momentum shifts, it is actually a non-trivial fact because our analysis based on quantum GHD goes beyond the semi-classical description to which the previous heuristic argument actually applies. Following Refs. [305–307], we employ the replica trick, and we first compute the  $n$ -th Rényi entropy

$$S_n(t) \equiv \frac{1}{1-n} \log \text{Tr}(\rho_A^n(t)), \quad (4.2.29)$$

for integer  $n \geq 2$ , and we eventually continue the results to  $n = 1$  in order to get the entanglement entropy

$$S(t) = \lim_{n \rightarrow 1} S_n(t). \quad (4.2.30)$$

For the sake of simplicity, we focus here on the case  $A = [x, \infty)$ , i.e., on the half-chain starting from  $x$ . Then we express  $\text{Tr}(\rho_A^n(t))$  in terms of the expectation value of a twist field  $\mathcal{T}_n(x)$  [306, 307], which acts as a cyclic permutation over the region  $A$ , as

$$\text{Tr}(\rho_A^n(t)) = \langle \mathcal{T}_n(x, t) \rangle \equiv {}^n \langle \Psi_0 | e^{iHt} \mathcal{T}_n(x) e^{-iHt} | \Psi_0 \rangle^n, \quad (4.2.31)$$

where  $|\Psi_0\rangle^n$  denotes the replicated initial state. We explain below the quantum GHD, following closely Ref. [56], which gives  $\langle \mathcal{T}_n(x, t) \rangle$  in terms of a chiral conformal field theory (CFT) associated to the Fermi contour in phase space. We focus on a partition with  $|x| \leq l(t)$ , thus having non-trivial dynamics and such that two corresponding Fermi points  $k_F^\pm(x, t)$  are present. We parameterize the Fermi contour through an angular variable  $\theta \in [-\pi, \pi]$  and we decompose  $\mathcal{T}_n(x, t)$  in a pair of chiral twist fields in the CFT, denoted by  $\tau_n(\theta^+)$  and  $\tilde{\tau}_n(\theta^-)$ , with  $\theta^\pm$  corresponding to the Fermi points  $(x, k_F^\pm(x, t))$  [56]. For the sake of convenience, we identify  $\theta$  as the momentum  $k$  corresponding to a generic point  $(x, k)$  of the Fermi contour, and we set  $\theta^\pm = k_F^\pm$ . Eventually, one expresses the expectation value of the twist field as [56]

$$\langle \mathcal{T}_n(x, t) \rangle = (\varepsilon_n(x, t))^{2h_n} \langle \tau_n(\theta^+) \tilde{\tau}_n(\theta^-) \rangle \left| \frac{d\theta^+}{dx} \right|^{h_n} \left| \frac{d\theta^-}{dx} \right|^{h_n}, \quad (4.2.32)$$

where  $h_n = (n - n^{-1})/24$  is the conformal dimension of  $\tau_n$ ,  $\varepsilon_n(x, t)$  is given by [236, 308–310]

$$\varepsilon_n(x, t) = \frac{\varepsilon_n}{\sin(\pi\rho(x, t))}, \quad (4.2.33)$$

and  $\varepsilon_n$  is a non-universal UV cutoff. We compute the two-point-function

$$\langle \tau_n(\theta^+) \tilde{\tau}_n(\theta^-) \rangle \equiv \left[ \frac{1}{2 \sin\left(\frac{\theta^+ - \theta^-}{2}\right)} \right]^{2h_n}, \quad (4.2.34)$$

fixed by conformal invariance, we express the Jacobian as

$$\left| \frac{d\theta^\pm}{dx} \right| = \left| \frac{dk_F^\pm(x, t)}{dx} \right| = \frac{1}{l(t)\sqrt{1-x^2/l^2(t)}}, \quad (4.2.35)$$

and, from Eq. (4.2.32), we eventually get

$$\langle \mathcal{T}_n(x, t) \rangle = \left[ \frac{\varepsilon_n}{2l(t)} \left( 1 - \frac{x^2}{l^2(t)} \right)^{-3/2} \right]^{2h_n}. \quad (4.2.36)$$

Inserting this expression in Eq. (4.2.29), we determine the analytic form of the Rényi entropies

$$S_n(t) = \frac{2h_n}{n-1} \log \left( l(t) \left( 1 - \frac{x^2}{l^2(t)} \right)^{3/2} \right) + \dots, \quad (4.2.37)$$

up to an omitted, non-universal constant. We note that this kind of calculation for  $h = 0$  can be found in Ref. [56]; the only difference compared to the present analysis is the expression of  $\rho(x, t)$  and  $k_F^\pm(x, t)$ . As anticipated above, the parameter  $h$  enters in Eq. (4.2.37) only via  $l(t)$ , which, as anticipated, amounts at replacing  $t$  with  $l(t)$  [see Eq. (4.2.23)] in the prediction of Ref. [236]. Finally, by taking the analytic continuation  $n \rightarrow 1$ , we get the von Neumann entropy

$$S(t) = \frac{1}{6} \log \left( l(t) \left( 1 - \frac{x^2}{l^2(t)} \right)^{3/2} \right) + \gamma, \quad (4.2.38)$$

where the non-universal constant  $\gamma \simeq 0.4785\dots$  is extracted from the result of Ref. [308]. In Fig. 4.5 we plot the quantum GHD prediction for the entanglement entropy compared with numerical data on the lattice in the hydrodynamic regime, finding perfect agreement. Beyond the entanglement entropy, the approach discussed above allows us to characterize also the fluctuations of the number of fermions, as explained in Ref. [53], and to predict analytically the full counting statistics. In fact, consider the operator

$$N_A \equiv \sum_{x \in A} \psi_x^\dagger \psi_x, \quad (4.2.39)$$

i.e., the number of fermions in the spatial region  $A$ . Its expectation value at time  $t$  is predicted by GHD to be given by the following semi-classical expression:

$$\langle N_A(t) \rangle \simeq \int_{x \in A} dx \rho(x, t). \quad (4.2.40)$$

Although all higher-order connected moments (which describe the quantum fluctuations related to the entanglement between  $A$  and  $\bar{A}$ ) vanish at the semi-classical level, their leading behavior can be computed via quantum GHD. In order to do this, we focus on the full-counting statistics

$$\langle e^{i\alpha N_A(t)} \rangle, \quad (4.2.41)$$

of  $A$ , i.e., the generating function of the moments of  $N_A$ . As done above and for the sake of simplicity, we consider  $A = [x, +\infty)$  and follow the same construction as that previously illustrated for the Rényi entropies. Here, it is important to identify the fields in the chiral CFT corresponding to  $e^{i\alpha N_A}$ , which are (chiral) vertex  $U(1)$  fields  $V_{\pm\alpha}$ . Their conformal dimension is given by

$$h_\alpha = \frac{1}{2} \left( \frac{\alpha}{2\pi} \right)^2, \quad \text{with } \alpha \in [-\pi, \pi]. \quad (4.2.42)$$

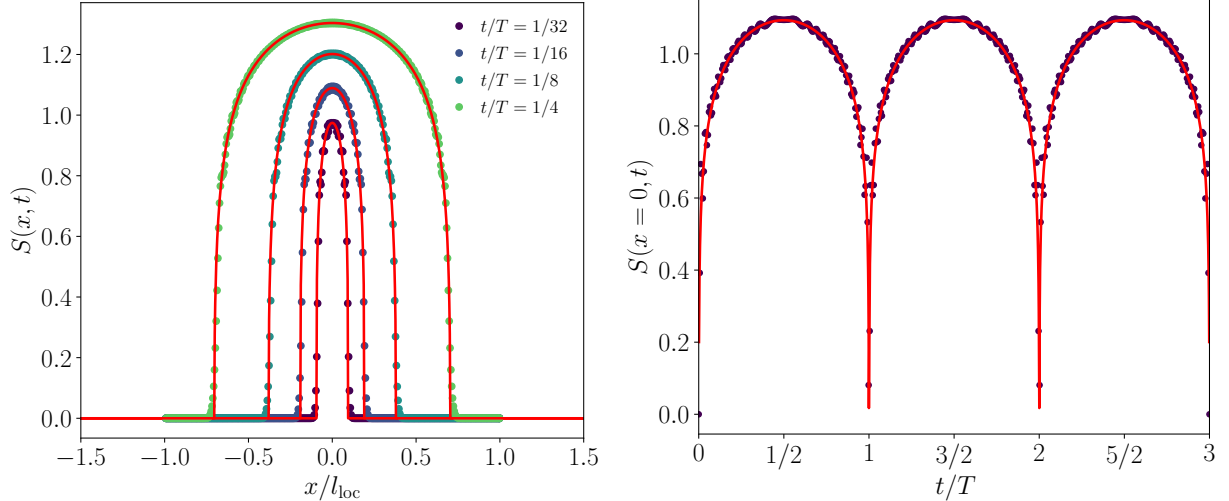


Figure 4.5: Evolution of the von Neumann entanglement entropy  $S(x, t)$  between  $A = [x, \infty)$  and  $\bar{A}$ , starting from a single domain wall located at  $x = 0$ . In the left panel  $S(x, t)$  is plotted as a function of  $x$  for various values of time  $t$ , while the right panel shows the periodic evolution of  $S(x = 0, t)$  as a function of  $t$ . As in the previous figures,  $x$  and  $t$  are rescaled by the natural  $h$ -dependent scales  $l_{\text{loc}}$  and  $T$  [see Eqs. (4.2.15) and (4.2.8)], respectively. In both panels, solid lines correspond to the prediction of quantum GHD in Eq. (4.2.38), while symbols indicate the numerical results obtained for a chain of (left)  $L = 400$  sites with field  $h = 0.01$  or (right)  $L = 300$  sites with  $h = 0.05$ .

Eventually, it is possible to express [53]

$$\frac{\langle e^{i\alpha N_A(t)} \rangle}{e^{i\alpha \langle N_A(t) \rangle}} = [\varepsilon_\alpha(x, t)]^{2h_\alpha} \langle V_{+\alpha}(\theta^+) V_{-\alpha}(\theta^-) \rangle \left| \frac{d\theta^+}{dx} \right|^{h_\alpha} \left| \frac{d\theta^-}{dx} \right|^{h_\alpha}, \quad (4.2.43)$$

and therefore, by using Eqs. (4.2.35), (4.2.33), and (4.2.34),

$$\log \langle e^{i\alpha N_A(t)} \rangle = i\alpha \langle N_A(t) \rangle - \left( \frac{\alpha}{2\pi} \right)^2 \log \left( l(t) \left( 1 - \frac{x^2}{l^2(t)} \right)^{3/2} \right) + \left( \frac{\alpha}{2\pi} \right)^2 \log \left( \frac{\varepsilon_\alpha}{2} \right), \quad (4.2.44)$$

with  $\varepsilon_\alpha$  being a  $\alpha$ -dependent non-universal UV-cutoff. Since the dependence on the CFT fields of Eqs. (4.2.32) and (4.2.43) enters only via the scaling dimensions of the involved fields, it is sufficient to replace  $h_n \rightarrow h_\alpha$  in Eq. (4.2.32) in order to get  $\langle e^{i\alpha N_A(t)} \rangle$ . We emphasize that while the average  $\langle N_A(t) \rangle$  is not directly predicted by field theory, it can be computed by GHD via Eqs. (4.2.40) and (4.2.19), and for  $A = [0, \infty)$  it is given by

$$\langle N_{A=[0, \infty)}(t) \rangle = \frac{l(t)}{\pi}. \quad (4.2.45)$$

Finally, it is worth mentioning that in the large-scale limit, namely under  $t \rightarrow \lambda t$ ,  $x \rightarrow \lambda x$ ,  $h \rightarrow h/\lambda$ , being  $\lambda$  a large dimensionless parameter, the average number of particles scales extensively as  $\langle N_A(t) \rangle \rightarrow \lambda \langle N_A(t) \rangle$ , while its variance grows logarithmically as  $\langle N_A^2(t) \rangle_c \rightarrow \log(\lambda) \langle N_A^2(t) \rangle_c$ , where  $\langle \dots \rangle_c$  stands for cumulants. By contrast, higher-order cumulants, which appear in Eq. (4.2.44) due to the  $\alpha$ -dependent cutoff as powers of  $\alpha$  larger than two, are finite as  $\lambda \rightarrow \infty$ , but cannot be determined within the quantum GHD formalism. These are typical features of free fermions at

equilibrium [311, 312], which might be affected, e.g., by the presence of defects [313]. In our case, these properties can be traced back to the fact that the scaling dimension of the  $U(1)$  vertex fields  $V_{\pm}(\alpha)$  is proportional to  $\alpha^2$ , see Eq. (4.2.42).

### 4.3 Stark localization in a generic potential

In this section, we go beyond the analysis of the linear potential, and we study the semi-classical dynamics of the Hamiltonian (4.1.7). We first provide an argument to establish the conditions under which a trajectory starting from  $(x, k) = (x_0, 0)$  at time  $t = 0$ , having an initial vanishing velocity  $v_0 = v(k = 0) = 0$ , experiences Stark localization in the presence of a generic potential  $V(x)$ . This is a relevant question for a wider class of systems, e.g., the long-range interacting model which, in this respect, was investigated in Ref. [206]. We anticipate here that the analysis presented below readily extends to the somehow equivalent initial condition in which the particle has, as above, a vanishing initial velocity  $v_0 = v(k_0) = 0$  but with a non-vanishing wave-vector  $k_0 = \pm\pi$ . In this case, the subsequent dynamics of the particle starting from  $x_0$  occurs in the direction in which the potential  $V(x)$  increases, because the value of the kinetic term in Eq. (4.1.7) can only decrease compared to its initial (maximum) value. Without loss of generality, we assume

$$V'(x_0) < 0, \quad (4.3.1)$$

as the analysis for  $V'(x_0) > 0$  would be identical, while if  $V'(x_0) = 0$  the trajectory reduces just to the initial point as no evolution occurs within the semi-classical approximation. Under the above assumption, the particle starting at  $(x, k) = (x_0, 0)$  is initially accelerated to the right of  $x_0$ . Then, it either stops at a certain position  $x = x_1 > x_0$  or it escapes towards infinity. If it stops, its velocity  $v(k) = \sin k$  at  $x = x_1$  has to vanish and therefore the corresponding momentum  $k_1$  of the particle is either  $k_1 = 0$  or  $k_1 = \pi (= -\pi)$ . By conservation of energy, one easily shows that in the former case

$$V(x_0) - V(x_1) = 0, \quad (4.3.2)$$

which corresponds to usual oscillations around the local *minimum* of the confining potential, while

$$V(x_0) - V(x_1) = 2 \quad (4.3.3)$$

in the latter. This means that if the potential  $V(x)$  for  $x > x_0$  is bounded by

$$V(x) \in (V(x_0) - 2, V(x_0)) \quad (4.3.4)$$

the particle cannot actually stop and reverse the direction of its motion and thus it moves towards  $x \rightarrow +\infty$ . Conversely, if this is not the case, one can identify the smallest value  $x_1$  of  $x$  for which  $V(x)$  escapes the interval in Eq. (4.3.4) from below. The existence of this  $x_1$  implies that the dynamics of the particle occurs within the region  $x \in [x_0, x_1]$ . Accordingly,  $V(x_0) - V(x_1)$  being equal to 0 or 2 indicates either usual periodic motion or Stark localization, respectively. The various cases discussed above are illustrated in Fig. 4.6: the black particle starting at  $x = x_0$  undergoes usual oscillations if the potential is given by the red curve [Eq. (4.3.2)], it experiences Stark localization if the potential is the one indicated in blue [Eq. (4.3.3)], while it escapes to infinity in the potential given by the green curve [Eq. (4.3.4)]. If the starting point is  $(x, k) = (x_0, \pm\pi)$ , the same analysis as the one done above indicates that Stark localization occurs for  $V(x_0) - V(x_1) = -2$ , while if  $V(x_0) - V(x_1) = 0$ , the particle oscillates around the local *maximum* of the potential occurring within the interval  $[x_0, x_1]$ .

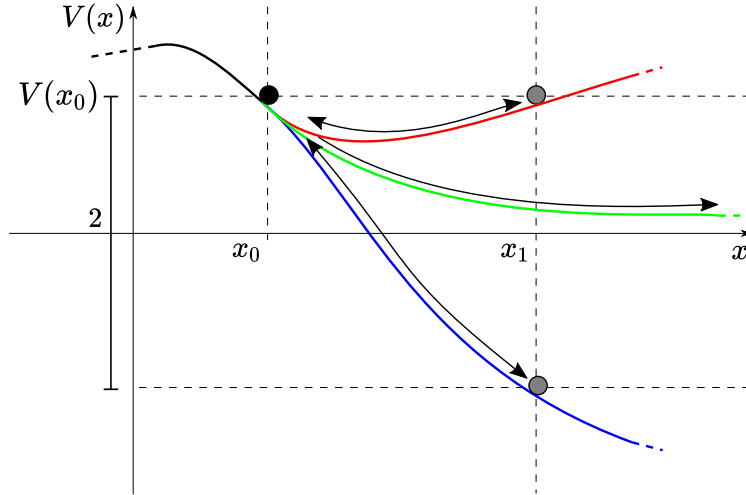


Figure 4.6: Different kinds of dynamics in a generic potential, in the presence of a bounded kinetic energy, see Eq. (4.1.7). The black particle at  $x = x_0$  has zero momentum at  $t = 0$  and the curves with different colors represent various possible potentials. If the particle is subject to the potential given by the red curve, it has a periodic motion, oscillating between  $x_0$  and  $x_1$ , where  $x_1$  is such that  $V(x_0) = V(x_1)$ . In the blue potential, the particle oscillates between  $x_0$  and  $x_1$  with  $V(x_0) - V(x_1) = 2$  because of Stark localization. In the case of the green curve, instead, the particle moves forever, since there is no  $x_1 > x_0$  such that  $V(x_0) - V(x_1) = 2$ .

### 4.3.1 Topological properties of the Hamiltonian flow

Here we adopt a topological perspective, and we analyze the way the trajectories of a particle foliate the entire phase space. This is particularly useful in this context because we argued above that Stark localization is connected to a topological property of the particle trajectories in phase space, i.e., their winding around the Brillouin zone. Let us consider the isoenergetic surface  $\Gamma_E$  with energy  $E$ , defined by

$$\Gamma_E = \{(x, k) | \mathcal{H}(x, k) = E\}, \quad (4.3.5)$$

with  $\mathcal{H}$  given by Eq. (4.1.7). In general,  $\Gamma_E$  is the union of many disconnected trajectories, some of which might experience Stark localization. As the energy  $E$  is varied,  $\Gamma_E$  may change its topology due to the presence of critical points  $(x_c, k_c)$  of the map  $(x, k) \rightarrow \mathcal{H}(x, k)$ . These points are defined by the condition

$$\nabla \mathcal{H}(x_c, k_c) = \mathbf{0}, \quad \text{i.e.,} \quad \begin{cases} k_c = 0 \quad \text{or} \quad \pm \pi, \\ V'(x_c) = 0. \end{cases} \quad (4.3.6)$$

In other words, whenever  $V(x)$  has a local minimum or maximum, a pair of critical points might appear in the phase space depending on the value of  $E$ . In order to characterize the nature of a possible critical point  $(x_c, k_c)$ , we linearize the dynamics around it, assuming for the sake of simplicity that  $V''(x_c) \neq 0$ . We define the deviation from the stationary points as

$$(\delta x, \delta k) \equiv (x - x_c, k - k_c), \quad (4.3.7)$$

and for  $k_c = 0$  we get

$$\begin{pmatrix} \delta \dot{x} \\ \delta \dot{k} \end{pmatrix} = \begin{pmatrix} 0 & 1 \\ -V''(x_c) & 0 \end{pmatrix} \begin{pmatrix} \delta x \\ \delta k \end{pmatrix} + \mathcal{O}(\delta x^2, \delta x \delta k, \delta k^2), \quad (4.3.8)$$

while for  $k_c = \pm\pi$  we have

$$\begin{pmatrix} \delta\dot{x} \\ \delta\dot{k} \end{pmatrix} = \begin{pmatrix} 0 & -1 \\ -V''(x_c) & 0 \end{pmatrix} \begin{pmatrix} \delta x \\ \delta k \end{pmatrix} + \mathcal{O}(\delta x^2, \delta x \delta k, \delta k^2). \quad (4.3.9)$$

Accordingly, from the sign of the determinants of the linearized maps above, one concludes that the critical point can be either elliptic (with  $V''(x_c) > 0$  and  $k_c = 0$  or  $V''(x_c) < 0$  and  $k_c = \pi$ ) or hyperbolic (with  $V''(x_c) < 0$  and  $k_c = 0$  or  $V''(x_c) > 0$  and  $k_c = \pi$ ).

We now investigate how the qualitative features of the possible periodic dynamics of the particle change when its energy  $E$  approaches a critical value  $E_c$ , i.e., a value for which the corresponding isoenergetic surface contains the critical points identified above. Consider first the case of a Stark-localized trajectory of energy  $E$ , which encircles periodically the Brillouin zone in a finite time. According to the characterization of these trajectories discussed above (see Fig. 4.6), if we slightly change the energy  $E$ , the resulting perturbed trajectories would generically be still Stark localized and periodic. However, when  $E$  approaches a critical value  $E_c$ , the corresponding trajectory of the particle gets close to a separatrix and, as a result, its period diverges. Upon crossing that critical value  $E_c$ , the trajectory might change its topology, ceasing to be Stark localized. The same conclusions apply to the other type of periodic orbits we are interested in, i.e., those corresponding to the usual periodic motion in which the trajectory does not encircle the first Brillouin zone. This means that a change of the qualitative features of the trajectories occurs only upon crossing a critical value of the energy.

It is then natural to ask whether it is possible to predict the topology of the trajectories within an interval of energy  $E$  delimited by two consecutive critical values  $E_{0,1}$ , i.e.,  $E \in (E_0, E_1)$ . In this respect, we point out that a local analysis of the Hamiltonian flow at its stationary points is not sufficient in this respect, as the following paradigmatic example demonstrates. Consider, in fact, an unbounded potential  $V(x)$  such that

$$V(x \rightarrow \pm\infty) = \mp\infty, \quad (4.3.10)$$

with, say, a local minimum at  $x = 0$  and a local maximum at  $x = 1$ . For simplicity, assume that  $V(0) = 0$  while we vary the value of  $V(1) > 0$ . A possible instance of this potential provided by

$$V(x) = -V(1)x^2(2x - 3). \quad (4.3.11)$$

The Hamiltonian  $\mathcal{H}(x, k)$  with this potential has critical points with  $x_c = 0$  or  $1$  and  $k = 0$  or  $\pi$  and corresponding critical energies  $\{-1, -1 + V(1), 1, 1 + V(1)\}$ . Clearly, the existence and location of these critical points and the hyperbolic/elliptic character of the corresponding linearized dynamics in Eqs. (4.3.8) and (4.3.9) are not affected by the actual value of  $V(1)$ .

However, a transition appears for  $V(1) = 2$ , namely, if  $V(1) > 2$  there are some Stark localized trajectories with energy  $E \in (-1, -1 + V(1))$  oscillating in the region  $x \in (0, 1)$ , which are not present for  $V(1) < 2$ . Rather surprisingly, the transition at  $V(1) = 2$  is not accompanied or highlighted by any sudden local change of the Hamiltonian flow, albeit a global change of the topology is present. This can be understood also by noticing that the ordered set of values of the critical energies as a function of  $V(1)$  features a crossing for  $V(1) = 2$ . As a consequence, there is a critical trajectory connecting the two hyperbolic points at  $x = 0$  and  $x = 1$  respectively. We show this mechanism in Fig. 4.7.

The presence of Stark localized orbits can be actually detected by making use of a topological invariant. In fact, consider in phase space a periodic trajectory  $(x(t), k(t))$  with period  $T$  (which, in general, depends on the trajectory) and define the winding number

$$\mathcal{N} = \oint \frac{dk}{2\pi} \equiv \frac{1}{2\pi} \int_0^T dt \dot{k}(t). \quad (4.3.12)$$

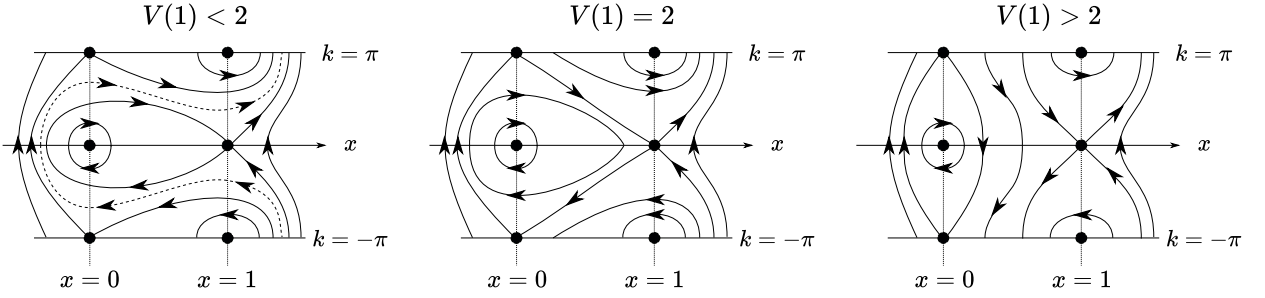


Figure 4.7: Illustration of the change in the topology of the trajectories when the value  $V(1) > 0$  of the local maximum of the potential in Eq. (4.3.11) at  $x = 1$  is varied. For  $V(1) < 2$  (left) there are trajectories which start at  $(x < 0, k = 0)$  and visit positions with  $x > 1$ , being the potential barrier sufficiently small. These trajectories do not experience Stark localization for  $x \in [0, 1]$  while they are localized only for  $x > 1$  (dashed line). For  $V(1) = 2$  (center) a separatrix which connects the two hyperbolic points at  $x = 0$  and  $x = 1$  appears, as a consequence of the degeneracy in the critical energies. When  $V(1) > 2$  (right) the two regions  $x < 0$  and  $x > 1$  are dynamically disconnected. This happens either because the high potential barrier confines the trajectory, or because Stark localization occurs.

This quantity corresponds to the number of times a trajectory winds around the Brillouin zone, as we explain below. We first observe that the integral defining  $\mathcal{N}$  in Eq. (4.3.12) is invariant under a time reparameterization  $t \mapsto \tau = \tau(t)$  of the trajectory, and thus it depends only on the shape of the trajectory. Moreover, the invariance of the integral under small deformation of the trajectory  $k(t) \rightarrow k(t) + \delta k(t)$  follows from the fact that  $k$  behaves like an angle variable and  $\mathcal{N}$  is a winding number. Stated more formally,  $dk$  is a closed 1-form (as  $d^2k = 0$ ), but it can be different from zero as  $dk$  is not an exact differential. Indeed, strictly speaking,  $k$  is not a smooth function of time, being defined up to  $2\pi\mathbb{Z}$ . As an example, let us calculate  $\mathcal{N}$  in Eq. (4.3.12) on a closed trajectory with turning points  $x_0$  and  $x_1$ . We parametrize the integral with the spatial variable  $x$  and, denoting by  $E$  the (conserved) energy of the trajectory and by  $T(E)$  the corresponding period, we get

$$\begin{aligned} \mathcal{N} &= \frac{1}{2\pi} \int_0^{T(E)} dt \dot{k}(t) \\ &= -\frac{1}{\pi} \int_{x_0}^{x_1} dx \frac{V'(x)}{\sqrt{1 - [V(x) - E]^2}} = \frac{1}{\pi} [\arcsin(V(x_1) - E) - \arcsin(V(x_0) - E)], \end{aligned} \quad (4.3.13)$$

where we used Eqs. (4.1.7), (4.1.8) and the fact that  $E = \mathcal{H}(x(t), k(t))$ . Since the velocity vanishes at the turning points, we have that  $V(x_{0,1}) - E$  can be either 1 or  $-1$ . As a consequence,  $\mathcal{N} = \pm 1$  — corresponding to Stark localization — or  $\mathcal{N} = 0$ .

### 4.3.2 The harmonic potential

We finally discuss in detail the case of the harmonic potential [314, 315], relating the semi-classical GHD predictions with the microscopic model in Eq. (4.1.1). In particular, we consider

$$V(x) = \frac{1}{2} \left( \frac{x}{\xi} \right)^2, \quad (4.3.14)$$

where  $\xi$  plays the role of a typical length, assumed to be much larger than the lattice spacing (i.e.,  $\xi \gg 1$ ). The critical points of the Hamiltonian  $\mathcal{H}(x, k)$  with this potential are  $(x_c, k_c) =$

$(0, 0)$ , which is elliptic and corresponds to the minimal energy  $-1$ , and  $(x_c, k_c) = (0, \pi)$ , which is hyperbolic and corresponds to  $E_c = 1$ . Accordingly, for  $E > E_c$  one observes Stark localization of the trajectories, while the usual oscillations — which would be present also in the absence of the lattice, i.e., with  $-\cos k$  in Eq. (4.1.7) replaced by  $-1 + k^2/2$  — arise for  $-1 < E < E_c$ . For later convenience, we write down explicitly the set of points belonging to the critical isoenergetic line (see Eq. (4.3.5)), i.e.,

$$\Gamma_{E=E_c} = \{(x, k) \mid x = \pm 2\xi \cos(k/2) \quad \text{with} \quad k \in [-\pi, \pi]\}. \quad (4.3.15)$$

The various type of trajectories in phase space are illustrated in Fig. 4.8. While for generic potentials it is not possible, in general, to proceed further, in this case we can actually make quantitative predictions for the time evolution. For this purpose, we focus on the dynamics of the domain-wall state (4.2.12) and we study the local occupation number  $n(x, k; t)$  and the value it takes along the classical trajectories. First, we observe that, for  $E > E_c = 1$ , the surface  $\Gamma_E$  in Eq. (4.3.5) contains two disjoint trajectories, which wind around the Brillouin zone and belong to the half-plane  $x > 0$  and  $x < 0$ , respectively (see Fig. 4.8). Since, at the initial time, these trajectories are either completely empty for  $x > 0$  (i.e.,  $n(x < 0, k; t = 0) = 1$ ) or filled for  $x > 0$  (i.e.,  $n(x > 0, k; t = 0) = 0$ ), the corresponding dynamics is simply given by

$$n(x, k; t) = n(x, k; t = 0), \quad \text{for} \quad (x, k) \in \Gamma_{E > E_c}. \quad (4.3.16)$$

We now consider  $E < E_c$  (with  $E > -1$ ), for which  $\Gamma_E$  contains a single trajectory, initially filled for  $x < 0$  and empty for  $x > 0$ . While an exact description of the dynamics at all times  $t > 0$  is possible, we focus here on the long-time average  $n_\infty$  of the occupation number  $n$ , defined as

$$n_\infty(x, k) \equiv \lim_{t \rightarrow \infty} \frac{1}{t} \int_0^t dt' n(x, k; t'). \quad (4.3.17)$$

In this way, the occupation along a trajectory, after this averaging, takes its mean value and therefore

$$n_\infty(x, k) = 1/2, \quad \text{for} \quad (x, k) \in \Gamma_{E < E_c}, \quad (4.3.18)$$

independently of the actual value of  $E$ . The resulting value of  $n_\infty(x, k)$  in phase space is indicated in Fig. 4.8: the darker azure region corresponds to  $n_\infty = 1$ , the lighter azure region to  $n_\infty = 1/2$ , and the white region to  $n_\infty = 0$ .

The time-averaged spatial density  $\rho_\infty(x)$  for a certain value of  $x$  can then be obtained by integrating this  $n_\infty(x, k)$  over the momentum  $k$ . This yields

$$\rho_\infty(x) \equiv \lim_{t \rightarrow \infty} \frac{1}{t} \int_0^t dt' \rho(x, t') = \int_{-\pi}^{\pi} \frac{dk}{2\pi} n_\infty(x, k) = \begin{cases} 1 & \text{for } x < -2\xi, \\ \frac{1}{\pi} \arccos\left(\frac{x}{2\xi}\right) & \text{for } |x| < 2\xi, \\ 0 & \text{for } x > 2\xi. \end{cases} \quad (4.3.19)$$

Figure 4.9 shows the time-averaged density profile  $\rho_\infty(x)$  as a function of  $x/\xi$ , as obtained numerically (symbols) for various values of  $\xi$  [see Appendix B.2 and, in particular Eq. (B.2.7) therein]. These data show data collapse upon increasing  $\xi$  and the resulting master curve agrees with the one predicted on the basis of GHD in Eq. (4.3.19), reported as a solid line. Interestingly, the numerical data are characterized by the presence of a plateau around  $x = 0$ , which is not predicted by GHD. However, the spatial extension  $\ell$  of this plateau turns out to grow slower than  $\xi$  upon increasing it, with  $\ell/\xi \sim \xi^{-1/2}$ , as shown in the inset of the figure. Accordingly, in the limit  $\xi \rightarrow \infty$  we are interested in, with  $x/\xi$  kept fixed, the plateau effectively vanishes and the

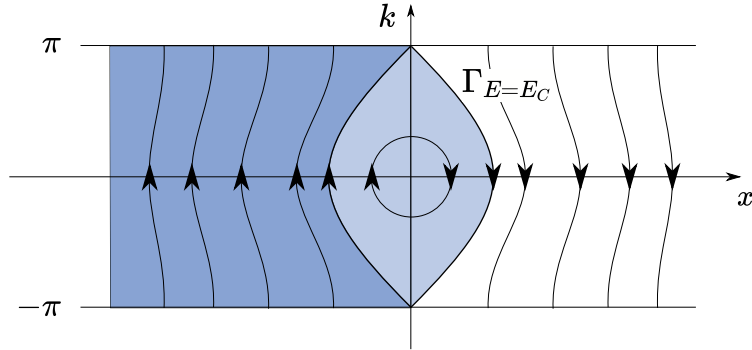


Figure 4.8: Trajectories in phase space of the Hamiltonian (4.1.6) with the quadratic potential in Eq. (4.3.14). The critical line  $\Gamma_{E=E_c}$  separates the region of phase space with  $E < E_c$ , in which oscillations occur, from the one with  $E > E_c$ , where the trajectories Stark localized. For a domain wall initially localized at  $x = 0$ , the long-time average  $n_\infty(x, k)$  of the occupation number  $n(x, k; t)$  calculated according to Eq. (4.3.17) equals 1 for  $(x, k)$  belonging to the region colored in darker azure,  $1/2$  within the region colored in lighter azure, and 0 otherwise.

prediction in Eq. (4.3.19) is recovered. The presence of this plateau can be actually explained as follows. At a given energy  $E$  slightly above  $E_c = 1$ , there are two Stark-localized trajectories (one for  $x < 0$  and the other for  $x > 0$ ) which, according to the semi-classical equation of motion, are dynamically disconnected. However, when these trajectories approach each other in the vicinity of the hyperbolic critical point  $(x_c, k_0) = (0, \pi)$ , quantum effects may mix them via quantum tunneling. This tunneling is expected to be suppressed as the two trajectories further separate in space and therefore it should occur predominantly for  $E \gtrsim E_c$  and  $x \simeq 0$ . Because of this tunneling, the resulting value of  $n_\infty$  would be the average  $1/2$  of the values that  $n_\infty$  would have on the two separate branches, in contrast to the semi-classical prediction and in agreement with the presence of the plateau in Fig. 4.9. Beyond this heuristic explanation, however, a quantitative study of this tunneling is beyond the scope of the present Chapter.

## 4.4 Conclusions

In this Chapter, we investigated the dynamics of the Fermi gas on a lattice in the presence of an external potential, and we study the phenomenon of Stark localization by using the approaches provided by generalized hydrodynamics (GHD) and quantum GHD. In particular, considering the case of a linear potential, we derive analytical predictions for the evolution of an initial domain-wall state. We compare these predictions with exact numerical computations at finite number of particles, finding perfect agreement in the thermodynamic limit. In the presence of a generic potential, we analyze the mechanism that is responsible for the localization of the particles. This analysis shows that the occurrence of localization does not require a fine-tuned external potential but it rather hinges on having a bounded kinetic energy, characterized by a finite band. Moreover, we argue that the topology of the classical trajectories in the phase space of the system is the key feature that determines the possible presence of Stark localization. As an illustrative example, we consider the dynamics in the presence of a quadratic potential — usually not discussed in the context of Stark localization — and show the agreement between our description and the results of numerical calculations.

We expect that GHD, which allowed us to derive easily the predictions presented in this Chapter, should be able to describe accurately the dynamics and the possible occurrence of Stark

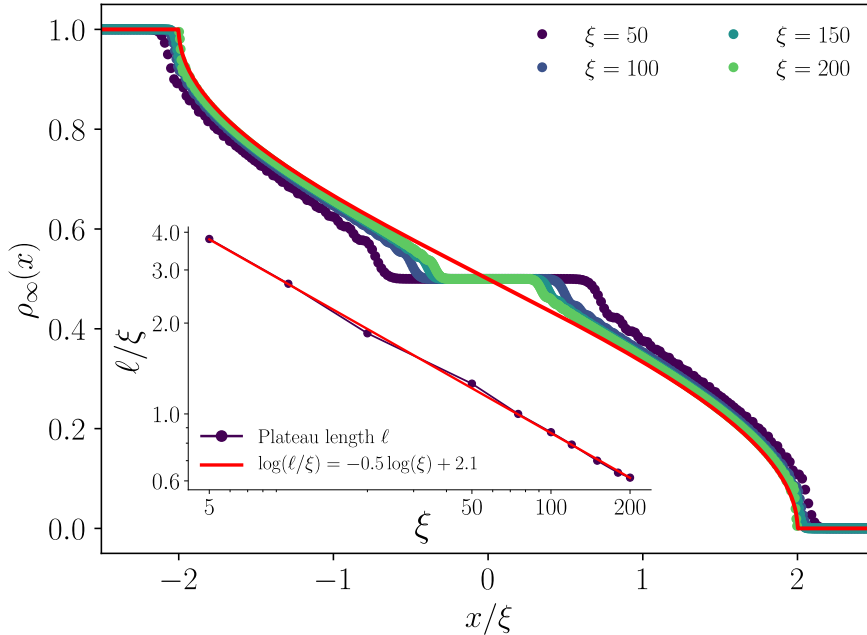


Figure 4.9: Infinite-time averaged density  $\rho_\infty(x)$  [see Eq. (4.3.19)] as a function of  $x/\xi$  for the quadratic potential in Eq. (4.3.14) and various values of  $\xi$ , starting from a domain wall localized at  $x = 0$ . Symbols correspond to the numerical data obtained by computing the time average using the diagonal ensemble (see Appendix B.2) on a chain of length  $L = 800$ . The red solid curve indicates the analytical prediction in Eq. (4.3.19), which the numerical data approach as  $\xi$  increases. In particular, the plateau of extension  $\ell$  which is clearly visible in the numerical data for  $x$  around 0 vanishes. In fact, the inset shows the decays of  $\ell/\xi$  as  $\xi$  increases, with a good fit  $\ell/\xi \sim \xi^{-1/2}$ . This indicates that, on the scale of  $\xi$ , the plateau vanishes as  $\xi$  increases.

localization in generic settings. In particular, modifications of the kinetic term, as long as they span a finite band, can be investigated as described in this Chapter and they are expected to result in a similar phenomenology. However, the most important generalization of the approach discussed here would be towards the study of integrable interacting models on the lattice, such as the XXZ model [49, 56, 316], by adapting the approach in Refs. [317, 318]. GHD methods are powerful enough to provide analytical predictions also in this case, although the calculations are significantly more challenging than those reported here because of the increasing complexity of the corresponding hydrodynamic equations. However, it is reasonable to expect that, with some effort, exact predictions can be obtained also for the interacting case, shedding some light on the phenomenon of many-body Stark localization [172, 173, 293].

We emphasize that our analysis requires that the potential varies on spatial scales which are large compared to the lattice spacing, so that the condition of applicability of the GHD is met. However, one might wonder whether it is possible to relax this assumption in order to describe, e.g., localized potentials arising from defects or impurities. While some specific protocols have been considered and some progress has been made in this direction [62, 319–322], a general theory is still lacking. In the case considered in this Chapter, a significant difficulty that hinders a straightforward application of the GHD approach, is the presence of long-range correlation generated at these defects by the quantum scattering and the subsequent ballistic spread across the system.



# Appendix of Part I



# Appendix A

## Additional information - Melting and Localization in the two-dimensional quantum Ising model

### A.1 Magnetization in the linear strip

We provide here a more detailed analysis of the dynamics of a linear strip of spins, treated in Sec. 2.2.1.

Let us start from the computation of the number  $C(L, l)$  of dynamically accessible configurations for a strip of spins of length  $L$ , in which  $l \leq L - 2$  spins are flipped compared to the initial configuration: due to the perimeter constraint,  $C(L, l)$  satisfies Eq. (2.2.2). This recursion relation is actually obtained by summing the number  $C(L - 1, l)$  of configurations in which the  $L - 1$ -th spin along the chain is not flipped (we recall that the  $L$ -th spin cannot flip) and the number  $C(L - 2, l - 1)$  of configurations in which it is flipped. As there is only one configuration with no spin flip, the initial condition for Eq. (2.2.2) is  $C(L, 0) = 1$  and its solution is thus given by Eq. (2.2.3): this is a direct consequence of Pascal's property of the binomial coefficient [323]. In order to determine the total number of accessible configurations starting from the strip, one needs also to know the maximum number  $l_{\max}$  of spins that can be flipped without violating the perimeter constraint. As anticipated above, the first and last spin cannot flip, and therefore one is left with  $L - 2$  potentially "active" spins. If  $L - 2$  is even, one can flip at most  $(L - 2)/2$  alternating spins, whereas if  $L - 2$  is odd, one can flip  $(L - 1)/2$  alternating spins. Accordingly,  $l_{\max}$  is given by Eq. (2.2.4) in the main text.

Under the assumption of an ergodic dynamics (see the main text), the magnetization profile can be determined by using the following argument. Consider the  $j$ -th spin of a chain of length  $L$ . The number of configurations having the  $j$ -th spin "up" are given by the total number of allowed configurations for the two sub-chains (consisting of  $j - 1$  and  $L - j$  spins, respectively) split by the  $j$ -th spin, that is  $F_{j-1} \times F_{L-j}$ . In the remaining  $F_L - F_{L-j}F_{j-1}$  allowed configurations of the strip the  $j$ -th spin is down, and therefore the magnetization at site  $j$  is simply given by

$$\langle m_L(j) \rangle = \frac{-(F_L - F_{L-j}F_{j-1}) + F_{L-j}F_{j-1}}{F_L} = 2\frac{F_{L-j}F_{j-1}}{F_L} - 1, \quad (\text{A.1.1})$$

as reported in Eq. (2.2.6), with the reflection symmetry  $\langle m_L(j) \rangle = \langle m_L(L - j + 1) \rangle$  and the boundary condition  $\langle m_L(j) \rangle = -1$ . Using the explicit expression of the Fibonacci numbers in

Eq. (2.2.7), one gets, for  $L \rightarrow \infty$

$$\langle m_\infty(j) \rangle = \frac{2}{(2\phi - 1)\phi} - 1 + \frac{2}{(\phi - 1)(2\phi - 1)} \left( \frac{1}{\phi} - 1 \right)^j, \quad (\text{A.1.2})$$

$\phi$  being the golden ratio. In the limit  $j \rightarrow \infty$ , one finds the magnetization at center of the strip  $\langle m_{\infty, \text{bulk}} \rangle = \lim_{j \rightarrow \infty} \langle m_\infty(j) \rangle$  to be given by Eq. (2.2.8), after using the expression of the golden ratio provided before Eq. (2.2.7). The dependence on  $j$  of Eq. (A.1.2) also implies that the approach to this asymptotic value is exponential with the typical length  $\xi_b$  indicated after Eq. (2.2.8).

## A.2 Useful properties of the Bessel functions

In this Appendix we collect a number of properties of Bessel functions which are useful and widely used to derive the results presented in the main text, and we provide also a sketch of their proofs. Many of these properties can actually be found in Refs. [245, 324, 325].

One of the equivalent definitions of the Bessel function of the first kind  $J_n$  is in terms of the integral:

$$J_n(\gamma) = \int_{-\pi}^{\pi} \frac{d\tau}{2\pi} e^{i(n\tau - \gamma \sin \tau)}. \quad (\text{A.2.1})$$

From this definition it follows immediately that

$$\sum_{n=-\infty}^{\infty} J_n(x) = 1, \quad (\text{A.2.2})$$

$J_n(-\gamma) = J_{-n}(\gamma)$ , and, for  $n \in \mathbb{Z}$ ,

$$J_{-n}(\gamma) = (-1)^n J_n(\gamma). \quad (\text{A.2.3})$$

Using again the definition, one can compute the following relation, useful in the calculation of the average of the number operator in Eq. (2.2.17), Sec. 2.2.2

$$\sum_{n=-\infty}^{\infty} J_{x-n}(\gamma) J_{y-n}(\gamma) e^{-2i\theta n} = \sum_{n=-\infty}^{\infty} \int_{-\pi}^{\pi} \frac{d\tau}{2\pi} \frac{d\tau'}{2\pi} e^{i((x-n)\tau - \gamma \sin \tau)} e^{i((y-n)\tau' - \gamma \sin \tau')} e^{-2i\theta n} \quad (\text{A.2.4})$$

$$= e^{-2iyht} \int_{-\pi}^{\pi} \frac{d\tau}{2\pi} e^{i[(x-y)\tau - \gamma(\sin \tau - \sin(\tau + 2ht))]} \quad (\text{A.2.5})$$

$$= e^{-i(x+y)ht} \int_{-\pi}^{\pi} \frac{d\tau}{2\pi} e^{i[(x-y)\tau + 2\gamma \sin ht \cos \tau]} \quad (\text{A.2.6})$$

$$= e^{-i(x+y)ht} j^{x-y} J_{x-y}(2\gamma \sin(ht)), \quad (\text{A.2.7})$$

where we used  $\sum_{n=-\infty}^{\infty} e^{inx} = 2\pi\delta(x + 2k\pi)$ . Setting  $t = 0$  we obtain the completeness relation

$$\sum_{n=-\infty}^{\infty} J_{n-m}(\gamma) J_{n-k}(\gamma) = \delta_{mk}, \quad (\text{A.2.8})$$

that also leads immediately to

$$\sum_{n=-\infty}^{\infty} J_n^2(\gamma) = 1. \quad (\text{A.2.9})$$

If the sums of the previous equation is restricted to positive integer values, using telescopic sums one obtains

$$\sum_{j=1}^{\infty} J_{j+m}(\gamma) J_{j+n}(\gamma) = \frac{\gamma [J_m(\gamma) J_{n+1}(\gamma) - J_{m+1}(\gamma) J_n(\gamma)]}{2(m-n)}, \quad (\text{A.2.10})$$

that reduces to

$$\sum_{j=0}^{\infty} J_{j+n}^2(\gamma) = \frac{\gamma}{2} [J_n(\gamma) \partial_n J_{n-1}(\gamma) - J_{n-1}(\gamma) \partial_n J_n(\gamma)] \quad (\text{A.2.11})$$

when the limit  $m \rightarrow n$  is taken. This relations allows us to compute explicitly the fluctuations of the number operator in Eq. (A.3.6), App. A.3. Using the same procedure as in Eq. (A.2.4) we can compute also

$$\sum_{k \in \mathbb{Z}} J_{mk-x}^2(\gamma) = \frac{1}{m} \sum_{0 \leq n < m} e^{2ixn\pi/m} J_0 \left( 2\gamma \sin \frac{n\pi}{m} \right), \quad (\text{A.2.12})$$

which is used in Eq. (2.2.20), in Sec. 2.2.2.

Another very useful tool is the asymptotic expansion of the Bessel functions for large order and argument (see Ref. [245]), which are useful for discussing the continuum limit of the dynamics in Sec. 2.2.3. For fixed  $\gamma$  and  $x \rightarrow \infty$  one finds

$$J_x(\gamma) \sim \frac{1}{\sqrt{2\pi x}} \left( \frac{e\gamma}{2x} \right)^x, \quad (\text{A.2.13})$$

i.e. the Bessel functions vanish faster than exponentially upon increasing  $x \gg \gamma$ . In the limit  $\gamma \rightarrow \infty$  with fixed  $x$ , instead, we have, at the leading order

$$J_x(\gamma) \sim \sqrt{\frac{2}{\pi\gamma}} \cos \left( \gamma - \frac{\pi}{2}x - \frac{\pi}{4} \right). \quad (\text{A.2.14})$$

If both the order and the argument of the Bessel function diverge, the asymptotic expansion is different if the argument is larger than the order or vice versa: at the leading order for  $x \rightarrow +\infty$ , one has

$$J_x(x \operatorname{sech} \alpha) \sim \frac{e^{x(\tanh \alpha - \alpha)}}{\sqrt{2\pi x \tanh \alpha}}, \quad \text{for } \operatorname{sech} \alpha < 1, \alpha > 0 \quad (\text{A.2.15})$$

$$J_x(x \sec \beta) \sim \sqrt{\frac{2}{\pi x \tan \beta}} \cos \left( x(\tan \beta - \beta) - \frac{\pi}{4} \right), \quad \text{for } \sec \beta > 1, \beta \in \left( 0, \frac{\pi}{2} \right) \quad (\text{A.2.16})$$

from which we notice the strong similarity between Eqs. (A.2.13)–(A.2.15) and Eqs. (A.2.14)–(A.2.16). This means that the asymptotic expansions of the Bessel function remain unaltered even when both the argument and the order scale linearly, but with different powers. Indeed, to see the transition between the regimes described by Eqs. (A.2.15) and (A.2.16) one has to consider  $J_x(x + ax^{1/3})$  for  $x \rightarrow \infty$  and fixed  $a$ , which is not important for our discussions. For the purpose of taking the continuum limit as explained in Sec. 2.2.3 and Sec. 2.3.1 we note that Eqs. (A.2.15) and (A.2.16) imply that, in the limit  $x, y \rightarrow +\infty$  with fixed  $y/x$ , one has

$$J_x^2(y) \sim \theta(y-x) \frac{1}{\pi} \frac{1}{y \sqrt{1 - (x/y)^2}}, \quad (\text{A.2.17})$$

where  $\theta(x)$  is the unit step function which equals 1 for  $x \geq 0$  and vanishes otherwise. This equality is valid after integration with a smooth function, i.e. in the sense of distributions. In fact, the

rapidly oscillating  $\cos^2$  term deriving from Eq. (A.2.16) has been replaced with its average value  $1/2$ , while the rapidly decaying exponential in Eq. (A.2.15) has been set to zero, as indicated by  $\theta(y-x)$  which appears in the expression above.

Another useful formula is

$$\sum_{k=-\infty}^{\infty} J_k^4(\gamma) = \frac{1}{\pi} \int_0^\pi d\theta J_0^2 \left( \sqrt{2\gamma^2 - 2\gamma^2 \cos \theta} \right), \quad (\text{A.2.18})$$

which is used in Eq. (2.4.8). In order to prove it, one can use a modified version of Neumann's addition theorem, i.e. the Graf's and Gegenbauer's addition theorem [245]

$$J_0 \left( \sqrt{x^2 + y^2 - 2xy \cos \theta} \right) = J_0(x)J_0(y) + 2 \sum_{k=1}^{\infty} J_k(x)J_k(y) \cos(k\theta). \quad (\text{A.2.19})$$

By setting  $x = y = \gamma$ , taking the square of both sides, and taking the angular average for  $\theta \in [0, \pi]$ , one gets

$$\frac{1}{\pi} \int_0^\pi d\theta J_0^2 \left( \sqrt{2\gamma^2 - 2\gamma^2 \cos \theta} \right) = J_0^4(\gamma) + 2 \sum_{k=1}^{\infty} J_k^4(\gamma) = \sum_{k=-\infty}^{\infty} J_k^4(\gamma), \quad (\text{A.2.20})$$

thus proving the identity.

We conclude this Section by reporting from Ref. [245] the relation

$$J_\nu(z)J_\nu(\zeta) = \frac{2}{\pi} \int_0^{\pi/2} d\theta J_{2\nu} \left( 2\sqrt{z\zeta} \sin \theta \right) \cos((z-\zeta) \cos \theta), \quad (\text{A.2.21})$$

that, setting  $z = \zeta$  and  $\nu = 0$  reduces to

$$J_0^2(z) = \frac{2}{\pi} \int_0^{\pi/2} d\theta J_0(2z \sin \theta). \quad (\text{A.2.22})$$

This expression is used to derive Eq. (2.4.16).

### A.3 Two-point functions

In order to obtain the fluctuations of the limiting shape  $\mu$  of the Young's diagrams, one needs the 2-point function of the number operator  $n$ , see also Eq. (2.2.10). For simplicity, we report here the computation done at equal times, but the same procedure can be extended also for different times. Let us start by computing

$$\langle \Psi_0 | n(x, t) n(y, t) | \Psi_0 \rangle = \langle \Psi_0 | \psi_x^\dagger(t) \psi_x(t) \psi_y^\dagger(t) \psi_y(t) | \Psi_0 \rangle. \quad (\text{A.3.1})$$

Also in this case, one can expand the initial state and use the time evolution of the fermionic operators. The expectation value one gets, using Wick contractions, is

$$\langle 0 | \psi_\infty \dots \psi_1 \psi_j^\dagger \psi_i \psi_l^\dagger \psi_k \psi_1^\dagger \dots \psi_\infty^\dagger | 0 \rangle = -\delta_{jk}^+ \delta_{il}^+ + \delta_{jk} \delta_{il}^+ + \delta_{ij}^+ \delta_{kl}^+, \quad (\text{A.3.2})$$

being, by definition,

$$\delta_{ab}^+ := \begin{cases} 1 & \text{if } a = b > 0 \\ 0 & \text{otherwise.} \end{cases} \quad (\text{A.3.3})$$

After some straightforward steps one arrives at

$$\langle \Psi_0 | n(x, t) n(y, t) | \Psi_0 \rangle = \left( \sum_{i>0} J_{i-x}^2(\omega_t) \right) \left( \sum_{i>0} J_{i-y}^2(\omega_t) \right) - \left( \sum_{i>0} J_{i-x}(\omega_t) J_{i-y}(\omega_t) \right)^2 + \quad (\text{A.3.4})$$

$$+ \delta_{x,y} \left( \sum_{i>0} J_{i-x}(\omega_t) J_{i-y}(\omega_t) \right), \quad (\text{A.3.5})$$

being  $\omega_t = 2|\gamma \sin(ht)|$ , as in the main text. Therefore, the connected 2-point function is

$$\langle \Psi_0 | n(x, t) n(y, t) | \Psi_0 \rangle_C = \delta_{xy} \left( \sum_{i>0} J_{i-x}^2(\omega_t) \right) - \left( \sum_{i>0} J_{i-x}(\omega_t) J_{i-y}(\omega_t) \right)^2. \quad (\text{A.3.6})$$

Using Eq. (A.2.10), one arrives at (see also Ref. [298])

$$\langle \Psi_0 | n(x, t) n(y, t) | \Psi_0 \rangle_C = \delta_{xy} \left( \sum_{i>0} J_{i-x}^2(\omega_t) \right) - \left( \frac{\omega_t [J_x(\omega_t) J_{y-1}(\omega_t) - J_{x-1}(\omega_t) J_y(\omega_t)]}{2(y-x)} \right)^2. \quad (\text{A.3.7})$$

The fluctuations of the number operator of the fermions along the chain is readily obtained from Eq. (A.3.4) by setting  $x = y$ :

$$\delta n(x, t) = \langle \Psi_0 | n(x, t)^2 | \Psi_0 \rangle_C = \sum_{i>0} J_{i-x}^2(\omega_t) \left( 1 - \sum_{i>0} J_{i-x}^2(\omega_t) \right). \quad (\text{A.3.8})$$

At this point, summing over space as it was done before, one arrives at the correlation function for the shape operator

$$\langle \Psi_0 | \mu(x', t) \mu(y', t) | \Psi_0 \rangle_C = - \sum_{x \leq x'} \sum_{y \leq y'} \left( \frac{\omega_t [J_x(\omega_t) J_{y-1}(\omega_t) - J_y(\omega_t) J_{x-1}(\omega_t)]}{x-y} \right)^2 + \quad (\text{A.3.9})$$

$$+ 4 \sum_{x \leq x'} \sum_{y \leq y'} \delta_{xy} \left( \sum_{i>0} J_{i-x}^2(\omega_t) \right) \quad (\text{A.3.10})$$

$$= 4 \sum_{x \leq x'} \sum_{y \leq y'} \left[ \delta_{xy} \left( \sum_{i>0} J_{i-x}^2(\omega_t) \right) - \mathcal{B}(x, y; \omega_t)^2 \right]. \quad (\text{A.3.11})$$

With the same procedure one can compute the expectation value of the current operator, defined as:

$$j(x, t) \equiv i(\psi_x^\dagger(t) \psi_{x+1}(t) - \psi_{x+1}^\dagger(t) \psi_x(t)). \quad (\text{A.3.12})$$

Using this definition, one obtains

$$\langle \Psi_0 | j(x, t) | \Psi_0 \rangle = \gamma \sin 2ht [J_x^2(2\gamma \sin ht) - J_{x+1}(2\gamma \sin ht) J_{x-1}(2\gamma \sin ht)]. \quad (\text{A.3.13})$$

At  $x = 0$  it reduces to

$$\langle \Psi_0 | j(0, t) | \Psi_0 \rangle = \gamma \sin 2ht [J_0^2(2\gamma \sin ht) + J_1^2(2\gamma \sin ht)]. \quad (\text{A.3.14})$$

Also the current-current correlator can be computed with the same tools: we report here the result for  $x = 0$ , which is given by

$$\langle \Psi_0 | j(0, t) j(0, 0) | \Psi_0 \rangle = J_1^2(2\gamma \sin ht) - J_0^2(2\gamma \sin ht). \quad (\text{A.3.15})$$

## A.4 Comparison with classical simple exclusion processes

In this Appendix we compare the predictions presented in Sec. 2.3.1 for the dynamics of the corner-shaped interface in the quantum Ising model, with those obtained for the classical simple exclusion processes (SEP) which, as discussed in the main text, represents the classical counterpart of the quantum Hamiltonian (2.2.11). In particular, we focus on the totally asymmetric simple exclusion process (TASEP) and the symmetric exclusion process (SSEP), discussing them in the appropriate continuum limits, which makes the comparison with Eqs. (2.3.5) and (2.3.6) immediate. For a discussion of these processes on the lattice, instead, we refer to the vast literature on the topic, e.g. Refs. [187, 204, 285, 326–328].

First, we note that, while the time evolution of the TASEP is ballistic [329], the one of SSEP is characterized by a diffusive scaling [328, 330]. Denoting respectively by  $n(x, t)$  and  $\mu(x, t)$  the density of particles and the interface height (as in Eq. (2.2.10)), it turns out [329] that the dynamics of the rescaled density

$$n_T(\xi, \tau) := \lim_{N \rightarrow \infty} \rho_T(\xi N, \tau N) \quad (\text{A.4.1})$$

of the TASEP (the subscript  $T$  stands for TASEP) obeys the Burgers equation

$$\frac{\partial}{\partial \tau} n_T = \frac{\partial}{\partial \xi} [n_T(1 - n_T)]. \quad (\text{A.4.2})$$

We have denoted with  $\rho_T$  the average number of particles on the lattice, while  $n_T$  denotes the average number in the continuum, which is obtained by taking the limit in Eq. (A.4.1), where  $N$  is the inverse of the lattice spacing. With the step initial condition  $n_T(\xi, 0) = \theta(\xi)$ —corresponding to the corner—one obtains the solution  $n_T(x, t) \equiv n_T(x/t)$ , with the scaling function

$$n_T(v) = \begin{cases} 0 & \text{for } v \leq -1, \\ \frac{1+v}{2} & \text{for } |v| < 1, \\ 1 & \text{for } v \geq 1. \end{cases} \quad (\text{A.4.3})$$

The corresponding interface height  $\mu_T(x, t)$ , determined according to Eq. (2.2.10) on the continuum, turns out to be given by  $\mu_T(x, t) = t \Omega_T(x/t)$ , with the scaling function

$$\Omega_T(v) = \begin{cases} |v| & \text{for } |v| \geq 1, \\ \frac{1+v^2}{2} & \text{for } |v| < 1. \end{cases} \quad (\text{A.4.4})$$

In the case of the SSEP, instead, the dynamics is diffusive and a different scaling of space and time has to be taken in order to obtain a non-trivial continuum limit. Specifically, the rescaled density  $n_S(\xi, \tau) = \lim_{N \rightarrow \infty} \rho_S(\xi \sqrt{N}, \tau N)$ , (the subscript  $S$  stands for SSEP) satisfies the heat equation [330]

$$\frac{\partial}{\partial \tau} n_S = \frac{1}{2} \frac{\partial^2}{\partial \xi^2} n_S. \quad (\text{A.4.5})$$

The same initial condition as before, i.e.  $n_S(\xi, 0) = \theta(\xi)$ , leads to the solution  $n_S(x, t) \equiv n_S(x/\sqrt{2t})$  with the scaling function

$$n_S(v) = \frac{1 + \operatorname{erf}(v)}{2}, \quad (\text{A.4.6})$$

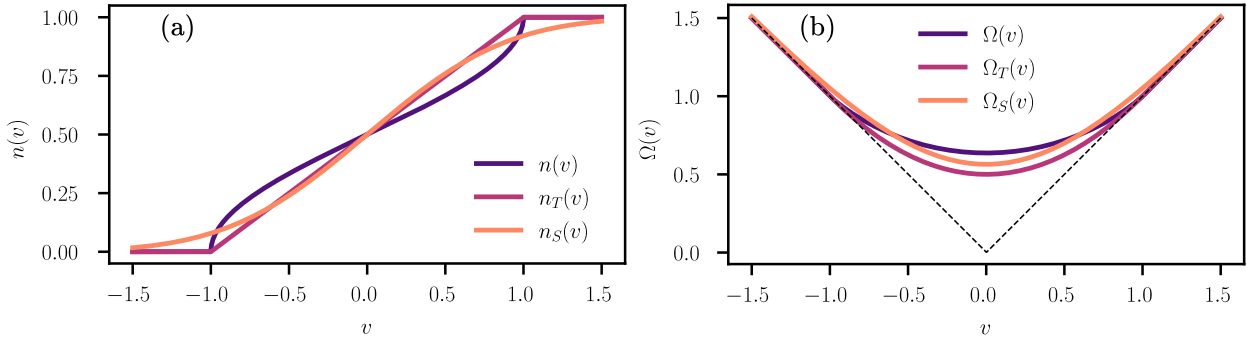


Figure A.1: (a) Comparison between the average number density  $n(v)$  in the quantum case, and the density profiles  $n_T(v)$  and  $n_S(v)$  of TASEP and SSEP, respectively. In particular,  $n(v = x/\omega_t) \equiv \langle n(x, t) \rangle$  is given by Eq. (2.3.5), expressed in terms of the ratio  $v = x/\omega_t$ , while  $n_T(v = x/t)$  and  $n_S(v = x/\sqrt{2t})$  are given by Eqs. (A.4.3) and (A.4.6), respectively. (b) Comparison between the interface limit shape  $\mu(v)$  of the quantum problem and the corresponding quantities  $\mu_T(v)$  and  $\mu_S(v)$  for TASEP and SSEP, respectively. The scaling function  $\Omega(v = x/\omega_t)$  is given by Eq. (2.3.7) and is the limit shape of the quantum system.  $\Omega_T(v = x/t)$  and  $\Omega_S(v = x/\sqrt{2t})$ , instead, are given by Eqs. (A.4.4) and (A.4.7), and correspond to the evolution of the shape of an initial corner (dashed line).

where we introduced the error function  $\text{erf}(x) = 2/\sqrt{\pi} \int_0^x e^{-t^2} dt$ . According to the continuum version of Eq. (2.2.10), the interface profile is given by  $\mu_S(x, t) = \sqrt{2t} \Omega_S(x/\sqrt{2t})$ , with the scaling function

$$\Omega_S(v) = \frac{e^{-v^2}}{\sqrt{\pi}} + v \text{erf}(v). \quad (\text{A.4.7})$$

In Fig. A.1 we compare the scaling forms obtained above for TASEP and SSEP with the one of the quantum model. In doing this comparison one should remember that the very scaling variables differ in the various cases with the sole exception of TASEP and the quantum Ising model with  $h = 0$ : in spite of the fact that they both show a ballistic scaling, the corresponding scaling functions are still different.

## A.5 Second order Schrieffer-Wolff and integrability breaking

In this Section, we perform a Schrieffer-Wolff transformation [191] to get a renormalized Hamiltonian, describing the effective degrees of freedom in each sector  $\mathcal{H}_l$  when  $g, h \ll J < +\infty$ . We remind that the Schrieffer-Wolff transformation consists in a renormalization procedure that progressively eliminates, order by order in perturbation theory, all the block-off-diagonal Hamiltonian matrix elements, i.e. the ones coupling different sectors  $\mathcal{H}_l$  and  $\mathcal{H}_{l'}$  with  $l \neq l'$ . Mathematically, it is a unitary rotation  $U = e^S$ , with  $S = S_1 + S_2 + \dots$ , that gives

$$e^S H e^{-S} = H_0 + H_1 + H_2 + \dots, \quad (\text{A.5.1})$$

where  $S_n$  and  $H_n$  are of order  $n$  in the perturbative coupling. Moreover, performing the expansion up to a finite  $n$  yields a rotated Hamiltonian in which the block-off-diagonal terms are of order  $n + 1$  or higher.

We will follow a recent derivation of the transformation, given in Refs. [179, 243], that gives directly the correct result at any desired order.

### A.5.1 First-order corrections: PXP Hamiltonian

Let us start by separating the original  $2d$  Ising Hamiltonian in Eq. (2.1.1) as follows:

$$H = H_{\text{Is}} = \left( -J \sum_{\langle i,j \rangle} \sigma_i^z \sigma_j^z \right) + \left( -g \sum_i \sigma_i^x - h \sum_i \sigma_i^z \right) \equiv H_0 + V_1. \quad (\text{A.5.2})$$

Setting, for the time being,  $h = 0$ , the Schrieffer-Wolff transformation amounts to the following iterative algorithm (starting from  $n = 1$ ):

1. Split  $V_n \equiv H_n + R_n$ , where  $H_n$  contains only the block-diagonal terms and  $R_n$  only the block-off-diagonal ones.
2. Determine  $S_n$  from the equation

$$[S_n, H_0] + R_n = 0. \quad (\text{A.5.3})$$

3. Set

$$V_{n+1} = \sum_{(k_1, \dots, k_p) \in [n+1]'} \frac{1}{p!} [S_{k_1}, [S_{k_2}, \dots, [S_{k_p}, H_0] \dots]] + \sum_{(k_1, \dots, k_p) \in [n]} \frac{1}{p!} [S_{k_1}, [S_{k_2}, \dots, [S_{k_p}, V] \dots]], \quad (\text{A.5.4})$$

where the summations run over the set  $[m]$  of the ordered partitions  $(k_1, \dots, k_p)$  of an integer  $m (= k_1 + k_2 + \dots + k_p)$ , and  $[m]'$  excludes the partition  $(k_1 = m)$  with  $p = 1$ .

Let us apply the algorithm described above to our case, up to order  $n = 2$ . First of all, we identify in  $V_1$  the block-diagonal terms:

$$H_1 = -g \sum_i \left( P_{\text{Li}}^\uparrow P_{\text{Di}}^\uparrow \sigma_i^x P_{\text{Ri}}^\downarrow P_{\text{Ui}}^\downarrow + P_{\text{Li}}^\uparrow P_{\text{Di}}^\downarrow \sigma_i^x P_{\text{Ri}}^\downarrow P_{\text{Ui}}^\uparrow + P_{\text{Li}}^\downarrow P_{\text{Di}}^\downarrow \sigma_i^x P_{\text{Ri}}^\uparrow P_{\text{Ui}}^\uparrow \right. \\ \left. + P_{\text{Li}}^\downarrow P_{\text{Di}}^\uparrow \sigma_i^x P_{\text{Ri}}^\uparrow P_{\text{Ui}}^\downarrow + P_{\text{Li}}^\uparrow P_{\text{Di}}^\downarrow \sigma_i^x P_{\text{Ri}}^\uparrow P_{\text{Ui}}^\downarrow + P_{\text{Li}}^\downarrow P_{\text{Di}}^\uparrow \sigma_i^x P_{\text{Ri}}^\downarrow P_{\text{Ui}}^\uparrow \right). \quad (\text{A.5.5})$$

and the block-off-diagonal terms:

$$R_1 = -g \sum_i \left( P_{\text{Li}}^\downarrow P_{\text{Di}}^\downarrow \sigma_i^x P_{\text{Ri}}^\downarrow P_{\text{Ui}}^\downarrow + P_{\text{Li}}^\downarrow P_{\text{Di}}^\downarrow \sigma_i^x P_{\text{Ri}}^\uparrow P_{\text{Ui}}^\uparrow + P_{\text{Li}}^\downarrow P_{\text{Di}}^\downarrow \sigma_i^x P_{\text{Ri}}^\uparrow P_{\text{Ui}}^\downarrow + P_{\text{Li}}^\downarrow P_{\text{Di}}^\uparrow \sigma_i^x P_{\text{Ri}}^\downarrow P_{\text{Ui}}^\downarrow \right. \\ \left. + P_{\text{Li}}^\downarrow P_{\text{Di}}^\uparrow \sigma_i^x P_{\text{Ri}}^\uparrow P_{\text{Ui}}^\uparrow + P_{\text{Li}}^\uparrow P_{\text{Di}}^\downarrow \sigma_i^x P_{\text{Ri}}^\downarrow P_{\text{Ui}}^\downarrow + P_{\text{Li}}^\uparrow P_{\text{Di}}^\downarrow \sigma_i^x P_{\text{Ri}}^\uparrow P_{\text{Ui}}^\uparrow \right. \\ \left. + P_{\text{Li}}^\uparrow P_{\text{Di}}^\uparrow \sigma_i^x P_{\text{Ri}}^\downarrow P_{\text{Ui}}^\uparrow + P_{\text{Li}}^\uparrow P_{\text{Di}}^\uparrow \sigma_i^x P_{\text{Ri}}^\uparrow P_{\text{Ui}}^\downarrow + P_{\text{Li}}^\uparrow P_{\text{Di}}^\uparrow \sigma_i^x P_{\text{Ri}}^\uparrow P_{\text{Ui}}^\uparrow \right). \quad (\text{A.5.6})$$

In the previous equations, the projectors  $P_i^{\uparrow, \downarrow}$  are those given in Eq. (2.1.4), while Li/Ri/Ui/Di stands for the left/right/above/below neighbour of the site  $i$ , as in the main text. One easily gets convinced that the terms in  $H_1$  couple states within each  $\mathcal{H}_l$ , since they conserve the number of domain walls; contrarily, each term in  $R_1$  changes their number.

Then, we need to solve Eq. (A.5.3), specified for  $S_1$ :

$$[S_1, H_0] + R_1 = 0. \quad (\text{A.5.7})$$

A bit of reasoning leads to the conclusion that one can compensate each term in  $R_1$ , of the form  $P_{\text{Li}}^\downarrow P_{\text{Di}}^\downarrow \sigma_i^x P_{\text{Ri}}^\downarrow P_{\text{Ui}}^\downarrow$ , with a term in  $S_1$  of the form  $P_{\text{Li}}^\downarrow P_{\text{Di}}^\downarrow \sigma_i^y P_{\text{Ri}}^\downarrow P_{\text{Ui}}^\downarrow$ . Fixing the correct signs, one

finds

$$\begin{aligned}
S_1 = -\frac{ig}{4J} \sum_i & \left( \frac{1}{2} P_{Li}^\downarrow P_{Di}^\downarrow \sigma_i^y P_{Ri}^\downarrow P_{Ui}^\downarrow + P_{Li}^\downarrow P_{Di}^\downarrow \sigma_i^y P_{Ri}^\downarrow P_{Ui}^\uparrow + P_{Li}^\downarrow P_{Di}^\downarrow \sigma_i^y P_{Ri}^\uparrow P_{Ui}^\downarrow + P_{Li}^\downarrow P_{Di}^\uparrow \sigma_i^y P_{Ri}^\downarrow P_{Ui}^\downarrow \right. \\
& - P_{Li}^\downarrow P_{Di}^\uparrow \sigma_i^y P_{Ri}^\uparrow P_{Ui}^\uparrow + P_{Li}^\uparrow P_{Di}^\downarrow \sigma_i^y P_{Ri}^\downarrow P_{Ui}^\downarrow - P_{Li}^\uparrow P_{Di}^\downarrow \sigma_i^y P_{Ri}^\uparrow P_{Ui}^\uparrow \\
& \left. - P_{Li}^\uparrow P_{Di}^\uparrow \sigma_i^y P_{Ri}^\downarrow P_{Ui}^\uparrow - P_{Li}^\uparrow P_{Di}^\uparrow \sigma_i^y P_{Ri}^\uparrow P_{Ui}^\downarrow - \frac{1}{2} P_{Li}^\uparrow P_{Di}^\uparrow \sigma_i^y P_{Ri}^\uparrow P_{Ui}^\uparrow \right). \quad (\text{A.5.8})
\end{aligned}$$

Finally, applying Eq. (A.5.4) for  $n = 2$  yields

$$V_2 = \frac{1}{2} [S_1, [S_1, H_0]] + [S_1, V_1] = -\frac{1}{2} [S_1, R_1] + [S_1, V_1]. \quad (\text{A.5.9})$$

The expression above generates a plethora of terms; however, we are interested *only in the block-diagonal part* of  $V_2$ , namely  $H_2$ : indeed, the block-off-diagonal part  $R_2$  can be removed by going to the next order in the perturbative construction. For now, we will compute only the terms in Eq. (A.5.9) that are *diagonal* in  $\sigma^z$  (thus leaving out terms involving  $\sigma^x$  and  $\sigma^y$  that are still block-diagonal). It is easy to identify them, since they come from commuting  $\sigma_i^x$  in  $R_1$  and  $V_1$  with  $\sigma_i^y$  in  $S_1$ , while leaving the projectors untouched (and therefore the 4 projectors around  $i$  have to be the same both in  $R_1$ ,  $V_1$  and  $S_1$ ). With a bit of patience, one may work out all the details, finding

$$\begin{aligned}
[H_2]_{\text{diag}} = \frac{g^2}{4J} \sum_i & \left( \frac{1}{2} P_{Li}^\downarrow P_{Di}^\downarrow \sigma_i^z P_{Ri}^\downarrow P_{Ui}^\downarrow + P_{Li}^\downarrow P_{Di}^\downarrow \sigma_i^z P_{Ri}^\downarrow P_{Ui}^\uparrow + P_{Li}^\downarrow P_{Di}^\downarrow \sigma_i^z P_{Ri}^\uparrow P_{Ui}^\downarrow \right. \\
& + P_{Li}^\downarrow P_{Di}^\uparrow \sigma_i^z P_{Ri}^\downarrow P_{Ui}^\downarrow - P_{Li}^\downarrow P_{Di}^\uparrow \sigma_i^z P_{Ri}^\uparrow P_{Ui}^\uparrow + P_{Li}^\uparrow P_{Di}^\downarrow \sigma_i^z P_{Ri}^\downarrow P_{Ui}^\downarrow - P_{Li}^\uparrow P_{Di}^\downarrow \sigma_i^z P_{Ri}^\uparrow P_{Ui}^\uparrow \\
& \left. - P_{Li}^\uparrow P_{Di}^\uparrow \sigma_i^z P_{Ri}^\downarrow P_{Ui}^\uparrow - P_{Li}^\uparrow P_{Di}^\uparrow \sigma_i^z P_{Ri}^\uparrow P_{Ui}^\downarrow - \frac{1}{2} P_{Li}^\uparrow P_{Di}^\uparrow \sigma_i^z P_{Ri}^\uparrow P_{Ui}^\uparrow \right). \quad (\text{A.5.10})
\end{aligned}$$

## A.5.2 First-order corrections: corner Hamiltonian

Now we specify the expression derived in the previous Section to the sector within  $\mathcal{H}_l$  which is dynamically connected to the corner considered in the main text, i.e. we restrict our attention to the Young diagrams subspace  $\mathcal{H}_Y$ . In the previous Section we have already determined the diagonal part of the second-order correction  $H_2$ , see Eq. (A.5.10). We just need to determine the off-diagonal (but block-diagonal) part. With a bit of reasoning, one may get convinced that the only allowed moves at the second-order perturbation theory, which bring a state out of  $\mathcal{H}_Y$  and then back in, are those represented in Fig. A.2. Correspondingly, the Schrieffer-Wolff Hamiltonian reads

$$\begin{aligned}
H_{2,Y} = [H_2]_{\text{diag}} - \frac{g^2}{4J} \sum_i & \left[ P_{Li}^\uparrow P_{LUi}^\uparrow P_{UUi}^\uparrow (\sigma_i^+ \sigma_{Ui}^+ + \sigma_i^- \sigma_{Ui}^-) P_{Ri}^\downarrow P_{RUi}^\downarrow P_{Di}^\downarrow \right. \\
& \left. + P_{Li}^\uparrow P_{Ui}^\uparrow P_{RUi}^\uparrow (\sigma_i^+ \sigma_{Ri}^+ + \sigma_i^- \sigma_{Ri}^-) P_{Di}^\downarrow P_{RD_i}^\downarrow P_{RR_i}^\downarrow \right]. \quad (\text{A.5.11})
\end{aligned}$$

The factor in front of the sum is fixed by a careful use of Eq. (A.5.9). Now that we have the Hamiltonian in  $2d$ , we can express it in the  $1d$  language of fermions. Before, however, it is

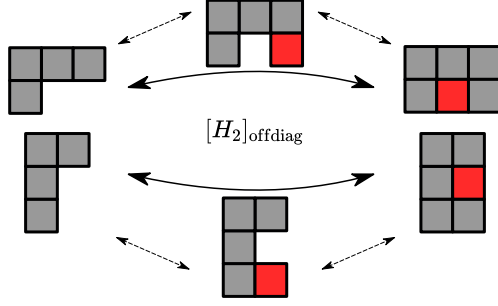


Figure A.2: Graphical representation of the off-diagonal part of  $H_{2,Y}$ , corresponding to next-nearest-neighbor hoppings (see Eq. (A.5.10)), constrained to Young diagrams configurations.

convenient to expand all the projectors  $P^{\uparrow,\downarrow}$  in terms of  $\sigma^z$ : one finds

$$\begin{aligned}
[H_2]_{\text{diag}} &= -\frac{5g^2}{64J} \sum_i (\sigma_{L_i}^z \sigma_i^z + \sigma_i^z \sigma_{R_i}^z + \sigma_i^z \sigma_{U_i}^z + \sigma_{D_i}^z \sigma_i^z) \\
&\quad + \frac{3g^2}{64J} \sum_i (\sigma_{L_i}^z \sigma_{D_i}^z \sigma_i^z \sigma_{R_i}^z + \sigma_{L_i}^z \sigma_{D_i}^z \sigma_i^z \sigma_{U_i}^z + \sigma_{D_i}^z \sigma_i^z \sigma_{R_i}^z \sigma_{U_i}^z + \sigma_{L_i}^z \sigma_i^z \sigma_{R_i}^z \sigma_{U_i}^z). \quad (\text{A.5.12})
\end{aligned}$$

The term with only two Pauli matrices gives a constant contribution on the Young diagram states, since it counts the number of horizontal and vertical frustrated bonds (it is a constant energy shift in the whole sector  $\mathcal{H}_l$ ). The term with four spins, instead, can be represented, up to a constant term in the subspace  $\mathcal{H}_Y$ , by an operator which counts the number of corners in each diagram. Accordingly, in the fermion language, one finds the Hamiltonian

$$H_{2,F} = -\frac{g^2}{4J} \sum_x \left( \psi_x^\dagger e^{-i\pi n_{x+1}} \psi_{x+2} + \text{H.c.} + 3n_x n_{x+1} \right) \quad (\text{A.5.13})$$

$$= -\frac{g^2}{4J} \sum_x \left( \psi_x^\dagger \psi_{x+2} + \text{H.c.} \right) + \frac{g^2}{4J} \sum_x \left( 2\psi_x^\dagger \psi_{x+1}^\dagger \psi_{x+1} \psi_{x+2} + \text{H.c.} - 3\psi_x^\dagger \psi_x \psi_{x+1}^\dagger \psi_{x+1} \right), \quad (\text{A.5.14})$$

where the first term is a correction to the kinetic energy and the second a four-fermions interaction.

## A.6 Participation ratio and localization length

In this Section we compute the (inverse) participation ratio, from which one can easily derive the localization length of the eigenfunctions. By definition

$$\text{IPR} = \sum_k J_k^A(\gamma) = \frac{1}{\pi} \int_0^\pi d\theta J_0^2(\gamma \sqrt{2 - 2 \cos \theta}), \quad (\text{A.6.1})$$

where we used both Neumann's addition theorem to write the sum as an integral and the explicit form of the eigenfunctions. With a change of variables, the integral can be cast in the form

$$\text{IPR} = \frac{2}{\pi} \int_0^1 dx \frac{J_0^2(2\gamma x)}{\sqrt{1-x^2}} = {}_2F_3 \left( \frac{1}{2}, \frac{1}{2}; 1, 1, 1; -4\gamma^2 \right), \quad (\text{A.6.2})$$

where  ${}_2F_3$  is the generalized hypergeometric function. For large  $\gamma$ , one can take the asymptotic expansion of the latter and the (non-oscillating part of the) IPR turns out to be given by

$$\text{IPR} = \frac{2\gamma_E + 5 \ln 4 + \ln \gamma^2}{2\pi^2\gamma} + \frac{3 - \gamma_E - \ln(32\gamma)}{64\pi\gamma^3} + O\left(\frac{1}{\gamma^5}\right), \quad (\text{A.6.3})$$

being  $\gamma_E$  the Euler constant. Since the localization length of the eigenfunctions is roughly  $\xi \approx 1/\text{IPR}$ , one finds

$$\xi \sim \frac{2\pi^2\gamma}{2\gamma_E + 5 \ln 4 + \ln \gamma^2}, \quad (\text{A.6.4})$$

which gives Eq. (2.4.9).

Alternatively, one can also determine the asymptotic expansion for the IPR directly from the integral, using the Mellin transform. In particular, for two functions  $f_{1,2}(x)$  and their Mellin transforms  $\tilde{f}_{1,2}(s)$ , it holds

$$\int_0^\infty dx f_1(x)f_2(x) = \frac{1}{2\pi i} \int_{c-i\infty}^{c+i\infty} ds \tilde{f}_1(1-s)\tilde{f}_2(s), \quad (\text{A.6.5})$$

being, in our case,  $f_1(x) = \frac{1}{\sqrt{1-x^2}}\theta(1-|x|)$  and  $f_2(x) = J_0^2(2\gamma x)$ . One gets then

$$\tilde{f}_1(s) = \frac{\sqrt{\pi}}{2} \frac{\Gamma\left(\frac{s}{2}\right)}{\Gamma\left(\frac{1+s}{2}\right)}, \quad \tilde{f}_2(s) = \frac{1}{(2\gamma)^s} \frac{\Gamma\left(\frac{1-s}{2}\right)\Gamma\left(\frac{s}{2}\right)}{2\sqrt{\pi}\Gamma^2\left(1-\frac{s}{2}\right)}. \quad (\text{A.6.6})$$

Accordingly, the first equality in Eq. (A.6.2) can be alternatively be written as

$$\text{IPR} = \frac{1}{2\pi i} \int_{c-i\infty}^{c+i\infty} ds \frac{1}{2\pi} \frac{1}{(2\gamma)^s} \frac{\Gamma^2\left(\frac{1-s}{2}\right)\Gamma\left(\frac{s}{2}\right)}{\Gamma^3\left(1-\frac{s}{2}\right)} \equiv \frac{1}{2\pi i} \int_{c-i\infty}^{c+i\infty} ds \mathcal{F}(s). \quad (\text{A.6.7})$$

The poles structure of the  $\Gamma$ -function sets  $c \in (0, 1)$ . To compute the integral, one can move the Bromwich path towards increasing values of  $\text{Re}(s)$ ; this way one has to go around the poles of the integrand, which are double poles located on the odd integer numbers, and use the residue theorem to compute their contribution to the integral. As an example, we report the residue at  $s = 1$ , for other values of  $s$  the computation is analogous. By definition one has

$$\text{Res}[\mathcal{F}(s), s = 1] = \frac{d}{ds} \left[ (s-1)^2 \frac{1}{2\pi} \frac{1}{(2\gamma)^s} \frac{\Gamma\left(\frac{1-s}{2}\right)^2 \Gamma\left(\frac{s}{2}\right)}{\Gamma\left(1-\frac{s}{2}\right)^3} \right] \Big|_{s=1}. \quad (\text{A.6.8})$$

Expanding around  $s = 1$  one has  $(s-1)^2 \Gamma\left(\frac{1-s}{2}\right) = 4(1 + \gamma_E(s-1)) + O(s-1)^2$ , from which it follows

$$\text{Res}[\mathcal{F}(s), s = 1] = -\frac{2\gamma_E + 5 \ln 4 + \ln \gamma^2}{2\pi^2\gamma}. \quad (\text{A.6.9})$$

Applying the residue theorem, one obtains a  $2\pi i$  factor that cancels the one in front of Eq. (A.6.7) and a minus sign given by the index of the contour, which is clockwise, obtaining the first term of Eq. (A.6.3). The other terms are obtained with the residues of the other poles. In general, from the dependence on  $1/\gamma^s$  in the integral, one can see that the residue of the pole at  $s = 2n + 1$  gives the order  $1/\gamma^{2n+1}$  of the asymptotic expansion. In this way, one obtains the same result as in Eq. (A.6.3) from the asymptotic expansion of the hypergeometric function. Notice that the residues of the poles give only the power series contribution to the whole integral. There is a bounded oscillating term missing, that comes from the remaining part of the integral on the Bromwich path.



## Appendix B

# Additional information - Hydrodynamic theory of Stark localization

### B.1 Derivation of the semi-classical Hamiltonian

In this Appendix we recall how to derive the semi-classical Hamiltonian in Eq. (4.2.3) starting from that of the original quantum chain in Eq. (4.1.1). The fundamental step consists in passing from a second-quantized to a first-quantized form of the operators appearing in the Hamiltonian. In this respect, consider an operator  $\hat{O}$  which can be written as  $\hat{O} = \sum_{i=1}^N \hat{o}(i)$ , where each operator  $\hat{o}(i)$  acts on the one-particle subspace of the  $i$ -th particle (with  $i \in \{1, \dots, N\}$ ). Then in second quantization, i.e., in Fock space,  $\hat{O}$  is written as  $\hat{O} = \sum_{r,s} c_r^\dagger \langle r | \hat{o} | s \rangle c_s$ , where  $c_r^\dagger$  and  $c_s$  are, respectively, the creation and annihilation operators for a particle in the state  $|r\rangle$  and  $|s\rangle$ , being  $|r\rangle$  and  $|s\rangle$  elements of a generic orthonormal basis of the Hilbert space. In order to derive the semiclassical Hamiltonian, we have first to perform the opposite change of basis, starting from the knowledge of the matrix elements  $\langle r | \hat{o} | s \rangle$ . In turn, the latter can be conveniently derived by diagonalizing the Hamiltonian in Eq. (4.1.1), which is quadratic. Focussing, first, on the kinetic term, it is convenient to introduce the operators  $c_p$  and  $c_p^\dagger$  in momentum space as

$$\psi_x = \frac{1}{\sqrt{L}} \sum_p e^{ipx} c_p \quad \text{and} \quad \psi_x^\dagger = \frac{1}{\sqrt{L}} \sum_p e^{-ipx} c_p^\dagger. \quad (\text{B.1.1})$$

where  $p = 2\pi n/L$ ,  $n \in \mathbb{Z}$ . A simple substitution leads to

$$\frac{1}{2} \sum_x (\psi_x^\dagger \psi_{x+1} + h.c.) = \sum_p (\cos p) c_p^\dagger c_p, \quad (\text{B.1.2})$$

which can be equivalently written [331] as  $\sum_{i=1}^N \cos \hat{p}_i$ , where  $\hat{p}_i$  the momentum operator defined in the one-particle subspace of the  $i$ -th particle. The second term in the Hamiltonian in Eq. (4.1.1) is already in diagonal form, and therefore we have

$$\sum_x V(x) \psi_x^\dagger \psi_x = \sum_{i=1}^N V(\hat{x}_i), \quad (\text{B.1.3})$$

where  $\hat{x}_i$  the position operator defined in the one-particle subspace of the  $i$ -th particle. Accordingly, the Hamiltonian can be written in terms of the fundamental one-particle operators  $\{\hat{x}_i, \hat{p}_i\}_i$  (i.e.,

in the form of the first quantization) as

$$H = \sum_{i=1}^N [-\cos \hat{p}_i + V(\hat{x}_i)]. \quad (\text{B.1.4})$$

The semiclassical approximation of Eq. (B.1.4) can now be done as usual, by substituting the quantum operators with the corresponding classical variables in phase space, leading to the Hamiltonian in Eq. (4.1.7).

## B.2 Numerical method

In this appendix, following Refs. [225, 232, 234, 332–334], we briefly explain the numerical methods employed in order to study the dynamics of the Hamiltonian in Eq. (4.1.1). The correlation matrix  $C(0)$  of a Gaussian state, defined in Eq. (4.1.4), evolves as

$$C(t) = e^{i\hat{H}t} C(0) e^{-i\hat{H}t}, \quad (\text{B.2.1})$$

where  $\hat{H}$  is the single-particle Hamiltonian defined by

$$H = \sum_{x,x'} \hat{H}_{x,x'} \psi_x^\dagger \psi_{x'}. \quad (\text{B.2.2})$$

Given  $C(t)$ , the particle density  $\rho(x, t)$  and the particle current  $j(x, t)$  are easily recovered from the definitions in Eqs. (4.1.9) and (4.1.10). In order to compute the Rényi entropies of a sublattice  $A$ , we first need to project  $C(t)$  over  $A$ , obtaining the restricted matrix

$$(C_A(t))_{x,x'} \equiv (C(t))_{x,x'}, \quad x, x' \in A. \quad (\text{B.2.3})$$

Then, one can show [332, 335] that the  $n$ -th Rényi entropy is expressed by

$$S_n(t) = \frac{1}{1-n} \text{Tr} \log (C_A^n(t) + (1 - C_A(t))^n). \quad (\text{B.2.4})$$

The long-time average  $C_\infty$  of  $C(t)$ , defined as

$$C_\infty \equiv \lim_{T \rightarrow \infty} \frac{1}{T} \int_0^T dt C(t), \quad (\text{B.2.5})$$

can be easily computed, once the eigenvalues of  $\hat{H}$  are known. In fact, assuming that the spectrum of  $\hat{H}$  is non-degenerate, a straightforward algebra yields

$$C_\infty = \sum_E |E\rangle \langle E| C(0) |E\rangle \langle E|, \quad (\text{B.2.6})$$

where  $\{|E\rangle\}_E$  is the set of eigenvectors of  $\hat{H}$ . In other words, the correlation function at long times thermalizes in average to its diagonal ensemble, as the oscillations around that value — due to transitions among distinct eigenvectors — are averaged out. From  $C_\infty$  one can extract directly the long-time average of one-particle observables. For example, the average density of particles  $\rho_\infty(x)$  can be expressed in terms of  $C_\infty$  as

$$\rho_\infty(x) \equiv (C_\infty)_{x,x}. \quad (\text{B.2.7})$$

## Part II

# Renormalization group and finite size effects in disordered localized systems



## Chapter 5

# Renormalization group analysis of Anderson localization in finite dimensions

*The next two Chapters are devoted to proposing a new approach to address localization phenomena based on the renormalization group (RG) technique. In this Chapter, we will address Anderson localization on finite-dimensional lattices by computing the RG  $\beta$ -function for numerically accessible spectral quantities. We generalize the results of the celebrated “Gang of Four” scaling theory and discuss how to take the limit of an infinite number of dimensions, that is relevant for interacting systems and will be discussed more in detail in Chapter 6. The results presented in this Chapter are based on Ref. [6].*

IT is a known fact, as we introduced at the beginning of this Thesis, that when the interaction between quantum particles can be neglected, if the disorder is sufficiently strong, the system undergoes a transition from an ergodic to a localized, Anderson insulator, phase [96, 101, 336] which has no counterpart in classical mechanics. The properties of the so-called Anderson transition are qualitatively understood to depend upon the physical dimension of space  $d$  and, as the  $d$  increases indefinitely, those properties have been a subject of growing interest in the recent past [130, 131, 134, 140, 337–339].

In part, this is due to the interest in the complementary case, in which the elementary excitations of the system *cannot* be thought of as non-interacting particles, and interaction needs to be considered in the analysis. The analog of Anderson localization, in this case, is the subject of Many-Body Localization (MBL) [35, 103, 105, 340]. The connection between MBL and the problem of Anderson localization occurs when thinking of the latter on infinite-dimensional lattices, or expander graphs, such as trees, and regular random graphs (RRG) [127, 129, 139]. Some of the difficulties in interpreting the numerical data supporting MBL (see for example [120, 122, 341–343]) have very much in common with the difficulties of interpreting the numerical data of the Anderson model on the RRG (where there is no doubt about the existence of the transition [344]).

In part, however, there is another reason for the current interest in the Anderson transition on expander graphs. The absence of an obvious upper critical dimension and the failure of  $\epsilon$  expansion around  $d = 2$  dimensions to fit the numerically found exponents [345] at  $\epsilon = 1$  ( $d = 3$ ), despite going to five loops in the sigma model [346], is also puzzling. Such mismatch could be due to a failure of the perturbation theory to converge [347], but it could also be due to something more

profound, and reveal a non-trivial behavior of the model in high dimension [135].

In this Chapter, we show how a single parameter scaling theory (a modern form of the one presented in Ref. [100]) can explain the numerics of the statistical properties of wave functions and spectrum. We also show that the irrelevant corrections, in the RG sense, to the one-parameter scaling evolve in the limit of infinite dimensions to give rise to a topologically different RG flow, which we will discuss in more detail in the next Chapter. More specifically, to set the stage, we first recall the scaling theory of Abrahams, Anderson, Licciardello, and Ramakrishnan [100], where the RG flow for the dimensionless conductance has been discussed for the first time. We then present how to extend the theory to spectral observables, that are more easily accessible numerically and that are equivalent to the dimensionless conductance, under the one-parameter scaling hypothesis. We argue that the fractal dimension of the eigenstates is a good observable for our purposes and we describe some general properties of its flow under the renormalization group. While its behavior can be predicted analytically in some regimes (as in the deep ergodic and localized regimes), we have to rely on numerical results for the properties near the critical point. We show that our framework is compatible with the existing numerical observations and gives a clear picture of the behavior of the model as the number of spatial dimensions is increased. This is achieved by matching the known exact results in  $2d$  – and perturbations away from it in the  $\epsilon$ -expansion framework – to the results on random regular graphs, that we argue to be the correct limit  $d \rightarrow \infty$ .

## 5.1 Concepts and definitions

As anticipated, in this Chapter and in the next one we will deal with the renormalization group  $\beta$ -function for the Anderson model. Before defining the model and analyzing its properties on different geometries, we introduce here the basic concepts that we will use in our discussions. In particular, our goal is that of inspecting the properties of the model through spectral observables, that we now present.

The main characters in our discussions will be the eigenstates' fractal dimensions and the average gap ratios of the eigenenergies. Let us first say that eigenstate and spectral properties must be qualitatively (and quantitatively) determined by the expected number of resonant sites at a fixed energy  $E$  (we will always focus on the middle of the spectrum <sup>1</sup>, so we will always assume  $E = 0$ ) within a distance  $L$ , that we will denote with  $\psi(L)$ . The number of resonances  $\psi$  can be introduced in the following way (in Chapter 7 we will investigate in more detail the definition of resonances and their characterization).

By denoting a normalized wavefunction at site  $i$  as  $\varphi(i)$ , following Refs. [350, 351], we define the *support set*  $S_\epsilon$  satisfying the relation  $\sum_{i \in S_\epsilon} |\varphi(i)|^2 = 1 - \epsilon$ , where the  $\varphi$ 's entering the sum are the largest ones in modulus. See Fig. 5.1 for a visual representation. The dimension of the set  $S_\epsilon$  is given by  $N_S(\epsilon) = \sum_{i \in S_\epsilon} 1$  [7].  $S_\epsilon$  does not contain explicitly a length (except the system size), so we need to better describe its structure, by introducing the number of elements in  $S_\epsilon$  at a distance smaller than  $L$  from the reference site, for some fixed  $\epsilon \ll 1$ . This is our proxy for the number of resonances  $1 + \psi(L)$ . Notice that 1 is added because there is at least one resonant site, even in the localized region, as the site is resonant with itself. It can be shown [350] that  $N_S(\epsilon)$ ,

---

<sup>1</sup>The reason for this choice is dictated by the known fact [348, 349] that the density of states of the Anderson model presents a mobility edge. This means that eigenstates close to the boundaries of the spectrum localize with a smaller disorder strength than the ones at the middle of the spectrum. This means that the system is completely localized only when also the infinite temperature (i.e. middle of the spectrum,  $E = 0$ ) states become localized. We will be interested here in this situation

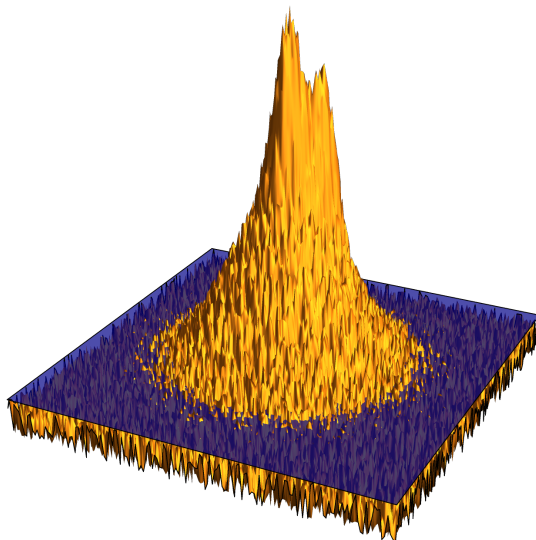


Figure 5.1: Visual representation of a localized wavefunction in two dimensions (orange): the points on the horizontal plane for which  $\varphi$  is larger than the blue plane belong to the support set  $S_\varepsilon$ .

and, hence,  $\psi$  in the delocalized phase (generally multifractal), scales as  $N_S \sim \psi \sim N^D \gg 1$  where

$$D = \frac{\partial \ln(1 + \psi)}{\partial \ln N} \approx \frac{\partial \ln(\psi)}{\partial \ln N}. \quad (5.1.1)$$

The dimension  $D$  is, in turn, easily determined numerically by the eigenfunctions Shannon entropy [350]

$$D = D_1 \equiv \lim_{N \rightarrow \infty} \frac{dS}{d \ln N} = \begin{cases} 1, & \text{ergodic states} \\ < 1, & \text{(multi)fractal states,} \\ 0, & \text{localized states} \end{cases} \quad S = S^1 = - \left\langle \sum_i |\varphi_n(i)|^2 \ln |\varphi_n(i)|^2 \right\rangle_n, \quad (5.1.2)$$

as one can easily see by using the fact that the typical size of the wavefunctions in the support set sites is  $|\varphi(i)|^2 \sim N^{-D}$ . It is also possible to introduce a family of fractal dimensions by using the eigenfunction Renyi entropy:

$$S^{(q)} = \frac{1}{1-q} \left\langle \ln \sum_i |\varphi_n(i)|^{2q} \right\rangle_n, \quad (5.1.3)$$

and their derivatives with respect to the logarithm of volume  $N$ , leading to the eigenfunction fractal dimension  $D_q$ , which gives important details of the multifractal eigenfunction distribution.

From the above discussion, it is clear that  $D$  is intimately related to spectral statistics. Among other spectral statistics the most popular recently was the  $r$ -parameter introduced in Ref. [104] and defined starting from the spectrum  $E_n$  and the gaps  $\Delta E_n = E_{n+1} - E_n$ ,

$$r = \frac{1}{N-2} \sum_{n=1}^{N-2} \frac{\min(\Delta E_n, \Delta E_{n+1})}{\max(\Delta E_n, \Delta E_{n+1})}. \quad (5.1.4)$$

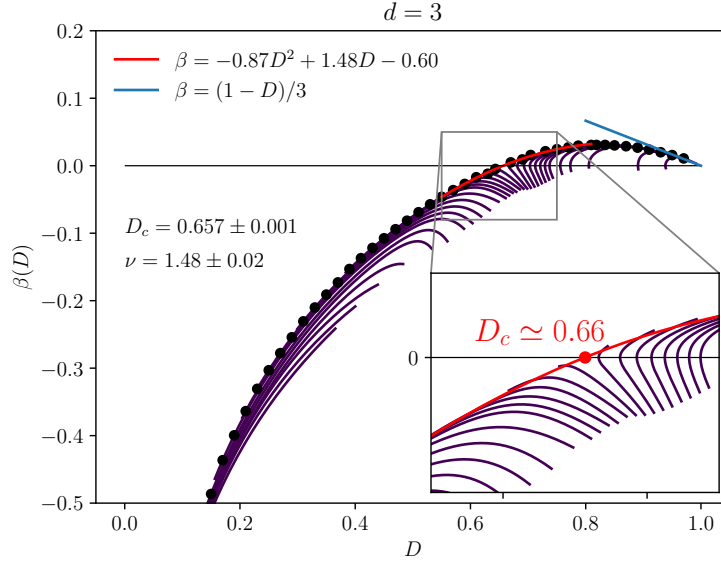


Figure 5.2: Renormalization group (RG) trajectories (solid lines) for  $3d$  Anderson model obtained from the numerical calculation of the eigenfunction Shannon entropy  $S(L)$  and the corresponding finite-size fractal dimension  $D(L) = dS(L)/d \ln N$ . The envelope of RG trajectories (black dots) is the single-parameter  $\beta$ -function  $\beta(D)$ . Its root  $D_c$  gives the fractal dimension of the critical wave functions and the slope of the red solid curve at  $D = D_c$  determines the relevant critical exponent  $\nu$ . The slope of  $\beta(D)$  at the ergodic fixed point  $D = 1$  (blue solid line) is  $(d-2)/d = 1/3$ . The accuracy of one-parameter scaling can be inferred from the length of the initial parts of the trajectories, ‘the hairs’, before merging with the single-parameter curve.

When  $E_n$ ’s are eigenvalues of a real Hamiltonian, the average of  $r$  takes values between  $r_{\text{GOE}} \simeq 0.5307$  and  $r_{\text{P}} = 2 \ln 2 - 1 \simeq 0.386$ . When  $r = r_{\text{GOE}}$  the spectrum behaves according to the predictions of random matrix theory (Gaussian orthogonal ensemble) and we expect the system dynamics to be ergodic. If instead  $r = r_{\text{P}}$ , the energy levels are distributed independently (absence of level repulsion) and ergodicity is broken. Across the Anderson transition, the value of  $r$  goes from  $r_{\text{GOE}}$  at small  $W$  to  $r_{\text{P}}$  at large  $W$ . It is useful to refine  $\phi = (r - r_{\text{P}})/(r_{\text{GOE}} - r_{\text{P}})$ , so that  $\phi \in [0, 1]$ .

## 5.2 Main results

The main result of this Chapter is the numerical calculation for three and the higher dimensions  $d = 4, 5, 6$  of the  $\beta$ -function, defined as

$$\beta(D) = \frac{d \ln D}{d \ln N}, \quad (5.2.1)$$

where  $D = D_1(L)$  is the finite-size fractal dimension defined in Eq. 5.1.2. An example for  $d = 3$  is presented in Fig. 5.2.

The  $\beta$ -function that corresponds to a single-parameter scaling is an *envelope* of RG trajectories parametrized by the size of the system. The initial part of each trajectory corresponds to small system sizes and is governed by the set of irrelevant exponents  $y_n$ . We identify the irrelevant exponents as originating from the high-gradient terms that emerge in the derivation of the effective field theory of localization [352, 353] but are omitted in the non-linear  $\sigma$ -model. The length of the

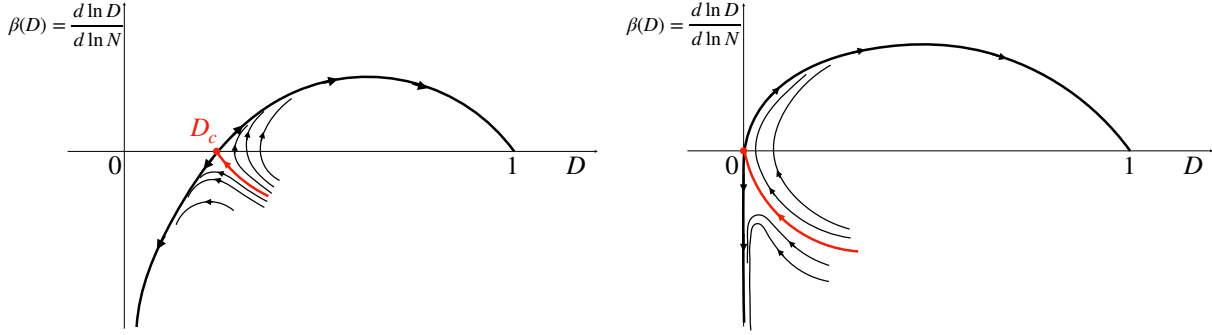


Figure 5.3: A sketch of the full  $\beta$ -function. (Left panel) Behavior at finite dimension, where  $0 < D_c < 1$  and the irrelevant direction at finite size becomes increasingly important as  $d$  grows. (Right panel) Behavior on expander graphs (as the RRG, discussed in Chapter 6), where, near the critical value of  $W$ , the irrelevant direction becomes the only one accessible at the available system sizes. The critical fractal dimension  $D_c \sim 1/d$  for finite  $d$  and vanishes in the  $d \rightarrow \infty$  limit, as in expander graphs. Also, the contribution of the irrelevant exponents becomes larger when  $d$  grows, ultimately becoming marginal when  $d \rightarrow \infty$ . This is reflected by the length of the critical trajectory, depicted in red.

initial part of trajectories increases when the irrelevant exponent decreases in the absolute value. We show that the principal irrelevant exponent  $y = -2 + 2\epsilon + O(\epsilon^2)$  increases (decreases in the absolute value) as the dimensionality  $d = 2 + \epsilon$  increases and finally it becomes marginal in the RG sense for the case of random regular graph [5], which corresponds to the limit  $d \rightarrow \infty$  (see Fig. 5.3).

We also conjecture that the critical fractal dimension  $D_c$  (see Fig. 5.2) has the lower bound  $D_c \geq 1/d$  and that the slope  $\alpha_c$  of  $\beta(D)$  at  $D = D_c$  is finite  $\alpha_c \rightarrow 2$  in the limit  $d \rightarrow \infty$ .

### 5.3 Anderson model and scaling theory for conductance

We consider here the Anderson model as originally introduced in Ref. [96]. It describes a single quantum particle (whose statistics is thus not important) hopping on a given lattice  $\Lambda$  in the presence of onsite random fields. In the case of a  $d$ -dimensional cubic lattice, that we study in this Chapter, the volume of the system (i.e. the number of sites) is  $N = L^d$ . The Hamiltonian operator defining the model is

$$H = -J \sum_{\langle i,j \rangle \in \Lambda} |i\rangle\langle j| + \text{h.c.} + \sum_{i \in \Lambda} \epsilon_i |i\rangle\langle i|. \quad (5.3.1)$$

In the above expression,  $\langle \cdot \rangle$  represent nearest neighbor sites on the lattice  $\Lambda$  and the on-site energies  $\epsilon_i$  are distributed uniformly according to the box distribution  $g(\epsilon) = \theta(|\epsilon| - W/2)/W$ . We choose the hopping rate as the unit of energy,  $J = 1$ . The eigenstates  $\psi_n$  have energy  $H|\psi_n\rangle = E_n|\psi_n\rangle$ .

It is known that the model can have a transition from diffusive/ergodic to localized/non-ergodic phase as the variance – or strength – of disorder  $W$  increases. The location of such transition (i.e. the critical value of  $W = W_c$ ) strongly depends on the structure of the lattice  $\Lambda$ , while the critical exponents at the transition are universal and depend only on the lattice dimensionality.

In the seminal work [100] (often called the “Gang of Four” paper) the dependence of dimensionless conductance on the system size and the strength of disorder has been investigated for different spatial dimensions  $d$ . The main result of the paper which determined the development of

the field for decades, was a formulation of the single-parameter scaling. It stated that the ‘speed’ of the evolution of conductance with the system size depends only on the conductance itself and not on the system size and the disorder strength separately. This allowed to uncover the crucial role of lattice dimensionality  $d$  and predict the absence of delocalized states in the thermodynamic limit for  $d = 1$  and  $d = 2$ , as well as the existence of the localization/delocalization transition for  $d > 2$ .

In Ref. [100] the main observable is the dimensionless conductance  $g(L)$ , where  $L$  is the linear size of the system.  $g(L)$  is defined as the ratio:

$$g(L) = \frac{E_{Th}}{\delta} = \frac{2\hbar}{e^2} \sigma L^{d-2}$$

where  $\hbar/E_{Th}$  is the time it takes for a wave packet to reach the sample boundary,  $\delta$  is the mean level spacing and  $\sigma$  is the conductivity. The mathematical formulation of the single parameter scaling is then given by the equation:

$$\frac{d \ln g(L)}{d \ln L} = \beta(g(L)), \quad (5.3.2)$$

where  $\beta(g)$  is the parameter-free  $\beta$ -function.

Already from the definition of  $g(L)$ , it is easy to see that in the developed metallic regime (where  $\sigma$  is  $L$ -independent), the  $\beta$ -function is a positive constant  $\beta(g) = (d - 2)$ . In the deep insulator regime  $\sigma \sim \exp(-L/\xi)$ , the  $\beta$ -function is  $(-L/\xi) = \ln(g)$  is negative. A continuous interpolation between these two regimes for  $d > 2$  inevitably leads to the unstable fixed point  $g_c$  such that  $\beta(g_c) = 0$  which corresponds to the localization/delocalization transition. If for small system sizes the initial value is  $g_0 > g_c$ , the conductance  $g(L)$  increases with  $L$  driving the system to the metallic regime, while at  $g_0 < g_c$  the conductance decreases with  $L$  and, eventually, the system reaches the deep insulating regime. In contrast to this scenario, if  $d < 2$  (e.g.  $d = 1$ ) the  $\beta$ -function is everywhere negative and the metallic behavior is not possible. The case of the two-dimensional lattice is special, as at  $g \rightarrow \infty$  we have  $\beta(g) \rightarrow 0$  (e.g.  $d = 2$  is a critical dimensionality). A more careful perturbative study in  $1/g$  shows that for disordered potentials without spin-orbit interaction this limit is reached from below, so that the simplest assumption of a monotonic  $\beta$ -function leads to the conclusion that  $\beta(g) < 0$  everywhere, e.g. on the absence of delocalized states for  $d = 2$ . Expanding the  $\beta$ -function around  $g = g_c$  it is possible to determine some critical properties, such as the exponent  $\nu = 1/s$ , where  $s$  is the logarithmic slope of the  $\beta$ -function at the critical point  $\beta(g) = s \ln(g/g_c)$ . For more details, we refer to [100].

## 5.4 $\beta$ -function for ‘modern’ observables

### 5.4.1 Numerically accessible scaling variables

The Anderson localization transition affects most observable properties of the system. The onset of the localized phase can be spotted not only from the absence of transport (as in the original work by Anderson [96]), but also through properties of the spectrum and statistics of eigenfunction. The conductance has a transparent physical meaning but it is not easy to compute numerically. It can be found using the Kubo formula in terms of numerically obtained eigenstates or, alternatively, using Green functions, as proposed by Lee and Fisher [97].

Modern libraries for high-performance computing make spectral statistics and eigenfunctions statistics more readily accessible and therefore preferable. Trusting the *one parameter scaling hypothesis*, these quantities are on the same footing as the conductance in describing the RG flow

of the properties of the system. Therefore we will focus on the observables introduced in Sec. 5.1, the eigenstates' fractal dimension  $D_1$  in particular, and the average gap ratio.

The special role of  $D_1$  is seen from its connection with the spectral property of level compressibility defined as  $\chi = \langle \delta n^2 \rangle / \langle n \rangle$ , where  $n$  is the number of energy levels in a given energy window and the average is over different positions of the energy window and over disorder realizations. It was shown [354] that for weak multifractality near the ergodic phase, the level compressibility is related to the fractal dimensions as  $\chi \approx (1 - D_2)/2$ . However, in this regime, it is degenerate with respect to  $q$ , namely  $(1 - D_2)/2 = (1 - D_q)/q$ . Later on, it has been shown analytically in Refs. [355, 356] that for some random matrix models where both  $\chi$  and  $D_q$  are known, only  $D_1$  satisfies the relation with  $\chi$ , even for strong multifractality. Therefore we are led to suppose that  $D_1$  has a spectral implication, in contrast to  $D_q$  with  $q \neq 1$ . This motivates our choice of using  $D \equiv D_1$  as the fundamental subject of our analysis.

We would like to mention here an important difference between the  $r$  parameter statistics (defined in Eq. 5.1.4) and the spectral compressibility, that is related to  $D(L)$  Eq. 5.1.2. The point is that the former is defined at a small energy scale of the order of the mean level spacing  $\delta$ , while the latter (and presumably also  $D(L)$ ) knows about level correlations at a scale much larger than  $\delta$ . This is important for sensing the multifractal-to-ergodic transition which in some cases does not show up in the  $r$ -statistics, as it happens, e.g. in the Rosenzweig-Porter random matrix model [357].

For these reasons, we choose in this Chapter the variable  $D(L)$  as the scaling parameter that stands for the dimensionless conductance in the RG equation:

$$\frac{d \ln D(L)}{d \ln N} = \beta(D(L), L). \quad (5.4.1)$$

Our goal is to compute numerically the l.h.s. of Eq. (5.4.1), without any *a priori* assumption about the single-parameter scaling. The single-parameter scaling implies that the  $\beta$ -function depends only on  $D(L)$  and thus the solution  $L(D)$  of this equation is a single-valued function. The inverse function  $D(L)$  may be few-valued, but in any case it should be represented by a single parametric curve. On the contrary, if there are other (hidden, or irrelevant in the RG language) parameters, there will be a family of curves satisfying Eq. (5.4.1), each curve corresponding to a certain initial condition. Thus numerical evaluation of the l.h.s. of Eq. (5.4.1) provides a framework for answering the question about the nature of the transition, allowing to discern single- from multiple-parameter scaling.

Before we come to numerics, we would like to review the general properties of the  $\beta$ -function if the single-parameter scaling is given for granted.

### 5.4.2 General properties of $\beta(D)$

In the localized phase, when  $D \ll D_c$ , and in particular when  $D \rightarrow 0$ , the eigenfunctions decay exponentially with the distance from the localization center  $\varphi(r) = A r^{-\alpha} \exp[-r/\xi]$ . Moreover, in finite spatial dimension  $d$ , the number of sites at a given distance  $r$  grows as  $n(r) \sim r^d$ . Therefore, the participation entropy becomes

$$\begin{aligned} S &\equiv - \left\langle \sum_x \varphi^2(x) \ln \varphi^2(x) \right\rangle \simeq - \sum_{r=0}^L n(r) A r^{-\alpha} e^{-r/\xi} \ln \left( A r^{-\alpha} e^{-r/\xi} \right) \\ &= - \ln A + \sum_{r=0}^L n(r) A r^{-\alpha} \left( -\alpha \ln r - \frac{r}{\xi} \right) e^{-r/\xi}, \end{aligned} \quad (5.4.2)$$

with  $\sum_{r=0}^L n(r) A r^{-\alpha} e^{-r/\xi} = 1$  from the wavefunction normalization. From the definition of  $D(L)$ , (5.1.2), and neglecting the logarithm in (5.4.2), being subleading, we get

$$D \simeq \frac{L^{2-\alpha} n(L)}{\xi d} A e^{-L/\xi} \simeq \left(\frac{L}{\xi}\right)^{d+2-\alpha} e^{-L/\xi}, \quad (5.4.3)$$

and using this result, the  $\beta$ -function turns out to be

$$\beta(D) = \frac{1}{d} \ln D - \frac{d - \alpha + 2}{d} \ln |\ln D| + O(1), \quad D_c \gg D \gtrsim 0. \quad (5.4.4)$$

At not very large  $d \sim 1$  and  $\alpha \sim 1$  the first term makes the leading contribution to  $\beta(D)$  in the insulator. At large  $d$  and close to criticality the exponent  $\alpha = d - d_1$ , as the structure of the wave function inside localization radius is close to that of a critical one and thus upon averaging over the volume  $r^d < \xi^d$  it acquires a power-law prefactor  $r^{d_1}/r^d = r^{-(d-d_1)}$ . According to the conjecture  $1 < d_1 < 2$  formulated later on in this Chapter, we have  $1 < d - \alpha < 2$  and it is finite in the limit  $d \rightarrow \infty$ . Thus the first term in Eq. (5.4.4) remains the leading one also for large  $d$ . It is important to note that the region of applicability of Eq. (5.4.4) shrinks to zero in the limit  $d \rightarrow \infty$ . This is a clear indication of the failure of single-parameter scaling to describe this limit properly.

In the other limiting case  $D \rightarrow 1$  we have  $\beta(D) \simeq \alpha_1(1 - D)$ . The slope  $\alpha_1$  is fixed by the results of the ‘‘Gang of Four’’ [100]. Close to the metallic limit in the orthogonal ensemble, the corrections to  $D$  must be proportional to the inverse of the dimensionless conductance:

$$D \approx 1 - c/g \simeq 1 - c'/L^{d-2}. \quad (5.4.5)$$

This means that

$$\beta_d(D) = \frac{d - 2}{d} \frac{1 - D}{D}, \quad D \lesssim 1, \quad (5.4.6)$$

which gives

$$\alpha_1 = \frac{d - 2}{d} \quad (5.4.7)$$

near  $D = 1$ . In the limit  $d \rightarrow \infty$  one obtains  $\alpha_1 = 1$ , the same scaling we find in RMT and for expander graphs [5, 140]. At  $d = 2$  we obtain  $\alpha_1 = 0$ ; we investigate more in detail the consequences of this observation later. Notice also that the above result obtained using a scaling argument can also be found performing the  $\epsilon$ -expansion around  $d = 2$ , as shown later.

At the Anderson localization transition (and in general close to an unstable fixed point of the RG equations) we must have

$$\beta(D) = \alpha_c(D - D_c), \quad (5.4.8)$$

where we are assuming that  $\beta(D)$  vanishes with a finite derivative; such assumption is valid in any finite dimension but is not necessarily true in the  $d \rightarrow \infty$  limit (see next Chapter and Ref. [5]). Later on we argue that, for short-range models like the Anderson model on a  $d$ -dimensional lattice,  $\alpha_c$  remains finite in this limit.

The slope  $\alpha_c$  determines the finite-size scaling exponent  $\nu$ . Indeed, plugging Eq. (5.4.8) into Eq. (5.4.1) and setting  $D \approx D_c$  one finds the solution:

$$\ln |D - D_c| - \ln |D_0 - D_c| = \alpha_c D_c d \ln L, \quad (5.4.9)$$

where  $D_0$  is the value of  $D(L)$  at the smallest  $L \sim 1$ . Then one readily obtains:

$$D = D_c \pm (L/\xi)^{1/\nu}, \quad \xi \sim |D_0 - D_c|^{-\nu} \sim |W_0 - W_c|^{-\nu}. \quad (5.4.10)$$

where  $\nu$  is the finite-size scaling exponent:

$$\nu = 1/(\alpha_c d D_c). \quad (5.4.11)$$

The values of  $\alpha_c$  and  $D_c$  depend on  $d$  and must be found from the numerics.

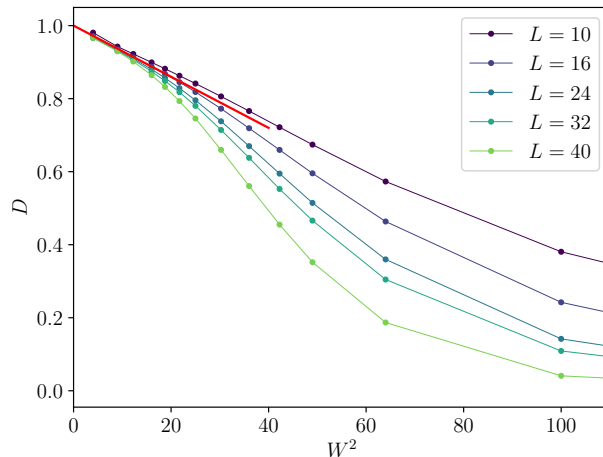


Figure 5.4: Fractal dimension for  $d = 2$  extracted from the participation entropy according to Eq. 5.1.2. It is clearly visible that near  $D \simeq 1$  the dependence is of the form  $D = 1 - aW^2$ , as indicated by the red line.

## 5.5 $\beta$ -function in two dimensions

After having presented some general properties of the  $\beta$ -function in the previous Section, we conduct here a more detailed analysis of its behavior at the lower critical dimension  $d = 2$ .

The  $\beta$ -function in  $d = 2$  is always negative and it has a shallow fixed point at  $D = 1$  (see Eq. 5.4.4 and Eq. 5.4.7)

$$\beta_2(D) = \begin{cases} \frac{1}{2} \ln D + O(1), & \text{if } D \ll 1 \\ -a(1 - D)^2, & \text{if } D \simeq 1. \end{cases} \quad (5.5.1)$$

From the numerics, we find  $a \simeq 1$  (see Fig. 5.6), which we will assume now to be the case, in agreement with  $\sigma$ -model calculations, in particular Eq. (5.7.5).

Let us consider the behavior at small  $W$  (i.e. near  $D = 1$ ). Inserting  $-(1 - D)^2$  into r.h.s. of the RG Eq. (5.4.1) we find:

$$d \left( \ln L^2 + \frac{1}{1 - D} \right) = 0. \quad (5.5.2)$$

This means that

$$\xi = L \exp \left( \frac{1}{2(1 - D(W, L))} \right) = \ell \exp \left( \frac{1}{2(1 - D(W, \ell))} \right),$$

is constant along the RG trajectory which is fixed by initial conditions, *i.e.* by the value of r.h.s. of Eq. (5.5.3) at the smallest length  $L = \ell$  where the single-parameter scaling is still valid (an ultraviolet cutoff). This is the localization length. To see its  $W$  dependence at small  $W$  we assume that:

$$D(W, \ell) = 1 - (W/W_0)^2 + O(W^3), \quad (5.5.3)$$

as one can see in Fig. 5.4 (the constant  $W_0$  depends on the cutoff  $\ell$ ).

This could have been inferred from the fact that, at finite  $L$ , when  $W \rightarrow 0$  all the observables are analytic in the variance and therefore must depend on  $W^2$  analytically. This implies that, at small  $W$ , one obtains:

$$\xi = \ell \exp \left( \frac{W_0^2}{2W^2} \right). \quad (5.5.4)$$

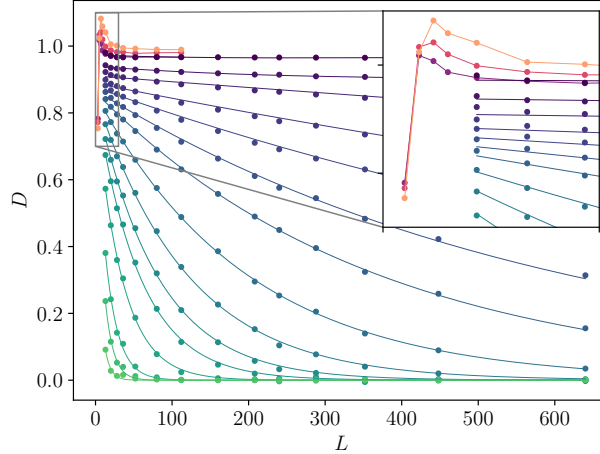


Figure 5.5: System size dependence of  $D(L)$  in  $d = 2$ , for different values of  $W$ . The solid lines in shades of green are interpolations of the data, used to produce the  $\beta$ -function in Fig. 5.6. For small sizes and small  $W$ ,  $D(L)$  may exceed  $D = 1$  even if the system is localized in the thermodynamic limit, as shown in the inset by the red-shaded curves. This behavior can be obtained analytically if the eigenfunction inside the localization radius is weakly multifractal. It happens because of the ‘basin’ regions where the eigenfunction amplitude  $\varphi^2 \sim N^{-1-\eta}$  decreases with the volume faster than  $N^{-1}$ . Such regions should have a large enough probability to overcome the dominance of the ergodic regions with  $\varphi^2 \sim N^{-1}$  in the normalization sum  $\sum_r \varphi(r)^2 = 1$ . The job to suppress the probability of ergodic regions is done by the regions with ‘elevated’  $\varphi^2 \sim N^{-1+\eta}$  which are always present in a weakly multifractal state together with the ‘basin’ areas. A similar behavior of  $D(L)$  is present in the Rosenzweig-Porter random matrix ensemble [357, 358].

This is in agreement with the well-known weak-localization result that in two dimensions  $\ln(\xi/\ell)$  is proportional to the Drude conductivity and thus to the mean free path (MFP). Indeed, from a simple calculation of the decay rate of a wave packet with definite momentum (in the middle of the band), we have  $\ell_{\text{MFP}} = vt_{\text{MFP}}$

$$\frac{\hbar}{t_{\text{MFP}}} = N \int d^2 k' \delta(E_k - E_{k'}) |\langle k | \hat{V} | k' \rangle|^2 \propto W^2, \quad (5.5.5)$$

where  $\hat{V}$  is the on-site potential and  $|k\rangle$  is the plane wave of momentum  $k$ . This gives  $\ell_{\text{MFP}} \sim 1/W^2$  and therefore  $\ln(\xi) \sim 1/W^2$ , as seen for example in [359].

We now consider the behavior at large  $W$ . In this regime we have according to Eq. (5.4.4):

$$\beta(D) \simeq \frac{1}{2} \ln D, \quad (5.5.6)$$

which is compatible with a solution of the form  $D \sim (1/W)^L = \exp[-L/\xi]$ , where

$$\xi \simeq \frac{1}{\ln W}. \quad (5.5.7)$$

The complete dependence of  $\xi$  on  $W$ , therefore, has to interpolate between  $\xi \sim \exp(c/W^2)$ , which is the *weak localization regime* and  $\xi \sim 1/\ln W$ , which is the *strong localization regime*. Therefore, the complete functional dependence should pass through a region of deceleration. We

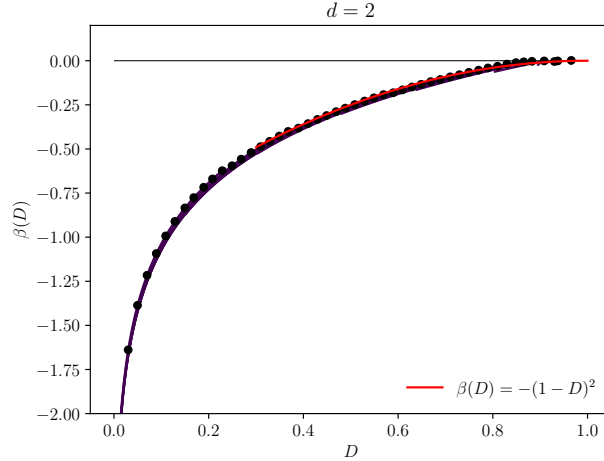


Figure 5.6: Plot of the  $\beta(D)$  for the Anderson localization model on a two-dimensional lattice. The dark lines are the numerical results, that are obtained from the participation entropy according to the definition, and the black dots are the envelope of the data, identifying the one-parameter scaling part of the  $\beta$ -function. In particular, the fractal dimension is computed by applying the discrete derivative to  $S$ , and the resulting points are interpolated using a Padé fit for  $W < W_c$  and an exponential fit for  $W > W_c$  (see Fig. 5.7 for more details on the interpolations). The red curve is  $\beta(D) = -(1 - D)^2$ , which perfectly fits the data and coincides with the correction given by the sigma model, according to Eq. (5.7.5)

believe this has led to some claims in the literature that the scaling  $\ln \xi \sim 1/W^\mu$  with  $\mu$  close or even equal to 1 [360].

Finally, we present the numerical results on the  $L$ -dependence of  $D(L)$  and obtain the  $\beta$ -function for a two-dimensional system. The set of data on the  $L$ -dependence of  $D(L)$  for different  $W$  obtained from Eq. (5.1.2) is presented in Fig. 5.5, where the eigenfunction Shannon entropy is computed from Eq. (5.1.2) using the eigenfunctions from the exact diagonalization of the Anderson model and averaging over disorder and eigenfunctions. From this set of data we obtain the plot  $\beta(D)$  vs  $D$  which is presented in Fig. 5.6. Remarkably, all the RG trajectories lie almost exactly on a single curve, just corroborating the single-parameter scaling as a very precise approximation in  $d = 2$ .

## 5.6 $\beta$ -function for higher dimensions

### 5.6.1 Numerical $\beta$ -function for $d = 3, 4, 5, 6$

The same procedure of numerical computing of  $\beta$ -function can be applied to higher dimensions, albeit with an accuracy that decreases as  $d$  increases. The results are presented in Fig. 5.7 and Fig. 5.8 as well as in Fig. 5.2 presented earlier in this Chapter.

Analyzing the results, we were able to extract the parameters  $D_c$ ,  $\alpha_c$  and  $\nu$  of a single-parameter curve and compare them with the available numerical results for  $\nu$  in Table 1. Surprisingly, the value of  $\nu$  for  $d = 3, 4, 5, 6$  extracted from the best fit of a single-parameter curve  $\beta(D)$  close to critical point  $D = D_c$  is very close to that described by the ‘semiclassical self-consistent theory’  $\nu = 1/2 + 1/(d - 2)$ , albeit the theory itself is seriously flawed.

Another important result of our numerics is that the effect of the irrelevant exponent (encoded

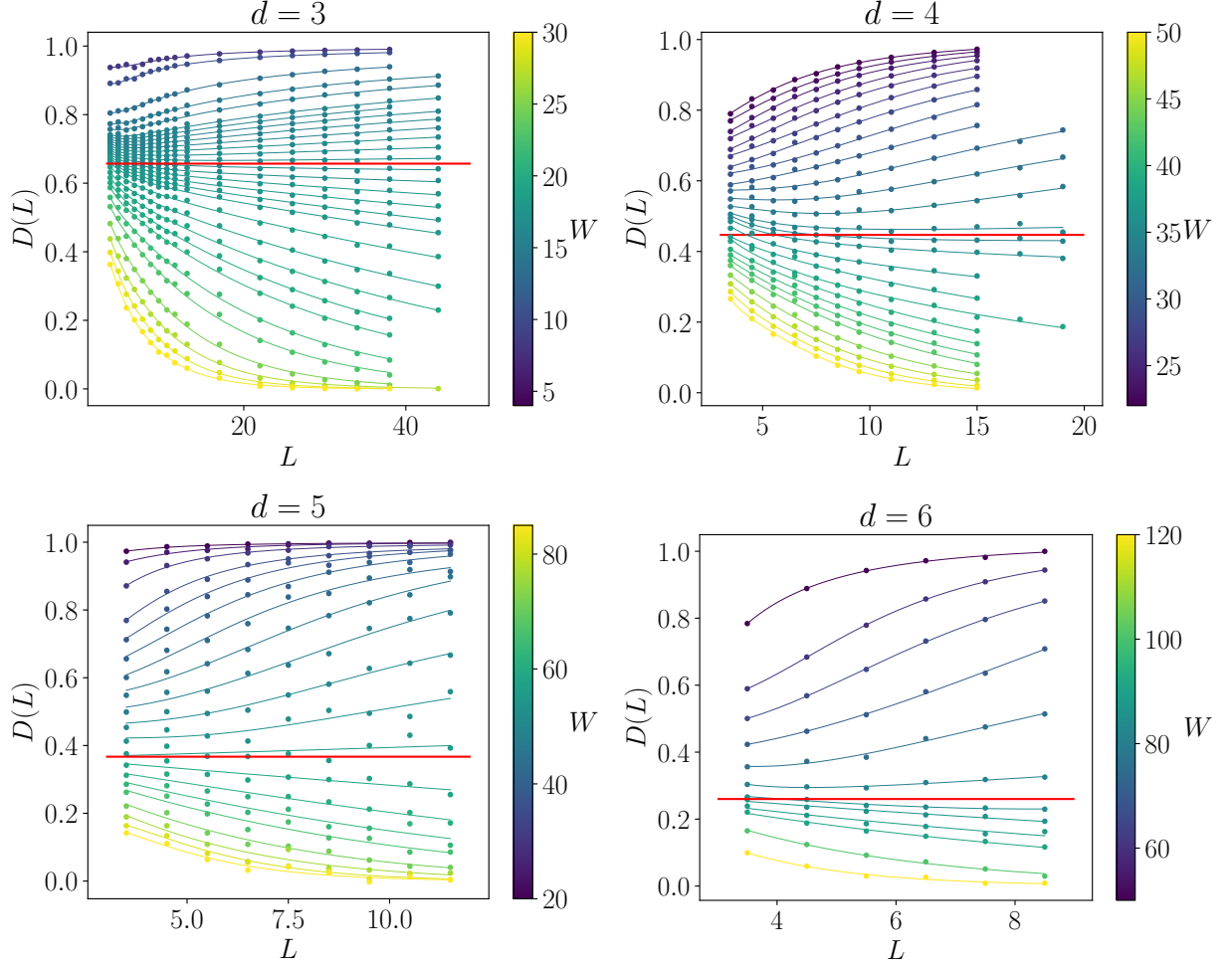


Figure 5.7: System size dependence of the numerical fractal dimension at different dimensions  $d = 3, 4, 5, 6$  and for different values of  $W$ . The solid lines are *interpolations* of the data, that we will use to produce the  $\beta$ -function. In particular, for  $W < W_c$  we interpolate using a Padé function  $D(L, d) = (L^{d-1} + aL^{d-2} + b)/(L^{d-1} + cL^{d-2} + k)$ , while for  $W > W_c$  we use  $D(L) = \exp\{-aL\}(bL + c)/(kL + m)$ . These choices are dictated by physical arguments, namely the behavior of  $\beta(D)$  at  $D \sim 1$  and the exponential decay of  $D$  in the localized phase. The red lines in each plot represent the values of the critical fractal dimension obtained as the point at which the  $\beta$ -function vanishes, and that are reported in Table 1.

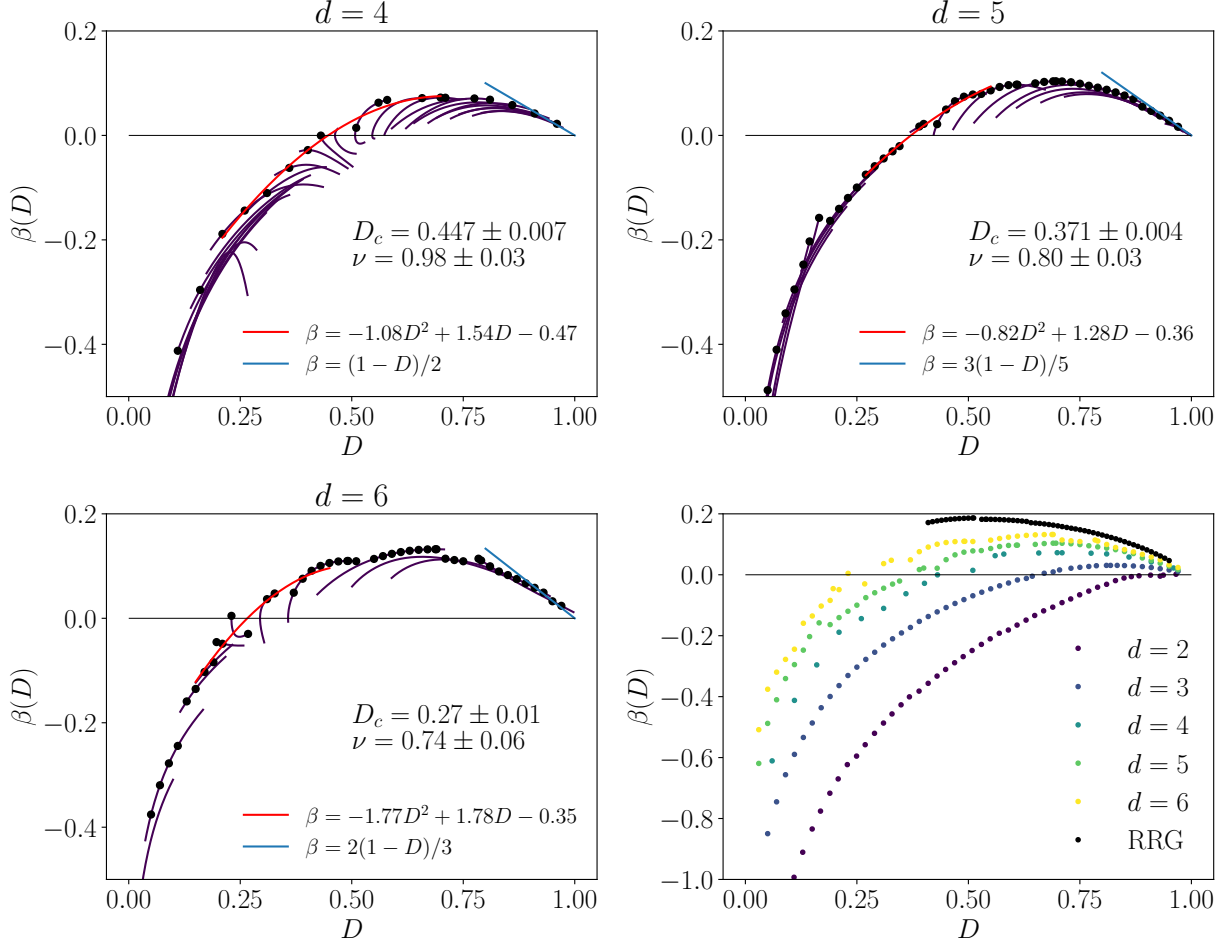


Figure 5.8: Plots of the  $\beta(D)$  for the Anderson localization model on higher-dimensional ( $d = 4, 5, 6$ ) lattices. The colored lines are the numerical results, that are obtained from the participation entropy according to the definition. In particular, the fractal dimension is computed by applying the discrete derivative to  $S$ , and the resulting points are interpolated using a Padé fit for  $W < W_c$  and an exponential fit for  $W > W_c$  (see Fig. 5.7 for more details on the interpolations). The black points are a proxy for the envelope of the data, while the red curves are quadratic fits of the envelope of the numerical data around  $\beta = 0$ , from which we extract  $D_c$  and  $\alpha_c$  as reported in the plots and Table 1. The blue line instead is the theoretical prediction for  $\beta$  near  $D = 1$ . The last plot is the set of envelopes for different dimensions and the RRG, displayed to highlight the flow for  $d \rightarrow \infty$ .

in the length of the RG trajectory at  $W = W_c$  before it hits the fixed point) increases as  $d$  increases (see also Fig. 5.10).

## 5.7 $\beta(D)$ in the $\epsilon$ -expansion and self-consistent theories

In this Section, we discuss the relationship between our analysis and previous analytical results obtained within the  $\sigma$ -model formalism. The discussion is necessarily technical and relies on results presented in the literature. The large- $d$  limit and the relation with expander graphs will be investigated in the next Section.

### 5.7.1 $\epsilon$ -expansion within non-linear $\sigma$ -model

Let us now move perturbatively away from  $d = 2$ . Here we employ the results of Refs. [361, 362] in  $d = 2 + \epsilon$  dimensions which are based on the nonlinear sigma model formalism. In the orthogonal symmetry class, they read:

$$-\frac{d \ln t}{d \ln L^d} = \frac{\epsilon}{d} - \frac{2}{d} t - \frac{12\zeta(3)}{d} t^4 + O(t^5), \quad (5.7.1)$$

$$1 - D_q^{(c)} = \frac{q\epsilon}{d} + \frac{\zeta(3)}{4d} q(q^2 - q + 1)\epsilon^4 + O(\epsilon^5), \quad (5.7.2)$$

where  $t(L)$  is the inverse dimensionless conductance, using the same notation as in the literature, and  $D_q^{(c)}$  is the  $q$ -th fractal dimension at  $W = W_c$ .

Now we introduce the scale-dependent fractal dimension  $D_q(L)$  away from the criticality and find the corresponding  $\beta$ -function. To this end we use the single-parameter scaling that implies  $D_q(L) = D_q(t(L))$  and require that  $D_q(t^*) = D_q^{(c)}$  given by Eq. (5.7.2), where  $t^*$  is the fixed point of RG equation Eq. (5.7.1).

Then expressing  $\epsilon$  in terms of  $t^*$  from Eq. (5.7.1), plugging it in Eq. (5.7.2) and replacing  $t^*$  by  $t = t(L)$  we obtain for  $D(L) \equiv D_1(t(L))$ :

$$1 - D = (2/d)(t + 8\zeta(3) t^4). \quad (5.7.3)$$

Differentiating Eq. (5.7.3) with respect to  $L^d$ , using the RG Eq. (5.7.1), expanding in  $t \ll 1$  up to  $t^4$  and using Eq. (5.7.3) we finally obtain:

$$\begin{aligned} \beta_D(D) = & (1 - D) \left( 1 - \frac{2}{dD} \right) + 3d^2(d - 2)\zeta(3) (1 - D)^4 \\ & - \frac{d^2(24 - d)}{4} \zeta(3) (1 - D)^5 + O[(1 - D)^6]. \end{aligned} \quad (5.7.4)$$

At small  $d - 2 = \epsilon$  one can expand Eq. (5.7.4) up to quadratic order in  $(1 - D)$ :

$$\beta_D(D) = (\epsilon/2)(1 - D) - (1 - D)^2 + O((1 - D)^3). \quad (5.7.5)$$

Notice that the coefficient 1 of  $(1 - D)^2$  agrees with what is extracted from the numerical data (see Fig. 5.6 and Eq. (5.5.1)). This is an independent check of our numerical procedure. In this parabolic approximation the slopes of the  $\beta$ -function,  $\alpha_c$  and  $\alpha_1$ , at  $D = D_c$  (where  $\beta_D(D_c) = 0$ ) and  $D = 1$ , obey the symmetry:

$$\alpha_c = -\alpha_1 = \frac{\epsilon}{2}. \quad (5.7.6)$$

However, this symmetry breaks down even in the  $\epsilon^2$  approximation when the subtle terms  $\sim \zeta(3)$  are still neglected.

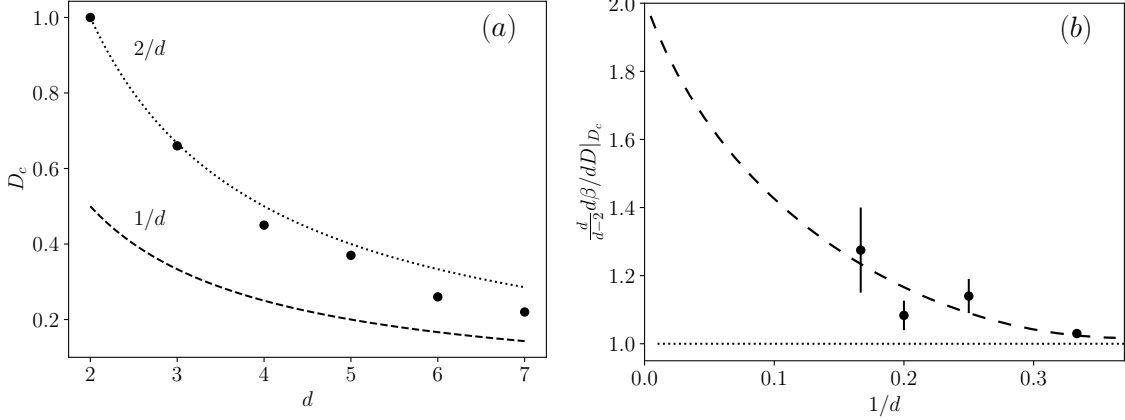


Figure 5.9: (a) The critical fractal dimension  $D_c$  and (b) the ratio of slopes  $d\beta_D/dD$  at  $D = D_c$  and  $D = 1$  as a function of  $d$  from exact diagonalization of the Anderson model on  $d$ -dimensional lattice. The last point  $d = 7$  on the left panel is obtained with very restricted system sizes  $L < 7$  and by a simplified method different from all other points. The dashed line in panel (b) qualitatively illustrates our conjecture, Eqs. (5.7.18),(5.7.19).

### 5.7.2 Self-consistent theory by Vollhardt and Woelfle and its violation

In the absence of the four-loop corrections proportional to  $\zeta(3)$  the critical point  $D_c$ , the slope  $\alpha_c$  of the  $\beta$ -function at  $D = D_c$  and the critical exponent  $\nu$ , Eq. (5.4.11), are found from Eq. (5.7.4) as:

$$D_c = \frac{2}{d}, \quad (5.7.7)$$

$$\alpha_c = \frac{d-2}{2}, \quad (5.7.8)$$

$$\nu = \frac{1}{d-2}. \quad (5.7.9)$$

This result coincides with the one of the so-called “self-consistent theory of localization” by Vollhardt and Woelfle (VW)[363]. If Eqs. (5.7.7),(5.7.8),(5.7.9) were exact for some  $d < d_{\text{up}}$ , where  $d_{\text{up}}$  is an upper critical dimension, then inevitably  $d_{\text{up}} = 4$ , as for  $d = 4$  the exponent  $\nu$  takes its mean field value  $\nu = 1/2$ . Furthermore, at  $d = 4$  within the VW theory, we obtain  $D_c = 1/2$  which is the lower limit for  $D$  where two randomly chosen fractal wave functions intersect and thus can be correlated resulting in the Chalker’s scaling [349, 364].

As a matter of fact, the values of  $D_c$  at  $d = 3$  and  $d = 4$  match Eq. (5.7.7) pretty well (but  $D_c$  is smaller than  $2/d$  for  $d > 4$ , see Table I). However, the value of  $\nu \approx 1.57 - 1.59$  at  $d = 3$ , that is found numerically in Refs. [101, 345, 365, 366], differs substantially from the result of this theory  $\nu = 1.0$ , thus invalidating it. Therefore, there is no reason to trust the result of the VW theory, Eqs. (5.7.8),(5.7.9), according to which the slope  $\alpha_c$  diverges in the limit  $d \rightarrow \infty$ .

Also, the values of  $\alpha_c$  which we found and collected in Table I, are not described by Eq. (5.7.8). Surprisingly, for  $d = 3, 4$  the values of  $\alpha_c$  are very close to  $-\alpha_1$  thus approximately exhibiting the symmetry Eq. (5.7.6) which should hold only at small  $d - 2 = \epsilon$ .

In fact, the contribution of the higher-order terms in the loop expansion in the nonlinear  $\sigma$ -model (the second term in Eq. (5.7.4)) makes the critical  $D_c$  smaller than  $2/d$ :

$$D_c = \frac{2}{d} - \frac{\zeta(3)}{8} \epsilon^4 + O(\epsilon^5), \quad (5.7.10)$$

The slope  $\alpha_c$  and the ratio  $\alpha_c/\alpha_1$  is also affected by these terms:

$$\alpha_c \equiv \left( \frac{d\beta_D}{dD} \right)_{D=D_c} = \frac{\epsilon}{2} + \frac{9}{8}\zeta(3)\epsilon^4 + O(\epsilon^5), \quad (5.7.11)$$

$$\alpha_1 \equiv \left( \frac{d\beta_D}{dD} \right)_{D=1} = -\frac{d-2}{d}, \quad (5.7.12)$$

$$\left| \frac{\alpha_c}{\alpha_1} \right| = 1 + \frac{\epsilon}{2} + \frac{9}{4}\zeta(3)\epsilon^3. \quad (5.7.13)$$

Notice that the product  $\alpha_c D_c$  that determines the exponent  $\nu$  reproduces the well-known result [346] obtained from the  $\beta$ -function for the variable  $t$ , Eq. (5.7.1):

$$\alpha_c D_c d = \nu^{-1} = \epsilon + \frac{9}{4}\zeta(3)\epsilon^4 + O(\epsilon^5). \quad (5.7.14)$$

This demonstrates the invariance of  $\nu$  with respect to the change of variables  $t(L) \rightarrow D(L)$  and provides proof of the correctness of our perturbative calculations.

Despite Eqs. (5.7.10)-(5.7.11) and Eqs. (5.7.13)-(5.7.14) are valid only at very small  $\epsilon \lesssim 0.1$  and do not apply even for the case  $d = 3$ , the tendency they show is correct and observed in the numerical simulations [see Fig. 5.9(a,b)]. In particular, the fact that  $D_c$  decreases faster than  $2/d$  with increasing  $d$  and that the ratio of the slopes obeys the following inequality:

$$\left| \frac{\alpha_c}{\alpha_1} \right| > 1, \quad (5.7.15)$$

and grows with increasing  $d$ , is convincingly confirmed.

### 5.7.3 Correlation between $D_c$ and $\alpha_c$ and a ‘semi-classical theory’ for $\nu_d$

As was already mentioned, the critical  $D_c$  for  $d = 3, 4$  is very close to the result of the VW self-consistent theory  $D_c = 2/d$ . Next, we would like to note that the derivative of the  $\beta$ -function  $\alpha_1 = -(d-2)/d$  at the fixed point  $D = 1$  is an exact result of Eq. (5.7.4) which is independent of the higher-order terms in  $(1-D)$ . It is interesting to see what happens if  $D_c = 2/d$  and the symmetry Eq. (5.7.6) is enforced beyond the lowest  $\epsilon$ -expansion. The immediate consequence of  $\alpha_c = |\alpha_1|$  is that the exponent  $\nu = (dD_c\alpha_c)^{-1} = (dD_c|\alpha_1|)^{-1}$  would take the form:

$$\nu = \frac{d}{2(d-2)} = \frac{1}{2} + \frac{1}{d-2}. \quad (5.7.16)$$

Surprisingly, we obtained the formula empirically suggested by many authors [345, 367, 368], most notably in Ref. [367] where a sort of derivation is presented in the spirit of VW self-consistent theory. We think, however, that this ‘semiclassical theory’ is seriously flawed. In this derivation the momentum dependence of a Cooperon was changed from  $\xi^2 q^2$  in the original VW paper to  $D_0 \xi^2 q^d$ , while the dependence of the correlation length  $\xi$  remained the same. This inevitably requires the dependence of  $D_0 \propto \ell^{d-2}$  on the ultraviolet cutoff  $\ell^{-1}$  which violates the single-parameter scaling. In contrast, our numerics demonstrates that the single-parameter scaling at  $d = 3, 4, 5, 6$  is a very reasonable approximation.

Notwithstanding this comment, the values of  $\nu$  obtained from Eq. (5.4.11) for  $d = 3, 4, 5, 6$  using  $D_c$  and  $\alpha_c$  found directly from the single-parameter  $\beta$ -function (see Fig. 5.8), are very close to the ones following from Eq. (5.7.16), obtained numerically in Ref. [368] and also experimentally in Ref. [369] for  $d = 4$ . At the same time, the values of  $D_c$  and  $\alpha_c$  significantly differ from  $2/d$  and

$(d - 2)/d$ , respectively (see Fig. 5.9). This implies highly correlated deviations of these quantities from the above naive predictions.

We would like to stress that, in order to obtain a single-parameter curve, we employed a procedure that is completely different from the numerical approach of Refs. [101, 345, 365, 366, 370]. In our approach, we extracted the single-parameter curve with no assumption on the number and values of the irrelevant exponents and then determined the relevant exponent  $\nu$  from this single-parameter curve. This procedure is more complicated compared to that of Refs. [101, 345, 365, 366, 370] and it inevitably leads to less accurate numerical estimates of the exponents <sup>2</sup>. However, the clear advantage of this procedure is that it gives a detailed picture of the RG flow and emergence of single-parameter scaling and it is free from the choice of the number and values of the irrelevant exponents. In any case, the surprisingly high accuracy of a simple formula Eq. (5.7.16) for different dimensionalities  $d = 3, 4, 5, 6$  raises again a question of its status and the approximation (which we think is still lacking) it can be obtained from.

#### 5.7.4 A conjecture about the lower bound on $D_c$

In the absence of the upper critical dimension ( $d_{\text{up}} = \infty$ ) it seems plausible that the exponent  $\nu$  tends to  $1/2$  in the limit  $d \rightarrow \infty$ , as was suggested by a number of authors (see e.g. Ref. [345]). Then the slope  $\alpha_c$  in this limit can be found from (5.4.11) as:

$$\alpha_c = \frac{2}{D_c d}. \quad (5.7.17)$$

An immediate consequence of this is that  $\alpha_c$  is finite in the  $d \rightarrow \infty$  limit if  $D_c$  decreases with increasing the dimensionality  $d$  as  $D_c \propto 1/d$  and this slope has an infinite limit if  $D_c$  decreases faster than  $1/d$ . Unfortunately, the numerical data up to  $d = 7$  of Table 1 and Fig. 5.9 allows both asymptotic behaviors, with a crossover dimensionality that we estimate around  $d^* \sim 10$ . In this situation of the lack of theory at large  $d$  (when the non-linear sigma model is no longer justified) and the inability of numerical simulation on the lattices of dimensionality  $d \gg d^*$  we would like to propose a conjecture on the lower bound for  $D_c$  for the Anderson model on  $d$ -dimensional lattices with short-range hopping. We argue that

$$D_c \geq \frac{1}{d}. \quad (5.7.18)$$

and if the upper critical dimension  $d^{\text{up}} = \infty$  this inequality saturates only at  $d = \infty$ .

The reason for this conjecture is that by definition  $D_c = d_c/d$ , where  $d_c$  is the dimensionality of the support set of multifractal wave function embedded into a lattice of dimensionality  $d$ . Clearly, if  $d_c < 1$  the support set cannot be connected and should look like a set of points with the typical distance between them much greater than the lattice constant. For a lattice model with short-range hopping, at high dimensions  $d$  the critical disorder  $W_c \sim d \ln d$  is large. Therefore the typical transmission amplitude between such points should be exponentially small so that the points may belong to the same support set only if their on-site energies are in resonance with an exponential accuracy. This situation is extremely rare and this is exactly the point why we believe  $d_c$  must be greater than 1 if the wave function is extended and the model is short-ranged.

Certainly, this argument does not apply to systems with long-range hopping, e.g. for the Power-Law Banded random matrices [371] or the Rosenzweig-Porter models [7, 357, 358]. In those cases,  $d = 1$  and it is known that  $d_c < 1$  can be arbitrarily small.

---

<sup>2</sup>Since the procedure involves finding the maximum of the numerical  $\beta(D, L)$  in a given small interval  $[D, D + \Delta D]$ , for different  $L, W$ , we believe our procedure can lead to a *systematical overestimate* by a few percent the values of  $\alpha_c, D_c$  and hence of  $\nu$ .

If the conjecture Eq. (5.7.18) is true then Eq. (5.7.17) immediately gives:

$$\lim_{d \rightarrow \infty} \alpha_c = 2, \quad (5.7.19)$$

that is, it is (a) finite and (b) twice larger than  $\lim_{d \rightarrow \infty} \alpha_1 = 1$ . This seemingly innocuous conclusion has an important implication for the critical scaling of the Anderson model on Random Regular Graphs (RRG). If, in fact,  $\beta(D)_{\text{RRG}} = \lim_{d \rightarrow \infty} \beta(D)_d$ , then this allows us to choose scenario I formulated in Chapter 6 as the only possible, and therefore the RRG has two diverging lengths as  $W \rightarrow W_c$ : one with exponent  $\nu = 1/2$  and one with exponent  $\nu = 1$ , which dominates (although sizes larger than the available ones are needed to observe  $\nu = 1$  in the numerical data). The existence of two critical exponents was also discussed, in a different context, in Ref. [133].

## 5.8 The high-gradient operators in the non-linear $\sigma$ -model and the irrelevant exponent $y$

As is seen from Fig. 5.8, the single-parameter scaling is an approximation that corresponds to the *envelope* of RG trajectories shown by a solid red line around  $\beta = 0$ . A given RG trajectory (shown by a solid black line) approaches this envelope at a sufficiently large system size  $L$ . To describe the initial part of RG trajectories one needs to invoke an *irrelevant exponent*  $y$  introduced in Ref. [365]. Apparently, this exponent is *beyond* the single-parameter scaling as described by the formalism of the non-linear sigma model [361, 362, 372].

In order to understand the origin of the operators corresponding to the exponent  $y$  one has to *extend* the conventional  $\sigma$ -model [372, 373]. The corresponding extension was done in Ref. [352, 353, 374] by adding to the  $\sigma$ -model, in addition to the conventional ‘diffusion’ term  $t^{-1} \text{Str}[(\nabla Q)^2]$ , also the higher-order ( $n > 1$ ) terms of the gradient expansion:

$$Z_n \ell^{2(n-1)} \text{Str}[(\nabla Q)^{2n}], \quad (5.8.1)$$

where  $Q$  is the Efetov’s super-matrix [373],  $\ell$  is the electron mean free path and  $\text{Str}$  denotes the super-trace. Such terms can be rigorously derived [352, 353, 374] starting from the model of free electrons in impure metals.

The additional terms have an irrelevant exponent  $y_n^{(0)} = -2(n-1)$  in the zero-order approximation of non-interacting diffusion modes (the conventional term proportional to  $(\nabla Q)^2$  has an exponent 0 in this approximation). The interaction of diffusion modes leads to a renormalization of the coupling constant  $t$  described by one-parameter scaling, Eq. (5.7.1). However, it also gives rise [352, 353, 374] to renormalization of  $Z_n$  in Eq. (5.8.1):

$$\frac{d \ln Z_n}{du} = n(n-1) + \text{higher order in } t \sim \epsilon, \quad (5.8.2)$$

where

$$u = \ln \left( \frac{\sigma_0}{\sigma(L)} \right) = \frac{(L/\ell)^\epsilon}{1 + (L/\xi)^\epsilon}. \quad (5.8.3)$$

Here  $\epsilon = d - 2$ ,  $\xi$  is the critical length,  $\sigma_0$  is the Drude conductivity, and  $\sigma(L)$  is that with effects of localization included.

At small  $\epsilon$  one may neglect the higher-order terms in  $t \sim \epsilon$  in Eq. (5.8.2), so that:

$$Z_n = Z_n^{(0)} \left[ \frac{(L/\ell)^\epsilon}{1 + (L/\xi)^\epsilon} \right]^{n(n-1)}. \quad (5.8.4)$$

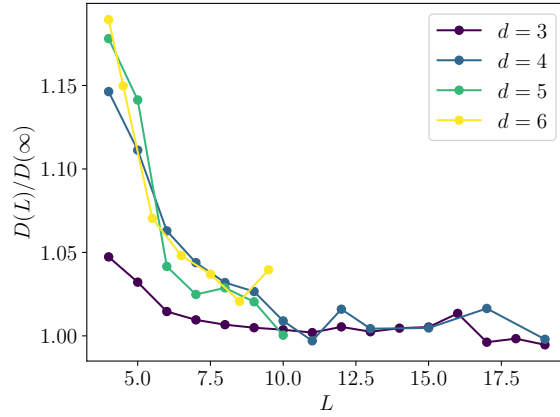


Figure 5.10: System size dependence of  $D(L)/D(L \rightarrow \infty)$  at  $W = W_c$  for different spatial dimensions. When  $d$  increases, also  $D(L = O(1))/D(L \rightarrow \infty)$  grows, that implies a longer length of the “hair” in the  $\beta$ -function. However, the saturation value is achieved approximately at the same linear size  $L = O(10)$ , as we discuss in the main text.

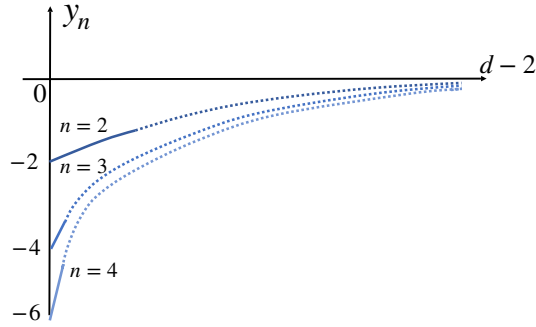


Figure 5.11: Dependence of the irrelevant exponents  $y_n$  on the spatial dimension of the system. The solid lines represent Eq. (5.8.5), while the dashed lines give a sketch of our conjecture as  $d$  increases. We conjecture that in the limit of large  $d$  all dashed lines merge and approach zero.

At criticality,  $L \ll \xi$ , the  $L$ -dependent term in the denominator of Eq. (5.8.4) can be neglected and we obtain  $Z_n \propto L^{\epsilon n(n-1)}$ . This gives a *positive* correction to  $y_n$  (see also Fig. 5.11):

$$y_n = -2(n-1) + \epsilon n(n-1) + o(\epsilon). \quad (5.8.5)$$

At  $\epsilon \ll 1$  the largest irrelevant exponent corresponds to  $n = 2$ , so that we obtain:

$$y = y_2 = -2 + 2\epsilon + o(\epsilon). \quad (5.8.6)$$

Equation (5.8.6) shows that the irrelevant exponent  $y > -2$  (which is always the case in numerics [366]) and grows with increasing the dimensionality  $\epsilon = d - 2$ . As usual in  $\epsilon$ -expansion in the localization problem, this equation is not applicable already for  $d = 3$ . However, it shows a tendency towards making the irrelevant exponent less irrelevant with increasing  $d$ . This results in the corrections to single-parameter scaling (and hence the length of the RG trajectories before merging with the single-parameter red curve, see Fig. 5.8) more significant, as  $d$  increases.

What happens at large  $d$ ? One of the possibilities is that the irrelevant exponent becomes relevant (positive) at some finite  $d = d^{\text{up}}$  and the single-parameter scaling will no longer hold for

| $d$ | $W_c$          | $D_c$             | $\alpha_c d$     | $\nu = \frac{1}{\alpha_c d D_c}$ | $\nu_{\text{num}}$                               | $\nu$ , Eq. (5.7.16) |
|-----|----------------|-------------------|------------------|----------------------------------|--|----------------------|
| 3   | $16.4 \pm 0.2$ | $0.657 \pm 0.001$ | $1.029 \pm 0.01$ | $1.48 \pm 0.02$                  | $1.57 \pm 0.004$ [370]<br>$1.52 \pm 0.06$ [368]  | $3/2$                |
| 4   | $34.3 \pm 0.2$ | $0.447 \pm 0.007$ | $2.28 \pm 0.10$  | $0.98 \pm 0.03$                  | $1.156 \pm 0.014$ [345]<br>$1.03 \pm 0.07$ [368] | 1                    |
| 5   | $56.5 \pm 0.5$ | $0.367 \pm 0.004$ | $3.25 \pm 0.13$  | $0.84 \pm 0.03$                  | $0.969 \pm 0.015$ [345]<br>$0.84 \pm 0.06$ [368] | $5/6 \approx 0.83$   |
| 6   | $83.5 \pm 0.5$ | $0.26 \pm 0.01$   | $5.1 \pm 0.5$    | $0.74 \pm 0.06$                  | $0.78 \pm 0.06$ [368]                            | $3/4$                |
| 7   | $110 \pm 2$    | $0.22 \pm 0.04$   | /                | /                                | /  | /                    |

Table 5.1: Numerical values for critical properties in  $d = 3, 4, 5, 6$ , compared with previous results in the literature. The values of  $W_c$  we find, corresponding to the red lines in Fig. 5.7, are compatible with the results in the literature [337, 370]. The values of  $D_c$  and critical exponents are found by analyzing the numerical data around  $\beta = 0$ . The errors displayed are the ones coming from a quadratic fit of the envelope of the  $\beta$ -function near the critical point (red curve in the plots). We expect the actual errors to be larger than the ones reported.

$d > d^{\text{up}}$ , even as an approximation. We, however, think that  $d^{\text{up}} = \infty$  and the breakdown of the single-parameter scaling happens only for localization problems on expander graphs like RRG, as we will discuss in the next Chapter.

We would like to emphasize that the scenario of breakdown of single parameter scaling at  $d > d^{\text{up}}$  described above is different from the one suggested recently by Zirnbauer [135, 138]. The true theory of the NEE phase with singular-continuous spectrum should, perhaps, be a combination of both, in which the higher-gradient terms should play an important role.

## 5.9 Approaching the critical point

One can see from our numerics (Figs. 5.2, 5.8) that  $D(L)$  has a minimum  $D_A$  which corresponds to  $\beta(D_A) = 0$  (see the sketch on the upper panel of Fig. 5.3). It is natural to ask how the minimum of  $D(L)$  is approached in different dimensions. As it happens on the Random Regular Graph [5], the  $\beta$ -function crosses the line  $\beta = 0$  with infinite derivative, therefore the simplest approximation for the  $\beta(D)$  is

$$\beta(D) \simeq -\sqrt{D - D_A}, \quad (5.9.1)$$

where  $\beta(D_A) = 0$ . By straightforwardly integrating the differential equation (5.4.1) it is easy to get for the volume  $V_A = L_A^d$  that corresponds to the minimum  $D_A$ :

$$V_A = V_0 \exp \left\{ \frac{2 \arccos \sqrt{D_A/D_0}}{\sqrt{D_A}} \right\} \quad (5.9.2)$$

In the above equation,  $V_0$  and  $D_0$  represent the initial condition and we can take  $V_0 < V_A$  to be independent of  $d$ , while in general  $D_0 = D_0(d) > D_A$ . We now move to the regime  $W \lesssim W_c$  and let us assume  $d$  is large enough so that  $D_A \gtrsim D_c \sim 1/d \ll 1$ . In this regime, we can expand Eq. (5.9.2) in  $D_A/D_0$  and we get

$$V_A = V_0 \exp \left\{ \left( \frac{\pi}{\sqrt{D_A}} - \frac{2}{\sqrt{D_0}} \right) \right\} = \tilde{V}_0 \exp \left\{ \left( \frac{\pi}{\sqrt{D_A}} \right) \right\} \quad (5.9.3)$$

$$\simeq \tilde{V}_0 \exp \left\{ (c\sqrt{d}) \right\}, \quad (5.9.4)$$

where  $c = O(1)$  is a constant. Note that the system volume where the minimum is reached is finite in the limit  $D_A \rightarrow D_c$ . Thus in any finite dimension  $d$  the length  $L_A = V_A^{1/d}$  that corresponds to the volume  $V_A$  is not critical, in (at least qualitative) agreement with the data in Fig. 5.10. Moreover, it is equal to the volume  $\tilde{V}_0 = O(1)$  in the limit  $d \rightarrow \infty$ . This is in contrast to the case of RRG where the corresponding length is critical  $L_A \sim (W_c - W)^{-1/2}$ . This is the consequence of the difference in the dependence of the volume on the length on a  $d$ -dimensional lattice and on a tree/RRG with finite branching number  $K_0$ . Indeed, if the relation between the volume  $V_A$  and the length  $L_A$  were like on a tree/RRG then we would obtain from Eq. (5.9.4) a divergent length  $L_A = \ln(V_A)/\ln K_0 \sim \sqrt{d}$  in the double limit  $D_A \rightarrow D_c$  and  $d \rightarrow \infty$ .

In any case, the result that the length  $L_A \sim O(1)$  in any finite dimensions implies that the critical length is associated with the single-parameter part of the trajectory and is given by Eq. (5.4.10) with  $D_0 \approx D_A$ . In contrast, on the RRG there are two critical lengths, provided that the slope  $\alpha_c$  is finite: one of them is  $L_A = (W_c - W)^{-1/2}$  and the other, the dominant one, is determined by the single-parameter part of the  $\beta$ -function. In this case the exponent  $\nu = 1$  independently of the (finite) slope  $\alpha_c$ .

This analysis tells us that the localization transition on the expander graphs like RRG is not simply that in the limit  $d \rightarrow \infty$  on a  $d$ -dimensional lattice. A qualitative jump happens in the critical behavior because the single-parameter character of the transition in  $d$ -dimensions is replaced by a two-parameter one on expander graphs (see Ref. [5] and next Chapter).

## 5.10 Increasing space dimensionality and the Random Regular Graph

In the previous sections, we have described in detail the behavior of the  $\beta$ -function for the Anderson model in finite dimensions, comparing our theoretical arguments with the numerical results from exact diagonalization.

The goal of this section is to summarize our knowledge and conjectures concerning the scaling behavior on a  $d$ -dimensional lattice in the limit  $d \rightarrow \infty$ . More details on the Anderson model on RRGs will be presented in Chapter 6.

- Let us first focus on the region  $D \rightarrow 1$ . As we already discussed, in  $d$  dimensions the  $\beta$ -function in this limit has slope  $\alpha_1 = (d - 2)/d$  (see (5.7.12)). For  $d \rightarrow \infty$  this readily gives  $\alpha_1 = 1$ , which is the prediction of RMT and is found in the Anderson model on RRG.
- We have seen numerically that the critical value of the fractal dimension  $D_c \leq 2/d$ , and we have argued that there are reasons to believe that  $D_c \geq 1/d$  for any  $d$ . Independently from the lower bound,  $D_c \rightarrow 0$  as  $d \rightarrow \infty$ , in agreement with the results on expander graphs [5, 140].
- As shown in Fig. 5.2 and Fig. 5.10 and schematically sketched in Fig. 5.3, the contribution of the irrelevant operators at the critical point becomes increasingly important as  $d$  grows (as evident from the length of the “hairs” in  $\beta(D)$ ). This implies that the irrelevant exponents become less irrelevant with increasing  $d$  until, eventually, a two-parameter scaling emerges for expander graphs like RRG.
- The critical behavior on a  $d$ -dimensional lattice, and even in the limit  $d \rightarrow \infty$ , is qualitatively different from that on an expanded graph like RRG. On a lattice of any dimension, it takes a finite length (sample size) to reach the minimum of  $D(L)$  when  $\beta(D) = 0$ , even as we

approach the critical disorder. In contrast, this length diverges at  $W \rightarrow W_c$  as  $(W_c - W)^{-1/2}$  on RRG.

- The sample size  $L_c$  when the true metallic behavior  $D \approx 1$  is reached for  $W < W_c$  is critically divergent  $L_c = (W_c - W)^{-\nu}$  in both cases. It is determined by the single-parameter part of the  $\beta$ -function. However, for the case of a  $d$ -dimensional lattice the exponent  $\nu = 1/(dD_c\alpha_c)$  depends both on the critical value of  $D_c$  and on the slope  $\alpha_c$  of the  $\beta$ -function and in the limit  $d \rightarrow \infty$  reaches the mean field value  $\nu = 1/2$ . In contrast, on RRG (where  $D_c = 0$ ),  $\nu = 1$  independently of the slope  $\alpha_c$ , provided that the slope is finite. This crucial difference is due to the qualitative change in the scaling, which is two-parameter with  $D_c = 0$  for RRG [5] and single-parameter with  $D_c > 0$  and corrections due to irrelevant operators for  $d$ -dimensional lattice.

## 5.11 Conclusions

In this Chapter, we presented a renormalization group-based framework for addressing the Anderson localization transition in finite dimension. We discussed how to use the ‘modern’ observables to construct the full  $\beta$ -function of the model in any spatial dimension  $d$ . For practical purposes, we chose the finite size fractal dimension  $D(N)$  as such an observable, albeit other (eigenfunction or spectral) observables can do the same job as long as one-parameter scaling holds. We showed that some basic properties can be derived analytically by simple arguments and, when this was not possible, we presented numerical results from which we derived critical properties, in agreement with previous results in the literature. More importantly, we showed how our technique connects the perturbative results in  $d = 2 + \epsilon$  dimensions up to  $d \rightarrow \infty$ , recovering the known results on RRGs, that will be presented in Chapter 6.

We believe that the method discussed here, and that will be applied to expander graphs in the next Chapter, is a new useful tool to understand the scaling properties of *ergodicity breaking* in disordered quantum systems, and especially to study the existence and properties of such purported transitions. This is of particular importance for interacting systems where the existence and the properties of non-ergodic phases are under long-standing debate.

## Chapter 6

# Renormalization group analysis of Anderson localization in infinite dimensions and random graphs

*This Chapter extends the results of the previous Chapter to the Anderson model on random regular graphs, corresponding to the limit of infinite dimensions. We show how the RG flow, which was one-parameter scaling in finite dimensions, is now two-parameter scaling at the critical point, because one of the irrelevant operators becomes marginal. This leads to a Berezinski-Kosterlitz-Thouless-like transition, with a line of fixed points parametrized by the localization length of the insulating phase. The results presented in this Chapter are based on the publication [5].*

WITH this Chapter, we aim to further explore the RG analysis of the Anderson model by directly delving into the infinite-dimensional limit, and we do so by tackling the Anderson localization problem on Random Regular Graphs. The geometry of Random Regular Graphs (RRGs) and their infinite counterparts, Cayley trees/Bethe lattices, being expander graphs [375] of formally infinite dimension, behaves peculiarly under the block transformation of the renormalization group. Unlike a  $d$ -dimensional cube [337], which is always connected to  $2d$  other cubes, irrespective of their size, when we divide an RRG of connectivity  $K_0$  in blocks of linear dimension  $L$  (much smaller than its diameter), such blocks will have connectivity  $K_0^L$  (see Fig.6.1). Connectivity is an important parameter in the Anderson model since, to a first approximation, localization is achieved when the disorder strength  $W$  measured in units of hopping rate is much larger than  $K$ . Therefore, under block decimation or composition (to follow Ref. [100] and subsequent works [376]) one needs to keep track of the ever-growing connectivity.

This *additional parameter* in the RG equations on expander graphs makes a big difference in terms of phenomenology, opening the door to something different from a simple  $d \rightarrow \infty$  limit of the equations in [100], and more on the line of the Berezinski-Kosterlitz-Thouless transition [377–379]. Similar phenomenological RG equations have been conjectured to underlie the MBL transition [380–383], but this time the connection came from an analogy with the *strong disorder* Ma-Dasgupta-Hu-Fisher RG equations [384–387]. That the “gang of four” RG equations [100], when applied to an RRG, should be modified to become more similar to that of a many-body problem is not surprising, as Cayley trees/Bethe lattices are proxies of quantum dots [139, 388] and spin chains [103, 110, 127, 129].

In this Chapter we show how, by considering the renormalization group equations for the number of resonances, it is possible to interpret in a novel way the finite-size scaling of eigenstate observables like their fractal dimension, and spectral indicators, like the  $r$ -parameter of Oganesyan and Huse [104]. The RG  $\beta$ -function for the number of resonances can not be completely fixed by theoretical arguments, and thus we rely on the state-of-the-art numerical results, presented in Ref. [140], to extract the missing information we need. We find, surprisingly, that the two-parameter scaling, present at small system sizes, reduces to a one-parameter scaling for sufficiently large sizes for  $W < W_c$ . This can be taken into account by splitting the  $\beta$ -function of any observable in two terms. One of them,  $\beta_0$ , does not contain the system size (or the connectivity  $K$ ) explicitly, and it governs the one-parameter scaling at large system sizes. The remainder, called  $\beta_1$ , will instead depend explicitly on  $K$ , and it does describe the two-parameter regime that becomes dominant close to  $W_c$  (see also [135, 138]).

A detailed analysis of the numerical results in Ref. [140] allows us to accurately describe the  $\beta$ -function for the fractal dimension  $D \gtrsim 0.3$ , and in particular near  $D = 1$ , while the behavior close to  $D = 0$  (*i.e.* the critical region) is not accessible by the available numerics. We, therefore, present some possible scenarios for the approach of the  $\beta$ -function to  $D = 0$  (coming from the delocalized region), explaining the consequences of each scenario for the critical exponents of the transition.

## 6.1 Renormalization Group Equations

We consider the Anderson model on a RRG of connectivity  $K_0$  (*i.e.* fixed vertex degree  $\mathcal{D} = K_0 + 1$ ), defined by the Hamiltonian

$$H = - \sum_{\langle i,j \rangle} (|i\rangle \langle j| + |j\rangle \langle i|) + \sum_i \epsilon_i |i\rangle \langle i|, \quad (6.1.1)$$

where  $\epsilon_i$  are independent and identically distributed random variables sampled according to the box distribution  $g(\epsilon) = \theta(|\epsilon| - W/2)/W$ . Since in an RRG each vertex has a fixed connectivity, it is locally a Cayley tree, while on large scales loops will become important to ensure the regularity of the graph. If  $\mathcal{N}$  is the number of vertices of the graph, it is possible to introduce a length scale  $L = \log_{K_0} \mathcal{N}$ , representing the diameter of the graph, *i.e.* the maximal length of the shortest paths connecting two nodes.

Starting from a tree with connectivity  $K_0$  (see Fig. 6.1, where  $K_0 = 2$ ) and proceeding in the spirit of the Kadanoff decimation procedure, we group subtrees of increasing depth creating new “effective” nodes. At step  $L$ , due to the Cayley tree geometry, the new node will have a larger coordination number  $\mathcal{D} = K(L) + 1$ , which coincides with the number of nodes at distance  $L$  in the original bare graph. This is the main difference with the situation in finite dimensions  $d$ , where the geometrical datum of the connectivity is independent of the renormalization scale  $L$ . According to this blocking procedure, the equation for the connectivity  $K(L)$  at step  $L$  is simply

$$\frac{dK}{d \ln L} = K \ln K, \quad (6.1.2)$$

This equation has the desired solution  $K(L) = K_0^L$  which reflects the geometry of a local tree. This equation represents the geometric datum of the RRG at scale  $L$  and we consider it now decoupled from the physical datum describing the structure of the eigenfunctions, the spectrum, or transport properties (like the conductance  $g$  of Ref. [100]) at the same scale. We will content ourselves with this approach, although it is possible that, in the future, on the way towards an analytic solution,

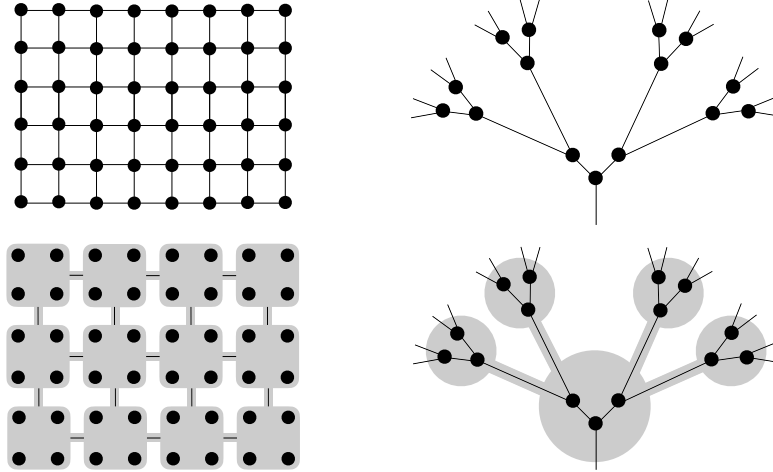


Figure 6.1: Grouping of sites under renormalization group. (*Left*) In finite dimensions, the connectivity of the blocks does not change, under RG block transformation. (*Right*) The RG transformation on a tree instead changes the connectivity of a block. One goes from  $K_0$  (in the drawing  $K_0 = 2$ ) to  $K_0^L$  when sites at distance  $L$  are grouped in the same effective node.

one might need to write directly coupled differential equations for effective geometric and physical quantities. Our simplification turns out to be sufficient in the metallic phase which we are mostly concerned with, so we will use it in the rest of the Chapter.

As a physically meaningful second parameter, Ref. [100] would use the dimensionless conductance  $g = L^{d-2}\sigma(\hbar/e^2)$ , where  $\sigma$  is the sample conductivity. We, however, will consider eigenstates and eigenvalue (spectral) properties, for two reasons. On one hand, they are more easily accessed in modern numerical calculations, on the other they represent intrinsic properties of the unitary dynamics of our system, while the conductance is affected by the form of the coupling to the leads *etc.*. Eigenstate and spectral properties must be qualitatively (and quantitatively) determined by the expected number of resonant sites at a fixed energy  $E$  (for example let us take the center of the band  $E = 0$ ) within a distance  $L$ . We can formally define the quantity  $\psi$  as follows. By denoting a normalized wavefunction at site  $i$  as  $\varphi(i)$ , following Refs. [350, 351], we define the *support set*  $S_\varepsilon$  satisfying the relation  $\sum_{i \in S_\varepsilon} |\varphi(i)|^2 = 1 - \varepsilon$ , where the  $\varphi$ 's entering the sum are the largest ones in modulus. The dimension of the set  $S_\varepsilon$  is given by  $K_S(\varepsilon) = \sum_{i \in S_\varepsilon} 1$  [7].  $S_\varepsilon$  does not contain explicitly a length (except the system size), so we need to better describe its structure, by introducing the number of elements in  $S_\varepsilon$  at a distance smaller than  $L$  from the reference site, for some fixed  $\varepsilon \ll 1$ . This is our proxy for the number of resonances  $1 + \psi(L)$ . Notice that 1 is added because there is at least one resonant site, even in the localized region, as the site is resonant with itself. It can be shown [350] that  $K_S(\varepsilon)$ , and, hence,  $\psi$  in the *delocalized phase* (generally multifractal), scales as  $K_S \sim \psi \sim K^D = K_0^{LD} \gg 1$  where

$$D = \frac{\partial \ln(1 + \psi)}{\partial \ln K} \approx \frac{\partial \ln(\psi)}{\partial \ln K}. \quad (6.1.3)$$

The dimension  $D$  is, in turn, easily determined numerically by the eigenfunctions Shannon entropy [350]:

$$D = D_1 = \frac{dS}{d \ln K}, \quad S = S_1 = - \left\langle \sum_{r < L} \varphi^2(r) \ln \varphi^2(r) \right\rangle \quad (6.1.4)$$

Deeply in the *localized phase* the expected number of resonances within a distance  $L$  decays exponentially  $\psi \sim K_0^{-L/\xi} \sim K^{-\alpha}$  which gives  $D = \frac{\partial \ln(1+\psi)}{\partial \ln K} \simeq \frac{\partial \psi}{\partial \ln K} \sim K^{-\alpha}$  as well.

We note that in the limit  $K \rightarrow \infty$ ,  $D$  is  $L$ -independent and equal to zero in the localized phase, equal to 1 in the ergodic phase, and is a number  $0 < D < 1$  in the multifractal phase. We now write an equation for the variable  $\psi(L)$ . The function  $\psi(L)$  has to decrease exponentially in the localized region, namely when  $\psi \ll 1$ , and, in the delocalized region to be at most  $K$ . Our RG equations must have two fixed points; one at  $\psi = 0$  (localized phase) and another one at  $\psi = K - 1 \approx K$  (delocalized phase). We write therefore our second equation as  $\frac{d\psi}{d \ln L} = \psi \ln \psi \gamma(K, \psi)$ , where the function  $\gamma(K, \psi)$  should obey the following property in the localized phase:

$$\gamma(K, \psi) \rightarrow 1 \quad \text{for all } \psi \ll 1. \quad (6.1.5)$$

This property ensures that in the localized region one can have arbitrary localization length:  $\psi = K_0^{-L/\xi}$ . In the delocalized phase  $\gamma(K, \psi \gg 1)$  should obey the property  $\gamma(K, K) = 1$  in order to ensure the stable fixed point  $\psi = K$ .

Eliminating  $L$  in favour of  $K$  with the help of Eq.(6.1.2), we can write a single equation:

$$\frac{d \ln \psi}{d \ln K} = \frac{\ln \psi}{\ln K} \gamma(K, \psi). \quad (6.1.6)$$

In order to make further progress we need a form of the function  $\gamma(K, \psi)$ . As  $\psi$  is not readily obtained from the numerics we instead use  $D(L)$  defined in Eqs. (6.1.3, 6.1.4) as an implicit function of  $K, \psi$ . The whole idea of this Chapter is to follow the RG flow of  $D(L)$  using the correspondence between RG flow and finite-size flow, and find the unknown RG functions from the numerics. We will show that even in the ergodic phase  $D(L)$  is a non-trivial function that plays the same role as the dimensional conductance  $g(L)$  does in the original ‘gang-of-four’ work [100].

The RG equation for this quantity defines the  $\beta_D$  function

$$\frac{d \ln D}{d \ln K} = \beta_D(D, K), \quad (6.1.7)$$

where  $\beta_D(D, K) = (\gamma(K, \psi) - 1)/\ln K$ . The function  $\beta_D(D, K)$ , unlike  $\gamma(K, \psi)$ , can be easily extracted from numerical data, and we make it now the main object of our study. First of all, notice that deep in the localized phase the scale-invariant law  $D \sim K^{-\alpha}$  means that the localized phase is a line of fixed points at  $D = 0$  where  $\beta = -\alpha$ . The critical point  $W = W_c$  corresponds to  $\alpha = 0$ . This is the first of many similarities we will find with the Kosterlitz-Thouless phase transition with  $\sqrt{D}$  being analogous to fugacity.

Moving to  $W < W_c$  we see from the numerical evidence (see Fig. 6.2) that the curves tend to a single curve  $\beta_0(D)$  and this allows us to make the central observation of the analysis presented in this Chapter, namely that the function  $\beta_D$  can be divided into two, conceptually different pieces

$$\beta_D(D, K) = \beta_0(D) + \beta_1(D, K), \quad (6.1.8)$$

where

$$\beta_0(D) = \max_K \beta_D(D, K). \quad (6.1.9)$$

By virtue of this definition  $\beta_1(D, K)$  is negative. In contrast,  $\beta_0(D)$  does not depend on  $K$  and *it is positive*  $\beta_0(D) \geq 0$ , vanishing for  $D = 0$  and  $D = 1$ . It can be extracted from the numerically obtained data (see Fig. 6.2) by maximizing  $\beta_D(D, K)$  at fixed  $D$ , *i.e.* along vertical lines in Fig. 6.2. Let us stress that the different values of  $\beta_D(D, K)$  at different  $K$  correspond to different orbits and therefore to different  $W$  (there is a one-to-one correspondence between  $(D, K)$  and  $(D, W)$ ).

A similar analysis on the (rescaled)  $r$ -parameter is shown in the Appendix. In Fig. C.3 of the Appendix we also show that the function  $\beta_0(D)$  does not depend on the initial connectivity of the

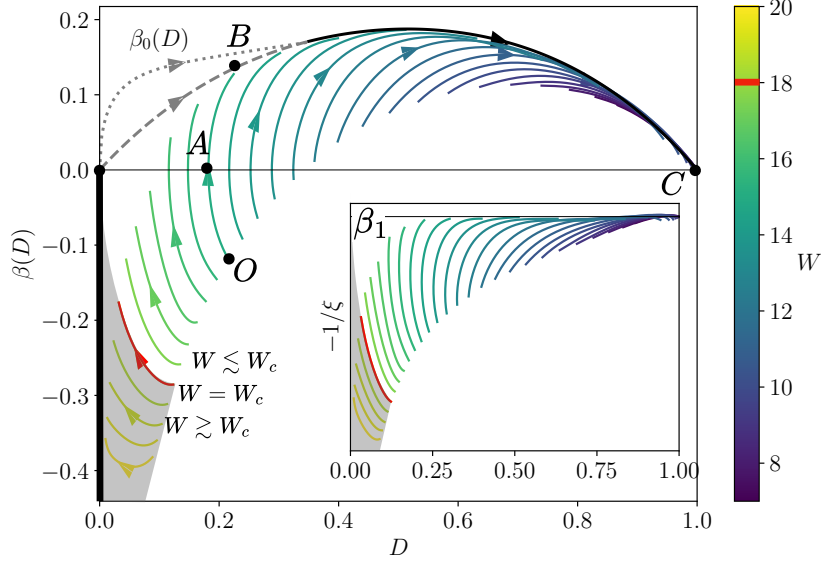


Figure 6.2: (*Main*) Numerical data for  $\beta_D(D, K)$  (color corresponds to disorder, arrows indicate increasing system size  $K$ ) and two possible behaviors of the function  $\beta_0(D)$  (dashed and dotted lines). For values of  $D \leq 0.3$ , the curves are gray to emphasize that the shape is dependent on the fitting function used, *i.e.* either  $\beta_0 \propto D$  (dashed) or  $\beta_0 \propto \sqrt{D}$  (dotted). (*Inset*) The function  $\beta_1(D, K)$ . The same numerical results for the  $r$  spectral parameter can be found in the Appendix. The existence of a “single-parameter arc”  $\beta_0(D) > 0$  implies that the non-ergodic extended phase does not exist in the thermodynamic limit [134, 338] but the multifractal behavior with  $0 < D < 1$  is observed at finite sizes in the vicinity of the localization transition [127]. The critical exponent  $\nu = 1/2$  [99, 389, 390] corresponds to evolution in the vicinity of point A in both scenarios. In scenario I we predict this exponent to be sub-leading at very large system sizes where the dominant behavior in the delocalized phase corresponds to  $\nu = 1$  [137, 351]

RRG, and thus *it defines unambiguously the universality class of the Anderson model in infinite dimensions.*

The emergence of a one-parameter scaling  $\beta_0$  occurs because of large loops in the RRG: indeed if one considers a finite Cayley tree, the fractal dimension would saturate to a finite value between 0 and 1 (in the RG language, there is a line of fixed points  $D \in [0, 1]$ ) [134]. In the RRG, the presence of loops favors the flow towards the ergodic fixed point  $D = 1$  along the “single-parameter arc”  $\beta_0(D)$  which describes the true asymptotic limit of the RG flow and the reaching of the emergent one-parameter scaling regime:

$$\frac{d \ln D}{d \ln K} = \beta_0(D). \quad (6.1.10)$$

The function  $\beta_1$  describes the evolution of the system at the beginning of the flow, before large loops are encountered, and both parameters,  $D$  and  $K$ , are necessary to describe the scaling in the critical region and in the localized regime.

The function  $\beta_0(D)$  has two zeros, at the fixed points  $D = 0, 1$ . A fit of the numerical data with a simple polynomial (see Appendix for details) which vanishes in 0 and 1, we get  $\beta_0(D) = 1 - D + O((1 - D)^2)$  for  $D \rightarrow 1$ . The derivative at  $D = 1$  is 1 within the statistical error (see Fig. 6.2, solid black curve). In fact, in the one-parameter scaling theory of Ref. [100],  $D$  is an analytic function of  $g$ . One can prove close to  $d = 2$ , that  $D = 1 - 1/g + O(\epsilon) + O(g^{-2})$

[6], but we believe this expansion to be valid for all  $d$  and even in the limit  $d \rightarrow \infty$ .<sup>1</sup> So, since  $D \simeq 1 - 1/g + \dots$  for  $g \rightarrow \infty$ , and  $g \sim L^{d-2}$ , in  $d$  dimensions this slope should be  $(d-2)/d$  (see previous Chapter). In the limit  $d \rightarrow \infty$  we recover the observed slope 1.

The situation near  $D \rightarrow 0$ , is more complicated. Our numerical data allow a reliable extraction of  $\beta_0$  only down to  $D \simeq 0.3$  so we must guess the form of  $\beta_0$  down to  $D = 0$ , where it must vanish. The two simplest situations are either a simple zero  $\beta_0(D) \propto D$  or  $\beta_0 \sim D^{1/2}$ . We will see later that these two possibilities imply two different physical pictures.

Other functional forms of  $\beta_0$  close to  $D = 0$  are also possible within our theory, but the main point of this Chapter stands: there exists a function  $\beta_0(D)$ , which describes the one parameter scaling flow of  $D$  away from the critical point  $D = 0$  and towards the ergodic critical point  $D = 1$ , thus excluding the multifractal behavior in the thermodynamic limit. This function must be calculable from first principles, but not necessarily from a Cayley tree calculation. In fact, on the Cayley tree the fractal dimension  $D_1$  can take any value in  $[0, 1]$  [134, 391] which is possible if  $\beta_0(D) = 0$  and the flow is generated by  $\beta_1(D, K)$ . We believe the function  $\beta_0(D)$  has not appeared in previous literature on the Anderson model on the RRG, although its analog  $\beta(g)$ , with  $g$  being dimensionless conductance, is central in the discussion of finite dimensional systems [100].

The one-parameter scaling motion is the solution of Eq. (6.1.10), obtained by integrating the differential equation by separation of variables. The result for the two different *ansatzes* is shown in Fig. C.2 of the Appendix.

Notice that as long as the evolution is on the one-parameter segment and Eq. (6.1.10) holds one obtains

$$\ln(K/K_{in}) = \int_{D_{in}}^D \frac{dD'}{D' \beta_0(D')} \equiv \ln F(D) - \ln F(D_{in}), \quad (6.1.11)$$

where  $F$  results from the integration and  $\ln K_{in}$  is a length scale for a system to evolve during a two-parameter regime from the initial condition at small system size through the minimum of  $D$  and subsequently during a single-parameter regime to  $D_{in} \lesssim 1$ . Now, inverting the function  $F(D)$ , we obtain:

$$D(K) = F^{-1}(K/K_c), \quad (6.1.12)$$

where  $K_c = K_{in}/F(D_{in})$  is a critical volume. Eq. (6.1.12) corresponds to a *volumic* scaling [132], which therefore holds in the delocalized phase as soon as evolution proceeds along the single-parameter arc.

The function  $\beta_1(D, K)$  is dominant, and it has a simple form near the critical line  $W_c \simeq 18.17$  [107, 390], but it becomes negligible for sufficiently large system sizes far from the critical point (inset of Fig. 6.2) yielding to the one parameter regime.

## 6.2 The critical region

In the delocalized region, the critical behavior which describes the divergence of  $K_B$  when  $W \rightarrow W_c$ , is obtained by looking at the “time”  $\ln(K/K(L = L_0))$  it takes one to reach the fixed point  $D = 1 - \epsilon$  with any given accuracy  $\epsilon \ll 1$ . The approach to the fixed point  $D = 1$  happens in two steps: first, the motion is governed by  $\beta_1$ , since  $|\beta_1| \gg \beta_0$ . Then, after the orbit approaches the asymptotic curve  $\beta_0(D)$  at some scale  $K \sim K_B$ , the motion is described by Eq. (6.1.10). Referring to the main panel of Fig. 6.2, we have two times to sum: the first one is the time necessary to go from the initial condition  $K_0, D(K_0)$  (or equivalently  $K_0, W$ ) until the one parameter curve  $\beta_0(D)$ , corresponding to the path  $OA + AB$  in the figure. Then one moves along the  $\beta_0$  curve till reaching the delocalized fixed point  $D = 1$ , corresponding to the path  $BC$  in the figure. The times along both  $OA$  and

<sup>1</sup>The vanishing of the  $1/g$  term can possibly occur for a different symmetry class of the Hamiltonian.

$AB$  diverge algebraically when  $W \rightarrow W_c$  with the same exponent  $\nu = 1/2$  independently of the behavior of  $\beta_0(D)$  near the origin, but the corresponding exponents for motion along  $\beta_0(D)$  in the vicinity of the point  $B$  are different for different choices of the function  $\beta_0(D)$  at  $D \ll 1$ .

Along the branch  $OA$ , when  $W \rightarrow W_c$  from the delocalized region, we must expect according to Ref. [136, 338]  $\beta_D(D, K) = 0$  for some value  $D_A$  which corresponds to the minimum in the dependence  $D(L)$  at a fixed  $W$ . As can be seen in the right panel of Fig. C.5 in the Appendix,  $D_A$  as a function of  $W$  is almost linear throughout the entire range of  $W$  where the minimum is observed. In fact, a simple linear extrapolation of the fit gives  $W_c = 18.0$ , a good estimate of the Anderson transition point. More specifically, the fit for  $W \rightarrow W_c$  reads

$$D_A = \eta \frac{W_c - W}{W_c}, \quad \text{with } \eta = 1.1 \pm 0.1, \quad (6.2.1)$$

a particularly simple result, which seems to hold *mutatis mutandis* for higher connectivities as well.

The system spends a large amount of RG time near the minimum  $D_A$ , diverging when  $D_A \rightarrow 0$ . In order to enter the truly ergodic, one-parameter region, one needs to have system sizes  $K \gg K_A$ . After that initial slow-down, the fractal dimension starts moving towards its final value  $D = 1$ .

In order to give a quantitative dependence of  $K_A$  on  $D_A$  we need a model of the function  $\beta_1(D, K)$ . The clue to finding this model is to remember that, at  $D = 0$ ,  $\beta$  defines the localization length. In fact,  $D \propto K^{\beta(D=0)} = K_0^{-L/\xi}$ . So,  $\beta = -1/\xi$ , and it must approach a constant at  $K \rightarrow \infty$ . Thus  $d\beta/d\ln K \rightarrow 0$  in this limit. However, in this very limit also  $D \rightarrow 0$  (see also Fig. 6.2). Therefore we come to a conclusion that  $d\beta/d\ln K = \phi(D)$ , where  $\phi(D)$  must vanish at  $D = 0$ . In principle, any function  $\phi(D)$  like  $D^\alpha$  ( $\alpha > 0$ ) may do the job. However, it is the simplest choice  $\phi(D) = cD$  with  $c \approx 1/2$  that corresponds to the numerics (see Fig. C.7 in Appendix).

This leads to the two equations:

$$\frac{d \ln D}{d \ln K} = \beta, \quad (6.2.2)$$

$$\frac{d\beta}{d \ln K} = cD, \quad (6.2.3)$$

which are solved implicitly by

$$\frac{1}{2}\beta^2(D, K) = c(D - D_A). \quad (6.2.4)$$

The time to pass the region around  $D = D_A$  (from the region  $D \gg D_A$ ) can be found from the solution of the equation:

$$\frac{d \ln D}{d \ln K} = -\sqrt{D - D_A}, \quad (6.2.5)$$

which is

$$D(\ln K) = \frac{D_A}{\cos^2\left(\frac{1}{2}\sqrt{D_A} \ln(K_A/K)\right)}, \quad (6.2.6)$$

Notice that the presence of the square root guarantees that the integral  $\int dD/(D\beta(D))$  is convergent at  $D = D_A$ , and therefore  $D_A$  is *not a fixed point* although the RG time spent in its vicinity diverges when  $D_A \rightarrow 0$ . In fact,  $D = D_A$  is a turning point where the function  $D(\ln K)$  reaches the minimum. Thus the solution Eq. (6.2.6) can be extended from  $K < K_A$  to  $K > K_A$ , where  $\beta > 0$ .

Now we can compute the RG time  $\ln(K_A/K(L = L_O))$  to go from  $O$  to  $A$ , where  $D_O = D(K(L = L_O)) \sim O(1)$  while  $D_A \rightarrow 0$ . This means that the argument of  $\cos^2$  should be close to

$\pi/2$  in order to compensate for the smallness of the numerator. We find, therefore, from Eq. (6.2.6):  $\ln(K_A/K(L = L_O)) = \pi D_A^{-1/2} \sim \pi(1 - W/W_c)^{-1/2}$ , which gives

$$K_A \sim e^{\frac{\pi}{\sqrt{1-W/W_c}}}. \quad (6.2.7)$$

This divergent volume corresponds to a critical exponent  $\nu = 1/2$ . The RG time to pass from  $A$  to  $B$  has the same type of divergence.

Notice that Eq. (6.2.6) can be written also in terms of  $L = \ln K$  and  $x = \sqrt{D_A} L = \sqrt{1 - W/W_c} L$ , for  $D_A \rightarrow 0$  as

$$D(L) = D_c(L) \frac{(\pi x/2)^2}{\sin^2(\frac{\pi x}{2})} \quad (0 < x < 1), \quad (6.2.8)$$

where  $D_c(L)$  is the fractal dimension on the critical line:

$$D_c(L) = \frac{1}{(\ln K)^2}. \quad (6.2.9)$$

Eq. (6.2.8) has a canonical form of the *linear* (i.e.  $L$  as opposed to the volumic  $K$  [132]) scaling associated to the critical region. Summarizing our discussion on the type of finite-size scaling, one can claim that the volumic scaling, Eq. (6.1.12), corresponds to the single-parameter scaling governed by  $\beta_0(D)$  in the extended phase, while the linear scaling is a signature of an essentially two-parameter RG in the localized and the near-critical extended regime.

The critical dependence of  $D$  on  $K$  in Eq. (6.2.9) is a universal law: it was observed for the first time in Ref. [140] for several ensembles of expander graphs of constant or even random connectivity, and it can be seen in Fig. C.6 of the Appendix. Let us mention that, in the context of RG analysis with scaling variable  $K$ , the behavior on the critical line corresponds to a *marginally irrelevant variable* since the inverse logarithmic dependence on  $K$  corresponds to a critical exponent  $y = 0^-$ .

If these were the only divergent timescales in the motion from the point  $O$  to the final region close to  $D = 1$  the critical exponent would be  $\nu = 1/2$  [99, 389]. However, we now encounter two possibilities depending on the behavior of the function  $\beta_0(D)$  close to  $D = 0$ , which we present here (see also Fig. 6.3).

1) *First scenario*:  $\beta_0(D) \propto D$ . In this case, the motion from  $A$  to  $B$  (see Fig. 6.2) intercepts  $\beta_0$  at  $D \sim D_A$ . The motion from  $B$  to any  $D = O(1)$  takes time  $\sim D_A^{-1} \sim (1 - W/W_c)^{-1}$  in view of Eq. (6.1.10). Notice that in this scenario there are two critical lengths  $L_1$  and  $L_2$ : one ( $L_1$ ) with the exponent  $1/2$  for reaching the single-parameter scaling and the other one ( $L_2$ ) with the exponent  $1$ , such that for  $L_1 < L < L_2$  the system behaves as approximately multifractal one with  $D_1 \approx D_A$ . This behavior is reminiscent of the one predicted for the Rosenzweig-Porter random matrix ensemble associated with RRG [392].

Two critical lengths in the localization problem on RRG with the exponents  $1/2$  and  $1$  were reported recently in Ref. [133]. However, this Chapter is concerned with the localized phase on RRG, rather than the extended phase that we study.

2) *Second scenario*:  $\beta_0(D) \propto D^{1/2}$ . In this scenario,  $\beta_0$  is the analytic continuation of the critical  $\beta_1(D, K)$ . No new length is introduced and therefore  $\nu = 1/2$ , which is what one obtains by solving for the fixed point of iterative, mean field equations in Refs. [99, 129, 338, 389].

We notice that the finite-size scaling exponent  $\nu$  is determined by the behavior of  $\beta_0(D)$  near the fixed point  $D_c = 0$ . This behavior is very sensitive to boundary conditions and for example it changes drastically between a finite Cayley tree and an RRG. In fact, it is known that in the finite Cayley tree the whole delocalized phase is multifractal [134, 391]. In our language this means  $\beta_0 = 0$  and the two-parameter scaling dominates the whole delocalized region. We believe then that the mean-field approach is too rough to distinguish between the two scenarios that we propose.

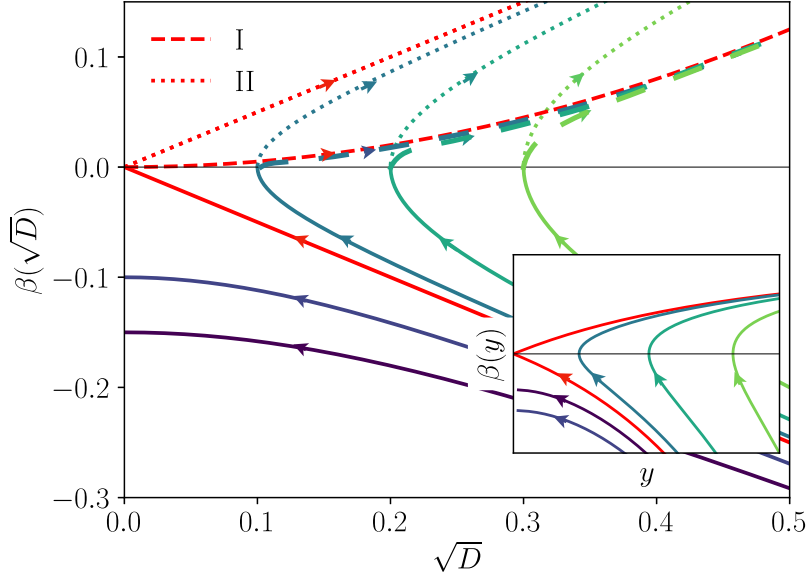


Figure 6.3: The  $\beta$ -function  $\beta(\sqrt{D}) = d \ln(\sqrt{D}) / d \ln K$  versus  $\sqrt{D}$  in the vicinity of the fixed point  $D_c = 0$  and the Kosterlitz-Thouless flow for the fugacity  $y$ , shown in the inset. The two possible forms of the single-parameter asymptotic behavior  $\beta_0(\sqrt{D})$  are shown by the red dashed and dotted lines. Scenario II gives the same behavior for  $\beta(\sqrt{D})$  as for the  $\beta$ -function  $d \ln(y) / d \ln L$  of the fugacity in the Kosterlitz-Thouless RG, while scenario I gives a different behavior and a new exponent emerges. Notice the existence of a minimum of both  $D$  and  $y$  and a square root behavior of the  $\beta$ -functions near this minimum. Such a behavior is not possible in the single-parameter scaling where the  $\beta$ -function must be smooth and single-valued. Notice also that the localized phase is similar to a superfluid one of Kosterlitz-Thouless RG, with the line of fixed points  $D = 0, \beta(D) < 0$  and  $y = 0, \beta(y) < 0$  respectively. Both of them cannot be obtained within the single-parameter scaling with  $D_c = 0$  or  $y_c = 0$ . Thus the second parameter  $K$  is relevant for RRG, in contrast to parameters with irrelevant exponents for the Anderson localization problem on  $d$ -dimensional lattice which only decorates the RG flow in the localized phase at small sample sizes [6].

On top of that, an identification is made between the exponent controlling the behavior of the diffusion coefficient [389] (and the typical local density of states [390]) for the *infinite* system and the exponent  $\nu$  of the *finite-size* scaling [133, 137], and the exponent that controls the localization radius in the localized phase. All of them describe different physics and they do not have to be the same.

The behavior  $\beta_0(D) \sim \pm \sqrt{D}$  around  $D = 0$  is also reminiscent of the Kosterlitz-Thouless flow for the square of fugacity  $y^2$  [377–379]. This is seen easily by passing from  $D$  to  $\sqrt{D}$  as we do in Fig. 6.3. Notice also the similarity of RG flow in the localized phase to that in the superfluid phase of the Kosterlitz-Thouless flow, the negative semi-axis  $D = 0, \beta(D) < 0$  ( $y = 0, \beta(y) < 0$ ) being the line of fixed points in both cases.

Figure 6.2 unequivocally shows that current numerical results cannot yet rule out any of these scenarios, and further analytical and numerical work is needed to resolve the issue. Recent analytical developments [135], in which a new field theory of localization was proposed and studied beyond the weak-coupling regime, give a picture that in many ways resembles the one presented in this Chapter. Further work is needed in this direction.

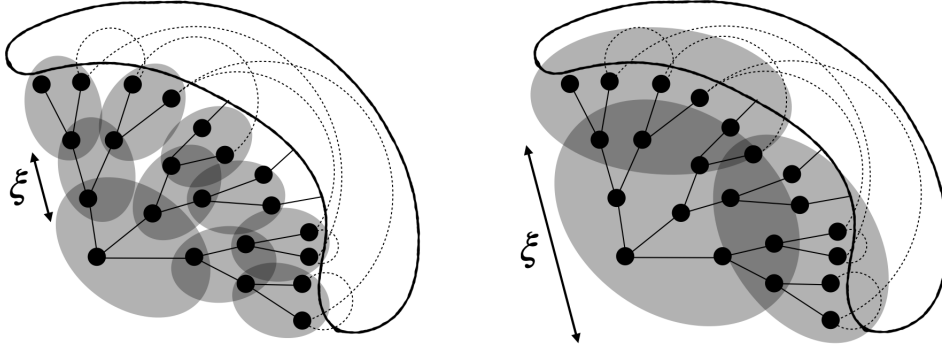


Figure 6.4: Pictorial representation of an RRG and the size of correlations at different disorder strengths. For small  $W$  (left), the correlation length is small, and under real space RG, the limit  $\xi/L \simeq 0$  is soon achieved, leading to RMT. For larger  $W$ ,  $\xi$  is larger, possibly leading to the failure of resonance hybridization, depending on the graph structure.

### 6.3 Role of loops and correlations in infinite dimensions

One of the outcomes of our considerations presented in this Chapter and the previous one is that the single-parameter  $\beta(D) > 0$  (a ‘single-parameter arc’) for RRG [5] is a smooth deformation of the corresponding arc for  $D > D_c$  on  $d$ -dimensional lattice as  $d$  increases and tends to infinity. On the other hand, it is known that in the absence of loops (i.e. on a tree) the Anderson model (with one orbital per site) displays multifractality in the entire delocalized phase [134, 351], where  $0 < D < 1$  in the thermodynamic limit. The corresponding  $\beta$ -function must, therefore, terminate somewhere on the line  $\beta(D) = 0$  depending on the initial conditions (e.g. the strength of disorder  $W$ ). This means that the single parameter arc in the case of a loopless tree is absent. Instead, there is a line of fixed points  $[0, 1]$  where the two-parameter RG trajectories terminate. This is a strong indication that the single-parameter arc (along which the system evolves to the ergodic fixed point) emerges due to the loops on a corresponding graph.

Indeed, let us consider an expander graph of diameter  $L$  and connectivity  $K$ , so that its volume is  $N = K^L$ . In the ergodic phase, let us denote the correlation length with  $\xi$ , defined as the characteristic length scale for the decay of the two-point function. Upon averaging,  $\xi$  is a function of the disorder strength: at small  $W$ ,  $\xi$  is small, since the system is chaotic; on the other hand, when approaching the critical point at  $W = W_c$ ,  $\xi$  diverges (see Fig. 6.4), as it is expected at a phase transition. The correlation length  $\xi$  can also be interpreted as the typical distance between resonances. In the localized phase the relevant length scale becomes the localization length. When  $\xi = O(1)$  resonances are very close, and under real space RG (or increasing system size) the regime  $\xi/L \sim 0$  is soon achieved. The system behaves as a fully connected quantum dot and exhibits random matrix properties. By increasing  $W$ , the distance between resonances grows, and they can eventually fail to hybridize. Their fate, though, depends on the properties of the graph. On a tree, the sites on the ‘leaves’ at remote branches are at a large distance from each other, as they can be connected only through the root (see right panel of Fig. 6.5). However, RRGs are characterized by the presence of large-scale loops connecting such sites and providing the shortcuts thereby (see left panel of Fig. 6.5). This means that the loops help in boosting the hybridization of resonances, reversing the RG flow and making it go to RMT along the single-parameter arc (see Fig. 5.3).

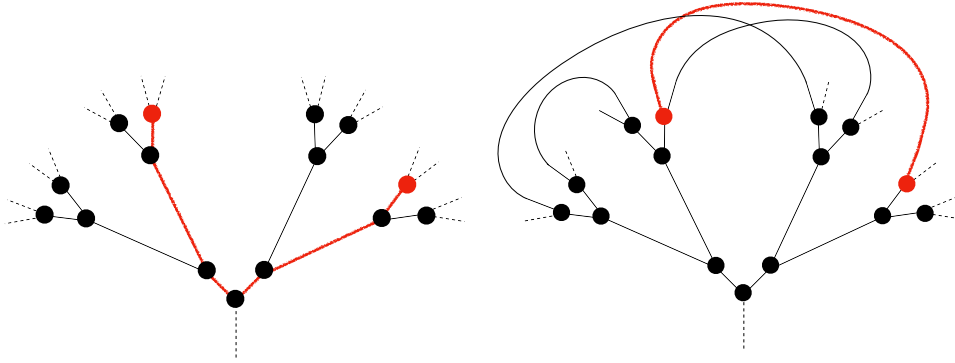


Figure 6.5: Resonances (pictorially represented as red dots) that are far apart on a tree (left) can become close on the RRG because of loops (right). This phenomenon facilitates the flow towards ergodicity, removing the fractal phase on the RRG.

## 6.4 Conclusions

We have presented the equations for a real space renormalization group analysis of the Anderson model on infinite dimensional graphs and applied it to the study of the fractal dimension of the eigenstates. In particular, the fact that the critical point has all the properties of the localized phase makes the RG flow close to it quite peculiar, distinguishing it from the RG flow for finite dimensions  $d$  described for the first time in Ref. [100] and from a typical Wilson-Fisher fixed point. We have introduced the division of the flow into a function that is responsible for the one-parameter scaling  $\beta_0(D)$  and which describes the approach to the ergodic fixed point  $D = 1$ , and a two-parameter scaling part  $\beta_1(D, K)$  which describes the remaining motion, in particular close to the minimum of  $D(K)$  and to the critical point  $D = 0$ .

We believe our work provides the correct perspective to look at Hamiltonians with localized critical points, among which it is believed there are many models displaying many-body localization phenomenology [174], showing that the whole beta function needs to be considered, and not only its linearization close to the fixed point. We also provided a clean way to describe non-perturbative effects in such systems, which go beyond the tree-geometry results. Among directions for future work, other than the MBL problem, we believe it would be very interesting to address the RG flow of models whose critical properties are quite well-established but unconventional, such as the quantum random energy model (or qREM) and the quantum Sun model. In fact, while their phase diagrams are known, the presence of strong mobility-edge effects (in the qREM) or unconventional ergodic fixed points (in the quantum Sun) might be better grasped through a thorough control of the full RG flow.



## Chapter 7

# Resonance counting and finite-size effects in random matrices

*In this Chapter we discuss more in detail the notion of resonances and their role in the breakdown of ergodicity in disordered quantum systems. In particular, we propose a new criterion for identifying resonances that is physically intuitive and has practical utility. We show how to relate the number of resonances computed via this criterion with the numerically accessible quantities and we benchmark our technique on a variety of Rosenzweig-Porter models. The results presented in this Chapter are based on the publication [7].*

**I**N the last two Chapters we discussed the localization properties in non-interacting disordered systems. In doing so, we emphasized that resonances are the fundamental building block for understanding localization transitions, and we now want to deepen the definition of resonances and their connection with the quantities considered previously.

In its traditional formulation, the notion of “resonance” is related to other concepts such as “level repulsion”, “anti-crossing”, or “avoided crossing” [242], and can be introduced as follows: the eigenvalues  $E_{1,2}$  of a  $2 \times 2$  real Hamiltonian  $H$  can be approximated by its diagonal elements  $\epsilon_{1,2}$  provided its off-diagonal element  $v$  is negligible compared to the difference between the diagonal elements, i.e.,  $v \ll \omega = \epsilon_2 - \epsilon_1$ . Hence, if

$$v \gtrsim \omega, \tag{7.0.1}$$

the shifts  $\Delta_{1,2} = E_{1,2} - \epsilon_{1,2}$  are also greater than or of the order of  $\omega$ , and the sites are said to be “in resonance” or “hybridized” [106], meaning that the eigenstates occupy both sites about equally. Therefore, the presence of many resonances eases transport across different portions of the system, thus leading to ergodicity. Given this simple construction, it is tempting to generalize this idea to  $N \times N$  matrices of arbitrary size  $N$ , saying that if there are  $M$  sites  $j = \{1, 2, \dots, M\}$  such that  $v_{0j} \gtrsim \epsilon_j - \epsilon_0$ , then the zeroth site should be “in resonance” with  $\sim M$  other sites, and the corresponding eigenstate should have at least  $\sim 1 + M$  relatively large components in the coordinate basis; this principle has found an extensive use not only in the studies of a single-particle localization [393–396] but also in the studies of the mesoscopic systems localization [397] and the many-body localization [398], including the ones considering the Anderson localization in the Hilbert space [399–402]. For example, provided the distribution of  $v$  has a typical scale  $v_{\text{typ}}$ , one can correspondingly define a typical critical value of the energy difference  $\epsilon_2 - \epsilon_1$  as  $\omega_{\text{crit}} \sim v_{\text{typ}}$ , meaning that all resonant sites should typically form a miniband of width  $\omega_{\text{crit}}$  and, hence, the

typical number of such resonant sites should be of the order of

$$M \sim \omega_{\text{crit}}/\delta_\varepsilon \sim v_{\text{typ}}/\delta_\varepsilon, \quad (7.0.2)$$

with  $\delta_\varepsilon$  being the mean onsite energies spacing. This generalization provides the lower-bound estimation for the number of sites where the eigenstate has a relevant weight and it is usually used in the thermodynamic limit  $N \rightarrow \infty$  to distinguish between localized and delocalized states, giving rise to the necessary criterion  $\lim_{N \rightarrow \infty} M(N) < \infty$  for the state to belong to the localized phase known as the Anderson localization criterion. Indeed, according to Anderson [96], the phase can be considered localized as long as the perturbation theory converges, and the condition  $v_{\text{typ}} \ll \delta_\varepsilon$  is the convergence criterion based on the first-order perturbation theory.

However, in Chapter 5 we referred to the notion of resonance in relation to concepts such as “fractal dimension,” “support set volume,” and “ergodic bubble”, and here is why: in its extreme, a wave function  $\psi$  having the majority of its weight on  $\Omega$  sites can be imagined as having only  $\Omega$  non-zero components of equal intensity  $\psi(i)^2 = 1/\Omega$ , leading to the participation entropy value  $S = -\sum_i \psi(i)^2 \ln \psi(i)^2 = \ln \Omega$ . In real-world situations, we can still introduce the support set volume  $\Omega$  via its relation to entropy as, e.g.,  $\Omega = \exp(S)$ , but then it would be as challenging to calculate it analytically as the entropy itself. On the other hand, from the analogy with the toy eigenstate having  $\Omega$  equal non-zero components, it is clear that the ergodic volume  $\Omega$  must be somehow related to the number of resonances  $M$  introduced above. And, while  $\Omega$  is indeed sometimes referenced as the “number of resonances”, as in Chapter 6, and thus it would be tempting to write  $\Omega = 1 + M$ , the actual relation is  $\Omega \gtrsim M + 1$ .

Hence, on the one hand, we have the easily calculable quantity  $M$ , which does not seem to have a clear relation to any observable in finite-size systems and, strictly speaking, can only be used in the thermodynamic limit to determine the localization transition. On the other hand, we have the ergodic volume  $\Omega$ , which is related to entropy and other commonly used observables but cannot be easily accessed analytically. On top of that, there is an intuition suggesting that there should probably be a more helpful relation between  $\Omega$  and  $M$  than the inequality above. In this work, we shed light on this relation.

The main result of the Chapter is a resonance criterion that doesn’t make use of arbitrary thresholds, but rather is self-consistent and automatically avoids the issue. We also propose an ansatz for the wave function supported independently by phenomenological and microscopical considerations that, combined with the resonance criterion, allows us to compute observable quantities such as the participation entropy and the support set dimension. We then test the predictive power of our theory against numerical results on different types of Rosenzweig-Porter models.

The rest of the Chapter is organized as follows. In Sec. 7.1.1, we discuss a relation between resonance counting and the Jacobi diagonalization procedure, which leads us to the concept of dressed hopping. In Sec. 7.1.2, we argue that the dressed hopping is not the end of the story and propose a modification to the naive resonance condition given in the Introduction. In Sec. 7.2, we discuss the common problems of the resonance conditions introduced earlier and propose the phenomenological self-consistent criterion that solves them all; this is the main result of our Chapter. Then, in Sections 7.3 and 7.4, we test our self-consistent approach to resonance counting by numerically comparing it to the results of exact diagonalization for a range of random matrix models. Finally, we re-derive the previously studied resonance conditions from the exact microscopic size-increment equations in Sec. 7.5.1, provide an in-detail comparison of the resulting approximations with the phenomenological results and exact numerics in Sec. 7.5.2, and conclude in Sec. 7.6.

## 7.1 Background and motivation

### 7.1.1 Resonance counting and Jacobi rotations

The reason why  $M$  defined via Eq. (7.0.2) only provides the lower-bound estimation for  $\Omega$  can be seen from the picture of Jacobi rotation [403]. For clarity, let us briefly introduce the Jacobi algorithm. The idea is very simple: given a symmetric matrix  $H$ , the iterative algorithm chooses an off-diagonal element  $H_{ij}$  and applies a Givens rotation  $U(i, j)$  on the  $2 \times 2$  submatrix with elements  $H_{ii}, H_{ij}, H_{ji}, H_{jj}$  in such a way that  $[U(i, j)HU(i, j)^\dagger]_{ij} = [U(i, j)HU(i, j)^\dagger]_{ji} = 0$ . This procedure, other than affecting the diagonal elements  $H_{ii}$  and  $H_{jj}$  causing level repulsion, will also affect all the matrix elements belonging to the same row or column of the decimated elements. This algorithm turns out to be effective in addressing properties in localized single-particle [404] and many-body quantum systems [405] and in well-thermalizing models [406]. Let us mention that different choices of the elements to decimate can be made. By choosing the current largest element one guarantees fast convergence, but in our setting it is useful to pick the off-diagonal element  $H_{ij}$  for which  $H_{ij}/(H_{ii} - H_{jj})$  is largest, representing the largest current resonance. This choice may not be the most efficient from the numerical point of view but, in some contexts, allows building successful analytic theories [393–396].

Consider a random matrix with a site having  $M_0$  resonances in the coordinate basis; that would mean we need to perform at least  $M_0$  rotations to eliminate these resonances and obtain the corresponding eigenstate. However, these  $M_0$  rotations may create new resonances, and we will have to perform even more rotations involving our state to eliminate them. So, if one wanted to improve the lower bound for  $\Omega$ , they would need to consider the resonances not only on the first but also on the latter steps of the Jacobi diagonalization procedure. Assuming the subsequent rotations do not undo the preceding ones, the improved lower bound estimation then takes the form  $\Omega \gtrsim 1 + \sum_i M_i$ , where  $M_i$ 's are the numbers of resonances eliminated by the subsequent rotations.

The presented picture of Jacobi rotations can be employed in the following way. Consider a random matrix and pick a site; then, while performing Jacobi rotations, only apply them to the rest of the system, i.e., diagonalize the submatrix excluding the chosen site. After this sub-diagonalization, the hopping between our site and the rest of the system is expressed in the eigenbasis of the submatrix, i.e., it is now “dressed” compared to the original “bare” hopping. Thus, since the distribution of the dressed hopping elements contains information about the ergodic volume of the submatrix, the number of resonances counted using this distribution should provide a better estimation for  $\Omega$  than the one utilizing the bare hopping distribution.

Another possible point of view on this construction is to consider the submatrix  $H_N$  as the original system and the chosen site as the addition, increasing the size of the original system (see Fig. 7.1). So, if the addition of the new site does not disturb the eigenenergy  $E_n$  of the original system too much, the corresponding eigenvector  $|n\rangle$  does not redistribute too much of its weight to the newly added site. In contrast, if some other eigenenergy  $E_k$  “resonates” with the newly added site, this site would now likely be in the support set of the corresponding deformed eigenstate of the extended system. Thus, for a system with  $M$  dressed resonances, we expect to see the newly added site in the support sets of  $M$  submatrix-originating eigenstates. Hence, the eigenstate originating from the additional site must occupy at least  $1 + M$  sites to be orthogonal to the rest of the eigenstates (it follows from counting the degrees of freedom). Therefore we get another lower-bound estimation for the support set volume, but this time, we expect it to be a much better bound than the one utilizing bare hopping instead of the dressed ones.

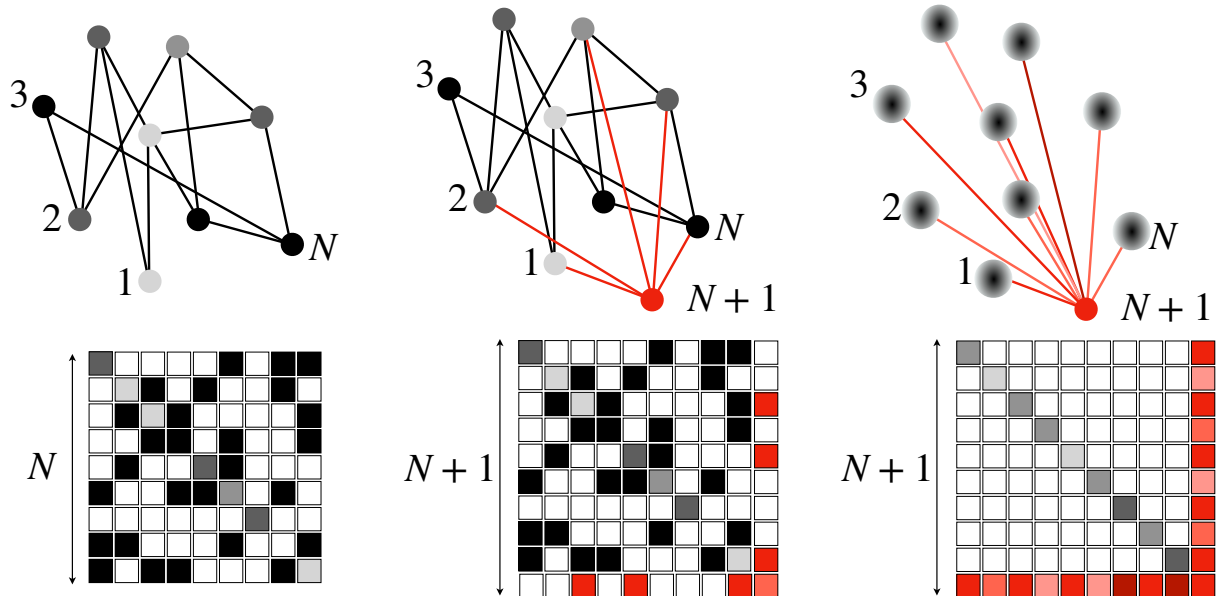


Figure 7.1: Pictorial representation of a site addition to a random graph (representing a random matrix). Different shading on nodes and edges represents different on-site energies and different hopping strengths. When a new site is added (right), a new row and column are added to the matrix, containing the hopping strength from the new site to the other sites (here represented in red shades).

### 7.1.2 Direct and indirect resonances

While the Jacobi rotations picture considerably improves the naive resonance counting, we want to make a further step so that we can address in principle also multifractal phases. Let us show why we need this with an example. Consider the Gaussian Rosenzweig-Porter (RP) ensemble [407] having independent uniformly distributed onsite energies  $H_{ii} = \epsilon_i \in [-w, w]$  and normally distributed hopping elements  $H_{ij} = v_{ij}$  with zero mean and size-dependent variance  $\langle v_{ij}^2 \rangle = N^{-\gamma}$ : due to the Gaussian distribution of the bare hopping, the dressed hopping has precisely the same distribution as the bare one, as a linear combination of normally distributed random variables is also normally distributed. Still, since the traditional resonance condition (7.0.1) predicts the typical number of resonances  $M$ , Eq. (7.0.2), to be of the order of the ratio  $v_{\text{typ}}/\delta$  with  $\delta \sim \sqrt{\langle \text{Tr}\{H^2\}/N \rangle}/N \sim \max\{w/N, N^{-(1+\gamma)/2}\}$  now denoting the mean level spacing,<sup>1</sup> the scaling of the number of resonances  $M \sim \min\{N^{1-\gamma/2}, N^{1/2}\}$  correctly predicts the Anderson localization transition  $\gamma_{AT} = 2$  but severely underestimates the support set volume  $\Omega \sim M$  in the delocalized phase, unable to correctly locate the ergodic-fractal transition  $\gamma_{ET} = 1$  even in the thermodynamic limit. The reason for that may be the resonance criterion itself as it is based on the analogy with the  $2 \times 2$  matrices and the first-order perturbation theory. Hence, it should probably be modified when one talks about matrices of arbitrary size in the delocalized phase.

To find out the appropriate modification, notice a similarity between the site-addition picture from the end of Sec. 7.1.1 and the Thouless criterion of localization [408] based on comparing the eigenenergies' shift  $\Delta$  induced by the boundary conditions change to the mean level spacing  $\delta$ . Indeed, the addition of the new site can be seen as an alteration of the boundary conditions for the

<sup>1</sup>The change of the meaning of  $\delta$  reflects the change of the physical picture in mind: while in the Introduction we were counting resonances between sites with certain onsite energies connected by bare hopping, here we count resonances between an arbitrary site and the eigenstates of the rest of the system, connected by the dressed hopping.

original system, which may cause an indirect (and mediated by the new site) resonance between close-in-energy unperturbed eigenstates, even in the absence of direct hopping between the two eigenstates [100]. Hence, the notion of the “sufficient disturbance” to the original eigenenergies can be reconsidered: when a shift of the order of  $\delta$  is enough for the state to hybridize with the newly added site, it looks like an overkill to require the shift  $\Delta$  to be of the order of  $\omega$  due to the direct resonance paradigm from the introduction of the Chapter.

To formulate the corresponding resonance condition mathematically, consider the extended  $(N + 1) \times (N + 1)$  Hamiltonian  $H_{N+1}$  and write the corresponding eigensystem equation in the block form as

$$H_{N+1} |E\rangle = \begin{bmatrix} H_N & |v\rangle \\ \langle v| & \varepsilon \end{bmatrix} \begin{bmatrix} P_N |E\rangle \\ \psi_E(\varepsilon) \end{bmatrix} = E \begin{bmatrix} P_N |E\rangle \\ \psi_E(\varepsilon) \end{bmatrix} = E |E\rangle. \quad (7.1.1)$$

In the above expression  $H_N$  is the Hamiltonian of the original  $N \times N$  system,  $|v\rangle$  is a hopping column vector connecting the new site to the original system,  $\varepsilon$  is the new site’s onsite energy,  $E$  and  $|E\rangle$  are the extended Hamiltonian’s eigenenergy and eigenstate,  $P_N$  is a projector to the original system’s Hilbert space, and  $\psi_E(\varepsilon)$  is the eigenstate’s amplitude on the new site, i.e.,  $|\psi_E(\varepsilon)|^2 = \langle E | (\mathbb{I} - P_N) E \rangle$ , with  $\mathbb{I}$  being the identity matrix. Then, acting in the spirit of Gaussian elimination, i.e., expressing  $\psi_E(\varepsilon)$  from the eigensystem equation as

$$\psi_E(\varepsilon) = \frac{\langle v | P_N | E \rangle}{E - \varepsilon} \quad (7.1.2)$$

and substituting it to the equation  $H_N P_N |E\rangle + \psi_E(\varepsilon) |v\rangle = E P_N |E\rangle$ , one finds that  $P_N |E\rangle$  satisfies the (nonlinear) eigensystem equation  $H_{\text{eff}}(E) P_N |E\rangle = E P_N |E\rangle$  with the effective Hamiltonian

$$H_{\text{eff}}(E) = H_N + V_{\text{eff}}(E) = H_N + \frac{|v\rangle \langle v|}{E - \varepsilon}. \quad (7.1.3)$$

Hence, after linearizing the equation by substituting  $E$  with the original Hamiltonian’s eigenenergy  $E_n$ ,  $H_N |n\rangle = E_n |n\rangle$ , we get from the perturbation theory for the linearized effective Hamiltonian  $H_{\text{eff}}(E_n)$  that

$$E - E_n = \Delta_n \sim \langle n | V_{\text{eff}}(E_n) | n \rangle \sim v_n^2 / \omega_n, \quad (7.1.4)$$

where  $v_n = \langle n | v \rangle$  is the hopping vector’s component in the eigenbasis  $|n\rangle$  of  $H_N$ , and  $\omega_n = E_n - \varepsilon$  is the difference between the original system’s eigenenergy under consideration and the new site’s onsite energy. Then, the new Thouless-inspired resonance condition takes the form

$$v_n^2 \gtrsim \min\{\omega_n^2, \omega_n \delta\}, \quad (7.1.5)$$

where the term  $\omega_n^2$  in the r.h.s. appears due to the necessity of counting also the direct resonances between the newly added site and the subsystem’s eigenstates having the closest eigenenergies to the site’s onsite energy. In contrast to Eq. (7.0.1), the resonance condition (7.1.5) applied to the RP model with  $1 < \gamma < 2$  predicts the number of resonances to scale as  $M \sim \omega_{\text{crit}} / \delta \sim v_{\text{typ}}^2 / \delta^2 \sim N^{2-\gamma}$  and gives the correct ergodic-fractal transition threshold at  $\gamma_{ET} = 1$  ( $M \propto N$ , the volume law) as well as correct Anderson localization transition at  $\gamma_{AT} = 2$  ( $M \propto N^0$ , finite support).

The reason why one should include the indirect resonances in the picture and relate the total number of all such resonances to the support set volume is the same as in Sec. 7.1.1, i.e., it is justified by counting the degrees of freedom. The only change is in the definition of the “sufficient disturbance” of the original eigenenergies: if the site’s addition can cause two eigenenergies of the original system to collide and the corresponding eigenstates to hybridize, it is reasonable to expect this site to be a part of their support sets.

## 7.2 Self-consistent resonance condition

While the resonance condition Eq. (7.1.5) looks more grounded than Eq. (7.0.1), they both have several problems in common. One of the problems is the threshold problem: what does “ $\gtrsim$ ” actually mean? Without answering this question, one can only estimate the scaling of  $M$  but cannot unambiguously compute the prefactor: while deriving Eq. (7.1.5), should we define the event of resonance as  $\Delta > \delta$ , or as  $\Delta > \delta/2$ , or as anything else? Moreover, the prefactor itself has little value unless the finite-size number of resonances  $M$  is linked to some measurable observable, and this is the second common problem of resonance counting defined via conditions Eq. (7.0.1) and Eq. (7.1.5): given the value of  $M$ , how to calculate, e.g., the participation entropy  $S$ ? To answer these questions, notice that, so far, the notion of resonances has always been related to the energy spectrum and eigenenergies shifts, while the target observables like  $\Omega$  or  $S$  are the properties of the wavefunctions. Hence, it seems reasonable to redefine the notion of resonances such that it would be directly linked to the wavefunctions’ shape, which is what we do in the present section.

Consider the exact expression (7.1.2) for the occupation of the newly added site; after approximating  $P_N |E\rangle$  by the unperturbed eigenstate  $|n\rangle$  of  $H_n$ , we obtain the perturbation theory result for the occupation as

$$\psi_n(\varepsilon)^2 \sim \frac{v_n^2}{(E_n - \varepsilon)^2} = \frac{v_n^2}{\omega_n^2}. \quad (7.2.1)$$

For each particular realization of the random Hamiltonian under consideration, the approximation (7.2.1) may or may not hold independently of the phase our system is in as the approximation’s applicability is only related to the very values of  $v_n^2$  and  $\omega_n^2$ ; for more detailed discussion of this fact, see Sec. 7.5.1. In other words, while  $v_n^2/\omega_n^2$  is small enough, the perturbation theory works, but it breaks down if this ratio becomes larger than some threshold. The threshold is there to omit the divergence of  $v_n^2/\omega_n^2$  at small  $\omega$ ’s, i.e., due to the normalization condition, and the dominant contribution to the normalization of the wavefunction is commonly attributed to the support set [350] consisting of strongly hybridized sites with roughly equal occupations, i.e., the ergodic bubble or the head of the wavefunction; here and below, the terms “support set”, “ergodic bubble”, and the “wavefunction’s head” will be used interchangeably due to their synonymous meaning. Based on this idealized picture, we conclude that the occupation of the newly added site by the eigenstate  $\psi_n$  should look like

$$\psi_n(\varepsilon)^2 \sim \begin{cases} \psi_{head}^2, & v_n^2/\omega_n^2 > C/\Omega \\ v_n^2/\omega_n^2, & v_n^2/\omega_n^2 < C/\Omega \end{cases}, \quad (7.2.2)$$

where  $\psi_{head}^2$  is distributed as components of a fully ergodic eigenstate,  $\Omega$  is the number of sites in the support set,<sup>2</sup> and  $C$  is the total weight of the state concentrated in its head, i.e.,  $C = \Omega \langle \psi_{head}^2 \rangle$  (see Fig. 7.2 for a visual representation of  $\psi^2$ ). From this point of view, the probability of a resonance can be unambiguously defined as the probability for the newly added site to become part of the perturbed eigenstate’s head, and the corresponding resonance condition takes the form

$$v_n^2 > \omega_n^2 C/\Omega, \quad (7.2.3)$$

where  $C$  and  $\Omega$  should be self-consistently determined from the equations

$$C = 1 - (N + 1 - \Omega) \langle v_n^2/\omega_n^2 \rangle_{tail}, \quad \Omega = 1 + NP(\Omega, C); \quad (7.2.4)$$

---

<sup>2</sup>Not to be confused with the relation  $\Omega = \exp(S)$  briefly mentioned in the Introduction of the Chapter; here and below,  $\Omega$  has a similar physical meaning but a more complicated relation to  $S$  which is discussed in the present section.

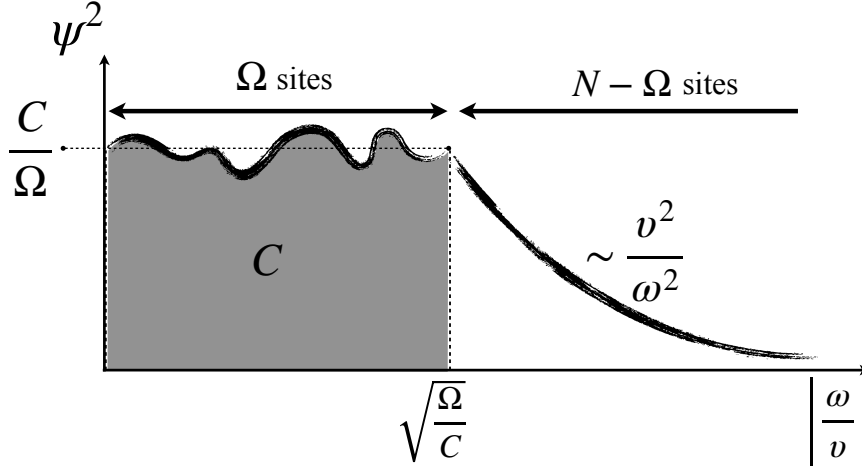


Figure 7.2: Visual representation of the wavefunction according to Eq. Eq. (7.2.2). It can be represented as split into two parts: the head, having support on  $\Omega$  sites and taken as a Haar random vector, and the tail, where there are no resonances and one can use the perturbation theory expression.

here,  $P(\Omega, C)$  is the probability for Eq. (7.2.3) to hold (i.e., the probability of resonance), while the averaging  $\langle \dots \rangle_{tail}$  in the expression for  $C$  is calculated only over the values of the ratio  $v_n^2/\omega_n^2$  which do not exceed  $C/\Omega$ . The above equations are easily obtained: the number  $\Omega$  of sites in the head is simply given by the number of resonances,  $N$  times the probability of resonance, plus “1” standing for the newly added site.<sup>3</sup> On the other hand, one minus the average value of  $\psi_n^2$  in the tails times the number of sites in the tails gives the total weight  $C$  in the head.

As one can see, the self-consistent resonance condition does not have the threshold problem as the threshold is determined self-consistently and has a clear physical meaning. Indeed, equating the l.h.s. and the r.h.s. of Eq. (7.2.3) and using Eq. (7.1.4), we see that, in the borderline case between resonant and non-resonant, the energy shift  $\Delta$  is of the order of  $\omega_{crit}C/\Omega \sim C\delta$ ; so, the value of the threshold is equal to  $C$ , the total eigenstate’s weight attributable to the resonant sites. However, since the definition of  $\omega_{crit}$  requires the existence of a typical scale of the dressed hopping distribution, one should not understand this threshold picture too literally but rather just use the self-consistent approach to resonance counting as described above.

Another advantage of this approach is its immediate connection to measurable observables like participation entropy. Indeed, provided all sites of the system are statistically equivalent, one can readily calculate such quantities using Eq. (7.2.2) as the ansatz for the wavefunction components. In this case, the distribution of  $\psi_{head}^2$  can be modeled by, e.g., the beta distribution, as it is the distribution of the components of the Gaussian Orthogonal/Unitary/Symplectic Ensemble Hamiltonian’s eigenstates, see App. D.1.

To conclude the Section and for further convenience, we provide here the analytical expressions for the probability of resonance  $P(\Omega, C)$ , the mean tail’s occupation  $\langle v_n^2/\omega_n^2 \rangle_{tail}$  entering the equations Eq. (7.2.4), and the participation entropy calculated using the ansatz Eq. (7.2.2). For simplicity, consider the eigenstates in the middle of the spectrum and put  $E_n = 0$  so that  $|\omega_n| \sim |\varepsilon|$ ;

<sup>3</sup>More concretely, this “1” comes from the fact that the approximation (7.2.1), being indexed by  $n = 1 \dots N$ , can approximate at most  $N$  out of the  $N + 1$  eigenstates of the extended system as it cannot approximate the eigenstate adiabatically connected with the one localized on the new site in the limit  $v_k \rightarrow 0$  for all  $k$ . By the adiabatic continuity, this special eigenstate always has (one of) the largest occupation(s) of this site and hence always counted as a part of the head. For more details on this, see Sec. 7.5.1 and Fig. 7.12(*Bottom*).

then, assuming the onsite energies to be uniformly distributed between  $\pm w$ , we get the probability for  $v_n^2$  to be larger than  $\omega_n^2 C/\Omega$  as

$$P(\Omega, C) = \int_0^w \frac{d\omega}{w} \int_{\omega^2 C/\Omega}^{\infty} p_{v^2}(\xi) d\xi = 1 - \int_0^{w^2 C/\Omega} d\xi p_{v^2}(\xi) \left( 1 - \sqrt{\frac{\xi \Omega}{w^2 C}} \right), \quad (7.2.5)$$

where  $p_{v^2}(\xi)$  is the probability distribution function (PDF) corresponding to the distribution of the dressed hopping elements squared. The mean tails occupation can be obtained similarly and takes the form

$$\left\langle \frac{v_n^2}{\omega_n^2} \right\rangle_{tail} = \int_0^{w^2 C/\Omega} d\xi p_{v^2}(\xi) \int_{\sqrt{\xi \Omega/C}}^w \frac{d\omega}{w} \frac{\xi}{\omega^2} = \int_0^{w^2 C/\Omega} d\xi p_{v^2}(\xi) \left( \sqrt{\frac{\xi C}{w^2 \Omega}} - \frac{\xi}{w^2} \right). \quad (7.2.6)$$

Finally, the specific mean tail's participation entropy  $s_{tail} = \langle -(v_n^2/\omega_n^2) \ln(v_n^2/\omega_n^2) \rangle_{tail}$  becomes

$$s_{tail} = - \int_0^{w^2 C/\Omega} d\xi p_{v^2}(\xi) \left( \sqrt{\frac{\xi C}{w^2 \Omega}} \left( \ln \left( \frac{C}{\Omega} \right) - 2 \right) + \frac{2\xi}{w^2} (1 + \ln w) - \frac{\xi \ln \xi}{w^2} \right), \quad (7.2.7)$$

and the total participation entropy for the beta-distributed head components takes the form

$$S = \Omega s_{head} + (N + 1 - \Omega) s_{tail} = C (H(\Omega/2) - H(1/2)) - C \ln(C) + (N + 1 - \Omega) s_{tail}, \quad (7.2.8)$$

where  $H(\Omega/2)$  is the Harmonic number, and  $s_{head}$  is calculated in App. D.1.

### 7.3 Analytical study of the Gaussian Rosenzweig-Porter model

Now, after having the improved resonance condition at our disposal, let us try it on the Gaussian Rosenzweig-Porter model, which is defined as

$$H_{\text{GRP}} = H_0 + V, \quad (H_0)_{ij} = \epsilon_i \delta_{ij}, \quad \epsilon_i \in [-w, w], \quad V = N^{-\gamma/2} H_{\text{GOE}}, \quad (7.3.1)$$

where the elements of  $H_{\text{GOE}}$  are i.i.d. Gaussian r.v.s, with zero mean and unit variance. This model has a non-trivial phase diagram, displaying, irrespectively of the value of  $w$ , an ergodic phase for  $\gamma < 1$ , a fractal phase for  $1 < \gamma < 2$ , and a localized phase for  $\gamma > 2$  [407, 409]. The main advantage of this model for our purposes is that the dressed hopping distribution is known exactly and, as it has already been mentioned in Sec. 7.1.2, coincides with the distribution of the bare hopping. Therefore we can directly substitute the PDF of the normal distribution to Eqs. (7.2.5) and (7.2.6), numerically solve Eqs. (7.2.4) and, using Eq. (7.2.2) with the beta-distributed head (see App. D.1), compute the participation entropy  $S(N)$  and the related quantities such as the support set dimension (see also Chapter 5.1)

$$D(N) = \frac{S(N)}{\ln(N)} \quad (7.3.2)$$

and the corresponding beta-function (see Sec. 7.3.1 for details)

$$\beta(N) = \frac{d \ln(D)}{d \ln(N)}; \quad (7.3.3)$$

the results are depicted in Fig. 7.3, and we discuss in some more detail the properties of the  $\beta$ -function in Sec. 7.3.1, as it is a new prediction showing some unexpected features. The code that

performs the analysis just described and that we used for producing the results reported in the next paragraphs can be found in the GitHub repository in Ref. [278].

Let us mention that the above definition of the support set dimension in Eq. (7.3.2) (which is just the fractal dimension  $D_q$  with  $q = 1$ ) is commonly used in the literature [409, 410], but different definitions are possible, e.g. the differential support set dimension  $\mathcal{D}(N) = dS(N)/d \ln(N)$ , which was used in Refs. [5, 6] for addressing the renormalization group flow in the Anderson model. The advantage of  $\mathcal{D}(N)$  consists of having milder finite-size effects, albeit being numerically less stable, because of the presence of the derivative. In the thermodynamic limit, the two quantities are equivalent, and here, since we do not aim at reducing the finite-size effects but at understanding them, we choose to work with Eq. (7.3.2) for better numerical stability and easier comparison with the literature on Rosenzweig-Porter models. As one can see, the self-consistent resonance condition (7.2.3) not only correctly reproduces the thermodynamic limit phase diagram but also qualitatively captures the finite-size effects.

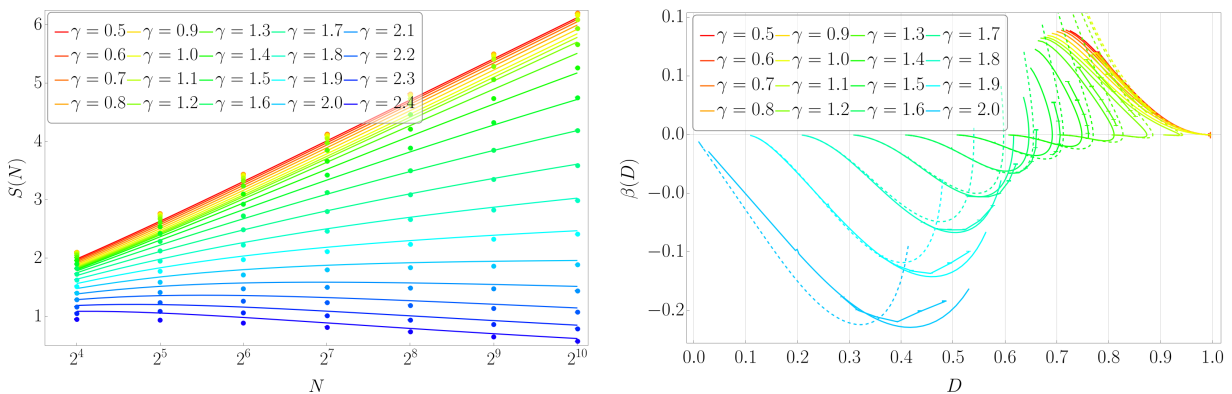


Figure 7.3: The participation entropy (left panel) and the support set dimension’s beta function (right panel) for the Gaussian RP model with  $w = 1$  obtained using exact diagonalization (points and broken lines) and the self-consistent resonance criterion (continuous curves). For the latter, the size varies from  $N = 2^4$  to  $N = 2^{100} - 2^{300}$ , depending on  $\gamma$ . Also, the dashed lines on the right panel show another analytical prediction for the same quantity derived in App. D.2 based on the ideas from Ref. [411]; for further discussion of this result, see App. D.2.

An intriguing and somehow unexpected behavior of the total head’s weight  $C$  is given in Fig. 7.4: as one can see, this quantity exhibits substantial finite size effects which can be observed even at  $N = 2^{100}$ . In addition to that,  $C$  has two limiting thermodynamic values corresponding to the ergodic/localized ( $C = 1$ ) and non-ergodic delocalized ( $C = 0.5$ ) phases, while, at the transition points  $\gamma_{AT} = 2$  and  $\gamma_{ET} = 1$ ,  $C$  saturates at intermediate  $w$ -dependent values.

### 7.3.1 The beta-function of the Gaussian Rosenzweig-Porter model

Let us discuss a bit more in detail the analytical prediction for the  $\beta$ -function of the Gaussian RP model. First of all, as we already emphasized, it matches the numerical results at a finite size, and therefore, its predictions are reliable. It is natural to compare it with the results obtained for the Anderson model on Random Regular Graphs [5] (see also the previous Chapter) and in finite dimension [6], as there are interesting differences.

Let us first mention some basic properties. The support set dimension  $D$  is bounded,  $0 \leq D \leq 1$ , while it is not true in general at finite size for the differential support set dimension  $\mathcal{D}$ ; see, e.g., the behavior of the participation entropy for  $\gamma > 2$  in the left panel of Fig. 7.3, where its slope

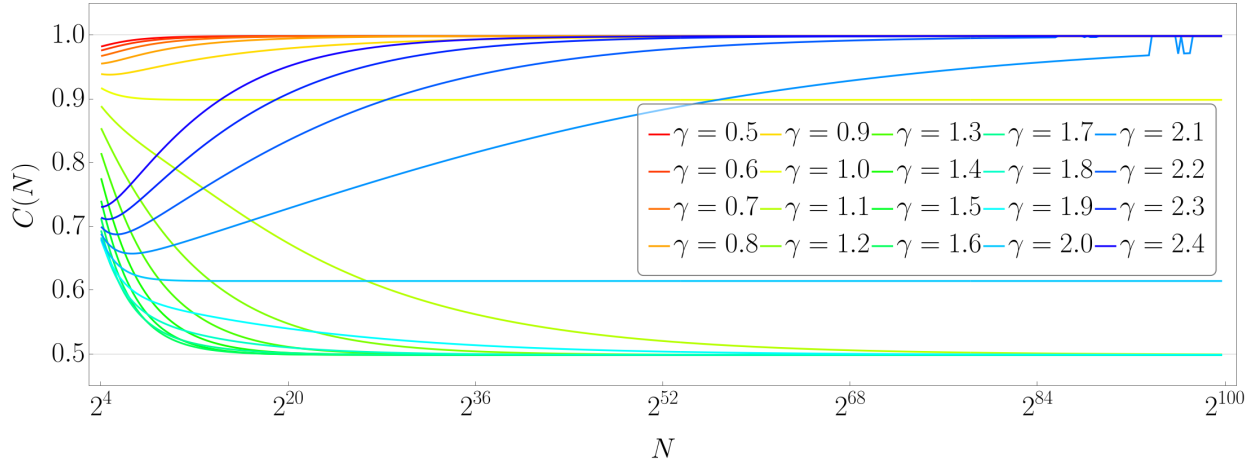


Figure 7.4: The total head's weight  $C$  according to the solution of Eq. (7.2.4) for  $w = 1$ . Given that the value of  $C$  can be associated with the threshold value for the indirect resonance condition (7.1.5), we can conclude that Eq. (7.1.5) should also work fairly well even without the self-consistent equations as  $0.5 \lesssim C \lesssim 1$ .

is negative and, hence,  $\mathcal{D} < 0$ . Also, at finite size, the flow curves have to have an infinite slope when approaching the  $\beta = 0$ , in order to cross it for a finite value of the system size. If, instead, the slope is finite, the  $\beta = 0$  line can be reached only in the thermodynamic limit. We can see in Fig. 7.3 this feature. Let us also remark that, as expected, for  $\gamma \in (1, 2)$  the termination point of the RG flow occurs at  $0 < D < 1$ , signaling the presence of the fractal phase.

Let us now discuss some differences with the RG flow in the Anderson model. Our aim is not to draw connections between these models, as there is no theoretical reason for them to have similarities in a renormalization group sense, but just to describe the differences the models display. In Refs. [5, 6] the authors describe the full renormalization group flow for the differential support set dimension in the Anderson model, both on Random Regular Graphs and in finite dimensions. From the behavior of the  $\beta$ -function, the authors can verify the one-parameter scaling hypothesis in both cases. In the present case, there cannot be one-parameter scaling in the fractal phase, by definition. But there is another interesting distinction: in the Anderson model, in the ergodic phase, the differential support set dimension displays a minimum and then saturates to the ergodic value  $\mathcal{D} = 1$  when the system size is increased. In the Gaussian RP model, the opposite happens in the fractal phase with the plain support set dimension  $D$ , which has a maximum at very small sizes before flowing to the saturation value.

## 7.4 Resonance counting in other Rosenzweig-Porter models

In this Section, we extend the results previously shown for the Gaussian Rosenzweig-Porter model to other random-matrix ensembles, still displaying a localization transition. However, for non-Gaussian cases, we are not able to compute explicitly the distribution of dressed hoppings, and thus we need to solve numerically the self-consistent resonance condition (7.2.3). Since our ultimate goal is to address the properties of the Anderson model, after a consistency check we will focus on Rosenzweig-Porter models resembling features of the Anderson model on random graphs.

Let us briefly explain how we numerically solve the self-consistent equations from Sec. 7.2. The main goal of the numerical solution is that of having the correct distribution of dressed hopping, since the analytical computation of the distribution lies beyond the scope of this Chapter. To

do so, we numerically compute the exact eigenvectors  $|n\rangle$  and eigenvalues  $E_n$  of many samples of random matrices. We then collect the corresponding samples of dressed hoppings  $v_n = \langle n|v\rangle$  by independently sampling the new hopping vectors  $|v\rangle$ , and the energy differences  $\omega_n = E_n - \epsilon$  by independently sampling new onsite energies  $\epsilon$ 's, ultimately obtaining a collection of  $\psi_n^2 = v_n^2/\omega_n^2$ . Once a sufficiently large sample (let us say of size  $m$ ) of  $\psi_n^2$ 's is collected, we sort it in ascending order and, while iterating through the sample with the index  $k$ , we compute the “current”  $P$ ,  $\Omega$ , and  $C$  as

$$P(k) = 1 - k/m, \quad \Omega(k) = 1 + NP(k), \quad C(k) = 1 - (N + 1 - \Omega(k))\langle\psi_j^2\rangle_{j<k}, \quad (7.4.1)$$

where  $k$  is the current position in the sample and  $\langle\dots\rangle_{j<k}$  represents the average of the elements up to the  $k$ -th. For each  $k$ , we check whether  $\psi_k^2 > C(k)/\Omega(k)$ ; when this condition is satisfied for the first time, we compute the entropy in the tails as

$$s_{tails} = -\frac{1}{k} \sum_{j=1}^k \psi_j^2 \log \psi_j^2 \quad (7.4.2)$$

and use the current values of  $\Omega$  and  $C$  to obtain the expression for the total entropy according to Eq. (7.2.8). The code that performs the analysis just described and that we used for producing the results reported in the next paragraphs can be found in the GitHub repository in Ref. [278].

#### 7.4.1 A further check on Gaussian Rosenzweig-Porter

As a first check, we compute numerically the probability of resonances, and consequently the participation entropy, for the Gaussian Rosenzweig-Porter model (that we solved analytically in Sec. 7.3). As it should, the match for participation entropy and support set dimension between exact diagonalization and numerical resonance counting due to the self-consistent resonance condition is remarkably good, as shown in Fig. 7.5.

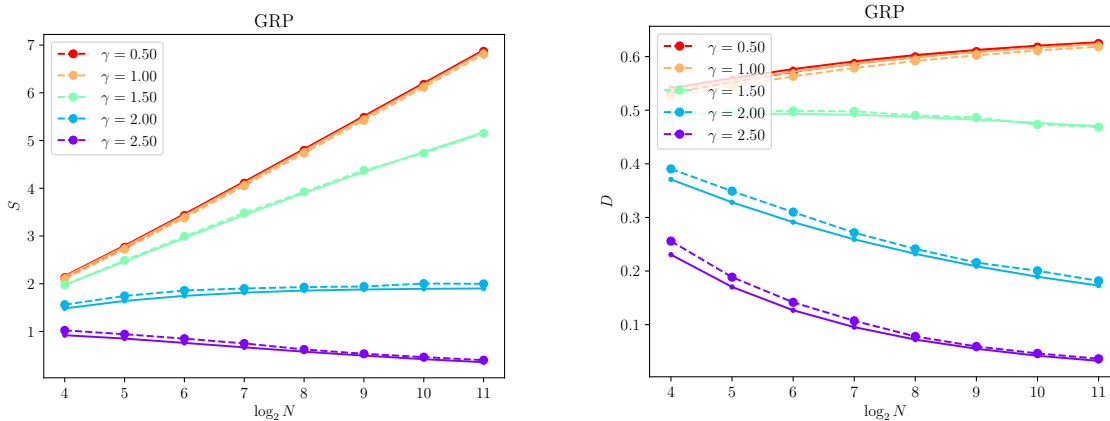


Figure 7.5: Comparison between exact diagonalization (solid lines) and analytical prediction (dashed) for the Gaussian Rosenzweig-Porter model. (Left) Participation entropy. (Right) support set dimension.

## 7.4.2 The Log-normal Rosenzweig-Porter model

Let us now take a more complicated Rosenzweig-Porter model, called Log-normal Rosenzweig-Porter model. It is defined by the matrix ensemble

$$H_{\text{LNRP}} = H_0 + V, \quad (H_0)_{ij} = \epsilon_i \delta_{ij}, \quad p_V(v) \propto \frac{1}{|v|} \exp\left\{-\frac{\ln^2(|v|/N^{-\gamma/2})}{2p \ln(N^{\gamma/2})}\right\}, \quad (7.4.3)$$

where  $\epsilon_i$  is, again, uniformly distributed,  $\epsilon_i \in [-w, w]$ . Setting  $p = 1$ , one obtains a phase diagram according to which the system is ergodic for  $\gamma < 4$  and localized for  $\gamma > 4$ , with  $\{p = 1, \gamma = 4\}$  being a tricritical point on the phase diagram in the variables  $\{p, \gamma\}$  [392, 409]. The interest in the Log-normal RP model resides in its similarity with the Anderson model on Random Regular Graphs. Indeed, it has been shown that the distribution of the effective long-range hopping in the Anderson model on RRGs is approximately given by the log-normal distribution with  $p = 1$  [412].

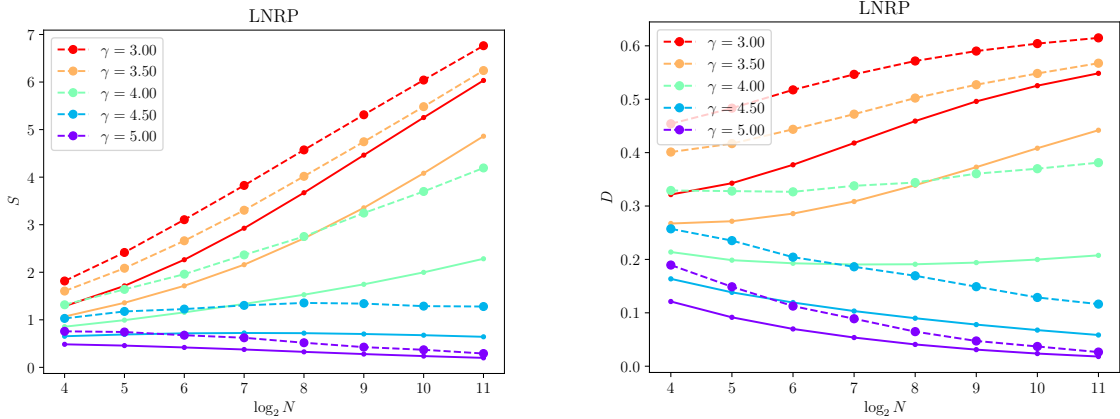


Figure 7.6: Comparison between exact diagonalization (solid lines) and analytical prediction (dashed) for the Log-normal Rosenzweig-Porter model. (Left) Participation entropy. (Right) support set dimension (7.3.2).

We show in Fig. 7.6 the comparison between the analytical prediction following from Eq. (7.2.3) and the numerical results coming from exact diagonalization. We can notice that the qualitative behavior of the numerical and analytical results is the same, and, despite the numerical values being different, the numerical and analytical curves tend to approach each other as the size grows, hinting that the physical behavior is correctly captured by our analytical description also in this case.

In particular, notice that, for  $\gamma = \gamma_c = 4$ , the analytical results for  $D$  display a minimum as the numerics do, for roughly the same values of the systems size. The fact of the minimum's existence is non-trivial. Indeed, as the function  $D(N; p, \gamma)$  is expected to be an analytic and, hence, smooth function of all the parameters at finite system sizes, the minimum cannot immediately disappear at  $\gamma > \gamma_c$  or  $\gamma < \gamma_c$ , implying the existence of a vast range of possible behaviors of the support set dimension at larger sizes. Assume, for example, that the critical point of the LN-RP model is localized; this assumption seems reasonable as the model is claimed to be a proxy for the Anderson model on RRGs, which is localized at its critical point. However, this would imply that the critical curve  $D(N)$  must have at least one more extremum at larger sizes – a maximum. Moreover, by the function's analyticity, this maximum would also be present in the close-to-criticality ergodic phase, i.e., at  $\gamma < 4$ , resulting in the support set dimension  $D(N)$  having at least three extrema at

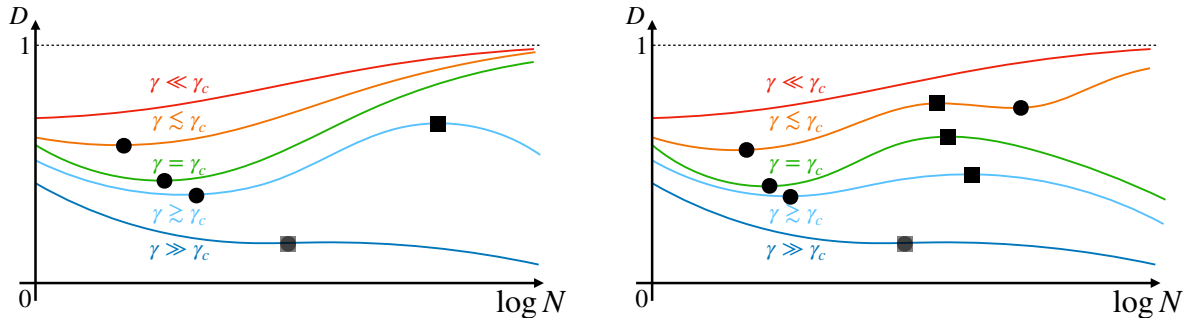


Figure 7.7: Sketch of the dependence of the support set dimension  $D$  on the system size  $L$ . (Left) As suggested by the numerical data and from previous results, for  $\gamma = \gamma_c$  the model is ergodic in the thermodynamic limit (differently from the RRG). This leads to the presence of a maximum in  $D$  at large sizes, as explained in the main text. For some  $\gamma$ , minimum and maximum merge in a saddle. (Right) Assuming the critical point is localized, as a consequence of continuity in  $\gamma$  there must be an additional maximum and minimum for  $\gamma \lesssim \gamma_c$ .

large but finite sizes, see the right panel of Fig. 7.7. On the other hand, if one would assume the critical point to be ergodic or at least fractal with the limiting support set dimension  $D(N = \infty)$  depending on  $w$ , it would be possible to avoid the introduction of an additional extrema in the ergodic phase; the localized one though would still have to have at least two extrema, with the maximum emerging from  $N = \infty$  as  $\gamma > \gamma_c$  deviates from its critical value, see the left panel of Fig. 7.7. In fact, there are indications that the critical point of the Log-normal Rosenzweig-Porter model is indeed delocalized; it can be inferred from, e.g., the self-consistent graphical solution for the LN-RP limiting support set dimension presented in [409], though the tricritical point lies at the very boundary of the graphical methods' applicability.<sup>4</sup> This fact, together with the complexity of the finite-size effects the model must show to have the tricritical point localized, poses questions about the extent of similarities between the LN-RP model and the Anderson model on RRG.

### 7.4.3 The Bernoulli Rosenzweig-Porter model

As a further step in the direction of the Anderson model on RRG, let us introduce the Bernoulli Rosenzweig-Porter model. It essentially consists of an Anderson model on an Erdos-Renyi graph [409], in the sense that, given  $N$  sites, each of them is connected to another one by a unit hopping with an assigned probability that, in our case, is  $K/N$ ; this also motivates the name ‘‘Bernoulli Rosenzweig-Porter model’’. This choice allows us to have, on average, connectivity  $K$ , as in the RRG, with the advantage of having the possibility of adding a single site without having to reshuffle the full adjacency matrix of the graph. On the other hand, the graph is not strictly regular, but only on average.

The Hamiltonian is therefore

$$H_{\text{ER}} = H_0 + V, \quad (H_0)_{ij} = \epsilon_i \delta_{ij}, \quad \epsilon_i \in [-w, w], \quad (7.4.4)$$

with  $V$  being the adjacency matrix of an Erdos-Renyi graph, i.e., with  $V_{ij} = 1$  if  $i$  is connected to  $j$  and zero otherwise. To the best of our knowledge, the Bernoulli Rosenzweig-Porter model

<sup>4</sup>In [409], the equation (51) defines a quantity  $c$ , related to the support set dimension as  $D = 1 - c$ , which vanishes as one approaches the tricritical point from either direction on the phase diagram, Figure 11, meaning that the limiting value of  $D$  at this point is 1, corresponding to the ergodic phase.

has never been introduced before (although similar models have been considered, e.g. Ref. [413]), so we do not know its properties such as the position of the localization transition precisely. We expect it to be comparable with the value  $W_c = 18.17$  of the RRG [390]. Our goal here is to test our analytical approximations against the exact numerical results, and the comparison is shown in Fig. 7.8.

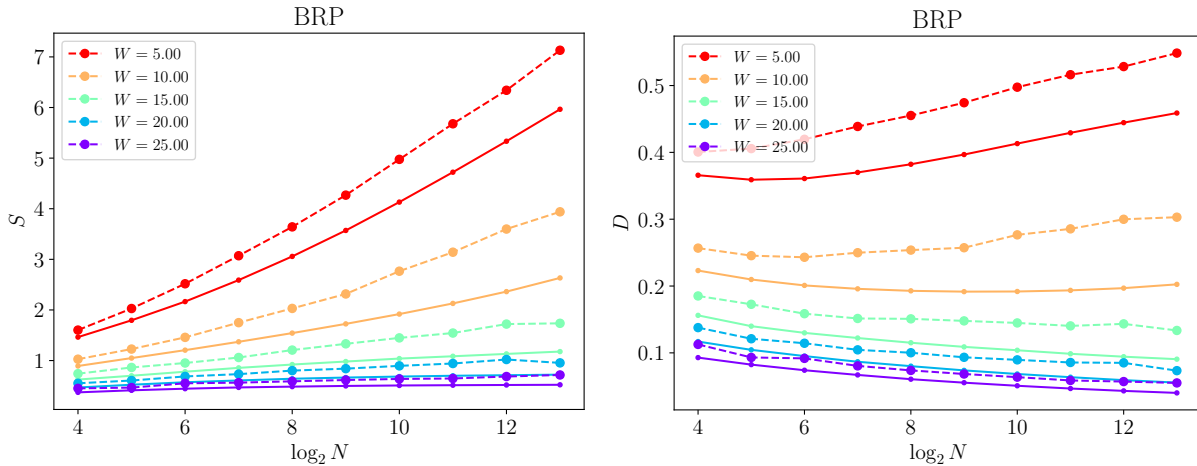


Figure 7.8: Comparison between exact diagonalization (solid lines) and analytical prediction (dashed) for the Bernoulli Rosenzweig-Porter model. (Left) Participation entropy. (Right) support set dimension.

Once again we can see that the qualitative picture is correctly captured by our resonance criterion, despite the quantitative difference between numerical and analytical results. This disagreement is most probably a consequence of the ansatz for the heads of the eigenstates, which might be not optimal for sparse matrices. However, the main goal is achieved also in this case: our self-consistent resonance criterion captures the finite-size effects qualitatively correctly, and we hope to find the quantitative correspondence also improving with size when the larger sizes become accessible to exact diagonalization.

## 7.5 Microscopic approach to resonance criteria

### 7.5.1 Asymptotic analysis of the exact size-increment equations

The resonance conditions Eq. (7.0.1) and Eq. (7.1.5) were introduced from the energy spectrum point of view, while the self-consistent condition (7.2.3) was based directly on the spatial eigenstates' configuration. Still, both Eq. (7.1.5) and Eq. (7.2.3) can correctly predict the full phase diagram in the thermodynamic limit and, for the Gaussian RP model, even give qualitatively similar values of  $\Omega$ .<sup>5</sup> In this section, we explore the connection between the spectrum-based and the wavefunction-based resonance conditions via careful asymptotic analysis of the exact equations for eigenenergies and eigenstates of the extended system.

To start with, consider we know everything about the Hamiltonian  $H^0$  and the arbitrary (not necessarily small) perturbation  $V$ ; our task is to find the eigensystem of  $H = H^0 + V$ . It can be

<sup>5</sup>It can be inferred from Fig. 7.4 and the applicability of the threshold picture to the Gaussian RP model, suggesting that the threshold  $C$  is of the order of 1 and does not significantly change with size, implying a rough equivalence between (7.1.5) and (7.2.3) in this particular case.

done as follows: first, we rewrite the eigensystem equation  $(H^0 + V)|E\rangle = E|E\rangle$  in the form

$$|E\rangle = G^0(E)V|E\rangle \quad (7.5.1)$$

with the resolvent  $G^0(E)$  defined as  $G^0(E) = (E - H^0)^{-1}$ ; second, we obtain the secular equation as  $\|G^0(E)V - \mathbb{I}\| = 0$ . If  $V$  is a rank-one matrix, e.g.,  $V = |g\rangle\langle g|$ , it gives the well-known secular equation of the Richardson model [414–418],  $\langle g|G^0(E)|g\rangle = 1$ . If  $V$  has rank two,  $V = |u\rangle\langle v| + |v\rangle\langle u|$ , the secular equation takes the form

$$\left\| \begin{array}{cc} G_{uv}^0(E) - 1 & G_{uu}^0(E) \\ G_{vu}^0(E) & G_{vv}^0(E) - 1 \end{array} \right\| = 0, \quad \text{with } G_{uv}^0(E) = \langle u|G^0(E)|v\rangle. \quad (7.5.2)$$

If the  $(N + 1) \times (N + 1)$  Hamiltonian  $H^0$  represents the system of  $N$  connected sites with eigenenergies  $E_n$  together with one disconnected site with onsite energy  $\varepsilon$ , the Hamiltonian  $H$  with

$$V = |v\rangle\langle\varepsilon| + |\varepsilon\rangle\langle v| \quad (7.5.3)$$

represents the system where this lonely site  $|\varepsilon\rangle$  is connected to the rest of the system via the hopping vector  $|v\rangle$ . In other words, if we consider the connected  $N \times N$  block of  $H^0$  as the Hamiltonian  $H_N$  of the original  $N$ -sites system, the Hamiltonian  $H$  can be seen as the Hamiltonian  $H_{N+1}$  of the extended system, and the exact secular equation Eq. (7.5.2) provides the way to study the evolution of the eigenenergies as we grow the system size site by site. The secular equation then takes a simpler form  $G_{vv}^0(E) = 1/G_{\varepsilon\varepsilon}^0(E) = E - \varepsilon$ , or, explicitly,

$$\sum_{n=1}^N \frac{v_n^2}{E - E_n} = E - \varepsilon, \quad (7.5.4)$$

where  $v_n = \langle n|v\rangle$  is the component of the hopping vector  $|v\rangle$  in the eigenbasis of  $H_N$ , i.e., the dressed hopping.

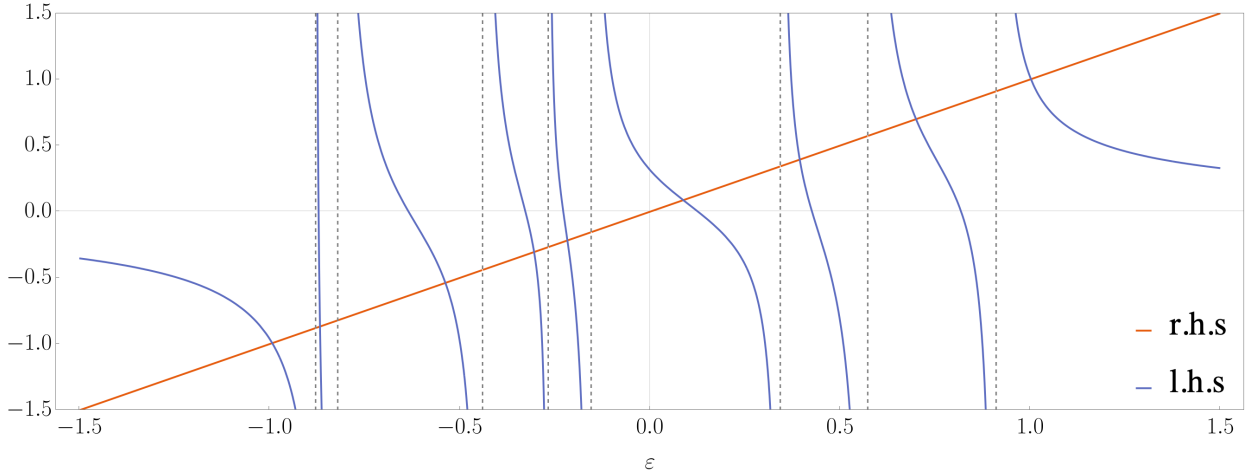


Figure 7.9: An example of a graphical solution to Eq. (7.5.4) with  $\varepsilon = 0$  for the Gaussian RP model with  $\gamma = 1.5$ ,  $N = 8$ , and  $w = 1$ ; the red line is the equation’s right-hand side, the blue curves represent the left-hand side, and their intersections represent the solutions,  $E$ . The vertical dashed lines mark the eight eigenenergies  $E_n$  of the original system.

As one can see from Fig. 7.9, the equation (7.5.4) has  $N + 1$  solutions for  $E$ , each of those lying in-between two neighboring eigenvalues  $E_n$  of the original system. This observation suggests

rewriting of Eq. (7.5.4) in the form

$$\Delta_k = v_k^2 / \left( E_k - \varepsilon + \Delta_k - \sum_{n \neq k} \frac{v_n^2}{\omega_{kn} + \Delta_k} \right), \quad (7.5.5)$$

where  $\omega_{kn} = E_k - E_n$ , and  $\Delta_k = E - E_k$  is the new unknown. For any fixed  $k$ , there are  $N + 1$  solutions for  $\Delta_k$ , as it should be; however, the goal behind this rewriting is not to find all roots for fixed  $k$ , but to find the least-absolute-value solutions for each  $k$ . Such solutions never exceed the corresponding level spacing and can be either of the order of the typical level spacing  $\delta$  or smaller, fitting in Thouless's picture of eigenvalues shifts from Sec. 7.1.2. Thus, assuming  $\Delta_k \ll \min\{\omega_{k,k+1}, \omega_{k,k-1}\}$ , we can write an asymptotic version of Eq. (7.5.5) as

$$\Delta_k \sim \frac{v_k^2}{E_k - \varepsilon - \sum_{n \neq k} v_n^2 / \omega_{kn} + \Delta_k (1 + \sum_{n \neq k} v_n^2 / \omega_{kn}^2)} = \frac{v_k^2}{\omega_k + \Delta_k \Gamma_k^2}, \quad (7.5.6)$$

which leads to an easily solvable quadratic equation for  $\Delta_k$ , resulting in

$$\Delta_k \sim \text{sign}(\omega_k) \frac{\sqrt{\omega_k^2 + 4v_k^2 \Gamma_k^2} - |\omega_k|}{2\Gamma_k^2}; \quad (7.5.7)$$

here, we chose the smallest  $\Delta_k$  and defined

$$\omega_k = E_k - \varepsilon - \sum_{n \neq k} v_n^2 / \omega_{kn}, \quad \Gamma_k^2 = 1 + \sum_{n \neq k} v_n^2 / \omega_{kn}^2. \quad (7.5.8)$$

Finally, we can substitute this approximate solution to the roughened version  $\Delta_k \ll \delta$  of the above approximation's applicability condition  $\Delta_k \ll \min\{\omega_{k,k+1}, \omega_{k,k-1}\}$  and obtain its explicit form as

$$v_k^2 \ll \Gamma_k^2 \delta^2 + \omega_k \delta. \quad (7.5.9)$$

If, in addition,  $\omega_k \gg \Delta_k \Gamma_k^2$ , instead of Eq. (7.5.7) we can get

$$\Delta_k \sim v_k^2 / \omega_k, \quad (7.5.10)$$

which is asymptotically correct provided both  $v_k^2 / \omega_k \ll \delta$  and  $v_k^2 / \omega_k \ll \omega_k / \Gamma_k^2$  hold, i.e.,

$$v_k^2 \ll \min\{\omega_k^2 / \Gamma_k^2, \omega_k \delta\}. \quad (7.5.11)$$

Here, one may notice a similarity between the approximation applicability condition (7.5.11) and the indirect resonance condition (7.1.5) as they differ only by the definitions of  $\omega_k$  and the factor  $1/\Gamma_k^2$  in the r.h.s. of Eq. (7.5.11). To see how this observation allows relating the conditions Eq. (7.1.5) and Eq. (7.2.3), let us now focus on the eigenstates but from the perspective of the exact equation (7.5.1). Substituting Eq. (7.5.3) into Eq. (7.5.1), we get

$$|E\rangle = \langle \varepsilon | E \rangle \sum_{n=1}^N \frac{v_n}{E - E_n} |n\rangle + \langle v | E \rangle \frac{1}{E - \varepsilon} |\varepsilon\rangle, \quad (7.5.12)$$

where  $|n\rangle$  are the eigenstates of  $H_N$  corresponding to the eigenenergies  $E_n$ . Then, multiplying Eq. (7.5.1) by  $\langle v |$  to get  $\langle v | E \rangle = \langle \varepsilon | E \rangle G_{vv}^0(E)$  and using the secular equation Eq. (7.5.4) in the form  $G_{vv}^0(E) = E - \varepsilon$ , we get

$$|E\rangle = \langle \varepsilon | E \rangle \left( |\varepsilon\rangle + \sum_{n=1}^N \frac{v_n}{E - E_n} |n\rangle \right), \quad (7.5.13)$$

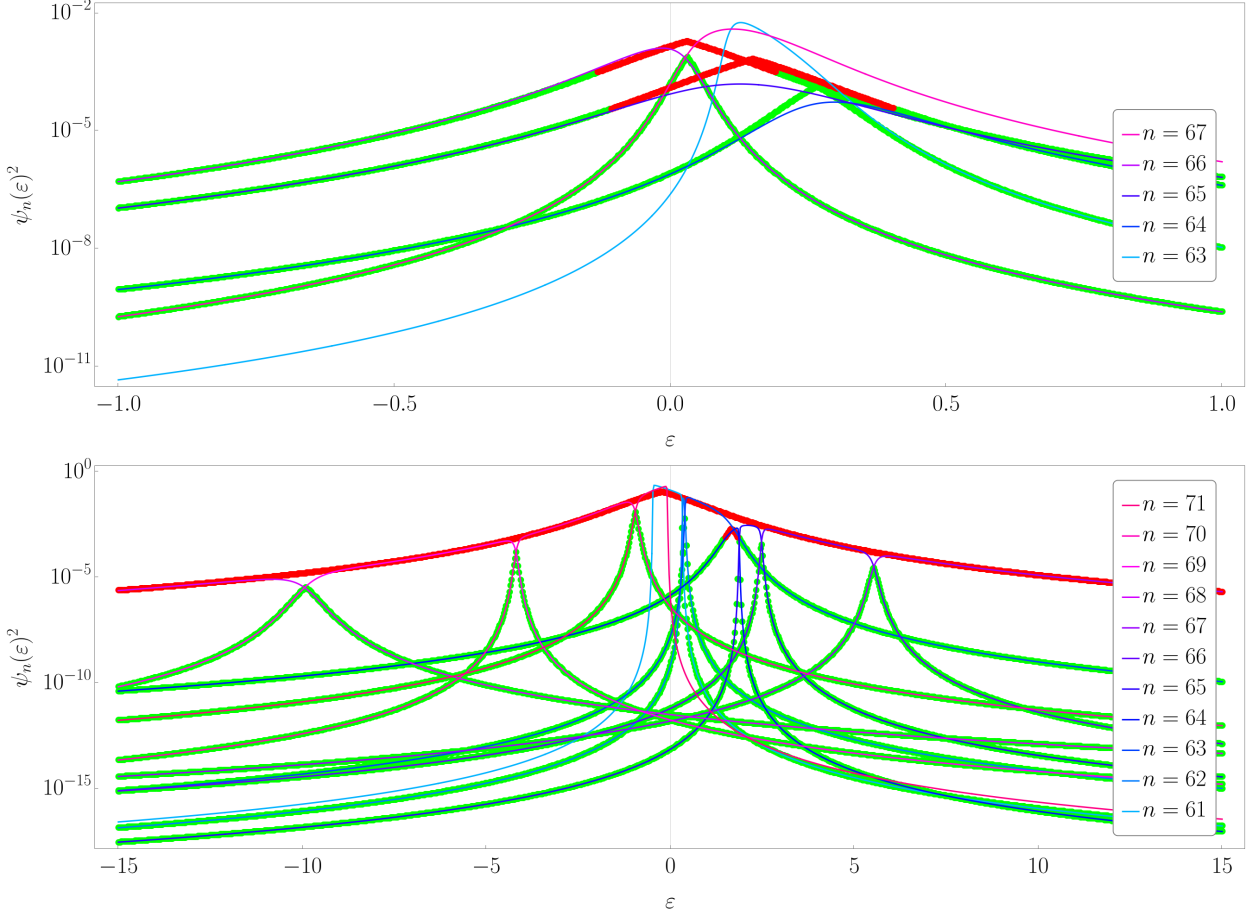


Figure 7.10: The validity check of Eq. (7.5.16). Each plot shows a single realization of a random matrix from the corresponding ensemble, with no averaging taken. Different continuous lines show the exact  $(N + 1)^{\text{th}}$  site's occupations  $\psi(\varepsilon)^2$  as functions of the corresponding onsite energy  $\varepsilon$ ; the legends show the indices of the considered eigenstates. The points show Eq. (7.5.16); their color shows if the condition (7.5.9) in the form  $|\Delta_k| < \min\{|E_k - E_{k\pm 1}|\}/2$  holds or not: green means it holds, and red means it does not. (*Top*) The Gaussian Rosenzweig-Porter model with  $N = 2^7$  and  $\gamma = 1.5$ ; the on-site disorder is sampled from the uniform distribution  $\varepsilon \in [-1, 1]$ . (*Bottom*) The Bernoulli Rosenzweig-Porter model with  $K = 3$ ,  $N = 2^7$ ; the on-site disorder is sampled from the uniform distribution  $\varepsilon \in [-15, 15]$ .

from where, employing the normalization condition  $\langle E|E \rangle = 1$ , we obtain

$$\psi_{E(\varepsilon)}^2 = \langle \varepsilon|E \rangle^2 = 1 \left/ \left( 1 + \sum_{n=1}^N \frac{v_n^2}{(E(\varepsilon) - E_n)^2} \right) \right. = \frac{dE(\varepsilon)}{d\varepsilon}; \quad (7.5.14)$$

here,  $E(\varepsilon)$  is one of the  $N + 1$  branches of the solution of Eq. (7.5.4), and the very last equality can be checked by directly differentiating Eq. (7.5.4). Finally, by passing from  $E(\varepsilon)$  to  $\Delta_k(\varepsilon)$ , isolating the term  $v_k^2/\Delta_k^2$  from the rest of the sum, multiplying the nominator and denominator by  $v_k^2$  and using Eq. (7.5.5), we rewrite the r.h.s. of Eq. (7.5.14) in the form

$$\psi_{E(\varepsilon)}^2 = v_k^2 \left/ \left( \left( E_k - \varepsilon + \Delta_k - \sum_{n \neq k} \frac{v_n^2}{\omega_{kn} + \Delta_k} \right)^2 + v_k^2 \left( 1 + \sum_{n \neq k} \frac{v_n^2}{(\omega_{kn} + \Delta_k)^2} \right) \right) \right., \quad (7.5.15)$$

which is still exact but seems to be a bit more suitable for asymptotic analysis as it reminds the Lorentzian form of the local density of states. To highlight the analogy even more, we can assume Eq. (7.5.9) to hold, neglect  $\Delta_k$  where needed, and get

$$\psi_E(\varepsilon)^2 \stackrel{(7.5.9)}{\sim} \frac{v_k^2}{(\omega_k + \Delta_k \Gamma_k^2)^2 + v_k^2 \Gamma_k^2}, \quad (7.5.16)$$

or, proceeding further with (7.5.11), get

$$\psi_E(\varepsilon)^2 \stackrel{(7.5.11)}{\sim} v_k^2 / \omega_k^2. \quad (7.5.17)$$

As we can see, the indirect resonance condition (7.1.5) (or, rather, (7.5.11)) plays the role of the applicability condition of the eigenstates' perturbation theory expression (7.2.1) (or, rather, (7.5.17)). The regularized occupation ansatz (7.2.2), in its turn, behaves similarly to the Lorentzian approximation (7.5.16), so we expect  $1/\Gamma_k^2$  to serve as a microscopic analog of the phenomenological threshold  $C/\Omega$ .

The numerical assessment of the approximation (7.5.16) is shown in Fig. 7.10. Looking at these plots, one may notice a curious fact that could have been seen from the approximation's derivation itself: each fixed-index curve plotted according to Eq. (7.5.16) approximates not one but two eigenstates with neighboring eigenenergies! Indeed, the approximation led to Eq. (7.5.5) states that the branch  $E(\varepsilon)$  corresponding to  $\Delta_k(\varepsilon) = E(\varepsilon) - E_k$  should be the closest one to  $E_k$ , and this non-analytic closeness condition forces our approximation to jump between different branches of  $E(\varepsilon)$ : for the large negative  $\varepsilon$  the closest  $E(\varepsilon)$  is larger than  $E_k$ , while for the large positive  $\varepsilon$  the closest  $E(\varepsilon)$  is smaller than  $E_k$ .

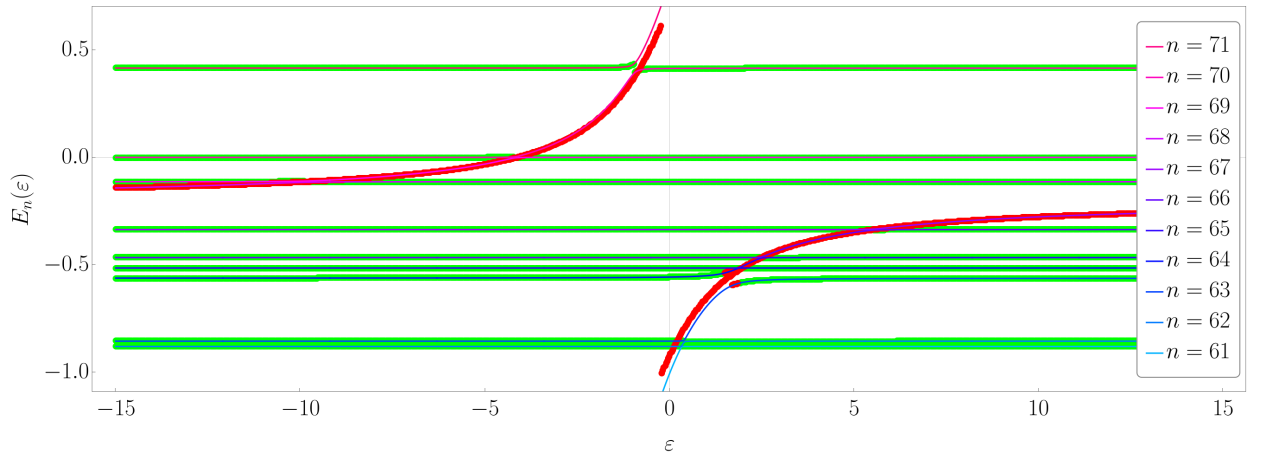


Figure 7.11: A few branches of  $E(\varepsilon)$  corresponding to Fig. 7.10(*Bottom*); the solid lines represent the exact branches, and the dashed horizontal lines mark the values of  $E_n$ . The points are plotted according to Eq. (7.5.7).

One more surprising thing one can notice from the comparison of the exact and approximate occupations in Fig. 7.10 is that sometimes the points' color turns red, signifying the approximation condition no longer holds, while the approximation still works pretty well. To understand why, consider Fig. 7.11: due to the spread of the values of  $v_n^2$ , terms from (7.5.4) with relatively large values of  $v_n^2$  are directly affecting not only their corresponding level spacings but also some next neighbors' ones. And, while, formally speaking, (7.5.16) can never hold for  $\Delta_k > \delta$ , the rare large realizations of  $v_k$ , providing  $v_n$ 's with  $n$  close to  $k$  are much smaller, force the corresponding

asymptotic expressions to “jump” between different branches, effectively describing an envelope of several different wave functions; see Fig. 7.12 for even more impressive demonstration of this effect. However, the quality of this occasionally good envelope approximation inevitably degrades as  $\Delta_k$  grows because  $\Gamma_k$  and  $\omega_k$  do not contain a valuable dependence on  $\Delta_k$ , which, eventually, cannot be ignored. In the next section, we derive a correct applicability condition for this “envelope approximation” and show its connection to the self-consistent resonance condition introduced in Sec. 7.2.

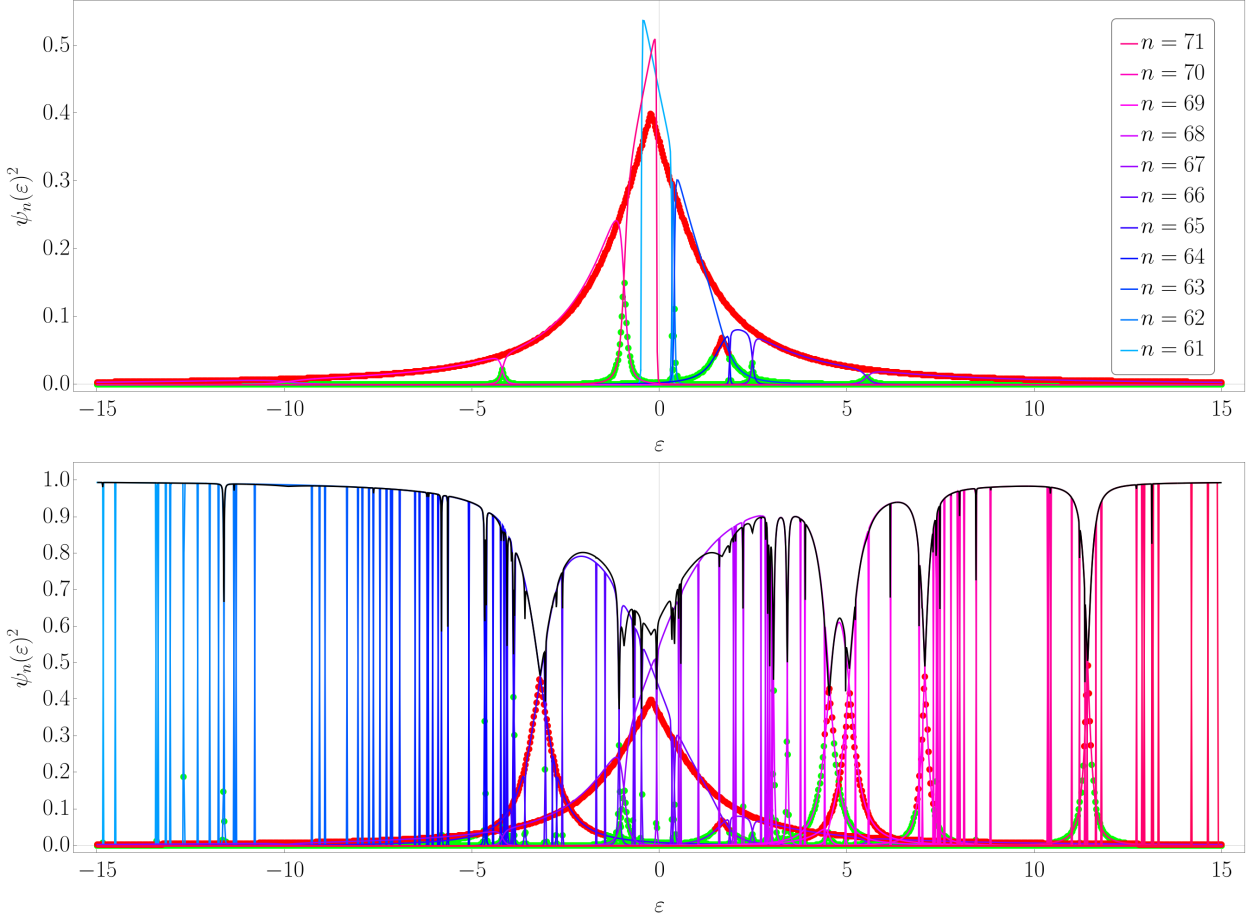


Figure 7.12: An illustration of how well (7.5.16) can work even beyond its mathematically justified range of applicability (7.5.9). Notice that the Lorentzian approximations (7.5.16) to the eigenstates of  $H_{N+1}$  are enumerated by the index  $k$  which takes only  $N$  values corresponding to the eigenstates of  $H_N$ ; hence, there is always one eigenstate which can never be approximated directly by Eq. (7.5.16) but, providing (7.5.16) works well for all other eigenstates, can be found from the normalization, as shown in the lower panel. This eigenstate corresponds to the largest occupation, always counted as a head, and corresponds to the “1+” part of the equations for  $\Omega$ , e.g., (7.2.4). (Top) The same eigenstates as in Fig. 7.10 (Bottom) approximated using Eq. (7.5.16) but in a linear scale. One can clearly see that the red envelope describes the occupations almost perfectly despite (7.5.9) does not hold. (Bottom) The whole spectrum of the eigenstates for the same realization as in Fig. 7.10 (Bottom) and in the upper panel with the additional  $(N + 1)$ th occupation (black solid line) obtained from the normalization condition by subtracting a sum of all other approximate occupations from one.

### 7.5.2 Self-consistent probabilistic approximation

To start with, let us reconsider the transformations leading from Eq. (7.5.14) to Eq. (7.5.16), and try to understand, without referencing the secular equation (7.5.4), why the Lorentzian approximation can work beyond the range of applicability set by Eq. (7.5.9). When isolating the term  $v_k^2/\Delta_k^2$  in the exact occupation expression (7.5.14), we set the stage for separating the contribution of this individual term in the sum  $\sum_{n=1}^N v_n^2/(E - E_n)^2$  from the collective contribution of all other terms. This means that the resulting approximation's applicability should be decided by the relation between the collective and individual contributions; hence, the applicability criterion should look like

$$\frac{v_k^2}{\Delta_k^2} \gg 1 + \sum_{n \neq k} \frac{v_n^2}{(\Delta_k + \omega_{kn})^2}, \quad (7.5.18)$$

where we did not rely on any approximation for  $\Delta_k$  and just used its exact value. Also, we now do not require  $\Delta_k$  to be the least-absolute-value solution for a given  $k$ ; instead, we fix a branch of  $E(\varepsilon)$  and look at all possible expressions for it,  $E(\varepsilon) = E_k + \Delta_k$ ,  $k = 1, \dots, N$ . Thus, if, for a given  $\varepsilon$  and a fixed branch of  $E(\varepsilon)$ , the condition (7.5.18) breaks down for all  $k$ , the approximation of an individual contribution fails, and we find ourselves inside the head of the wavefunction where the occupation is determined by the collective contribution. This would mean that the r.h.s. of Eq. (7.5.18) is of the order of the corresponding inverse occupation  $1/\psi_E(\varepsilon)^2$  for any  $k$ , meaning that removing any single term from the sum does not significantly affect its value. Given that we do not know how to write this collective contribution explicitly, we propose a probabilistic analog of the exact condition (7.5.18) in the form

$$\frac{v_k^2}{\Delta_k^2} \gg \Gamma_{head}^2, \quad (7.5.19)$$

where we defined  $\Gamma_{head}^2$  as a random variable emulating the distribution of the r.h.s. of Eq. (7.5.18) when its fluctuations with  $k$  are negligible. The corresponding probabilistic version of the Lorentzian occupation approximation (7.5.16) is then

$$\psi_E(\varepsilon)^2 \sim \begin{cases} 1/\Gamma_{head}^2, & \Delta_k^2/v_k^2 \gtrsim 1/\Gamma_{head}^2 \\ \Delta_k^2/v_k^2, & \Delta_k^2/v_k^2 \ll 1/\Gamma_{head}^2 \end{cases}. \quad (7.5.20)$$

In contrast to all other criteria and approximations discussed in Sec. 7.5.1, this pair cannot be compared with an individual realization of an eigenstate, but it is designed to predict a *distribution* of the tails' components of the eigenstates.

Let us now discuss how to estimate the distribution of  $\Delta_k$ . According to the exact expression (7.5.14), a site's occupation is equal to the derivative of the corresponding eigenenergy with respect to the site's onsite energy. Hence,  $\psi_E(\varepsilon)^2 = d\Delta_k/d\varepsilon$ , and we can integrate the r.h.s. of Eq. (7.5.20) to get

$$\Delta_k \sim \begin{cases} \varepsilon/\Gamma_{head}^2 + \text{const}, & \Delta_k^2/v_k^2 \gtrsim 1/\Gamma_{head}^2 \\ v_k^2/(\mathcal{E}_k - \varepsilon) \sim v_k^2/\omega_{head}, & \Delta_k^2/v_k^2 \ll 1/\Gamma_{head}^2 \end{cases}, \quad (7.5.21)$$

where  $\mathcal{E}_k$  is the integration constant. Because the above arguments do not allow an exact calculation of this constant, we introduce  $\omega_{head}$  similarly to how we did earlier with  $\Gamma_{head}^2$ , i.e., as a random variable emulating the actual distribution of  $\mathcal{E}_k - \varepsilon$ . Provided the width of the distribution of  $\mathcal{E}_k$  is small compared to the onsite disorder, one can assume  $\omega_{head}$  to be distributed as  $\varepsilon - E$ , where  $E$  marks the energy under consideration.

Finally, recalling that the piecewise form used in Eqs. (7.5.20) and (7.5.21) (and even in (7.2.2)) is just a way to regularize the otherwise singular expressions, one can rewrite the newly derived expression in a form closely resembling Eq. (7.5.16), namely, as

$$\psi_E(\varepsilon)^2 \sim \frac{v_k^2}{\omega_{tail}^2 + v_k^2 \Gamma_{head}^2}. \quad (7.5.22)$$

Associating  $1/\Gamma_{head}^2$  with  $\psi_{head}^2$  from Eq. (7.2.1), we finally obtain the mathematical justification for the extended range of applicability of the Lorentzian approximation Eq. (7.5.16) and realize it is just the microscopic version of the self-consistent criterion phenomenologically introduced in Sec. 7.2. In fact, we could have used this Lorentzian regularization instead of Eq. (7.2.2) already there, but, given that it does not drastically improve predictions while significantly complicates formulas, we prefer the piecewise regularization as given by Eq. (7.2.2).

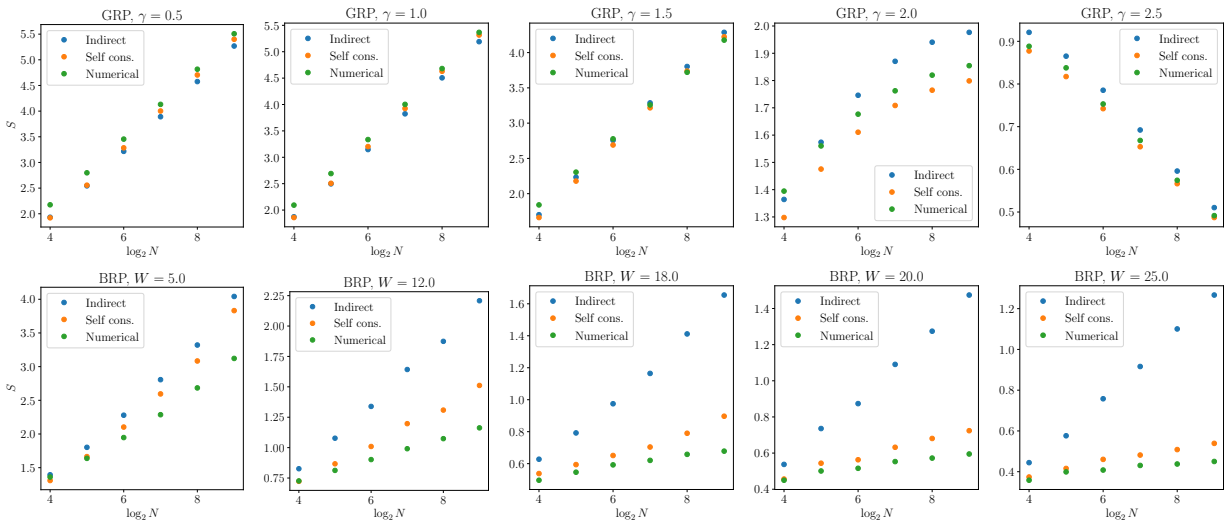


Figure 7.13: Comparison between different resonance conditions for the Gaussian RP model at different  $\gamma$ 's (top row) and the Bernoulli RP model at different  $w$ 's (bottom row). The blue points (named “Indirect”) are computed using the indirect resonance condition  $\Delta_k > \min(|E_{k-1} - E_k|, |E_k - E_{k+1}|)$  with  $\Delta_k$  from Eq. (7.5.7) to separate tails from heads and using the Lorentzian approximation (7.5.16) to calculate  $C$  and  $S$  via Eq. (7.2.4) and Eq. (7.2.8). The orange points (named “Self cons.”) are obtained using the self-consistent criterion (7.2.3) and the equations below but with  $\omega_k$  calculated via Eq. (7.5.8). The green points are obtained numerically using the exact eigenfunctions.

As one final remark, let us get back to the threshold problem and its solution we discussed in Sec. 7.2. As we mentioned there, provided the distribution of the dressed hopping has a characteristic scale, the self-consistent resonance condition (7.2.3) is roughly equivalent to the indirect resonance condition (7.1.5) derived from the prescription  $\Delta < C\delta$ , with  $C$  being the correct threshold. However, as  $C$  is the total weight of the eigenstate’s head, it cannot be larger than one. How is it then possible to claim that the self-consistent condition (7.2.3) can explain the extended range of applicability of Eq. (7.5.16) when the corresponding  $\Delta_k$  clearly exceeds the mean level spacing? The answer lies in the absence of the characteristic scale of the Bernoulli RP’s dressed hopping distribution. Indeed, since the distribution is clearly heavy-tailed, the threshold argument from the Sec. 7.2 is not applicable here, and the resonance condition (7.2.3) for the Bernoulli RP model goes beyond the condition (7.1.5), which we can see in the Fig. 7.13.

A summary of all the resonance conditions, eigenstate approximations, their applicability conditions, and their interrelations studied throughout the Chapter, is given in Table 7.1.

| Phenomenological condition                             | Its microscopic analog           | Wave function profile           |
|--|----------------------------------|---------------------------------|
| Direct, $\Delta \gtrsim \omega$ , (7.0.1)              | –                                | –                               |
| Indirect, $\Delta \gtrsim \min\{\delta, v\}$ , (7.1.5) | Applicability condition (7.5.11) | Singular, (7.2.1) & (7.5.17)    |
|  | Applicability condition (7.5.9)  | Lorentzian, (7.5.16)            |
| Self-consistent, (7.2.3)                               | Probabilistic condition (7.5.19) | Regularized, (7.2.2) & (7.5.22) |

Table 7.1: Resonance conditions studied throughout the Chapter and their relations to the applicability conditions from Sec. 7.5.1 and to each other.

## 7.6 Conclusion

In this Chapter, we have systematically addressed the concept of resonances, intending to bridge the gap between the naive, physically intuitive definition and a predictive tool able to reliably compute relevant quantities such as participation entropies and their corresponding fractal dimensions. We have achieved this goal by introducing a self-consistent resonance criterion, that has many advantages. First of all, it is physically grounded and formally justified, both in terms of a perturbation theory expansion for the wave function of a new site added to the system and via a controlled approximation of the exact size-increment equation describing the site addition (see Sec. 7.5.1). Moreover, it is free from a problem that is typical of other definitions of resonances: it does not make use of an arbitrary threshold to decide whether a site is in resonance or not, but the self-consistency automatically amends this issue.

We have also proposed an ansatz for approximating the wave function, which is tightly bonded to the resonances picture and distinguishes between components according to the resonance criterion prescription: the support set components are approximated with Haar random vectors, while the tails are approximated according to the second-order perturbation theory. Within this ansatz, we could predict analytically the participation entropy and the support set dimension of the finite size Gaussian Rosenzweig-Porter model, in perfect agreement with the numerical results and with other approaches (see Ref. [411] and App. D.2). We could also make new predictions for the  $\beta$ -function of the model. The analytical solution of this model has been possible because of the known distribution of the dressed hoppings. We have also tested our method on other, more complicated random matrix models, for which the distribution of the dressed hoppings is not known, forcing us to compute it numerically. Also in those cases, we have shown how our method captures correctly the behavior of the system, with the analytical predictions that seem to approach the numerical curves as the size grows. However, for these other models, the ansatz we have proposed is not as precise as for the Gaussian Rosenzweig-Porter model, thus leading to a discrepancy in the numerical values. We leave for future work the goal of finding a more refined ansatz for the ergodic part of the wave function and the analytical computation of the dressed hopping distribution.

Finally, the careful finite-size analysis we performed for the Log-normal Rosenzweig-Porter model raised questions about whether it can actually serve as a proxy to the Anderson model on RRG, and to what extent. As an alternative, we introduced the Bernoulli Rosenzweig-Porter model which is expected to serve as a better proxy while preserving the simplicity of the RP models and thus saving the hope of obtaining its analytical description, sooner or later.

## Chapter 8

# Non-parametric unsupervised learning and localization transitions

*In this Chapter we take a different viewpoint on the issues discussed in Part II of the Thesis and propose an unsupervised learning approach to address the localization transition induced by disorder. The approach we will use here is based on the analysis of the data space generated by multiple samplings of the wave function, making the method suitable for experimental applications. We show that this technique gives results that are fully compatible with the exact numerical results constituting the state of the art in the field. In particular, we determine the critical point and critical exponents for the Anderson model on RRGs (discussed previously in Chapter 6) and on a prototypical interacting model. The results presented in this Chapter are based on the publication [7].*

TOGETHER with the huge theoretical effort in understanding non-equilibrium phases of matter, there has been increasingly large attention to these unusual phases of matter also in the experimental community; as a consequence of the possibility of realizing theoretical models in the laboratory [419–424]. However, it is often difficult to find observables that are readily accessible and theoretically predictable.

In this Chapter, we propose a data-science-inspired method in the context of disordered quantum systems, with the goal of showing that localization transitions can also be investigated through the behavior of the classically encoded configurations in data space. The advantages of using this class of methods are twofold: on the one hand, the agnosticism guaranteed by the approach makes it applicable to a large variety of systems (as we will partly show in the rest of the Chapter), while on the other hand, it is easily applicable to real experiments, as the only input of the method is a data-set, no matter if obtained numerically or in the lab. To achieve our goal, we employ principal components analysis (PCA), which is used to detect the most relevant directions in data space and to compress (to project) the data set toward the significant and restricted manifold [425, 426]. From the eigendecomposition of the sample covariance matrix, we introduce the Rényi-entropy of the normalized eigenvalues  $\lambda_j$ 's ( $\sum_{j=1}^d \lambda_j = 1$ ) as

$$S_{\text{PCA}}^{(n)} := \frac{1}{1-n} \ln \sum_{j=1}^d \lambda_j^n, \quad (8.0.1)$$

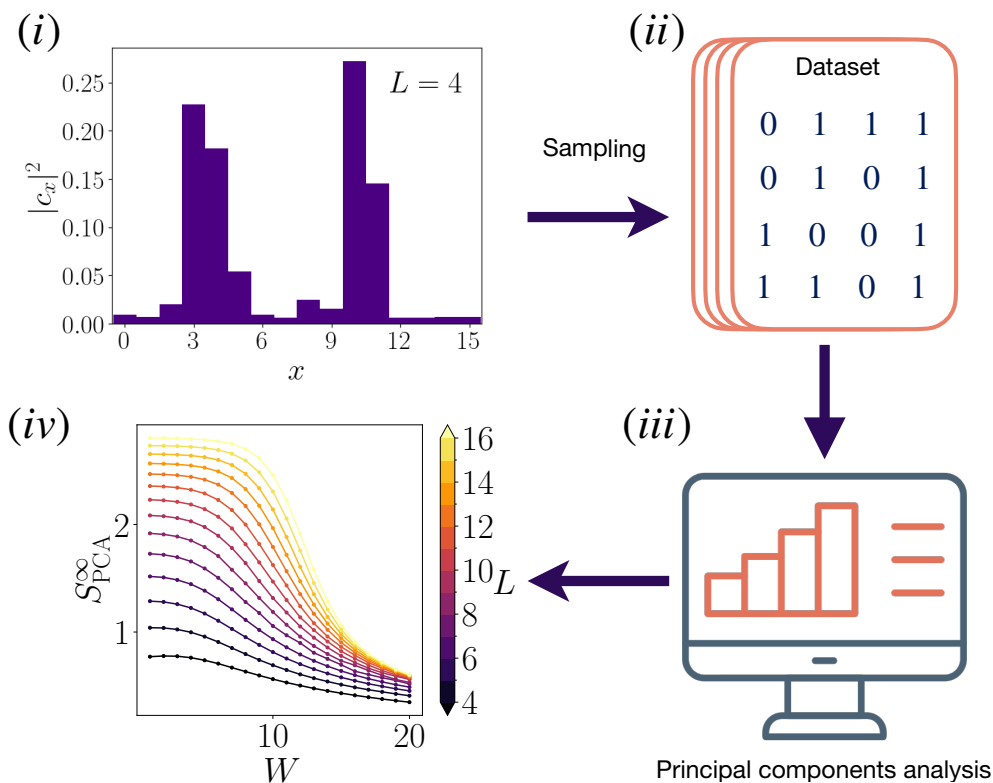


Figure 8.1: Sketch of the approach used in this Chapter. Given a quantum state  $|\psi\rangle$ , (i) we chose a basis  $|\psi_x\rangle$  and we sample (measure) the state according to the probability distribution  $|c_x|^2 = |\langle\psi_x|\psi\rangle|^2$ . In this example, we consider a system with Hilbert space dimension equal to  $2^L$  ( $L = 4$ ). (ii) We encode the measurement outcome as a string of zeros and ones corresponding to the binary representation of the integer  $x \in [0, 2^L]$ , labeling the basis state. (iii) We perform the principal components analysis (PCA) and extract the information we are interested in by averaging over several realizations of the disorder. In (iv), we show the behavior of  $S_{\text{PCA}}^\infty = -\ln \lambda_1$  (see Eq. 8.0.1 and text for details) as a function of the disorder strength  $W$ , for several sizes  $L$ .

and we show analytically that  $S_{\text{PCA}}$ , i.e.  $S_{\text{PCA}}^{(n=1)}$ , is linked to the participation entropy, often employed for investigating disordered induced transitions [5, 7, 140]. Therefore, unlike usual non-parametric approaches, our physically informed method is guaranteed to work, in the limit of sufficiently large samples. We show that the infinite-order  $S_{\text{PCA}}^\infty$  can be employed to estimate the critical point with remarkable accuracy in agreement with recent results [140, 427] and displays universal behavior around the transition. Moreover, we employ a data set whose dimension is smaller than the full Hilbert space, thus being readily applicable in modern quantum simulators where large data sets of snapshots of the state of the system are routinely collected [428–431].

We remark here that data-science-inspired approaches have already found several successful applications in various fields, ranging from classical and quantum statistical physics [432–440] to molecular science and quantum chemistry [441, 442].

To prove the validity of our approach, we showcase it on a prototypical example of disordered quantum systems displaying a localization transition: the Anderson model on random regular graphs (RRGs). The latter displays Anderson localization [96] with an usual scaling of expectation values with system size [5, 107, 127, 129, 140, 338, 339, 351, 443], and is especially hard to tackle numerically [137, 140], thus being the ideal test bench for the method we propose. We also present results for a many-body disordered model that is believed to display a localization transition, showing that the method presented in this Chapter is also effective for interacting systems.

The remainder of the Chapter is structured as follows. In Sec. 8.1 we present the method we use to sample the wavefunction and the rationale behind the analysis of the data. In Sec. 8.2 we exploit the Anderson model on RRGs, giving a quick presentation of the system and its properties, and showcasing the effectiveness of the approach. Finally, in Sec. 8.4 we give our conclusions and discuss possible outlooks.

## 8.1 Wavefunction sampling and analysis

The interest in non-parametric unsupervised learning methods relies on their vast range of applicability, a consequence of their agnosticism towards the problem under analysis. Such versatility is ensured by the fact that the only required input is a data set, which in principle can come from any sort of source, and whose geometrical properties are analyzed to extract information from the underlying physical system. In our case, the data sets consist of matrices in which each row corresponds to a single snapshot of a wave function, i.e. a measurement in a given basis (see Fig. 8.1 (ii)). However, the method presented here may be applied to a plethora of experimental and numerical situations.

In practice, let us assume to have a state described by

$$|\psi\rangle = \sum_{x=1}^{\mathcal{N}} c_x |\psi_x\rangle, \quad (8.1.1)$$

where  $\{|\psi_x\rangle\}_{x=1,\dots,\mathcal{N}}$  is a suitable basis in the Hilbert space  $\mathcal{H}$  of dimension  $\mathcal{N} = \dim(\mathcal{H})$ . The sampling of  $|\psi\rangle$  amounts to sample, according to the probabilities  $|c_x|^2$ , the corresponding basis vectors  $|\psi_x\rangle$ . The choice of the relevant basis and the encoding of the sampling into an actual data set is one of the aspects to be investigated. For example, considering a chain of qubits, one could measure a state  $|\psi\rangle$  in the computational basis and getting as an outcome a string of zeros and ones. In this Chapter, we label as  $X_i = (n_{i,1}, \dots, n_{i,d})$  an element of the configuration space, where each  $n_{i,x}$ , called ‘feature’, encodes some information of the sampled state; e.g. in the previous scenario, each feature corresponds to the measured state of the qubit (say 0 or 1) and the total number of features  $d$  is equal to the size of the system. The full target data set is a collection

of  $N_r$  repetitions of  $X_i$  :

$$X = (X_1, X_2, \dots, X_{N_r}) \quad (8.1.2)$$

and can be represented as a  $(N_r \times d)$  matrix  $X_{i,j}$ .

Concretely, the method we employ is the following. We define the centered data set  $X_c$ , whose elements are

$$(X_c)_{i,j} = X_{i,j} - \frac{1}{N_r} \sum_i X_{i,j} \quad (8.1.3)$$

and compute the covariance matrix  $C = X_c^T X_c / (N_r - 1)$ . Then, we perform the eigendecomposition  $C = V^T K V$ , where  $K = \text{diag}(k_1, \dots, k_r)$  is the diagonal matrix of the  $r$  eigenvalues of  $C$  ordered in descending order, and  $V = (v_1, \dots, v_r)$  is the rotation whose columns  $v_j$  identify the  $j$ -th relevant directions. In the new reference frame defined by  $V$ , the variance of the data along the  $j$ -th direction is given by  $k_j$ , and thus  $\lambda_j \equiv k_j / (\sum_i k_i)$  represents the percentage of encoded information along the direction  $v_j$  and is dubbed  *$j$ -th explained variance ratio* ( $\lambda_1 > \lambda_2 > \dots > \lambda_r$ ).

The motivation for our study comes from the understanding that the  $S_{\text{PCA}}$  — recently introduced as a measure of the information content of a physical data set [436, 438] — is connected to the participation entropy. This is particularly relevant since the participation entropy is the typical quantity of interest when studying disordered systems and is used for estimating an order parameter: the fractal dimension [5, 140, 351, 409, 444]. The presence of such a connection between  $S_{\text{PCA}}$  and participation entropy is intriguing as, in usual scenarios, when non-parametric estimators are employed, a clear physical picture is missing. Here we show that studying the principal components is physically meaningful as they are connected to an order parameter and thus they are guaranteed to store information of the physical process.

Let us link  $S_{\text{PCA}}$  and participation entropy by considering the sampling of a state written as in Eq.(8.1.1). For each sample on the basis  $\{|\psi_x\rangle\}_{x=1,\dots,\mathcal{N}}$ , we obtain as an outcome an integer  $x$  with probability  $|c_x|^2$ . Let us assume to encode this as an  $\mathcal{N}$ -dimensional vector with only a non-zero entry corresponding to the index  $x$  of the sampled basis vector  $|\psi_x\rangle$ . Then, the element of the configuration space would be vectors of the type  $X_i = (0, \dots, 0, 1, 0, \dots, 0)$ . In Appendix E, we prove that for a large enough number of samplings  $N_r \gg \mathcal{N}$ , one gets  $C = X^T X / (N_r - 1) = \text{diag}(|c_1|^2, |c_2|^2, \dots, |c_{\mathcal{N}}|^2)$  and the  $S_{\text{PCA}}$  becomes

$$S_{\text{PCA}} = - \sum_j |c_j|^2 \ln |c_j|^2, \quad (8.1.4)$$

which is exactly the definition of the participation entropy. However, let us observe that the correspondence we have shown is only true in the limiting case  $N_r \gg \mathcal{N}$  and that the data set contains exponentially large vectors. Therefore, one could ask if working with different choices of encoding and finite sampling could provide estimates on the critical parameters of the transition as well.

We show that this is valid by studying the behavior of  $S_{\text{PCA}}^\infty = -\ln \lambda_1$ . The rationale behind this is that  $\lambda_1$  contains all the information needed for spotting the localization transition. In fact, in the localized phase we expect a single wavefunction coefficient  $c_x$  to be dominant. The sampled data set should be such that the first explained variance ratio  $\lambda_1$  is much larger than all the others, namely there should be a single predominant direction in the data space manifold. On the other hand, in the ergodic regime, all wavefunction components should be of the same order, and thus the principal components of the samplings should have all the same importance. There should not be a preferred direction in data space, and the explained variance ratios should vanish with the system size (since the normalization  $\sum_j \lambda_j = 1$  is enforced).

In the remainder, we showcase these predictions by exploiting the Anderson model on RRGs. We find that with appropriate analysis, it is possible to retrieve remarkably good estimations on

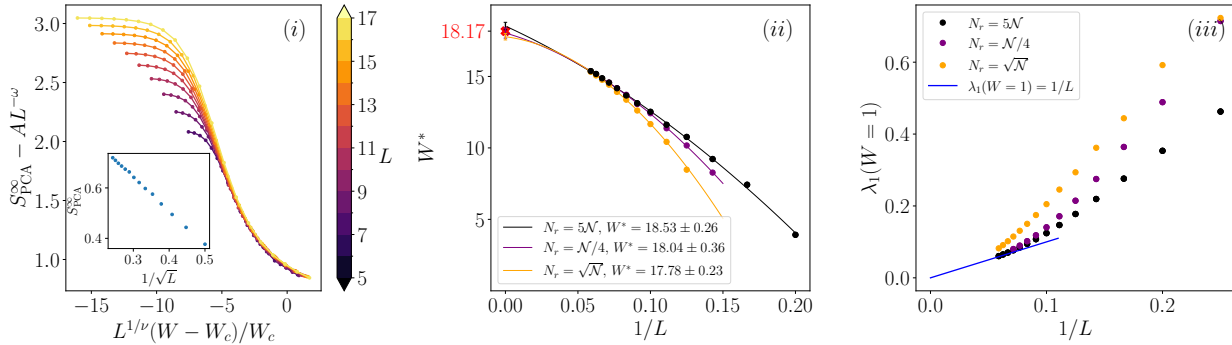


Figure 8.2: (i) Plot of the finite size scaling of  $S_{\text{PCA}}^{\infty}$  (as in Eq. (8.2.2)). We fix  $\nu = 1$  and  $\omega = 1/2$  and only tune the parameter  $A$  to obtain the collapse. The plot of  $S_{\text{PCA}}^{\infty} = -\log \lambda_1$  is reported in panel (iv) of Fig. 8.1. (i – inset) Behavior of  $S_{\text{PCA}}^{\infty}$  at  $W = W_c$  as a function of  $L^{-1/2}$ ; we observe  $S_{\text{PCA}}^{\infty} \sim L^{-\omega}$  with  $\omega = 1/2$ . (ii) Plot of  $W^*$  vs  $1/L$ . The extrapolation to  $L \rightarrow \infty$  gives the correct position of the critical point  $W_c = 18.17$ , denoted with a red cross. Three different sets of points are shown: black dots obtained by sampling the eigenstates  $N_r = 5\mathcal{N}$  times; purple points employing  $N_r = \mathcal{N}/4$  samples; and orange dots using  $N_r = \sqrt{\mathcal{N}}$ . A parabolic fit in  $1/L$ , the easiest curve accounting for the curvature of the points, is performed and the critical value of  $W$  is extrapolated at  $1/L = 0$ . The fitting functions are  $W^* = 18.53 \pm 0.26 + (-46.73 \pm 4.66)/L + (-128.27 \pm 18.57)/L^2$  (black),  $W^* = 18.04 \pm 0.36 + (-29.31 \pm 7.01)/L + (-272.44 \pm 32.85)/L^2$  (purple) and  $W^* = 17.78 \pm 0.23 + (-13.45 \pm 5.40)/L + (-475.69 \pm 31.19)/L^2$  (orange). In Appendix E we elaborate more on the fitting procedure. (iii) Behavior of  $\lambda(W = 1)$  vs  $1/L$ , both for  $N_r = 5\mathcal{N}$  (black) and  $N_r = \mathcal{N}/4$  (orange) samples. It is expected, at large sizes, that  $\lambda_1$  in the ergodic phase goes as  $1/L$ , being the inverse of the rank of the matrix  $C$ . This behavior is indeed reached at large sizes as all sets of points approach the  $1/L$  line in blue, which is a guide for the eye.

the position of the critical point of the disordered induced transition and perform a clean finite-size scaling. We do so by employing a modest number of measurements and obtain results that are in agreement with the literature and with statistical errors that are compatible with state-of-the-art methods.

## 8.2 Anderson model and results

Let us consider the Anderson model for a single quantum particle on a random regular graph (RRG), as we introduced in Chapter 6. We remind that the Hamiltonian of the model is [96]

$$H = - \sum_{\langle x,y \rangle} (|x\rangle \langle y| + |y\rangle \langle x|) + \sum_x \epsilon_x |x\rangle \langle x|, \quad (8.2.1)$$

where  $x, y$  are integers that label the node of the graph. The Hamiltonian consists of two terms. The first one is the adjacency matrix of the graph ( $\langle x, y \rangle$  denotes nearest neighbor sites), in which, by construction, each node (or vertex) has connectivity  $K_0$  (i.e. fixed vertex degree  $\mathcal{D} = K_0 + 1$ ). The second term represents a random field applied on each site, with the parameters  $\epsilon_i$  being independent and identically distributed random variables sampled according to the box distribution  $g(\epsilon) = \theta(|\epsilon| - W/2)/W$ . Denoting with  $\mathcal{N}$  the number of vertices of the graph, we introduce a length scale  $L = \ln_{K_0} \mathcal{N}$ , representing the diameter of the graph, i.e. the maximal length of the shortest paths connecting two nodes.

For  $K_0 = 2$ , which will be assumed in the rest of the Chapter, the critical value of the disorder is known to be  $W_c \simeq 18.17$  [107, 137, 140, 390]. For  $W \ll W_c$  the system is ergodic, and spectral quantities in the thermodynamic limit assume the values predicted by random matrix theory. By increasing  $W$  at finite system size, the model displays a crossover to the localized regime, where Poisson statistics describes the energy spectrum. Such crossover becomes a phase transition in the thermodynamic limit, with the crossover point drifting to larger  $W$  as  $\mathcal{N}$  is increased and reaching  $W_c$  in the  $\mathcal{N} \rightarrow \infty$  limit [5, 137, 140]. To find the critical disorder for which the whole system ceases to be ergodic, one has to focus on eigenstates near the middle of the spectrum, i.e. around zero energy for the model under consideration. This is because the eigenstates in the middle of the spectrum are those that need more disorder to localize [348, 445] (on the contrary, the ground state is always localized).

The numerical simulations on the model in Eq. (8.2.1) are performed as follows. To find the eigenstates, we execute a full exact diagonalization of its matrix for  $L \leq 14$ , or employ the POLFED algorithm for larger system sizes [446]. We calculate  $\sim \sqrt{\mathcal{N}}$  eigenvectors in the middle of the spectrum. For each one (see Fig. 8.1), (i) we sample, according to the probabilities  $|c_x|^2$ , the corresponding basis vectors  $|\psi_x\rangle$ . Since the problem is single-particle, we consider the basis  $|\psi_x\rangle = |x\rangle$  where the particle occupies the site  $x$ . Then, the output of a single sampling will be the position of the particle  $x$ . (ii) We encode the information as a  $L$ -dimensional vector corresponding to the binary representation of the integer  $x$ ; (iii) we perform the analysis on the data set and (iv) average the results over a number of realizations of the disordered Hamiltonian in Eq. (8.2.1) ranging from  $O(10^4)$  for the smallest sizes to  $O(10^2)$  for  $L = 17$ .

We look at the behavior of  $S_{\text{PCA}}^\infty$  as a function of the strength of the disorder  $W$  and for different sizes of the graph, that we distinguish via the length scale  $L$  (see Fig. 8.1 (iv)). We observe that  $S_{\text{PCA}}^\infty = -\ln \lambda_1$  shows a crossover from the delocalized to the localized phase. In the limit of infinite disorder, the wavefunction is fully localized and it is expected that  $S_{\text{PCA}}^\infty$  approaches 0. On the other side, in the limiting case  $W \sim 0$ , there is no preferential configuration sampled. All the non-vanishing  $\lambda_j$  are the same, and thus  $\lambda_1 \sim 1/L$ . This holds for any  $W < W_c$  in the large  $L$  limit. We show the behavior of  $\lambda_1$  for  $W = 1$  in Fig. 8.2(iii), as a function of  $1/L$ , observing that it displays the expected behavior for large  $L$ .

To address the critical exponents, we perform a finite-size scaling of  $S_{\text{PCA}}^\infty$ . We employ the scaling ansatz presented in Ref. [140] for the average gap ratio, which in our case takes the form

$$S_{\text{PCA}}^\infty = f((W - W_c)L^{1/\nu}) + L^{-\omega} f_1((W - W_c)L^{1/\nu}), \quad (8.2.2)$$

where  $f(x)$  and  $f_1$  are, respectively, the leading and subleading scaling functions and  $\nu$  and  $\omega$  are the critical exponents. Here,  $\nu$  governs the divergence of the correlation length at the critical point when  $W \rightarrow W_c^-$  and does not depend on the specific observable. In Ref. [140] it is found to be  $\nu = 1$ . On the other hand,  $\omega$  governs the behavior of the observable under analysis at the critical point  $W = W_c$ . In the case of the average gap ratio, it is found  $\omega = 2$  [140]. In our case, we find  $\omega = 1/2$  for  $S_{\text{PCA}}^\infty$ , as it can be seen from the inset of Fig. 8.2(i). Setting  $\nu = 1$  we obtain a very clean collapse in Fig. 8.2(i). We have approximated the subleading scaling function  $f_1(x)$  with a constant  $A$ , which is the only free parameter of our analysis, and we have set  $W_c = 18.17$  [107, 137, 140, 390].

To estimate the critical point  $W_c$ , we study the intersection of  $S_{\text{PCA}}^\infty$  with the horizontal line  $S_{\text{PCA}}^\infty = 1$ , since the position of the intersection point  $W^*$  drifts when increasing the size of the graph, approaching eventually  $W_c$ . Different choices of the position of the line give results compatible with the ones shown here. We plot the behavior of  $W^*$  as a function of  $1/L$  in Fig. 8.2(ii). Here we report the results in the case  $N_r = \sqrt{\mathcal{N}}$  (orange),  $N_r = \mathcal{N}/4$  (purple) and  $N_r = 5\mathcal{N}$  (black) and we perform a parabolic fit in  $1/L$  to estimate  $W_c$ . We observe that both

extrapolations give a value that is compatible with the one in the literature, also in the case of a modest number of configurations sampled. In particular, we find  $W_c(\sqrt{\mathcal{N}}) = 17.78 \pm 0.23$ ,  $W_c(\mathcal{N}/4) = 18.04 \pm 0.36$  and  $W_c(5\mathcal{N}) = 18.53 \pm 0.26$ , where the critical value of the disorder is  $W_c = 18.17 \pm 0.01$ . Let us remark here that the critical value  $W_c = 18.17 \pm 0.01$  is obtained by solving self-consistent equations for the propagator on the Bethe lattice [390], thus allowing for a higher precision. Instead, state-of-the-art numerical methods to estimate  $W_c$  on RRGs have errors on the estimates that are compatible with the ones of our approach [137, 140].

### 8.3 Study of many-body localization

In the previous Section, we have shown how the method we presented, based on the principal-component analysis of the wave-functions samplings, allows us to predict with good accuracy the critical properties of the Anderson transition on RRGs. As already mentioned, the choice of that model is twofold: on the one hand, its critical properties are known from other methods, allowing us to benchmark the predictive power of our method. On the other hand, despite being a single-particle problem, it displays features that are typical of interacting systems, making it a non-trivial model to study.

Now we want to show explicitly that our method can be applied, without modifications, to genuine disordered interacting systems that are believed to present a localization transition. For this purpose, we consider the ‘Imbrie model’ [116, 120], defined by the Hamiltonian

$$H = \sum_{i=1}^{L-1} J_i \sigma_i^z \sigma_{i+1}^z + \sum_{i=1}^L (h_i \sigma_i^z + \sigma_i^x), \quad (8.3.1)$$

where  $\sigma_i^\alpha$  ( $\alpha = x, y, z$ ) are the Pauli matrices on site  $i$ ,  $J_i \in [0.8, 1.2]$  and  $h_i \in [-W, W]$ . This model has been used in Ref. [116] to prove the existence of many-body localization in quantum spin chains at infinite temperature, despite there are concerns about the validity of the proof [125, 177, 447]. The results are displayed in Fig. 8.3.

The analysis performed is exactly the same we have used in the previous Section for the RRG. We consider the crossing point of  $S_{\text{PCA}}^\infty$  with a horizontal line and analyze the flow of the crossing points  $W^*(L)$  when the system size is increased, as we show in Fig. 8.3 (iii). Our analysis gives a finite value of the critical disorder  $W_c = 7.0 \pm 0.3$ , compatible with the literature [120]. However, the behavior of  $W^*(L)$  might change when the system sizes are increased by orders of magnitude, leading to a larger value of  $W_c$ . Speculating on the true position of the localization transition is beyond the scope of this work. The inability to perform quantitative comparisons is the main motivation that has led us to use the Anderson model on RRGs as the benchmark for our method.

### 8.4 Conclusions

In this Chapter, we introduced a non-parametric unsupervised learning approach to tackle localization transitions. We have connected analytically the eigendecomposition of the sample covariance matrix to the participation entropy, physically motivating our approach. We have showcased it on the Anderson model on a random regular graph that, even if non-interacting, displays important features that are reminiscent of many-body localization and presents a serious challenge both analytically and numerically. Exploiting this example we have shown that disordered quantum systems can be characterized with data-science-inspired approaches and localization transitions can also be seen as geometric transitions in data space.

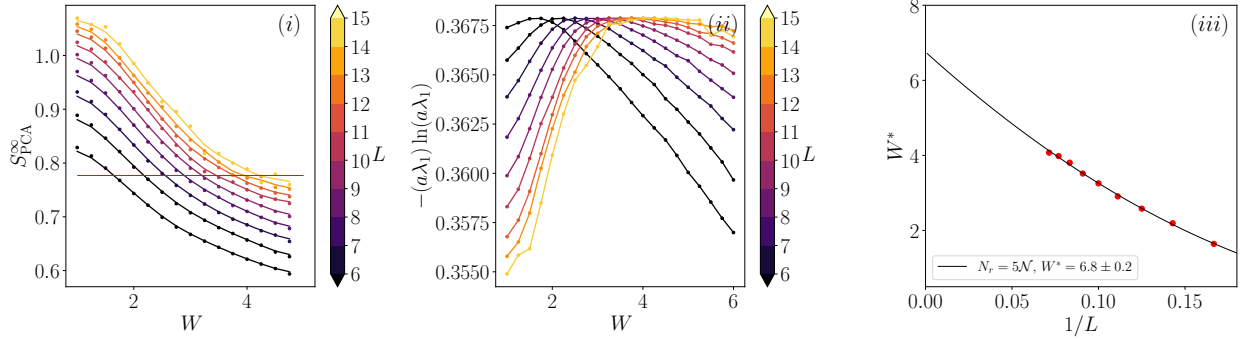


Figure 8.3: (i) Plot of  $S_{\text{PCA}}^{\infty}$  for the ‘Imbrie model’ defined in Eq. (8.3.1). We look at the crossing point between  $S_{\text{PCA}}^{\infty}$  and the horizontal line in red to identify the critical point. With the available sizes, the optimal choice is the line  $S_{\text{PCA}}^{\infty}(W^*(L), L) = 1 + \ln a$ , with  $a = 0.8$ . The values  $W^*(L)$  of the crossing points correspond to the positions of the maxima of the function  $-(a\lambda_1) \ln(a\lambda_1)$ . In the plot, the dots are the numerical data, while the continuous lines are obtained by applying a Gaussian filter to the data and are a guide for the eye. (ii) Plot of  $-(a\lambda_1) \ln(a\lambda_1)$ , with  $a = 0.8$ . The position of the maxima is identified by the red points. The points flow with increasing system size towards the critical value of the disorder. (iii) Plot of  $W^*(L)$  in  $1/L$  scale. For the model investigated the slope of the points  $(W^*(L), 1/L)$  grows with  $L$ . A quadratic fit gives a good interpolation of the points and predicts a critical value of the disorder  $W_c = 7.0 \pm 0.3$ . This result is in agreement with previous results in the literature [120].

We have studied the infinite order Rényi entropy  $S_{\text{PCA}}^{\infty}$  of the eigenvalues covariance matrix as a function of disorder strength and system size, to extract an estimate of the critical value of the disorder  $W_c$ , that is remarkably in agreement with results in the literature — in particular considering the hard challenge presented by the model investigated [137, 140]. As observed in Fig. 8.2(ii), a modest number of measurements suffices for estimating the transition point, such that the approach described here can be considered of practical use for nowadays quantum simulators with local addressing.

Furthermore, we have performed a finite size scaling of  $S_{\text{PCA}}^{\infty}$  by employing the scaling ansatz presented in Ref. [140] for the average gap ratio, and we have obtained results compatible with the literature.

We observe that the method employed requires no a priori knowledge of the physical system under investigation, being then a powerful tool also in the study of other physical scenarios, in particular many-body problems. Indeed, we also presented results for the ‘Imbrie model’ [116, 120], which is believed to display many-body localization, and thus we exploit it to prove that our method applies also to interacting scenarios.

We note that the same analysis could be performed to tackle problems such as out-of-equilibrium phase transitions or the classification of quantum phases of matter. Moreover, one could try to understand if this kind of approach could be used in combination with randomized measurements [448, 449], to extract relevant features of many-body quantum states prepared in the laboratory.

## Appendix of Part II



## Appendix C

# Additional information - Renormalization group analysis of Anderson localization in infinite dimensions and random graphs

### Data analysis for the fractal dimension

As mentioned in the main text, the numerical data for the fractal dimension are extracted from the participation entropy, defined as

$$S_q = \left\langle \frac{1}{1-q} \log_2 \sum_{i=1}^K |\varphi(i)|^{2q} \right\rangle, \quad (\text{C.0.1})$$

and in particular we used  $S_q$  for  $q \rightarrow 1$ , which is the von Neumann entropy

$$S_1 = - \left\langle \sum_{i=1}^K |\varphi(i)|^2 \log_2 |\varphi(i)|^2 \right\rangle. \quad (\text{C.0.2})$$

From  $S_1$ , the fractal dimension can be extracted as  $D(L) = dS_1/dL$  (or equivalently as the  $S_1(L) = D(L)L + c(L)$  [140]). We have absorbed here the  $\ln K_0 = \ln 2$  factor in the definition of  $S_q$ . Having at our disposal finite increments in the system size  $L$ , we computed the fractal dimension as

$$D(L) = S_1(L+1) - S_1(L) \quad (\text{C.0.3})$$

and we then consider, for the numerical analysis,  $\overline{D}(L+1/2) = (D(L+1) + D(L))/2$ .

In order to obtain continuous curves, we *interpolated* the numerical values of  $\overline{D}(\ln K)$  with two different fits, depending on the value of  $W$ . Denoting  $\ln K = x$  for brevity, we use a Padé-like function for the fit at  $W \leq 17$

$$f(x) = \frac{x^3 + c_1x^2 + c_2x + c_3}{x^3 + d_1x^2 + d_2x + d_3}, \quad (\text{C.0.4})$$

so that  $f(x) = 1$  for  $x \rightarrow \infty$ , as it should in the delocalized phase. For larger values of  $W$  instead, we use a fourth-order polynomial fit in  $1/x$ , that perfectly fits the numerical data. We use these

functions to compute the  $\beta$ -function using the definition and to produce the plot in Fig. 2 of the Letter, employing only the range of system sizes for which we have numerical data so that we are just interpolating, without extrapolations.

We then used these data also to determine two possible forms for the function  $\beta_0$ . The function  $\beta_0$  has to fit the envelope that the numerical data are generating for  $D \gtrsim 0.3$ , and we numerically do so by fitting the set of points that are obtained by considering, for any small interval  $dD$  ( $D \geq 0.3$ ), the maximum value of  $\beta(D, K)$  for all  $W$ . We use two different fitting functions, having different behaviors in  $D = 0$ . The dashed line in Fig. 6.2 is obtained through

$$g(x) = a_1 x(1-x) + a_2 x(1-x)^2 + a_3 x(1-x)^3 + a_4 x^2(1-x) + a_5 x^2(1-x)^2 + a_6 x^3(1-x), \quad (\text{C.0.5})$$

while the dotted line is obtained using the fitting function

$$h(x) = b_1 \sqrt{x}(1-x) + b_2 \sqrt{x}(1-x)^2 + b_3 x(1-x) + b_4 x^{3/2}(1-x). \quad (\text{C.0.6})$$

We report the fitting coefficients in Tab. C.1, and the resulting interpolations compared with the bare data in Fig. C.1

| $g(x)$ |       | $h(x)$ |       |
|--------|-------|--------|-------|
| $a_1$  | 0.153 | $b_1$  | 0.986 |
| $a_2$  | 0.235 | $b_2$  | 0.266 |
| $a_3$  | 0.476 | $b_3$  | 2.517 |
| $a_4$  | 0.285 | $b_4$  | 2.429 |
| $a_5$  | 0.366 |        |       |
| $a_6$  | 0.501 |        |       |

Table C.1: Fit coefficients for the functions  $g(x)$  (Eq. (C.0.5)) and  $h(x)$  (Eq. (C.0.6))

Let us remark that the function  $\beta_0$  obtained using the fitting function  $g(x)$  in Eq. (C.0.5) turns out to have the symmetry  $D \rightarrow 1 - D$  within the precision of the fit even if  $g(x)$  doesn't have such symmetry.

### $\beta$ -function for the $r$ -parameter

The same analysis performed on the fractal dimension can be reproduced for the  $r$ -parameter, once rescaled so that it ranges between 0 and 1 as

$$\phi = \frac{r - r_P}{r_{WD} - r_P}, \quad (\text{C.0.7})$$

where  $r_P \simeq 0.386$  and  $r_{WD} \simeq 0.5307$ . The same procedure outlined above for the fractal dimension  $D$  is applied to the data for the  $r$ -parameter, and the resulting  $\beta$ -function is displayed in the left panel of Fig. C.3.

Let us mention that near  $\phi = 1$  the envelope of the functions  $\beta(\phi)$  is different from  $\beta_0(D)$  and, in particular, a best fit is obtained assuming that the derivative  $\beta'(\phi \rightarrow 1)$  diverges logarithmically. This gives a qualitative approach  $\phi \rightarrow 1$

$$\phi \simeq 1 - e^{-(K/K_0)^a}, \quad (\text{C.0.8})$$

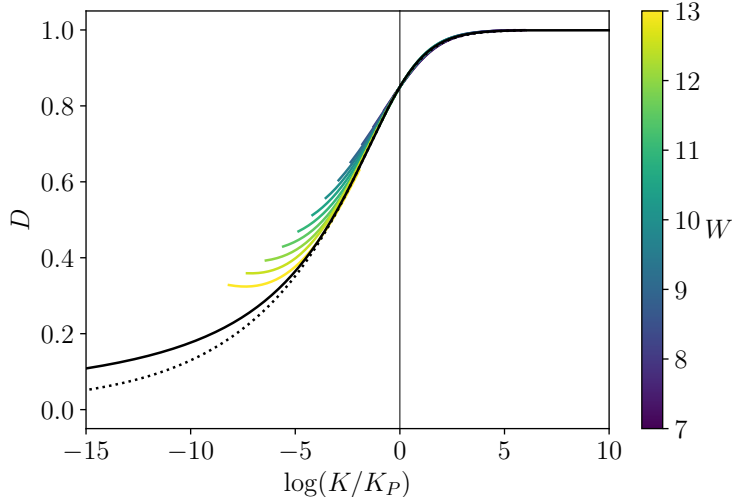


Figure C.1: Numerical data of the fractal dimension as a function of  $K$  (dots) and their interpolation using Eq. (C.0.5) and Eq. (C.0.6).

with  $a = 0.43 \simeq 1/2$ . Such difference is still explained in the one-parameter scaling, and it originates from the non-linear dependence of  $\phi$  on  $D$  (or vice-versa) near  $D, \phi = 1$ , when plotted together as in Fig. C.4.

We report in Fig. C.5 the values of  $\phi_A$  such that  $\beta(\phi_A) = 0$ , as we did for the fractal dimension. Also in this case a linear fit gives a good prediction for the critical value of the disorder. Moreover, the critical behavior of the  $\beta_1(\phi) \sim -\sqrt{\phi}$  implies that

$$\phi_c(K) \propto \frac{1}{(\ln K)^2}, \quad (\text{C.0.9})$$

which has been already observed in [140]. We report in Fig. C.6 the plot presented in [140], showing the  $1/L^2$  approach to  $r_P$  of the  $r$ -parameter, which turns out to be universal for many models of random graphs.

## C.1 $\beta$ -function in the critical region

In this Section, we want to elaborate on Equation (16) for the  $\beta$ -function presented in the main text. In particular, we want to show that, for small  $D$ , in Eq. (15) the constant  $c$  is of order unity and does not depend on  $D$  and/or  $D_A$ . In fact, in general, we could have

$$\frac{d\beta}{d \ln K} = c(D/D_A)D. \quad (\text{C.1.1})$$

We are interested in the behavior of  $c(D/D_A \simeq 1)$ , which means that we can trade  $D$  with  $D_A$ . In Fig. C.7 we show the numerical data for  $\beta^2(D)$ . If  $c(1)$  had a dependence on the initial condition, say  $c(1) \simeq D_A$ , one would have that the slope of  $\beta(D = D_A)$  would depend on  $D_A$ , and for our example we would have that the slope vanishes at the critical point, where  $D_A = 0$ . If instead  $c(1) = O(1)$  for all  $D_A$ , the slope would not depend on  $W$  and it would be finite at the critical point. We can see in Fig. C.7 that this is actually the case, with, in particular  $c = 1/2$ , proving that  $\beta_1(D, K) = \pm\sqrt{D - D_A} + O(D - D_A)$ . Let us mention, however, that different expressions for  $c(1)$  are possible for different models, for example the Cayley tree.

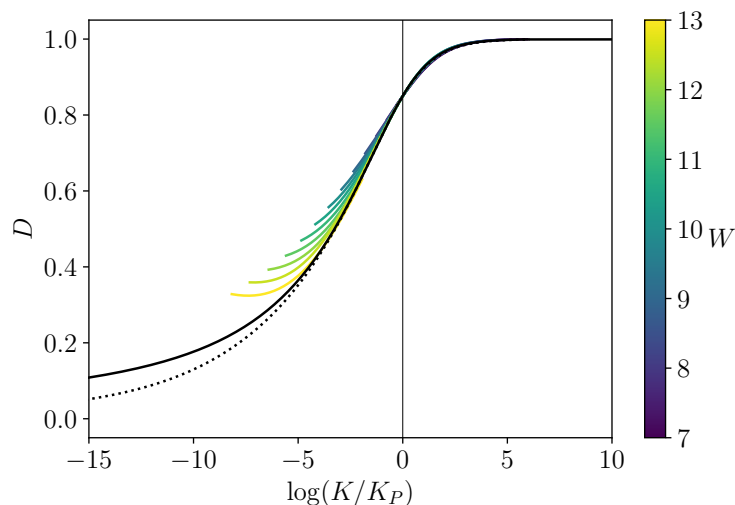


Figure C.2: The function  $D(\ln K)$  in the one-parameter scaling regime, for two best fits for  $\beta_0$ , the one vanishing linearly in  $D = 0$  (solid) and the one with square root singularity at the origin (dotted). The integration constant  $K_P$  is chosen in such a way that all the curves intersect in one point  $K = K_P$ , where  $D(K_P) = 0.85$  for all curves, numerical and analytical. The numerical data are shown as thin colored lines for  $W \in [7, 13]$ .

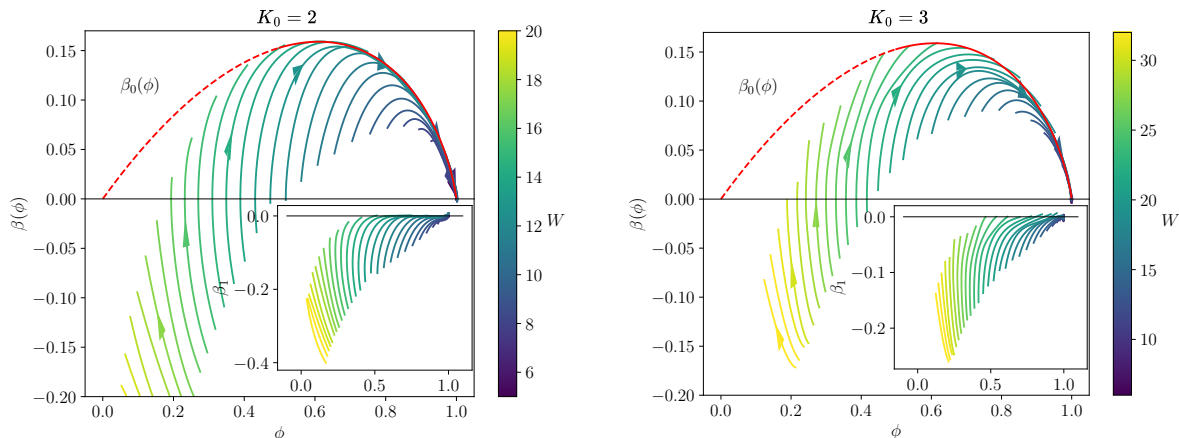


Figure C.3: (*Left*)  $\beta$ -function for  $\phi$ , i.e. the rescaled  $r$ -parameter. The data analysis performed is the same that has been done for the fractal dimension. The red curve is obtained by fitting the envelope with the function  $z(x) = -a(1-x)\ln(1-x) + bx(1-x) + cx^2(1-x)$  ( $a \simeq 0.43$ ,  $b \simeq 0.06$ ,  $c \simeq -0.11$ ). In particular, the  $\beta$ -function approaches  $\phi = 1$  with an infinite derivative, as it is also confirmed by the right panel. For  $\phi < 0.5$  we just extrapolated the fitting function used for the points at  $\phi > 0.5$ , and therefore can be not accurate given the limits of the numerics. (*Right*) Same analysis performed for a RRG with  $\mathcal{D} = 4$ . The  $\beta_0(D)$  function is the same as in the  $\mathcal{D} = 3$  case, and it is in perfect agreement with the data, supporting the universality of the function  $\beta_0$ .

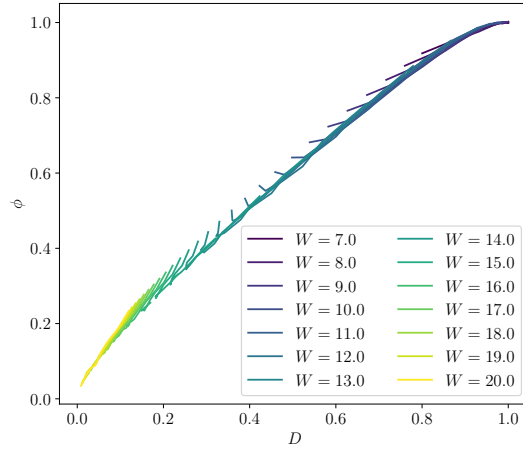


Figure C.4:  $\phi$  vs  $D$ . For intermediate values of  $D$  (and  $\phi$ ), the two quantities are almost perfectly proportional one to the other. Near  $D, \phi \sim 1$  however, the curve has a vanishing derivative.

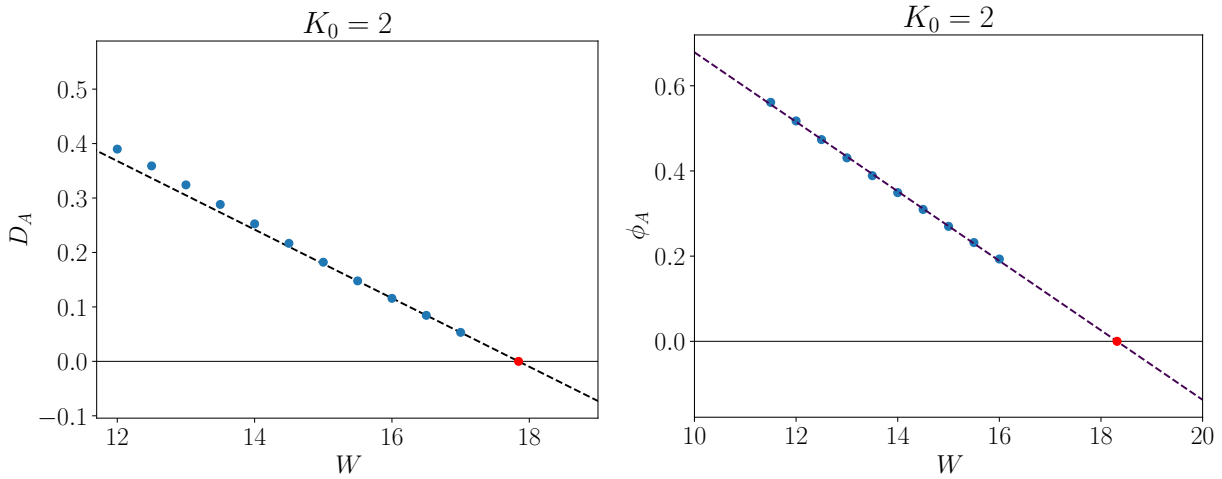


Figure C.5: Values of  $\phi_A$ , i.e. the values of the rescaled  $r$ -parameter such that  $\beta(\phi_A) = 0$ , for different values of  $W$  (blue dots). A linear extrapolation gives a critical value for the disorder  $W_c = 18.3 \pm 0.1$  (red dot), which is in very good agreement with the known position of the transition  $W_c = 18.17$ .

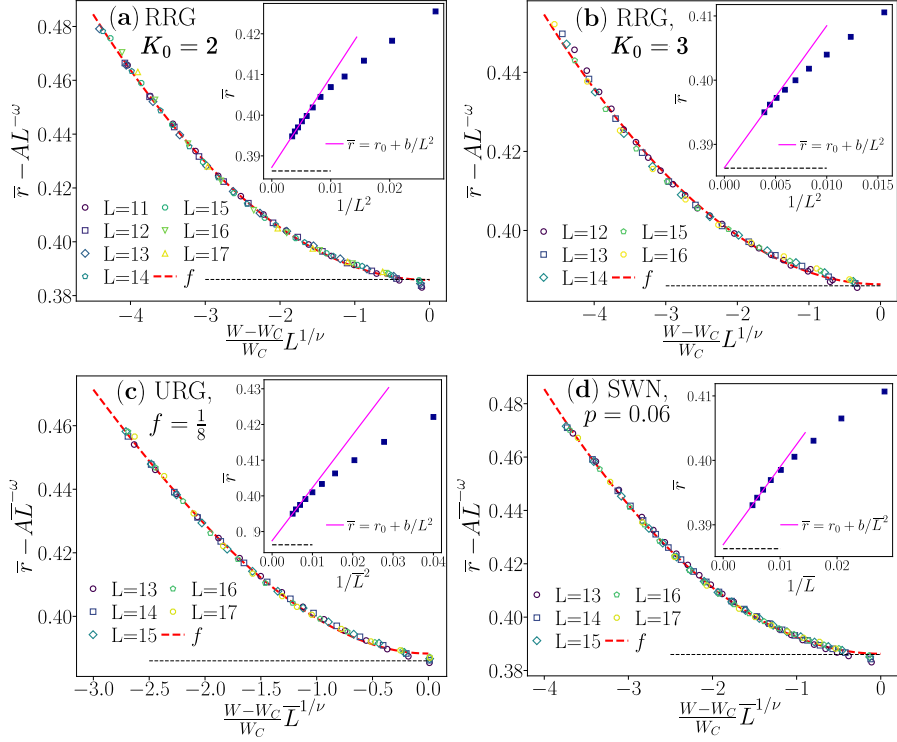


Figure C.6: Figure taken from Ref. [140]. The main figures show the collapse of the  $r$ -parameter for different values of  $W$  and system size. The collapse is obtained by setting  $\omega = 2$  and  $\nu = 1$  (see [140] for a description of the critical exponents and data collapse). The insets show the behavior of the average gap ratio at the critical point, displaying a  $1/L^2$  scaling, which is predicted by our renormalization group equations. Different subfigures ((a), (b), (c), and (d)) correspond to different types of network, respectively RRGs with  $K_0 = 2$ ,  $K_0 = 3$ , uniform random networks and small-world networks (notice that here  $D$  in the plots is the vertex coordination number  $K_0 + 1$ ).

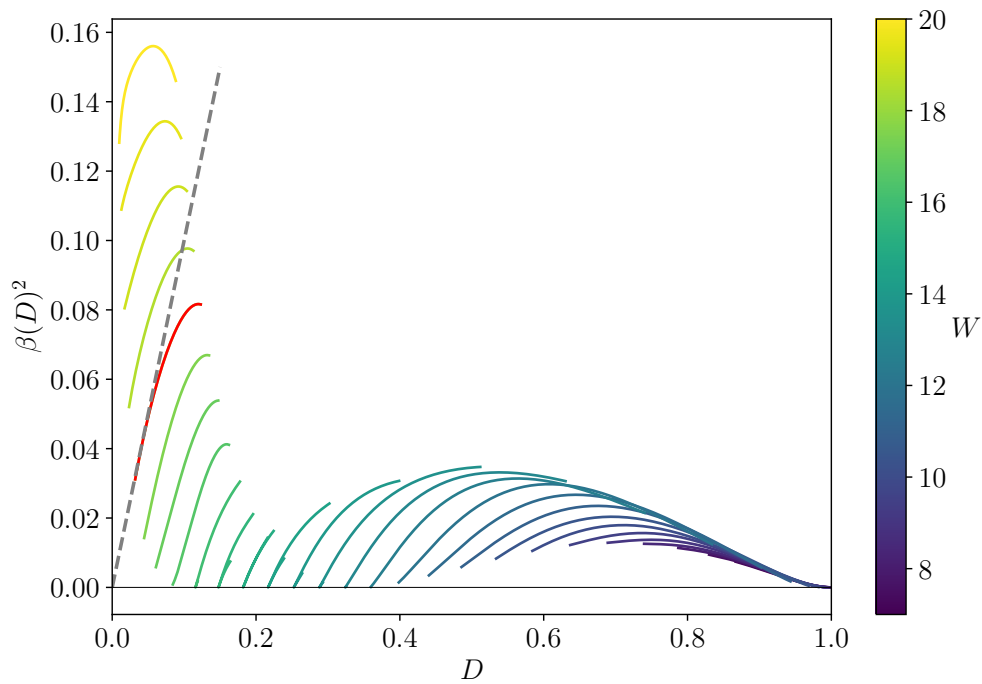


Figure C.7: Plot of  $\beta^2(D)$  vs  $D$ . As explained in the text, we notice that the slope of the curves near  $D = D_A$  (i.e.  $\beta \simeq 0$ ) does not depend significantly on  $D_A$  (or equivalently  $W$ ). Moreover, the critical curve, represented in red, follows the curve  $\beta^2(D) = D$  (dashed line in the plot), meaning that  $c = 1/2$ .



## Appendix D

# Additional information - Resonance counting and finite-size effects in random matrices

### D.1 Exact entropy for the rotational-invariant random matrices

In rotational-invariant random matrix ensembles such as the Gaussian Orthogonal Ensemble (GOE), Gaussian Unitary Ensemble (GUE), or Gaussian Symplectic Ensemble (GSE), the eigenvectors, due to the rotational symmetry, are distributed uniformly over all directions, meaning that the individual components' distribution does not depend on the basis we are working on. An example of a basis-independent vector distribution is a multivariate normal distribution with a unit covariance matrix. However, the multivariate normal distribution does not respect the normalization; hence, we take the *normalized* multivariate normal distribution, e.g., the corresponding occupations  $|\phi(i)|^2$  of the site  $i$  can be described by the expression

$$|\phi(i)|^2 = \frac{\sum_{\alpha=1}^{\beta} x_{\alpha}^2(i)}{\sum_{\alpha=1}^{\beta} x_{\alpha}^2(i) + \sum_{j \neq i}^N \sum_{\alpha=1}^{\beta} x_{\alpha}^2(j)}, \quad (\text{D.1.1})$$

where  $N$  is the size of the matrix,  $x_{\alpha}(i)$  are the i.i.d. standard Gaussian random variables, and  $\beta$  is the Dyson index ( $\beta_{GOE} = 1$ ,  $\beta_{GUE} = 2$ ,  $\beta_{GSE} = 4$ ). Thus, the distribution of  $|\phi(i)|^2$  can then be written as

$$p_{\phi^2}(\nu) = \int_0^{\infty} dx dr \delta\left(\nu - \frac{x}{x+r}\right) \chi_{\beta}^2(x) \chi_{\beta(N-1)}^2(r), \quad (\text{D.1.2})$$

where  $\chi_k^2(x)$  stands for the PDFs of the chi-squared distribution with  $k$  degrees of freedom. After taking this integral, one finds that  $p_{\phi^2}(\nu) \propto \nu^{\beta/2-1} (1-\nu)^{\beta(N-1)/2-1}$ ; i.e.,  $|\phi(i)|^2$  is distributed according to the beta distribution,  $|\phi(i)|^2 \sim \mathcal{B}(\beta/2, \beta(N-1)/2)$ . So, having the explicit exact expression for the PDF of the occupations, we can obtain the exact expression for the corresponding participation entropy as

$$S_{\beta}(N) = -N \langle |\phi(i)|^2 \ln |\phi(i)|^2 \rangle = H(\beta N/2) - H(\beta/2), \quad (\text{D.1.3})$$

where  $H(x)$  is the Harmonic number.

Due to their maximal ergodicity, the eigenstates of the rotational-invariant ensembles can serve as a reasonable model for the heads of the more complicated ensembles' eigenstates. For example, for  $\beta = 1$ , the total entropy of such a head according to the ansatz Eq. (7.2.2) would be

$$S_{head}(\Omega, C) = \Omega s_{head} = -\Omega \langle C \phi^2 \ln(C \phi^2) \rangle = C S_1(\Omega) - C \ln C. \quad (\text{D.1.4})$$

## D.2 Another analytical approach to the Gaussian RP model

In the right panel of Fig. 7.3, we compare our analytical prediction for the support set dimension beta function of the Gaussian RP model with the exact numerical results and with the analytical results based on Ref. [411]. In this section, we summarize the idea of that paper and describe how we apply it to our case.

The main idea of ref. [411] lies in the ansatz for the distribution of the Gaussian RP eigenfunctions' components which is composed of two parts: the Lorentzian local density of states ('a Breit-Wigner formula with the spreading width  $\Gamma$  calculated by the Fermi golden rule') and the Gaussian fluctuations ('a local Porter-Thomas law') on top of it. The distribution is then reads as

$$p_{\psi_E}(x) = \int \frac{\rho(\epsilon) d\epsilon}{\sqrt{2\pi \langle |\psi_E(\epsilon)|^2 \rangle}} \exp \left\{ -\frac{x^2}{2 \langle |\psi_E(\epsilon)|^2 \rangle} \right\}, \quad \langle |\psi_E(\epsilon)|^2 \rangle \sim \frac{C}{(E - \epsilon)^2 + \Gamma(E)^2}, \quad (\text{D.2.1})$$

where  $C$  is a constant to find from the normalization,  $\rho(\epsilon)$  represents a PDF of the onsite energies, and  $\Gamma(E) \sim \pi N^{1-\gamma} \rho(E)$  providing  $\gamma > 1$  and  $N \gg 1$ . This ansatz has its problems: e.g., due to the infinite support of the Gaussian, it always gives a non-zero probability for the normalization to be violated. But, for large enough  $N$ , the corresponding effects should be negligible, and this is what the authors of Ref. [411] prove with their beautiful numerics using  $\rho(\epsilon) \propto e^{-\epsilon^2/2}$ . So, let us now use this ansatz to calculate the participation entropy  $S(N)$  in the middle of the spectrum of the Gaussian RP model with the box-distributed onsite energies.

First, let us compute the normalization constant  $C$  using  $\rho(\epsilon) = 1/2w$  for  $-w < \epsilon < w$  and  $\rho(\epsilon) = 0$  otherwise. From the requirement  $\langle \psi_0^2 \rangle = 1/N$  where we explicitly put  $E$  to zero, we find

$$\frac{1}{N} = \int_{-\infty}^{\infty} x^2 p_{\psi_0}(x) dx = \int_{-w}^w \frac{d\epsilon}{2w} \frac{C}{\epsilon^2 + \Gamma^2} = C \frac{\tan^{-1}(\frac{w}{\Gamma})}{w\Gamma} \implies C = \frac{w\Gamma}{N \tan^{-1}(\frac{w}{\Gamma})}, \quad (\text{D.2.2})$$

with  $\Gamma = \Gamma(0) = \pi N^{1-\gamma}/2w$ . Next, we compute the participation entropy as

$$\begin{aligned} S &= -N \int_{-\infty}^{\infty} x^2 \ln(x^2) p_{\psi_0}(x) dx \\ &= N \int_{-w}^w \frac{d\epsilon}{2w} \int_{-\infty}^{\infty} \frac{-x^2 \ln(x^2) d\epsilon}{\sqrt{2\pi \langle |\psi_E(\epsilon)|^2 \rangle}} \exp \left\{ -\frac{x^2}{2 \langle |\psi_E(\epsilon)|^2 \rangle} \right\} \\ &= N \int_{-w}^w \frac{d\epsilon}{2w} \langle |\psi_0(\epsilon)|^2 \rangle (\gamma + \ln(2) - 2 - \ln(\langle |\psi_0(\epsilon)|^2 \rangle)) \\ &= \gamma + \ln(2/C) - 2 + NC \int_{-w}^w \frac{d\epsilon \ln(\epsilon^2 + \Gamma^2)}{2w \epsilon^2 + \Gamma^2}, \end{aligned} \quad (\text{D.2.3})$$

where  $\gamma$  stands for the Euler gamma. The last integral can be expressed using a generalized hypergeometric function (or a polylogarithm), and the result for the corresponding support set dimension's  $\beta$ -function can be seen as the dashed lines in the right panel of Fig. 7.3. As follows from the comparison, the result is equivalent to ours for large  $N$  but deviates from the numerical results and the self-consistent resonance counting prediction for intermediate sizes as well as at

the Anderson transition,  $\gamma = 2$ . A reason for this discrepancy may lie in the nature of the Breit-Wigner approximation as it assumes the broadening  $\Gamma$  to self-average, while this assumption fails at intermediate sizes, critical points, and localized phases.



## Appendix E

# Additional information - Non-parametric unsupervised learning and localization transitions

### E.1 PCA entropy analysis

We focus here on the PCA entropy, as described in Ref. [436]. The PCA entropy can be defined starting from the  $\lambda_j$  obtained from the matrix  $C$  introduced in Sec. II. Noticing that the  $\lambda_j$  satisfy (i)  $\lambda_j \geq 0$  for all  $j$  (as they are proportional to the squared singular values of  $C$ , and (ii)  $\sum_j \lambda_j = 1$  (by construction), we can follow Shannon's entropy formula to define

$$S_{\text{PCA}} := - \sum_{j=1}^d \lambda_j \ln(\lambda_j). \quad (\text{E.1.1})$$

In general, the PCA entropy in Eq. (E.1.1) can be used as a measure of the correlations among the input variables in the analyzed data set. Indeed, note that for an extremely 'correlated' data set, which under PCA can be fully described by a single principal component (i.e.,  $\lambda_1 \sim 1$ ,  $\lambda_n \sim 0$ , for  $n \geq 2$ ), we get  $S_{\text{PCA}} = 0$ . Instead, for a fully 'uncorrelated' data set (e.g., a collection of independent random variables), for which  $\lambda_j = 1/d$  for all  $j$ , we have  $S_{\text{PCA}} = \ln d$ . This quantity has not been studied in quantum statistical mechanics at equilibrium so far. Here, we want to show that  $S_{\text{PCA}}$  is actually dependent on the type of encoding used for the problem at stake and draw its connection with the participation entropy. In the following, we will show that while it holds the signature of the crossover, it is not possible to efficiently extract estimates on the microscopic features of the transition (namely critical points and scaling parameters).

#### Encoding and participation entropy

We started our discussion interested in studying a quantum state written as in Eq. (1) of the main text.

Let us assume to build a data set in the following way: we sample, according to the probabilities  $|c_x|^2$ , the corresponding basis vectors  $|\psi_x\rangle$ ; we encode the information as a  $\mathcal{N}$ -dimensional vector with a single non-zero component corresponding to the index  $x$ . We call this ' $\mathcal{N}$ -encoding'. Each vector will be one row of the data set  $X$ , so that all the rows will be orthogonal to each other and



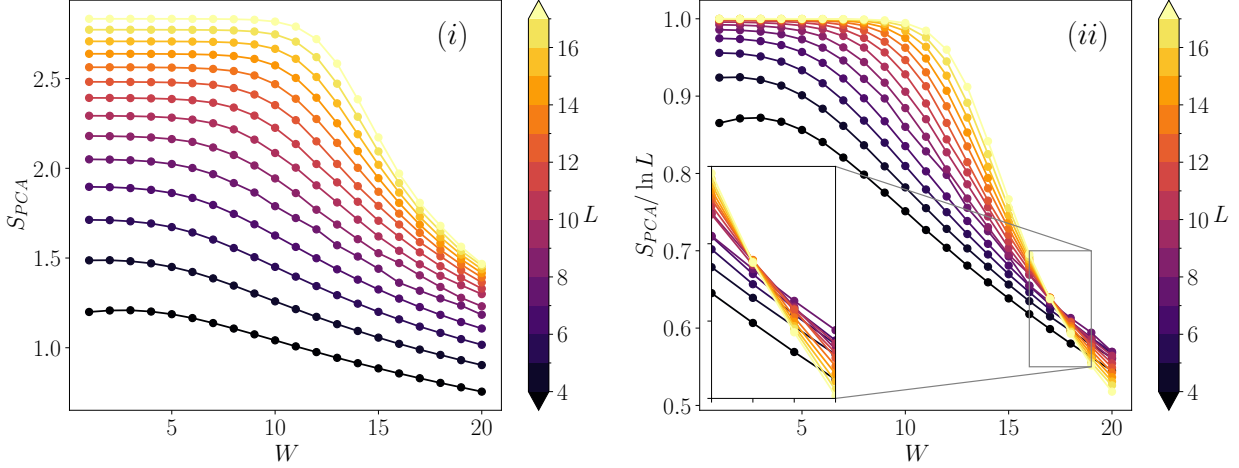


Figure E.2: (i) PCA entropy computed using the ‘ $L$ -encoding’. While the curves are always decreasing with  $W$ , as for the participation entropy, quantitatively the behavior is different. In particular, at small  $W$  a long plateau develops increasing the system size, and the derivative wrt the system size does not give the participation entropy. (ii) PCA entropy computed using the ‘ $L$ -encoding’ and normalized with  $\ln L$ , so that  $S_{PCA}/\ln L = 1$  at small  $W$ . As usually happens in spectral observables, e.g. the  $r$ -parameter or the participation entropy [140], curves corresponding to different sizes cross. In our case, however, the position of the crossing point moves to smaller  $W$  as  $L$  grows, forbidding to identify the correct position of the critical point.

In general, the eigenvalues of  $C = X_c^T X_c / (N_r - 1)$  do not coincide with  $|c_i|^2$  for any choice of the  $k_i$ ’s. However, when all the  $k_i$ ’s are of the same order (this happens in the delocalized phase in our problem), then one can approximate  $(X_c^T X_c)_{ii} \sim k_i$  and  $(X_c^T X_c)_{ij} \sim 0$  and the non-centered case is retrieved, thus giving a good approximation of the participation entropy. This can be seen in Fig. E.1.

Let us observe that the encoding proposed is not numerically efficient, for the dimension of the data set scales exponentially with the Hilbert space dimension, and also requires an exponentially large number of samples  $N_r$  to recover the same information as the participation entropy. In practice, the encoding of the sampling into an actual data set and the PCA procedure can be skipped altogether as what matters is the counting of the repetitions of  $|\psi_x\rangle$ . Hence, in this particular scenario/encoding, the data analysis approach described here becomes pointless.

The discussion above is the reason why in this Chapter a different encoding has been employed, let us call it ‘ $L$ -encoding’. Namely, as in the previous case we sample, according to the probabilities  $|c_x|^2$ , the corresponding basis vectors  $|\psi_x\rangle$ ; we store the information as a  $L$ -dimensional vector that encodes the index  $x$  as a binary number. Thus, each row of the data set  $X$  will be a  $L$ -dimensional string of zeros and ones. Then we perform the PCA as described at the beginning of App. E.1.

In the next section we discuss the numerical results of  $S_{PCA}$  in the case of both encodings.

## Numerical simulations

As described in the main text, we perform an exact diagonalization of the model in Eq. (5) of the main text employing the POLFED algorithm [446] and we perform a PCA on the eigenvectors in the middle of the spectrum. In Fig. E.3 we employ the ‘ $N$ -encoding’ described before sampling  $N_r \sim 5N$  configurations for each eigenstate. We show a plot of  $S_{PCA}$  as a function  $W$  (disorder

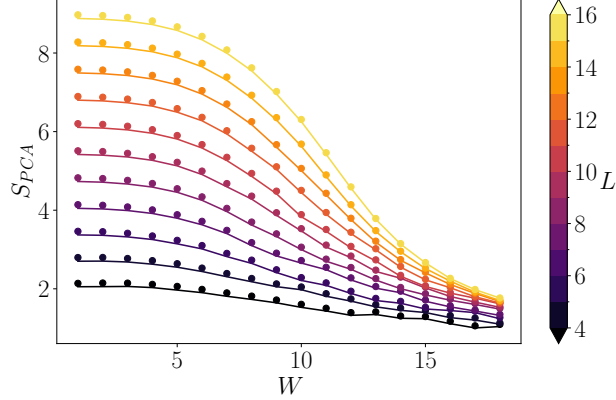


Figure E.3: Comparison of  $S_{\text{PCA}}$  (points) without centering the data and participation entropy (lines) for the ‘N encoding’ case.  $N_r = 5\mathcal{N}$  samples have been used.

strength) for different sizes of the graph. The points correspond to  $S_{\text{PCA}}$  while the lines are the estimated participation entropies for different  $L$ , averaged over  $\sim O(10^3)$  realizations of disorder. We observe that they coincide as suggested by Eq. (E.1.3). The interest in the participation entropy relies on the fact that from it one can obtain the fractal dimension of the wavefunction via the definition

$$D \equiv \frac{\partial S}{\partial \ln N} = \frac{1}{\ln 2} \frac{\partial S}{\partial L}. \quad (\text{E.1.6})$$

Many works have addressed the properties of the fractal dimension (see e.g. [5, 140, 351, 409, 444]) as it can be used as an order parameter for the localization transition. In fact, if a wavefunction is localized, with localization length  $\xi \ll L$ , then by increasing the system size no change in  $S$  occurs, and thus  $D \rightarrow 0$ . If, on the other hand, the wavefunction is delocalized, it will have support over the whole system, and the participation entropy will be  $S = L \ln 2$  (assuming  $|c_x|^2 = 2^{-L}$ ). Thus, for  $L \rightarrow \infty$ ,  $0 \leq D \leq 1$ .

At this point, it is natural to consider the PCA entropy for the more efficient ‘ $L$ -encoding’, but one does not recover the eigenfunction participation entropy. This can be understood from the analogous of Eq. (E.1.2) for the ‘ $L$ -encoding’: now, for each  $j$ , there will be  $k_j$  rows containing a vector whose entries are the binomial representation of the number  $j$ . Of course, such rows can have more than one entry with value 1, and when taking the product  $X^T X$  this will not give simply the number  $k_j$ , and thus one cannot recover the coefficients  $|c_j|^2$ . Alternatively, this can be understood from the fact that, with the ‘ $L$ -encoding’, the matrix  $C$  has rank  $L = \log_2 \mathcal{N}$ , while in general there are  $\mathcal{N}$  non-zero wavefunction coefficients, meaning that the eigenvalues of  $C$  will be a non-trivial combination of the  $|c_j|^2$ . Consequently, the form of the PCA entropy for the ‘ $L$ -encoding’ will be different from the one of the ‘ $N$ -encoding’, as shown in Fig. E.2 (i). Naturally, the decrease with  $W$  is present also for the ‘ $L$ -encoding’, reflecting the fact that fewer configurations are sampled with high probability at large  $W$ . However, the quantitative behavior is different, and no easy way of obtaining information about the transition point has been found. For example, by rescaling SPCA with  $\ln L$  (see Fig. E.2 (ii)), i.e. the value in the ergodic phase where all eigenvalues are equal, one gets crossing points between curves for different sizes. Despite being roughly at the correct value of  $W$ , the crossing points move to smaller  $W$  when increasing  $L$ , which is the opposite behavior with respect to the expected one — namely with respect to what happens, for instance, in the case of the participation entropy.

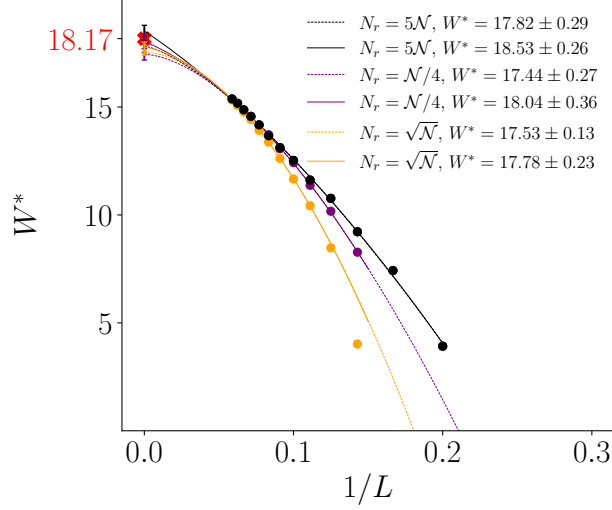


Figure E.4: Extrapolation of the critical disorder, as shown in Fig. (2 - ii) of the main text. The solid lines are fits of the form  $W^* = a + b/L + c/L^2$  (the same shown in the main text), while the dashed lines are fits of the form  $W^* = a + bL^{-c}$

### Extrapolation of $W_c$

In this Section, we briefly comment on the extrapolation of  $W_c$  shown in the main text. As discussed in the main text, the quadratic fit in  $1/L$  gives results perfectly compatible with the known results from different methods. Different fits for the same data are possible, and taking inspiration from the analysis of crossing points in the  $r$ -parameter shown in Ref. [140], we show in Fig. E.4 also the results for the fit  $W^* = a + bL^{-c}$  and the corresponding extrapolated values of  $W_c$ .

While giving qualitative good results, for some data sets the fit  $W^* \sim L^{-c}$  gives less precise results, and overall it is less stable upon addition or removal of fitting points. This suggests that for having a more precise extrapolation value using this fit, data at larger sizes are needed, and this goes beyond our scopes.



## Chapter 9

# Final remarks

*In this final Chapter we briefly summarize the results presented in this thesis and we put forward some possible future directions that can be within reach thanks to the results developed during my Ph.D.*

**B**EING at the end of the thesis, we want to briefly summarize the contents of parts I and II and discuss some possible future directions. Some more specific comments can be found at the end of each Chapter.

The main focus in part I was the quantum dynamics of the two-dimensional Ising model. Specifically, in Chapter 2 we addressed the unitary evolution of smooth spin-domains interfaces, showing that in a physically relevant strong-coupling limit, it is possible to describe exactly their dynamics by using a holographic mapping to a one-dimensional free fermionic chain. One of the main results of the Chapter is the prediction of the Stark-localized dynamics of the interface when the original Ising model is subject to an external magnetic field: this is translated into a linear potential on the associated fermionic chain. We also checked that these predictions are robust away from the strict strong-coupling limit for large timescales. Moreover, an intriguing connection between our results and the measure concentration phenomena in random partitions (i.e., on random Young diagrams) is found and explained.

We think that the possibility of addressing the dynamics of quantum systems in higher dimensions (in some limits) employing a correspondence with lower dimensional solvable models is powerful and can be utilized in other cases. For example, our preliminary explorations suggest that a similar approach can be used for the  $3d$  Ising model, which is holographically equivalent to a dimer model on a hexagonal lattice or, equivalently, a constrained set of fermionic chains. Moreover, an intriguing direction would be that of addressing the dynamics of interfaces starting from configurations that allow them to break into disjoint domains. A first insight into this problem could be obtained by studying toy models with easy interface configurations and then generalizing the observed behavior to more complicated situations. Such a result would be the first important step toward a deeper understanding of Coleman's false vacuum decay [158, 247] on the lattice in higher dimensions, as explained in more details in Chapter 2.

Motivated by the localization phenomenon found in Chapter 2, in Chapter 3 we considered the same model but subject to a random external field, with the aim of investigating the presence of

many-body localization (MBL) in a two-dimensional system. In the presence of disorder, we did not find localization in spectral observables, ruling out the MBL scenario. Probing the real-time dynamics, instead, it turned out that it is unexpectedly slow, possibly slower than sub-diffusive, when considering a wedge initial state, as done in Chapter 2. While the absence of MBL can be expected when considering the effective kinetically constrained Hamiltonian describing the model and the non-locality of the holographic mapping, the slow dynamics was less expected. We think that the motivation resides in an entropic effect in the Hilbert space when starting from the initial state considered; in fact, the initial wedge state, intended as a site in Hilbert space, has much smaller connectivity than a typical configuration, and therefore the dynamics has less channels for leaving the initial state.

It would be desirable to have a more in-depth understanding of the onset of sub-diffusive and even slower dynamics in the model, possibly relating it to the choice of the initial state. The current numerics does not allow the exploration of many initial states, as other starting configurations would exceed the available Hilbert space, which is limited.

We concluded part I by investigating, in Chapter 4, through the lens of generalized hydrodynamics (GHD), the dynamics and the entanglement entropy evolution of the Stark-localized free fermions that appeared in Chapter 2. Using the GHD formalism we easily recovered the exact lattice results (in the hydrodynamic limit) for the time-evolution of fermionic density and current, but we also found the leading contribution to the entanglement entropy, that cannot be obtained directly on the lattice. Moreover, we discussed how to generalize the Stark-localization phenomenon identifying the basic ingredients that are responsible for its emergence and relating them to topological properties of the Hamiltonian flow.

The technique used in this Chapter and already applied in other contexts has the advantage of being applicable to many different systems. A possible step forward could be that of computing not only the expectation value of operators but also their fluctuations. Also, the full-counting statistics is within reach for GHD, and it would allow one to compute the full interface profile of the  $2d$  Ising model of Chapter 2. Moreover, exactly solvable localized free fermions can be a useful setting for probing new effects, such as those generated by the presence of impurities.

In part II we moved to a more in-depth study of localization induced by disorder in quantum systems. More specifically, in Chapters 5 and 6 we built a numerically-based renormalization group approach to the Anderson transition in finite-dimensional lattices and on expander graphs, formally of infinite dimension. Being able to compute the complete  $\beta$ -function for spectral quantities, we have been able, in Chapter 5, to recover known results in the literature. More importantly, we have been able to study the flow of critical properties upon changing the space dimensionality, extrapolating to infinite dimension, a limit that is relevant for interacting problems. Not only, one of the advantages of having the numerical  $\beta$ -function is that of directly observing the irrelevant RG flow. Therefore we were able to carry out a detailed analysis of the scaling properties around the critical point taking into account the irrelevant corrections. When the same analysis is performed on expander graphs, in particular random regular graphs (RRGs), the outcome is different. While in finite dimensions the RG flow is described by just one relevant parameter also at the critical point, this is not the case for RRGs, where a two-parameter scaling develops, leading to a BKT localized phase. Such behavior is compatible with the infinite-dimensional limit considered in the previous Chapter. Our picture also naturally explains some numerical results observed in previous literature that were not yet understood.

We think that the RG approach which, so far, we applied to the Anderson model can also provide insights into other systems, starting from interacting disordered models. In fact, by ex-

exploiting this RG technique, we gained a deeper understanding of relatively understood systems such as the Anderson model on various graphs. We expect that the same can happen in the context of many-body localization, where the community does not even agree on the presence or absence of a genuine localization transition in the thermodynamic limit. Our method for analyzing the exact diagonalization results could give a new perspective on the problem. A complementary approach to deal with the interacting case would be that of inverting the order of limits with respect to what we did in Chapter 5, namely keeping the linear size  $L$  fixed and considering the infinite-dimensional limit. This leads to the quantum random energy model, which is a good model for interacting systems (having the same Hilbert space geometry), although with some caveat (the uncorrelation of onsite energies).

In Chapter 7 we continued the analysis of finite-size effects (and renormalization) of disordered quantum systems displaying localization phenomena. In particular, we developed a criterion for counting resonances in the system that has a two-fold advantage. On the one hand, it is connected with other spectral indicators that are numerically easily accessible, thus allowing for analytic predictions of otherwise just numerical results. On the other hand, differently from other criteria, it is self-consistent, meaning that it does not rely on arbitrary cutoffs to discern the resonances. We showed the power of our method on a set of different random matrix ensembles, where both analytical calculations using our criterion and numerical simulations are accessible. We showed a remarkable agreement between spectral observables computed analytically using our self-consistent criterion and the numerics, allowing us also to produce a full renormalization group flow up to the thermodynamic limit, which is out of reach of numerical results.

Having tested the resonance criterion on some random matrix models, it would be desirable to apply it to genuine local Hamiltonians, such as the Anderson model. Moreover, we applied our definition of resonances to compute the eigenstates' fractal dimension, but it would be desirable to have better control of other spectral indicators, like the  $r$ -parameter (which we introduced in Chapter 5).

In Chapter 8 we took a different point of view from what we discussed in the rest of part II and we utilized unsupervised non-parametric learning techniques to address disorder-induced localization transitions. The content of this Chapter, despite not containing, strictly speaking, new physical results, is an important step forward for the experimental setups, that increasingly powerful and can nowadays probe physical properties which, so far, were predicted only theoretically. The technique we proposed has several advantages from this perspective; we showed that it allows a precise determination of the critical point and critical exponents in models where also state-of-the-art numerics is not straightforward, with the advantage of being agnostic about the system under analysis. Moreover, as we mentioned, it is experimentally relevant, being based on repeated measurements of the wave functions of the system, and in our case, we built a solid connection with physical quantities, that typically is not possible.

The unsupervised learning methods such as the principal component analysis are becoming a useful tool in the study of physical systems, despite not often offering a physical understanding of the model under consideration. In our case, we built this connection and we think that the same can be done in other cases (mentioned in Chapter 8), also outside the realm of disordered quantum systems and for other types of quantum critical points.



# Acknowledgments

I'm still coming to terms with it, but it seems my PhD journey is nearing its end. Reflecting on the past four years, I realize how quickly time has flown. They say time flies when you're having fun, and I can confirm that it's true; I've had a wonderful experience in Trieste since mid-2020.

Most of the credit goes to the incredible people I've met along the way. I'd like to start by thanking my supervisors, Andrea Gambassi and Antonello Scardicchio, who have been instrumental in my journey.

My first interaction with Andrea was during the admission exam. Over time, through numerous informal interactions, I discovered the kind person behind the accomplished scientist. I've shared not only research work with him (which he often reminds me isn't over yet) but also extra activities, such as organizing a conference for our mutual "scientific grandfather", Sergio Caracciolo, to whom I remain deeply indebted.

I met Antonello when I asked him to be my supervisor for my Master's thesis. I vividly remember his response to my initial email, where he wrote as if we had known each other for a long time. Since then, we've worked on numerous projects, most of which started during the summer, free from daily routines. Antonello has taught me a great deal, both scientifically and personally. Over time, I've come to see him as a paternal figure—demanding yet rewarding in his unique way, which has truly motivated me to do my best. I hope I have lived up to his expectations.

A special thanks goes to Federico Balducci, who has been a colleague, a flatmate, and most importantly, a very good friend. He has been like an older brother to me when I first moved to Trieste. As a colleague, he taught me many indispensable tricks over the years, for which I am immensely grateful. Behind his sharp critiques, often delivered in a Roman accent, lies a very good physicist. I hope we continue collaborating on our random projects, which seem to arise every couple of months.

I also want to thank Boris Altshuler and Vladimir Kravtsov, as it has been an honor to interact with them. Initially, I was quite shy around these renowned scientists. Boris is one of the most brilliant minds I've encountered, and our interactions over the past year have shown me his uncanny ability to understand things instantly and see the path ahead clearly. Volodya, a leading expert in localization, works with the enthusiasm of a young scientist, sending numerous emails daily and nightly out of sheer passion. His dedication has been truly inspiring.

I'm also grateful to Vittorio Vitale, whom I first met as a friend and later became a colleague. Working with him was enjoyable, and together we probably produced the fastest good paper I'll ever write. His apparent gloom often motivated me to strive harder, though he is almost always happy despite his inability to show it.

I want to extend my thanks to friends and colleagues Anton Kutlin and Luca Capizzi. Both are brilliant, and I have learned much from working alongside them. I'm also grateful to Giacomo Bracci Testasecca and Jacopo Niedda for the enjoyable discussions on renormalization groups, KL divergences, and how to (almost) crash the SISSA cluster.

Thank you to Pasquale Calabrese for his interactions and constant availability, and to Alessio Lerose for our side-by-side work and useful suggestions on both physics and bureaucracy. I am very thankful to Anushya Chandran and David Long for our ongoing collaboration and the fantastic time I spent in Boston working with them.

I am also thankful to David Huse and Sarang Gopalakrishnan for our slow-moving but valuable collaboration and their hospitality in Princeton. A special thank you to Piotr Sierant for the amazing code he shared and the prompt assistance he provided, often replying within two minutes despite my entry-level coding skills.

A special thanks goes also to Giuliano Chiariacò: despite we never really worked together, we often had discussions, not only about physics, and a very good time together.

Beyond my direct collaborators, I am grateful for the many friends with whom I've enjoyed discussing physics and related topics. Though too numerous to list, I want to mention Anna Delmonte, Martina Frau, Cristiano Muzzi, Marcin Pruszczyk, Elaheh Saadat, Emanuele Tirrito, and Ludmila Viotti for the time spent together at ICTP or SISSA, whether in the canteen, bar, or car rides. I also want to thank Daniel Baldwin, Guido Giachetti, Andrea Grigoletto, and Alessandro Santini for the enjoyable times spent together, often discussing physics even outside the office.

I also want to deeply thank Leticia Cugliandolo and Chris Laumann for having refereed this thesis.

Finally, I want to express my gratitude to Paul Steinhardt and Salvatore Torquato for hiring me as a postdoctoral researcher at Princeton University. I am genuinely thrilled about the forthcoming years of work together.

There are many other important people who have played a fundamental role in my life, not only during my PhD but also before and undoubtedly in the future, but I prefer to not mention them here.

# Bibliography

- [1] F. Balducci, A. Gambassi, A. Leroze, A. Scardicchio, and C. Vanoni, “Localization and melting of interfaces in the two-dimensional quantum Ising model”, *Phys. Rev. Lett.* **129**, 120601 (2022).
- [2] F. Balducci, A. Gambassi, A. Leroze, A. Scardicchio, and C. Vanoni, “Interface dynamics in the two-dimensional quantum Ising model”, *Phys. Rev. B* **107**, 024306 (2023).
- [3] F. Balducci, A. Scardicchio, and C. Vanoni, “Slow melting of a disordered quantum crystal”, *Phys. Rev. B* **107**, 024201 (2023).
- [4] L. Capizzi, C. Vanoni, P. Calabrese, and A. Gambassi, “A hydrodynamic approach to Stark localization”, *J. Stat. Mech.: Theor. Exp.* **2023**, 073104 (2023).
- [5] C. Vanoni, B. L. Altshuler, V. E. Kravtsov, and A. Scardicchio, “Renormalization group analysis of the Anderson model on random regular graphs”, [arXiv:2306.14965](https://arxiv.org/abs/2306.14965) (2023).
- [6] B. L. Altshuler, V. E. Kravtsov, A. Scardicchio, P. Sierant, and C. Vanoni, “Renormalization group for Anderson localization on high-dimensional lattices”, [arXiv:2403.01974](https://arxiv.org/abs/2403.01974) (2024).
- [7] A. Kutlin and C. Vanoni, “Investigating finite-size effects in random matrices by counting resonances”, [arXiv:2402.10271](https://arxiv.org/abs/2402.10271) (2024).
- [8] C. Vanoni and V. Vitale, “An analysis of localization transitions using non-parametric unsupervised learning”, [arXiv:2311.16050](https://arxiv.org/abs/2311.16050) (2023).
- [9] O. Babelon, D. Bernard, and M. Talon, Introduction to classical integrable systems, Cambridge Monographs on Mathematical Physics (Cambridge University Press, 2003).
- [10] E. Fermi, J. Pasta, and S. Ulam, “Studies of nonlinear problems”, Los Alamos National Laboratory Report No. LA-1940 (1955).
- [11] T. Cretegny, T. Dauxois, S. Ruffo, and A. Torcini, “Localization and equipartition of energy in the  $\beta$ -fpu chain: chaotic breathers”, *Physica D* **121**, 109–126 (1998).
- [12] G. Berman and F. Izrailev, “The Fermi–Pasta–Ulam problem: fifty years of progress”, *Chaos* **15**, 015104 (2005).
- [13] P. G. Kevrekidis, The Discrete Nonlinear Schrödinger Equation (Springer, Berlin, 2009).
- [14] K. Ø. Rasmussen, T. Cretegny, P. G. Kevrekidis, and N. Grønbech-Jensen, “Statistical mechanics of a discrete nonlinear system”, *Phys. Rev. Lett.* **84**, 3740 (2000).
- [15] M. Johansson and K. Ø. Rasmussen, “Statistical mechanics of general discrete nonlinear Schrödinger models: Localization transition and its relevance for Klein-Gordon lattices”, *Phys. Rev. E* **70**, 066610 (2004).
- [16] B. Rumpf, “Simple statistical explanation for the localization of energy in nonlinear lattices with two conserved quantities”, *Phys. Rev. E* **69**, 016618 (2004).

- [17] B. Rumpf, “Transition behavior of the discrete nonlinear Schrödinger equation”, *Phys. Rev. E* **77**, 036606 (2008).
- [18] S. Iubini, R. Franzosi, R. Livi, G.-L. Oppo, and A. Politi, “Discrete breathers and negative-temperature states”, *New J. Phys.* **15**, 023032 (2013).
- [19] W. De Roeck and F. Huveneers, “Asymptotic localization of energy in nondisordered oscillator chains”, *Commun. Pure Appl. Math.* **68**, 1532–1568 (2015).
- [20] C. Arezzo, F. Balducci, R. Piergallini, A. Scardicchio, and C. Vanoni, “Localization in the discrete non-linear Schrödinger equation and geometric properties of the microcanonical surface”, *J. Stat. Phys.* **186** (2022).
- [21] S. F. Edwards and P. W. Anderson, “Theory of spin glasses”, *J. Phys. F: Metal Physics* **5**, 965 (1975).
- [22] D. Sherrington and S. Kirkpatrick, “Solvable model of a spin-glass”, *Phys. Rev. Lett.* **35**, 1792–1796 (1975).
- [23] G. Parisi, “Infinite number of order parameters for spin-glasses”, *Phys. Rev. Lett.* **43**, 1754–1756 (1979).
- [24] J.-P. Bouchaud, L. F. Cugliandolo, J. Kurchan, and M. Mezard, “Out of equilibrium dynamics in spin-glasses and other glassy systems”, [arXiv:cond-mat/9702070](https://arxiv.org/abs/cond-mat/9702070) (1997).
- [25] L. F. Cugliandolo and J. Kurchan, “Analytical solution of the off-equilibrium dynamics of a long-range spin-glass model”, *Phys Rev. Lett.* **71**, 173–176 (1993).
- [26] L. F. Cugliandolo and J. Kurchan, “On the out-of-equilibrium relaxation of the sherrington-kirkpatrick model”, *J. Phys. A: Math. Gen.* **27**, 5749–5772 (1994).
- [27] E. Vincent, J. Hammann, M. Ocio, J.-P. Bouchaud, and L. F. Cugliandolo, “Slow dynamics and aging in spin glasses”, in *Lecture notes in physics* (Springer Berlin Heidelberg), pp. 184–219.
- [28] M. Mézard and A. Montanari, *Information, Physics, and Computation*, Oxford Graduate Texts (OUP Oxford, 2009).
- [29] M. Mézard, G. Parisi, and M. A. Virasoro, *Spin glass theory and beyond*, Lecture Notes in Physics Series (World Scientific Publishing Company, Inc., 1987).
- [30] J. D. Bryngelson and P. G. Wolynes, “Spin glasses and the statistical mechanics of protein folding.”, *PNAS* **84**, 7524–7528 (1987).
- [31] W. Krauth and M. Mezard, “Learning algorithms with optimal stability in neural networks”, *J. Phys. A: Math. Gen.* **20**, L745 (1987).
- [32] M. Mézard, “Spin glasses and optimization”, in Heidelberg colloquium on glassy dynamics, edited by J. L. van Hemmen and I. Morgenstern (1987), pp. 354–372.
- [33] Y. Fu and P. W. Anderson, “Application of statistical mechanics to NP-complete problems in combinatorial optimisation”, *J. Phys. A: Math. Gen.* **19**, 1605 (1986).
- [34] S. Caracciolo, A. D. Gioacchino, E. M. Malatesta, and C. Vanoni, “Average optimal cost for the Euclidean TSP in one dimension”, *J. Phys. A: Math. Theor.* **52**, 264003 (2019).
- [35] D. A. Abanin, E. Altman, I. Bloch, and M. Serbyn, “Colloquium: Many-body localization, thermalization, and entanglement”, *Rev. Mod. Phys.* **91**, 021001 (2019).
- [36] L. D’Alessio, Y. Kafri, A. Polkovnikov, and M. Rigol, “From quantum chaos and eigenstate thermalization to statistical mechanics and thermodynamics”, *Adv. Phys.* **65**, 239–362 (2016).

- [37] J. M. Deutsch, “Quantum statistical mechanics in a closed system”, *Phys. Rev. A* **43**, 2046–2049 (1991).
- [38] M. Srednicki, “Chaos and quantum thermalization”, *Phys. Rev. E* **50**, 888–901 (1994).
- [39] M. Rigol, V. Dunjko, and M. Olshanii, “Thermalization and its mechanism for generic isolated quantum systems”, *Nature* **452**, 854–858 (2008).
- [40] G. Mussardo, *Statistical Field Theory: An Introduction to Exactly Solved Models in Statistical Physics* (Oxford University Press, Mar. 2020).
- [41] R. J. Baxter, *Exactly solved models in statistical mechanics* (Academic Press, 1982).
- [42] A. B. Zamolodchikov and A. B. Zamolodchikov, “Factorized S-matrices in two dimensions as the exact solutions of certain relativistic quantum field theory models”, *Ann. Phys.* **120**, 253–291 (1979).
- [43] H. Bethe, “Zur Theorie der Metalle”, *Z. Phys.* **71**, 205–226 (1931).
- [44] M. Rigol, V. Dunjko, V. Yurovsky, and M. Olshanii, “Relaxation in a completely integrable many-body quantum system: an ab initio study of the dynamics of the highly excited states of 1D lattice hard-core Bosons”, *Phys. Rev. Lett.* **98**, 050405 (2007).
- [45] S. Sotiriadis and P. Calabrese, “Validity of the GGE for quantum quenches from interacting to noninteracting models”, *J. Stat. Mech.: Theor. Exp.* **2014**, P07024 (2014).
- [46] L. Vidmar and M. Rigol, “Generalized Gibbs ensemble in integrable lattice models”, *J. Stat. Mech.: Theor. Exp.* **2016**, 064007 (2016).
- [47] F. H. L. Essler and M. Fagotti, “Quench dynamics and relaxation in isolated integrable quantum spin chains”, *J. Stat. Mech.: Theor. Exp.* **2016**, 064002 (2016).
- [48] O. A. Castro-Alvaredo, B. Doyon, and T. Yoshimura, “Emergent hydrodynamics in integrable quantum systems out of equilibrium”, *Phys. Rev. X* **6**, 041065 (2016).
- [49] B. Bertini, M. Collura, J. De Nardis, and M. Fagotti, “Transport in out-of-equilibrium XXZ chains: exact profiles of charges and currents”, *Phys. Rev. Lett.* **117**, 207201 (2016).
- [50] M. Fagotti, “Higher-order generalized hydrodynamics in one dimension: the noninteracting test”, *Phys. Rev. B* **96**, 220302 (2017).
- [51] M. Fagotti, “Locally quasi-stationary states in noninteracting spin chains”, *SciPost Phys.* **8**, 048 (2020).
- [52] B. Bertini, M. Fagotti, L. Piroli, and P. Calabrese, “Entanglement evolution and generalised hydrodynamics: noninteracting systems”, *J. Phys. A: Math. Theor.* **51**, 39LT01 (2018).
- [53] S. Scopa and D. X. Horváth, “Exact hydrodynamic description of symmetry-resolved Rényi entropies after a quantum quench”, *J. Stat. Mech.: Theor. Exp.* **2022**, 083104 (2022).
- [54] P. Wendenbaum, M. Collura, and D. Karevski, “Hydrodynamic description of hard-core bosons on a Galileo ramp”, *Phys. Rev. A* **87**, 023624 (2013).
- [55] B. Bertini and L. Piroli, “Low-temperature transport in out-of-equilibrium XXZ chains”, *J. Stat. Mech.: Theor. Exp.* **2018**, 033104 (2018).
- [56] S. Scopa, P. Calabrese, and J. Dubail, “Exact hydrodynamic solution of a double domain wall melting in the spin-1/2 XXZ model”, *SciPost Phys.* **12**, 207 (2022).
- [57] L. Piroli, J. De Nardis, M. Collura, B. Bertini, and M. Fagotti, “Transport in out-of-equilibrium XXZ chains: nonballistic behavior and correlation functions”, *Phys. Rev. B* **96**, 115124 (2017).

- [58] M. Collura, A. De Luca, and J. Viti, “Analytic solution of the domain-wall nonequilibrium stationary state”, *Phys. Rev. B* **97**, 081111 (2018).
- [59] V. Alba, B. Bertini, M. Fagotti, L. Piroli, and P. Ruggiero, “Generalized-hydrodynamic approach to inhomogeneous quenches: correlations, entanglement and quantum effects”, *J. Stat. Mech.: Theor. Exp.* **2021**, 114004 (2021).
- [60] V. B. Bulchandani, R. Vasseur, C. Karrasch, and J. E. Moore, “Solvable hydrodynamics of quantum integrable systems”, *Phys. Rev. Lett.* **119**, 220604 (2017).
- [61] M. Borsi, B. Pozsgay, and L. Pristyák, “Current operators in Bethe Ansatz and generalized hydrodynamics: an exact quantum-classical correspondence”, *Phys. Rev. X* **10**, 011054 (2020).
- [62] C. Rylands and P. Calabrese, “Transport and entanglement across integrable impurities from generalized hydrodynamics”, *Phys. Rev. Lett.* **131**, 156303 (2023).
- [63] F. Ares, S. Scopa, and S. Wald, “Entanglement dynamics of a hard-core quantum gas during a Joule expansion”, *J. Phys. A: Math. Theor.* **55**, 375301 (2022).
- [64] B. Bertini, L. Piroli, and P. Calabrese, “Universal broadening of the light cone in low-temperature transport”, *Phys. Rev. Lett.* **120**, 176801 (2018).
- [65] B. Doyon and T. Yoshimura, “A note on generalized hydrodynamics: inhomogeneous fields and other concepts”, *SciPost Phys.* **2**, 014 (2017).
- [66] P. Ruggiero, P. Calabrese, B. Doyon, and J. Dubail, “Quantum generalized hydrodynamics of the Tonks-Girardeau gas: density fluctuations and entanglement entropy”, *J. Phys. A: Math. Theor.* **55**, 024003 (2021).
- [67] S. Scopa, A. Krajenbrink, P. Calabrese, and J. Dubail, “Exact entanglement growth of a one-dimensional hard-core quantum gas during a free expansion”, *J. Phys. A: Math. Theor.* **54**, 404002 (2021).
- [68] M. Fava, S. Biswas, S. Gopalakrishnan, R. Vasseur, and S. A. Parameswaran, “Hydrodynamic nonlinear response of interacting integrable systems”, *PNAS* **118**, 2106945118 (2021).
- [69] M. Kulkarni, G. Mandal, and T. Morita, “Quantum quench and thermalization of one-dimensional Fermi gas via phase-space hydrodynamics”, *Phys. Rev. A* **98**, 043610 (2018).
- [70] I. Bouchoule and J. Dubail, “Generalized hydrodynamics in the one-dimensional Bose gas: theory and experiments”, *J. Stat. Mech.: Theor. Exp.* **2022**, 014003 (2022).
- [71] I. Bouchoule, B. Doyon, and J. Dubail, “The effect of atom losses on the distribution of rapidities in the one-dimensional Bose gas”, *SciPost Phys.* **9**, 044 (2020).
- [72] J. D. Nardis, B. Doyon, M. Medenjak, and M. Panfil, “Correlation functions and transport coefficients in generalized hydrodynamics”, *J. Stat. Mech.: Theor. Exp.* **2022**, 014002 (2022).
- [73] U. Agrawal, S. Gopalakrishnan, and R. Vasseur, “Generalized hydrodynamics, quasiparticle diffusion, and anomalous local relaxation in random integrable spin chains”, *Phys. Rev. B* **99**, 174203 (2019).
- [74] M. Medenjak, J. De Nardis, and T. Yoshimura, “Diffusion from convection”, *SciPost Phys.* **9**, 075 (2020).
- [75] J. De Nardis, D. Bernard, and B. Doyon, “Diffusion in generalized hydrodynamics and quasiparticle scattering”, *SciPost Phys.* **6**, 049 (2019).

- [76] J. De Nardis, D. Bernard, and B. Doyon, “Hydrodynamic diffusion in integrable systems”, *Phys. Rev. Lett.* **121**, 160603 (2018).
- [77] J. Durnin, A. De Luca, J. De Nardis, and B. Doyon, “Diffusive hydrodynamics of inhomogeneous Hamiltonians”, *J. Phys. A: Math. Theor.* **54**, 494001 (2021).
- [78] V. B. Bulchandani, S. Gopalakrishnan, and E. Ilievski, “Superdiffusion in spin chains”, *J. Stat. Mech.: Theor. Exp.* **2021**, 084001 (2021).
- [79] A. Bastianello, J. De Nardis, and A. De Luca, “Generalized hydrodynamics with dephasing noise”, *Phys. Rev. B* **102**, 161110 (2020).
- [80] A. Bastianello, A. De Luca, and R. Vasseur, “Hydrodynamics of weak integrability breaking”, *J. Stat. Mech.: Theor. Exp.* **2021**, 114003 (2021).
- [81] P. Ruggiero, P. Calabrese, B. Doyon, and J. Dubail, “Quantum generalized hydrodynamics”, *Phys. Rev. Lett.* **124**, 140603 (2020).
- [82] F. H. Essler, “A short introduction to generalized hydrodynamics”, *Physica A* **631**, 127572 (2023).
- [83] S. Scopa and D. Karevski, “Scaling of fronts and entanglement spreading during a domain wall melting”, *Eur. Phys. J.* **232**, 1763–1781 (2023).
- [84] N. Malvania, Y. Zhang, Y. Le, J. Dubail, M. Rigol, and D. S. Weiss, “Generalized hydrodynamics in strongly interacting 1D Bose gases”, *Science* **373**, 1129–1133 (2021).
- [85] M. Schemmer, I. Bouchoule, B. Doyon, and J. Dubail, “Generalized hydrodynamics on an atom chip”, *Phys. Rev. Lett.* **122**, 090601 (2019).
- [86] H. Bernien, S. Schwartz, A. Keesling, H. Levine, A. Omran, H. Pichler, S. Choi, A. S. Zibrov, M. Endres, M. Greiner, V. Vuletić, and M. D. Lukin, “Probing many-body dynamics on a 51-atom quantum simulator”, *Nature* **551**, 579–584 (2017).
- [87] C. J. Turner, A. A. Michailidis, D. A. Abanin, M. Serbyn, and Z. Papić, “Weak ergodicity breaking from quantum many-body scars”, *Nature Phys.* **14**, 745–749 (2018).
- [88] E. J. Heller, “Bound-state eigenfunctions of classically chaotic hamiltonian systems: scars of periodic orbits”, *Phys. Rev. Lett.* **53**, 1515–1518 (1984).
- [89] W. W. Ho, S. Choi, H. Pichler, and M. D. Lukin, “Periodic orbits, entanglement, and quantum many-body scars in constrained models: matrix product state approach”, *Phys. Rev. Lett.* **122**, 040603 (2019).
- [90] M. Serbyn, D. A. Abanin, and Z. Papić, “Quantum many-body scars and weak breaking of ergodicity”, *Nature Phys.* **17**, 675–685 (2021).
- [91] I. Lesanovsky and H. Katsura, “Interacting Fibonacci anyons in a Rydberg gas”, *Phys. Rev. A* **86**, 041601 (2012).
- [92] C. J. Turner, A. A. Michailidis, D. A. Abanin, M. Serbyn, and Z. Papić, “Quantum scarred eigenstates in a Rydberg atom chain: Entanglement, breakdown of thermalization, and stability to perturbations”, *Phys. Rev. B* **98**, 155134 (2018).
- [93] A. A. Michailidis, C. J. Turner, Z. Papić, D. A. Abanin, and M. Serbyn, “Stabilizing two-dimensional quantum scars by deformation and synchronization”, *Phys. Rev. Res.* **2**, 022065 (2020).
- [94] B. van Voorden, J. ř. Miná ř, and K. Schoutens, “Quantum many-body scars in transverse field Ising ladders and beyond”, *Phys. Rev. B* **101**, 220305 (2020).

- [95] F. M. Surace, M. Votto, E. G. Lazo, A. Silva, M. Dalmonte, and G. Giudici, “Exact many-body scars and their stability in constrained quantum chains”, *Phys. Rev. B* **103**, 104302 (2021).
- [96] P. W. Anderson, “Absence of diffusion in certain random lattices”, *Phys. Rev.* **109**, 1492–1505 (1958).
- [97] P. A. Lee and D. S. Fisher, “Anderson localization in two dimensions”, *Phys. Rev. Lett.* **47**, 882–885 (1981).
- [98] M. R. Zirnbauer, “Anderson localization and non-linear sigma model with graded symmetry”, *Nucl. Phys. B* **265**, 375–408 (1986).
- [99] A. D. Mirlin and Y. V. Fyodorov, “Localization transition in the Anderson model on the Bethe lattice: spontaneous symmetry breaking and correlation functions”, *Nucl. Phys. B* **366**, 507–532 (1991).
- [100] E. Abrahams, P. W. Anderson, D. C. Licciardello, and T. V. Ramakrishnan, “Scaling theory of localization: absence of quantum diffusion in two dimensions”, *Phys. Rev. Lett.* **42**, 673–676 (1979).
- [101] T. Ohtsuki, K. Slevin, and T. Kawarabayashi, “Review of recent progress on numerical studies of the Anderson transition”, *Ann. Phys.* **511**, 655–664 (1999).
- [102] R. Abou-Chacra, D. J. Thouless, and P. W. Anderson, “A selfconsistent theory of localization”, *J. Phys. C* **6**, 1734–1752 (1973).
- [103] D. M. Basko, I. L. Aleiner, and B. L. Altshuler, “Metal-insulator transition in a weakly interacting many-electron system with localized single-particle states”, *Ann. Phys.* **321**, 1126–1205 (2006).
- [104] V. Oganesyan and D. A. Huse, “Localization of interacting fermions at high temperature”, *Phys. Rev. B* **75**, 155111 (2007).
- [105] P. Sierant, M. Lewenstein, A. Scardicchio, L. Vidmar, and J. Zakrzewski, “Many-body localization in the age of classical computing”, [arXiv:2403.07111](https://arxiv.org/abs/2403.07111) (2024).
- [106] F. Pietracaprina, V. Ros, and A. Scardicchio, “Forward approximation as a mean-field approximation for the Anderson and many-body localization transitions”, *Phys. Rev. B* **93**, 054201 (2016).
- [107] G. Parisi, S. Pascazio, F. Pietracaprina, V. Ros, and A. Scardicchio, “Anderson transition on the Bethe lattice: an approach with real energies”, *J. Phys. A: Math. Theor.* **53**, 014003 (2019).
- [108] D. A. Huse, R. Nandkishore, and V. Oganesyan, “Phenomenology of fully many-body-localized systems”, *Phys. Rev. B* **90**, 174202 (2014).
- [109] M. Serbyn, Z. Papić, and D. A. Abanin, “Local conservation laws and the structure of the many-body localized states”, *Phys. Rev. Lett.* **111**, 127201 (2013).
- [110] V. Ros, M. Müller, and A. Scardicchio, “Integrals of motion in the many-body localized phase”, *Nucl. Phys. B* **891**, 420–465 (2015).
- [111] A. Chandran, I. H. Kim, G. Vidal, and D. A. Abanin, “Constructing local integrals of motion in the many-body localized phase”, *Phys. Rev. B* **91**, 085425 (2015).
- [112] K. Agarwal, S. Gopalakrishnan, M. Knap, M. Müller, and E. Demler, “Anomalous Diffusion and Griffiths Effects Near the Many-Body Localization Transition”, *Phys. Rev. Lett.* **114**, 160401 (2015).

- [113] M. Žnidarič, A. Scardicchio, and V. K. Varma, “Diffusive and subdiffusive spin transport in the ergodic phase of a many-body localizable system”, *Phys. Rev. Lett.* **117**, 040601 (2016).
- [114] D. J. Luitz and Y. B. Lev, “The ergodic side of the many-body localization transition”, *Ann. Phys. (Berlin)* **529**, 1600350 (2017).
- [115] S. R. Taylor and A. Scardicchio, “Subdiffusion in a one-dimensional Anderson insulator with random dephasing: Finite-size scaling, Griffiths effects, and possible implications for many-body localization”, *Phys. Rev. B* **103**, 184202 (2021).
- [116] J. Z. Imbrie, “On many-body localization for quantum spin chains”, *J. Stat. Phys.* **163**, 998–1048 (2016).
- [117] J. Z. Imbrie, V. Ros, and A. Scardicchio, “Local integrals of motion in many-body localized systems”, *Ann. Phys.* **529**, 1600278 (2017).
- [118] I. Šuntajs, J. Bonča, T. Prosen, and L. Vidmar, “Quantum chaos challenges many-body localization”, *Phys. Rev. E* **102**, 062144 (2020).
- [119] J. Šuntajs, J. Bonča, T. Prosen, and L. Vidmar, “Ergodicity breaking transition in finite disordered spin chains”, *Phys. Rev. B* **102**, 064207 (2020).
- [120] D. Abanin, J. Bardarson, G. De Tomasi, S. Gopalakrishnan, V. Khemani, S. Parameswaran, F. Pollmann, A. Potter, M. Serbyn, and R. Vasseur, “Distinguishing localization from chaos: Challenges in finite-size systems”, *Ann. Phys. (Amsterdam)* **427**, 168415 (2021).
- [121] P. J. D. Crowley and A. Chandran, “A constructive theory of the numerically accessible many-body localized to thermal crossover”, *SciPost Phys.* **12**, 201 (2022).
- [122] R. K. Panda, A. Scardicchio, M. Schulz, S. R. Taylor, and M. Žnidarič, “Can we study the many-body localisation transition?”, *Europhys. Lett.* **128**, 67003 (2020).
- [123] T. Thiery, F. Huveneers, M. Müller, and W. De Roeck, “Many-body delocalization as a quantum avalanche”, *Phys. Rev. Lett.* **121**, 140601 (2018).
- [124] P. J. D. Crowley and A. Chandran, “Mean-field theory of failed thermalizing avalanches”, *Phys. Rev. B* **106**, 184208 (2022).
- [125] A. Morningstar, L. Colmenarez, V. Khemani, D. J. Luitz, and D. A. Huse, “Avalanches and many-body resonances in many-body localized systems”, *Phys. Rev. B* **105**, 174205 (2022).
- [126] D. Sels, “Bath-induced delocalization in interacting disordered spin chains”, *Phys. Rev. B* **106**, L020202 (2022).
- [127] A. De Luca, B. Altshuler, V. Kravtsov, and A. Scardicchio, “Anderson localization on the Bethe lattice: Nonergodicity of extended states”, *Phys. Rev. Lett.* **113**, 046806 (2014).
- [128] G. Biroli and M. Tarzia, “Delocalized glassy dynamics and many-body localization”, *Phys. Rev. B* **96**, 201114 (2017).
- [129] K. Tikhonov and A. Mirlin, “From Anderson localization on random regular graphs to many-body localization”, *Ann. Phys. (Amsterdam)* **435**, 168525 (2021).
- [130] I. García-Mata, J. Martin, O. Giraud, B. Georgeot, R. Dubertrand, and G. Lemarié, “Critical properties of the Anderson transition on random graphs: Two-parameter scaling theory, Kosterlitz-Thouless type flow, and many-body localization”, *Phys. Rev. B* **106**, 214202 (2022).
- [131] M. Baroni, G. G. Lorenzana, T. Rizzo, and M. Tarzia, “Corrections to the Bethe lattice solution of Anderson localization”, arXiv:2304.10365 (2023).

- [132] I. García-Mata, O. Giraud, B. Georgeot, J. Martin, R. Dubertrand, and G. Lemarié, “Scaling theory of the anderson transition in random graphs: ergodicity and universality”, [Phys. Rev. Lett. \*\*118\*\*, 166801 \(2017\)](#).
- [133] I. García-Mata, J. Martin, R. Dubertrand, O. Giraud, B. Georgeot, and G. Lemarié, “Two critical localization lengths in the Anderson transition on random graphs”, [Phys. Rev. Res. \*\*2\*\*, 012020 \(2020\)](#).
- [134] K. S. Tikhonov and A. D. Mirlin, “Fractality of wave functions on a Cayley tree: Difference between tree and locally treelike graph without boundary”, [Phys. Rev. B \*\*94\*\*, 184203 \(2016\)](#).
- [135] J. Arenz and M. R. Zirnbauer, “Wegner model on a tree graph: U(1) symmetry breaking and a non-standard phase of disordered electronic matter”, [arXiv:2305.00243 \(2023\)](#).
- [136] B. L. Altshuler, E. Cuevas, L. B. Ioffe, and V. E. Kravtsov, “Nonergodic phases in strongly disordered random regular graphs”, [Phys. Rev. Lett. \*\*117\*\*, 156601 \(2016\)](#).
- [137] M. Pino, “Scaling up the Anderson transition in random-regular graphs”, [Phys. Rev. Res. \*\*2\*\*, 042031 \(2020\)](#).
- [138] M. R. Zirnbauer, “Wegner model in high dimension: U(1) symmetry breaking and a non-standard phase of disordered electronic matter, I. One-replica theory”, [arXiv:2309.17323 \(2023\)](#).
- [139] B. L. Altshuler, Y. Gefen, A. Kamenev, and L. S. Levitov, “Quasiparticle lifetime in a finite system: A nonperturbative approach”, [Phys. Rev. Lett. \*\*78\*\*, 2803–2806 \(1997\)](#).
- [140] P. Sierant, M. Lewenstein, and A. Scardicchio, “Universality in Anderson localization on random graphs with varying connectivity”, [SciPost Physics \*\*15\*\*, 045 \(2023\)](#).
- [141] E. Ising, “Beitrag zur Theorie des Ferromagnetismus”, [Z. Phys. \*\*31\*\*, 253–258 \(1925\)](#).
- [142] A. Polkovnikov, K. Sengupta, A. Silva, and M. Vengalattore, “*Colloquium* : nonequilibrium dynamics of closed interacting quantum systems”, [Rev. Mod. Phys. \*\*83\*\*, 863–883 \(2011\)](#).
- [143] V. E. Korepin, N. M. Bogoliubov, and A. G. Izergin, Quantum inverse scattering method and correlation functions (Cambridge University Press, 1993).
- [144] T. Giamarchi, Quantum physics in one dimension (Oxford University Press, 2003).
- [145] U. Schollwöck, “The density-matrix renormalization group in the age of matrix product states”, [Ann. Phys. \*\*326\*\*, 96–192 \(2011\)](#).
- [146] H. Labuhn, D. Barredo, S. Ravets, S. De Léséleuc, T. Macrì, T. Lahaye, and A. Browaeys, “Tunable two-dimensional arrays of single Rydberg atoms for realizing quantum Ising models”, [Nature \*\*534\*\*, 667–670 \(2016\)](#).
- [147] E. Guardado-Sanchez, P. T. Brown, D. Mitra, T. Devakul, D. A. Huse, P. Schauß, and W. S. Bakr, “Probing the quench dynamics of antiferromagnetic correlations in a 2D quantum Ising spin system”, [Phys. Rev. X \*\*8\*\*, 021069 \(2018\)](#).
- [148] P. Scholl, M. Schuler, H. J. Williams, A. A. Eberharter, D. Barredo, K.-N. Schymik, V. Lienhard, L.-P. Henry, T. C. Lang, T. Lahaye, et al., “Quantum simulation of 2D antiferromagnets with hundreds of Rydberg atoms”, [Nature \*\*595\*\*, 233–238 \(2021\)](#).
- [149] S. Ebadi, T. T. Wang, H. Levine, A. Keesling, G. Semeghini, A. Omran, D. Bluvstein, R. Samajdar, H. Pichler, W. W. Ho, et al., “Quantum phases of matter on a 256-atom programmable quantum simulator”, [Nature \*\*595\*\*, 227–232 \(2021\)](#).

- [150] D. Bluvstein, H. Levine, G. Semeghini, T. T. Wang, S. Ebadi, M. Kalinowski, A. Keesling, N. Maskara, H. Pichler, M. Greiner, V. Vuletić, and M. D. Lukin, “A quantum processor based on coherent transport of entangled atom arrays”, *Nature* **604**, 451–456 (2022).
- [151] D. Bluvstein, A. Omran, H. Levine, A. Keesling, G. Semeghini, S. Ebadi, T. T. Wang, A. A. Michailidis, N. Maskara, W. W. Ho, et al., “Controlling quantum many-body dynamics in driven Rydberg atom arrays”, *Science* **371**, 1355–1359 (2021).
- [152] U. Agrawal, R. Vasseur, and S. Gopalakrishnan, “Quasiperiodic many-body localization transition in dimension  $d > 1$ ”, *Phys. Rev. B* **106**, 094206 (2022).
- [153] A. Štrkalj, E. V. H. Doggen, and C. Castelnovo, “Coexistence of localization and transport in many-body two-dimensional Aubry-André models”, *Phys. Rev. B* **106**, 184209 (2022).
- [154] A. Bray, “Theory of phase-ordering kinetics”, *Adv. Phys.* **43**, 357–459 (1994).
- [155] A. Onuki, Phase transition dynamics (Cambridge University Press, 2002).
- [156] S. Karthika, T. K. Radhakrishnan, and P. Kalaichelvi, “A review of classical and nonclassical nucleation theories”, *Crystal Growth & Design* **16**, 6663–6681 (2016).
- [157] I. Y. Kobzarev, L. B. Okun, and M. B. Voloshin, “Bubbles in metastable vacuum”, *Yad. Fiz.* **20**, 1229–1234 (1974).
- [158] S. Coleman, “Fate of the false vacuum: semiclassical theory”, *Phys. Rev. D* **15**, 2929–2936 (1977).
- [159] C. G. Callan and S. Coleman, “Fate of the false vacuum. II. first quantum corrections”, *Phys. Rev. D* **16**, 1762–1768 (1977).
- [160] S. Coleman, Aspects of symmetry: Selected Erice lectures (Cambridge University Press, 1988).
- [161] A. H. Guth, “Inflation and eternal inflation”, *Phys. Rep.* **333**, 555–574 (2000).
- [162] B. Song, S. Dutta, S. Bhave, J.-C. Yu, E. Carter, N. Cooper, and U. Schneider, “Realizing discontinuous quantum phase transitions in a strongly correlated driven optical lattice”, *Nature Phys.* **18**, 259–264 (2022).
- [163] E. Farhi, J. Goldstone, S. Gutmann, J. Lapan, A. Lundgren, and D. Preda, “A quantum adiabatic evolution algorithm applied to random instances of an NP-complete problem”, *Science* **292**, 472–475 (2001).
- [164] E. Crosson, E. Farhi, C. Y.-Y. Lin, H.-H. Lin, and P. Shor, “Different strategies for optimization using the quantum adiabatic algorithm”, *arXiv:1401.7320* (2014).
- [165] C. R. Laumann, R. Moessner, A. Scardicchio, and S. L. Sondhi, “Quantum annealing: The fastest route to quantum computation?”, *Eur. Phys. J. Spec. Top.* **224**, 75–88 (2015).
- [166] F. Barahona, “On the computational complexity of ising spin glass models”, *J. Phys. A: Math. Gen.* **15**, 3241 (1982).
- [167] B. Altshuler, H. Krovi, and J. Roland, “Anderson localization makes adiabatic quantum optimization fail”, *PNAS* **107**, 12446–12450 (2010).
- [168] V. Bapst, L. Foini, F. Krzakala, G. Semerjian, and F. Zamponi, “The quantum adiabatic algorithm applied to random optimization problems: the quantum spin glass perspective”, *Phys. Rep.* **523**, 127–205 (2013).
- [169] M. Bellitti, F. Ricci-Tersenghi, and A. Scardicchio, “Entropic barriers as a reason for hardness in both classical and quantum algorithms”, *Phys. Rev. Res.* **3**, 043015 (2021).

- [170] A. Yoshinaga, H. Hakoshima, T. Imoto, Y. Matsuzaki, and R. Hamazaki, “Emergence of Hilbert space fragmentation in Ising models with a weak transverse field”, *Phys. Rev. Lett.* **129**, 090602 (2021).
- [171] O. Hart and R. Nandkishore, “Hilbert space shattering and dynamical freezing in the quantum Ising model”, *Phys. Rev. B* **106**, 214426 (2022).
- [172] M. Schulz, C. A. Hooley, R. Moessner, and F. Pollmann, “Stark many-body localization”, *Phys. Rev. Lett.* **122**, 040606 (2019).
- [173] E. van Nieuwenburg, Y. Baum, and G. Refael, “From Bloch oscillations to many-body localization in clean interacting systems”, *PNAS* **116**, 9269–9274 (2019).
- [174] A. D. Luca and A. Scardicchio, “Ergodicity breaking in a model showing many-body localization”, *Europhys. Lett.* **101**, 37003 (2013).
- [175] D. J. Luitz, N. Laflorencie, and F. Alet, “Many-body localization edge in the random-field Heisenberg chain”, *Phys. Rev. B* **91**, 081103(R) (2015).
- [176] W. De Roeck and J. Z. Imbrie, “Many-body localization: stability and instability”, *Phil. Trans. R. Soc. A* **375**, 20160422 (2017).
- [177] W. De Roeck and F. Huveneers, “Stability and instability towards delocalization in many-body localization systems”, *Phys. Rev. B* **95**, 155129 (2017).
- [178] P. P. Mazza, G. Perfetto, A. Lerose, M. Collura, and A. Gambassi, “Suppression of transport in nondisordered quantum spin chains due to confined excitations”, *Phys. Rev. B* **99**, 180302 (2019).
- [179] A. Lerose, F. M. Surace, P. P. Mazza, G. Perfetto, M. Collura, and A. Gambassi, “Quasilocalized dynamics from confinement of quantum excitations”, *Phys. Rev. B* **102**, 041118 (2020).
- [180] J. Maldacena, “The Large-N limit of superconformal field theories and supergravity”, *Int. J. Theor. Phys.* **38**, 1113–1133 (1999).
- [181] S. Gubser, I. Klebanov, and A. Polyakov, “Gauge theory correlators from non-critical string theory”, *Phys. Lett. B* **428**, 105–114 (1998).
- [182] E. Witten, “Anti de Sitter space and holography”, [arXiv:hep-th/9802150](https://arxiv.org/abs/hep-th/9802150) (1998).
- [183] B. F. Logan and L. A. Shepp, “A variational problem for random Young tableaux”, *Adv. Math.* **26**, 206–222 (1977).
- [184] A. Vershik and S. Kerov, “Asymptotics of the Plancherel measure of the symmetric group and the limit form of Young tableaux”, *Soviet Math. Doklady* **18**, 527–531 (1977).
- [185] A. Vershik and S. Kerov, “Asymptotics of the maximal and typical dimension of irreducible representations of symmetric group”, *Funct. Anal. Appl.* **19**, 21–31 (1985).
- [186] A. Okounkov, “Random matrices and random permutations”, *Intl. Math. Res. Not.* **2000**, 1043–1095 (2000).
- [187] P. L. Krapivsky, “Stochastic dynamics of growing Young diagrams and their limit shapes”, *J. Stat. Mech.: Theor. Exp.* **2021**, 013206 (2021).
- [188] A. Santini, G. E. Santoro, and M. Collura, “Clean two-dimensional Floquet time crystal”, *Phys. Rev. B* **106**, 134301 (2022).
- [189] H. Aoki, N. Tsuji, M. Eckstein, M. Kollar, T. Oka, and P. Werner, “Nonequilibrium dynamical mean-field theory and its applications”, *Rev. Mod. Phys.* **86**, 779–837 (2014).

- [190] H. Spohn, “Kinetic equations for quantum many-particle systems”, arXiv:0706.0807 (2007).
- [191] J. R. Schrieffer and P. A. Wolff, “Relation between the Anderson and Kondo Hamiltonians”, *Phys. Rev.* **149**, 491–492 (1966).
- [192] P. Schauß, M. Cheneau, M. Endres, T. Fukuhara, S. Hild, A. Omran, T. Pohl, C. Gross, S. Kuhr, and I. Bloch, “Observation of spatially ordered structures in a two-dimensional Rydberg gas”, *Nature* **491**, 87–91 (2012).
- [193] P. Fendley, K. Sengupta, and S. Sachdev, “Competing density-wave orders in a one-dimensional hard-boson model”, *Phys. Rev. B* **69**, 075106 (2004).
- [194] H. Bernien, S. Schwartz, A. Keesling, H. Levine, A. Omran, H. Pichler, S. Choi, A. S. Zibrov, M. Endres, M. Greiner, et al., “Probing many-body dynamics on a 51-atom quantum simulator”, *Nature* **551**, 579 (2017).
- [195] N. Chepiga and F. Mila, “Kibble-Zurek exponent and chiral transition of the period-4 phase of Rydberg chains”, *Nature Comm.* **12**, 414 (2021).
- [196] P. Chandra and E. W. Weisstein, Fibonacci numbers, From *MathWorld* – A Wolfram Web Resource, 2022.
- [197] M. Schecter and T. Iadecola, “Many-body spectral reflection symmetry and protected infinite-temperature degeneracy”, *Phys. Rev. B* **98**, 035139 (2018).
- [198] K. Fujimoto, R. Hamazaki, and Y. Kawaguchi, “Family-Vicsek scaling of roughness growth in a strongly interacting Bose gas”, *Phys. Rev. Lett.* **124**, 210604 (2020).
- [199] K. Fujimoto, R. Hamazaki, and Y. Kawaguchi, “Dynamical scaling of surface roughness and entanglement entropy in disordered fermion models”, *Phys. Rev. Lett.* **127**, 090601 (2021).
- [200] K. Fujimoto, R. Hamazaki, and Y. Kawaguchi, “Impact of dissipation on universal fluctuation dynamics in open quantum systems”, *Phys. Rev. Lett.* **129**, 110403 (2022).
- [201] T. Jin, A. Krajenbrink, and D. Bernard, “From stochastic spin chains to quantum Kardar-Parisi-Zhang dynamics”, *Phys. Rev. Lett.* **125**, 040603 (2020).
- [202] H. Rost, “Non-equilibrium behaviour of a many particle process: density profile and local equilibria”, *Zeit. Wahr. Ver. Geb.* **58**, 41–53 (1981).
- [203] T. M. Liggett, *Stochastic interacting systems: contact, voter and exclusion processes* (Springer, Berlin, Heidelberg, 1999), pp. 209–316.
- [204] G. Schütz, in *Phase transitions and critical phenomena*, Vol. 19, edited by C. Domb and J. Lebowitz (Academic Press, 2001), pp. 1–251.
- [205] G. Grosso and G. Parravicini, *Solid state physics* (Academic Press, London, 2000).
- [206] A. Lerose, B. Žunkovič, A. Silva, and A. Gambassi, “Quasilocalized excitations induced by long-range interactions in translationally invariant quantum spin chains”, *Phys. Rev. B* **99**, 121112(R) (2019).
- [207] D. Richardson, “Random growth in a tessellation”, *Math. Proc. Cambridge Phil. Soc.* **74**, 515–528 (1973).
- [208] J. Krug and H. Spohn, in *Solids far from equilibrium*, edited by C. Godrèche (Cambridge University Press, 1991), pp. 479–572.
- [209] H. Spohn, “Exact solutions for KPZ-type growth processes, random matrices, and equilibrium shapes of crystals”, *Physica A* **369**, 71–99 (2006).

- [210] P. L. Krapivsky, S. Redner, and J. Tailleur, “Dynamics of an unbounded interface between ordered phases”, *Phys. Rev. E* **69**, 026125 (2004).
- [211] R. Dijkgraaf, D. Orlando, and S. Reffert, “Quantum crystals and spin chains”, *Nucl. Phys. B* **811**, 463–490 (2009).
- [212] T. Araujo, D. Orlando, and S. Reffert, “Quantum crystals, Kagome lattice, and plane partitions fermion-boson duality”, *Phys. Rev. D* **103**, 026020 (2021).
- [213] P. L. Krapivsky and J. Olejarz, “Limiting shapes in two-dimensional Ising ferromagnets”, *Phys. Rev. E* **87**, 062111 (2013).
- [214] P. L. Krapivsky, “Limiting shapes of Ising droplets, Ising fingers, and Ising solitons”, *Phys. Rev. E* **85**, 011152 (2012).
- [215] A. Borodin, A. Okounkov, and G. Olshanski, “Asymptotics of Plancherel measures for symmetric groups”, *J. Amer. Math. Soc.* **13**, 481–515 (2000).
- [216] A. Okounkov, “Infinite wedge and random partitions”, *Selecta Mathematica* **7**, 57 (2001).
- [217] A. Okounkov, N. Reshetikhin, and C. Vafa, in *The unity of mathematics* (Springer, 2006), pp. 597–618.
- [218] E. Fradkin, M. Srednicki, and L. Susskind, “Fermion representation for the  $Z_2$  lattice gauge theory in 2+1 dimensions”, *Phys. Rev. D* **21**, 2885–2891 (1980).
- [219] A. Polyakov, “Quantum geometry of fermionic strings”, *Phys. Lett. B* **103**, 211–213 (1981).
- [220] N. Iqbal and J. McGreevy, “Toward a 3d Ising model with a weakly-coupled string theory dual”, *SciPost Phys.* **9**, 19 (2020).
- [221] T. Antal, Z. Rácz, A. Rákos, and G. M. Schütz, “Transport in the XX chain at zero temperature: emergence of flat magnetization profiles”, *Phys. Rev. E* **59**, 4912–4918 (1999).
- [222] C. A. Tracy and H. Widom, “Level spacing distributions and the Bessel kernel”, *Commun. Math. Phys.* **161**, 289–309 (1994).
- [223] A. Kuijlaars, in *The Oxford Handbook on Random Matrix Theory*, edited by G. Akemann, J. Baik, and P. D. Francesco (Oxford University Press, Oxford, 2011) Chap. 6, pp. 103–134.
- [224] M. L. Mehta, *Random matrices* (Elsevier, 2004).
- [225] I. Peschel and V. Eisler, “Reduced density matrices and entanglement entropy in free lattice models”, *J. Phys. A: Math. Theor.* **42**, 504003 (2009).
- [226] C. A. Tracy and H. Widom, “Level-spacing distributions and the Airy kernel”, *Phys. Lett. B* **305**, 115–118 (1993).
- [227] C. A. Tracy and H. Widom, “Level-spacing distributions and the Airy kernel”, *Commun. Math. Phys.* **159**, 151–174 (1994).
- [228] B. Doyon, “Lecture notes on generalised hydrodynamics”, *SciPost Phys. Lect. Notes*, **18** (2020).
- [229] V. Eisler, G. D. Giulio, E. Tonni, and I. Peschel, “Entanglement Hamiltonians for non-critical quantum chains”, *J. Stat. Mech.: Theor. Exp.* **2020**, 103102 (2020).
- [230] V. Eisler and Z. Rácz, “Full counting statistics in a propagating quantum front and random matrix spectra”, *Phys. Rev. Lett.* **110**, 060602 (2013).
- [231] V. Eisler, F. Iglói, and I. Peschel, “Entanglement in spin chains with gradients”, *J. Stat. Mech.: Theor. Exp.* **2009**, P02011 (2009).

- [232] I. Peschel, “On the reduced density matrix for a chain of free electrons”, *J. Stat. Mech.: Theor. Exp.* **2004**, P06004 (2004).
- [233] F. Rottoli, S. Scopa, and P. Calabrese, “Entanglement Hamiltonian during a domain wall melting in the free Fermi chain”, *J. Stat. Mech.: Theor. Exp.* **2022**, 063103 (2022).
- [234] I. Peschel, “Calculation of reduced density matrices from correlation functions”, *J. Phys. A: Math. Gen.* **36**, L205–L208 (2003).
- [235] S.-A. Cheong and C. L. Henley, “Many-body density matrices for free fermions”, *Phys. Rev. B* **69**, 075111 (2004).
- [236] J. Dubail, J.-M. Stéphan, J. Viti, and P. Calabrese, “Conformal field theory for inhomogeneous one-dimensional quantum systems: the example of non-interacting Fermi gases”, *SciPost Phys.* **2**, 002 (2017).
- [237] E. Tonni, J. Rodríguez-Laguna, and G. Sierra, “Entanglement hamiltonian and entanglement contour in inhomogeneous 1D critical systems”, *J. Stat. Mech.: Theor. Exp.* **2018**, 043105 (2018).
- [238] W. Fulton, *Young tableaux* (Cambridge University Press, 1996).
- [239] A. Okounkov, “The uses of random partitions”, [arXiv:math-ph/0309015](https://arxiv.org/abs/math-ph/0309015) (2003).
- [240] A. Vershik, “Two lectures on the asymptotic representation theory and statistics of Young diagrams”, in *Asymptotic combinatorics with applications to mathematical physics* (Springer Berlin Heidelberg, 2003), pp. 161–182.
- [241] M. Aizenman and S. Warzel, *Random operators: Disorder Effects on Quantum Spectra and Dynamics* (AMS, 2015).
- [242] A. Scardicchio and T. Thiery, “Perturbation theory approaches to Anderson and many-body localization: some lecture notes”, [arXiv:1710.01234](https://arxiv.org/abs/1710.01234) (2017).
- [243] D. Abanin, W. De Roeck, W. W. Ho, and F. Huveneers, “A rigorous theory of many-body prethermalization for periodically driven and closed quantum systems”, *Commun. Math. Phys.* **354**, 809–827 (2017).
- [244] W. Morong, F. Liu, P. Becker, K. S. Collins, L. Feng, A. Kyprianidis, G. Pagano, T. You, A. V. Gorshkov, and C. Monroe, “Observation of Stark many-body localization without disorder”, *Nature* **599**, 393–398 (2021).
- [245] F. W. J. Olver, A. B. Olde Daalhuis, D. W. Lozier, B. I. Schneider, R. F. Boisvert, C. W. Clark, B. R. Miller, B. V. Saunders, H. S. Cohl, and M. A. McClain, eds., *NIST Digital Library of Mathematical Functions*, Release 1.1.6 of 2022-06-30, 2022.
- [246] S. B. Rutkevich, “Decay of the metastable phase in  $d = 1$  and  $d = 2$  Ising models”, *Phys. Rev. B* **60**, 14525–14528 (1999).
- [247] G. Lagnese, F. M. Surace, M. Kormos, and P. Calabrese, “False vacuum decay in quantum spin chains”, *Phys. Rev. B* **104**, L201106 (2021).
- [248] O. Pomponio, M. A. Werner, G. Zarand, and G. Takacs, “Bloch oscillations and the lack of the decay of the false vacuum in a one-dimensional quantum spin chain”, *SciPost Phys.* **12**, 61 (2022).
- [249] B. Kloss, J. C. Halimeh, A. Lazarides, and Y. B. Lev, “Absence of localization in interacting spin chains with a discrete symmetry”, [arXiv:2208.13793](https://arxiv.org/abs/2208.13793) (2022).
- [250] R. Cerf and R. Kenyon, “The Low-Temperature Expansion of the Wulff Crystal in the 3D Ising Model”, *Commun. Math. Phys.* **222**, 147–179 (2001).

- [251] R. Kenyon, A. Okounkov, and S. Sheffield, “Dimers and amoebae”, [Ann. Math. \*\*163\*\*, 1019–1056 \(2006\)](#).
- [252] A. Okounkov and N. Reshetikhin, “Correlation function of Schur process with application to local geometry of a random 3-dimensional Young diagram”, [J. Amer. Math. Soc. \*\*16\*\*, 581–603 \(2003\)](#).
- [253] P. L. Ferrari and H. Spohn, “Step fluctuations for a faceted crystal”, [J. Stat. Phys. \*\*113\*\*, 1–46 \(2003\)](#).
- [254] S. Torquato, A. Scardicchio, and C. E. Zachary, “Point processes in arbitrary dimension from fermionic gases, random matrix theory, and number theory”, [J. Stat. Mech.:Theor. Exp. \*\*2008\*\*, P11019 \(2008\)](#).
- [255] A. Scardicchio, C. E. Zachary, and S. Torquato, “Statistical properties of determinantal point processes in high-dimensional Euclidean spaces”, [Phys. Rev. E \*\*79\*\*, 041108 \(2009\)](#).
- [256] H. Ooguri and M. Yamazaki, “Crystal melting and toric Calabi-Yau manifolds”, [Commun. Math. Phys. \*\*292\*\*, 179–199 \(2009\)](#).
- [257] I. Lesanovsky, “Liquid ground state, gap, and excited states of a strongly correlated spin chain”, [Phys. Rev. Lett. \*\*108\*\*, 105301 \(2012\)](#).
- [258] M. D. Lukin, M. Fleischhauer, R. Cote, L. M. Duan, D. Jaksch, J. I. Cirac, and P. Zoller, “Dipole blockade and quantum information processing in mesoscopic atomic ensembles”, [Phys. Rev. Lett. \*\*87\*\*, 037901 \(2001\)](#).
- [259] P. Sierant, E. G. Lazo, M. Dalmonte, A. Scardicchio, and J. Zakrzewski, “Constraints induced delocalization”, [Phys Rev. Lett. \*\*127\*\*, 126603 \(2021\)](#).
- [260] H. Théveniaut, Z. Lan, G. Meyer, and F. Alet, “Transition to a many-body localized regime in a two-dimensional disordered quantum dimer model”, [Phys. Rev. Res. \*\*2\*\*, 033154 \(2020\)](#).
- [261] F. Pietracaprina and F. Alet, “Probing many-body localization in a disordered quantum dimer model on the honeycomb lattice”, [SciPost Phys. \*\*10\*\*, 44 \(2021\)](#).
- [262] A. Chandran, A. Pal, C. R. Laumann, and A. Scardicchio, “Many-body localization beyond eigenstates in all dimensions”, [Phys. Rev. B \*\*94\*\*, 144203 \(2016\)](#).
- [263] R. M. Nandkishore and S. L. Sondhi, “Many-body localization with long-range interactions”, [Phys. Rev. X \*\*7\*\*, 041021 \(2017\)](#).
- [264] S. Gopalakrishnan and D. A. Huse, “Instability of many-body localized systems as a phase transition in a nonstandard thermodynamic limit”, [Phys. Rev. B \*\*99\*\*, 134305 \(2019\)](#).
- [265] S. Gopalakrishnan and S. Parameswaran, “Dynamics and transport at the threshold of many-body localization”, [Phys. Rep. \*\*862\*\*, 1–62 \(2020\)](#).
- [266] C. Artiago, F. Balducci, and A. Scardicchio, “Signatures of many-body localization in the dynamics of two-level systems in glasses”, [Phys. Rev. B \*\*103\*\*, 214205 \(2021\)](#).
- [267] S. Moudgalya, S. Rachel, B. A. Bernevig, and N. Regnault, “Exact excited states of nonintegrable models”, [Phys. Rev. B \*\*98\*\*, 235155 \(2018\)](#).
- [268] V. Khemani, C. R. Laumann, and A. Chandran, “Signatures of integrability in the dynamics of Rydberg-blockaded chains”, [Phys. Rev. B \*\*99\*\*, 161101 \(2019\)](#).
- [269] M. Griffiths and N. Lord, “The hook-length formula and generalised Catalan numbers”, [Math. Gazette \*\*95\*\*, 23–30 \(2011\)](#).
- [270] E. Cuevas, M. Feigel’man, L. Ioffe, and M. Mezard, “Level statistics of disordered spin-1/2 systems and materials with localized Cooper pairs”, [Nat. Commun. \*\*3\*\*, 1128 \(2012\)](#).

- [271] S. Sachdev and J. Ye, “Gapless spin-fluid ground state in a random quantum Heisenberg magnet”, *Phys. Rev. Lett.* **70**, 3339–3342 (1993).
- [272] A. Kitaev, A simple model of quantum holography, <http://online.kitp.ucsb.edu/online/entangled15/kitaev/>, <http://online.kitp.ucsb.edu/online/entangled15/kitaev2/>, 2015.
- [273] D. Areán, L. A. Pando Zayas, I. S. Landea, and A. Scardicchio, “Holographic disorder driven superconductor-metal transition”, *Phys. Rev. D* **94**, 106003 (2016).
- [274] P. Sierant, M. Lewenstein, A. Scardicchio, and J. Zakrzewski, “Stability of many-body localization in Kicked Ising model”, [arXiv:2203.15697](https://arxiv.org/abs/2203.15697) (2022).
- [275] P. Sierant, M. Lewenstein, and A. Scardicchio, “Universality in Anderson localization on random graphs with varying connectivity”, [arXiv:2205.14614](https://arxiv.org/abs/2205.14614) (2022).
- [276] B. Li and J. Wang, “Anomalous heat conduction and anomalous diffusion in one-dimensional systems”, *Phys. Rev. Lett.* **91**, 044301 (2003).
- [277] J. J. Mendoza-Arenas, M. Žnidarič, V. K. Varma, J. Goold, S. R. Clark, and A. Scardicchio, “Asymmetry in energy versus spin transport in certain interacting disordered systems”, *Phys. Rev. B* **99**, 094435 (2019).
- [278] GitHub repository at <https://github.com/fbaldux/Ising-Melting-dis>.
- [279] P. Calabrese and J. Cardy, “Entanglement and correlation functions following a local quench: a conformal field theory approach”, *J. Stat. Mech.: Theor. Exp.* **2007**, P10004 (2007).
- [280] A. Nahum, J. Ruhman, S. Vijay, and J. Haah, “Quantum entanglement growth under random unitary dynamics”, *Phys. Rev. X* **7**, 031016 (2017).
- [281] A. Nahum, S. Vijay, and J. Haah, “Operator spreading in random unitary circuits”, *Phys. Rev. X* **8**, 021014 (2018).
- [282] A. Chan, A. De Luca, and J. T. Chalker, “Solution of a minimal model for many-body quantum chaos”, *Phys. Rev. X* **8**, 041019 (2018).
- [283] M. Balazs, E. Cator, and T. Seppalainen, “Cube root fluctuations for the corner growth model associated to the exclusion process”, [arXiv:math/0603306](https://arxiv.org/abs/math/0603306) (2006).
- [284] P. L. Ferrari and H. Spohn, “Random growth models”, [arXiv:1003.0881](https://arxiv.org/abs/1003.0881) (2010).
- [285] B. Derrida, “An exactly soluble non-equilibrium system: the asymmetric simple exclusion process”, *Phys. Rep.* **301**, 65–83 (1998).
- [286] D. Khoromskaia, R. J. Harris, and S. Grosskinsky, “Dynamics of non-Markovian exclusion processes”, *J. Stat. Mech.: Theor. Exp.* **2014**, P12013 (2014).
- [287] R. Jose, C. Arita, and L. Santen, “Bidirectional non-Markovian exclusion processes”, *J. Stat. Mech.: Theor. Exp.* **2020**, 033207 (2020).
- [288] F. Bloch, “Über die Quantenmechanik der Elektronen in Kristallgittern”, *Z. Phys.* **52**, 555–600 (1929).
- [289] G. H. Wannier, “Wave functions and effective Hamiltonian for Bloch electrons in an electric field”, *Phys. Rev.* **117**, 432–439 (1960).
- [290] G. H. Wannier, “Dynamics of band electrons in electric and magnetic fields”, *Rev. Mod. Phys.* **34**, 645–655 (1962).

- [291] T. Hartmann, F. Keck, H. J. Korsch, and S. Mossmann, “Dynamics of Bloch oscillations”, *New J. Phys.* **6**, 2 (2004).
- [292] X.-Y. Guo, Z.-Y. Ge, H. Li, Z. Wang, Y.-R. Zhang, P. Song, Z. Xiang, X. Song, Y. Jin, L. Lu, K. Xu, D. Zheng, and H. Fan, “Observation of Bloch oscillations and Wannier-Stark localization on a superconducting quantum processor”, *npj Q. Info.* **7**, 51 (2021).
- [293] E. V. H. Doggen, I. V. Gornyi, and D. G. Polyakov, “Stark many-body localization: Evidence for Hilbert-space shattering”, *Phys. Rev. B* **103**, L100202 (2021).
- [294] A. Bastianello and A. De Luca, “Nonequilibrium steady state generated by a moving defect: the supersonic threshold”, *Phys. Rev. Lett.* **120**, 060602 (2018).
- [295] E. Wigner, “On the quantum correction for thermodynamic equilibrium”, *Phys. Rev.* **40**, 749–759 (1932).
- [296] K. E. Cahill and R. J. Glauber, “Density operators and quasiprobability distributions”, *Phys. Rev.* **177**, 1882–1902 (1969).
- [297] M. Glück, A. R. Kolovsky, and H. J. Korsch, “Wannier–Stark resonances in optical and semiconductor superlattices”, *Phys. Rep.* **366**, 103–182 (2002).
- [298] T. Antal, P. L. Krapivsky, and A. Rákos, “Logarithmic current fluctuations in nonequilibrium quantum spin chains”, *Phys. Rev. E* **78**, 061115 (2008).
- [299] V. Eisler and F. Maislinger, “Hydrodynamical phase transition for domain-wall melting in the XY chain”, *Phys. Rev. B* **98**, 161117 (2018).
- [300] T. Platini and D. Karevski, “Relaxation in the XX quantum chain”, *J. Phys. A: Math. Theor.* **40**, 1711 (2007).
- [301] D. S. Bhakuni and A. Sharma, “Characteristic length scales from entanglement dynamics in electric-field-driven tight-binding chains”, *Phys. Rev. B* **98**, 045408 (2018).
- [302] V. Eisler and D. Bauernfeind, “Front dynamics and entanglement in the XXZ chain with a gradient”, *Phys. Rev. B* **96**, 174301 (2017).
- [303] N. Allegra, J. Dubail, J.-M. Stéphan, and J. Viti, “Inhomogeneous field theory inside the arctic circle”, *J. Stat. Mech.: Theor. Exp.* **2016**, 053108 (2016).
- [304] C.-N. Yang and C. P. Yang, “Thermodynamics of a one-dimensional system of bosons with repulsive delta-function interaction”, *J. Math. Phys.* **10**, 1115–1122 (1969).
- [305] P. Calabrese and J. Cardy, “Entanglement entropy and quantum field theory”, *J. Stat. Mech.: Theor. Exp.* **2004**, P06002 (2004).
- [306] P. Calabrese and J. Cardy, “Entanglement entropy and conformal field theory”, *J. Phys. A: Math. Theor.* **42**, 504005 (2009).
- [307] J. L. Cardy, O. A. Castro-Alvaredo, and B. Doyon, “Form factors of branch-point twist fields in quantum integrable models and entanglement entropy”, *J. Stat. Phys.* **130**, 129–168 (2007).
- [308] B.-Q. Jin and V. E. Korepin, “Quantum spin chain, Toeplitz determinants and the Fisher-Hartwig conjecture”, *J. Stat. Phys.* **116**, 79–95 (2004).
- [309] P. Calabrese and J. Cardy, “Evolution of entanglement entropy in one-dimensional systems”, *J. Stat. Mech.: Theor. Exp.* **2005**, P04010 (2005).
- [310] P. Calabrese and F. H. L. Essler, “Universal corrections to scaling for block entanglement in spin-1/2 XX chains”, *J. Stat. Mech.: Theor. Exp.* **2010**, P08029 (2010).

- [311] I. Klich and L. Levitov, “Quantum noise as an entanglement meter”, *Phys. Rev. Lett.* **102**, 100502 (2009).
- [312] P. Calabrese, M. Mintchev, and E. Vicari, “Exact relations between particle fluctuations and entanglement in Fermi gases”, *Europhys. Lett.* **98**, 20003 (2012).
- [313] L. Capizzi, S. Murciano, and P. Calabrese, “Full counting statistics and symmetry resolved entanglement for free conformal theories with interface defects”, *J. Stat. Mech.: Theor. Exp.* **2023**, 073102 (2023).
- [314] M. Collura, S. Sotiriadis, and P. Calabrese, “Equilibration of a Tonks-Girardeau gas following a trap release”, *Phys. Rev. Lett.* **110**, 245301 (2013).
- [315] M. Collura, S. Sotiriadis, and P. Calabrese, “Quench dynamics of a Tonks-Girardeau gas released from a harmonic trap”, *J. Stat. Mech.: Theor. Exp.* **2013**, P09025 (2013).
- [316] M. Collura, A. De Luca, P. Calabrese, and J. Dubail, “Domain wall melting in the spin- $\frac{1}{2}$  XXZ spin chain: emergent Luttinger liquid with a fractal quasiparticle charge”, *Phys. Rev. B* **102**, 180409 (2020).
- [317] P. Zechmann, A. Bastianello, and M. Knap, “Tunable transport in the mass-imbalanced Fermi-Hubbard model”, *Phys. Rev. B* **106**, 075115 (2022).
- [318] A. Bastianello and A. De Luca, “Integrability-protected adiabatic reversibility in quantum spin chains”, *Phys. Rev. Lett.* **122**, 240606 (2019).
- [319] L. Capizzi, S. Scopa, F. Rottoli, and P. Calabrese, “Domain wall melting across a defect”, *Europhys. Lett.* **141**, 31002 (2023).
- [320] M. Ljubotina, S. Sotiriadis, and T. Prosen, “Non-equilibrium quantum transport in presence of a defect: the non-interacting case”, *SciPost Phys.* **6**, 004 (2019).
- [321] G. Del Vecchio Del Vecchio, A. D. Luca, and A. Bastianello, “Transport through interacting defects and lack of thermalisation”, *SciPost Phys.* **12**, 060 (2022).
- [322] A. Bastianello, “Lack of thermalization for integrability-breaking impurities”, *Europhys. Lett.* **125**, 20001 (2019).
- [323] E. W. Weisstein, Binomial coefficient, From *MathWorld* – A Wolfram Web Resource, 2022.
- [324] E. W. Weisstein, Bessel Function of the First Kind, From *MathWorld* – A Wolfram Web Resource, 2022.
- [325] M. Abramowitz and I. A. Stegun, Handbook of mathematical functions, 9th (Dover, New York, 1964).
- [326] B. Derrida, M. R. Evans, V. Hakim, and V. Pasquier, “Exact solution of a 1d asymmetric exclusion model using a matrix formulation”, *J. Phys. A: Math. Gen.* **26**, 1493–1517 (1993).
- [327] B. Derrida and A. Gerschenfeld, “Current fluctuations of the one dimensional symmetric simple exclusion process with step initial condition”, *J. Stat. Phys.* **136**, 1–15 (2009).
- [328] B. Derrida, J. L. Lebowitz, and E. R. Speer, “Large deviation of the density profile in the steady state of the open symmetric simple exclusion process”, *J. Stat. Phys.* **107**, 599–634 (2002).
- [329] I. Corwin, P. L. Ferrari, and S. Péché, “Limit processes for TASEP with shocks and rarefaction fans”, *J. Stat. Phys.* **140**, 232–267 (2010).
- [330] A. De Masi, P. A. Ferrari, and E. Presutti, “Symmetric simple exclusion process with free boundaries”, *Proba. Theor. Rel. Fiel.* **161**, 155–193 (2015).

- [331] J. Negele, Quantum many-particle systems (CRC Press, 1998).
- [332] I. Peschel, “Special review: entanglement in solvable many-particle models”, *Braz. J. Phys.* **42**, 267–291 (2012).
- [333] M.-C. Chung and I. Peschel, “Density-matrix spectra of solvable fermionic systems”, *Phys. Rev. B* **64**, 064412 (2001).
- [334] I. Peschel, M. Kaulke, and Ö. Legeza, “Density-matrix spectra for integrable models”, *Ann. Phys.* **511**, 153–164 (1999).
- [335] V. Alba and P. Calabrese, “Quench action and Rényi entropies in integrable systems”, *Phys. Rev. B* **96**, 115421 (2017).
- [336] F. Evers and A. D. Mirlin, “Anderson transitions”, *Rev. Mod. Phys.* **80**, 1355 (2008).
- [337] E. Tarquini, G. Biroli, and M. Tarzia, “Critical properties of the Anderson localization transition and the high-dimensional limit”, *Phys. Rev. B* **95**, 094204 (2017).
- [338] K. S. Tikhonov, A. D. Mirlin, and M. A. Skvortsov, “Anderson localization and ergodicity on random regular graphs”, *Phys. Rev. B* **94**, 220203 (2016).
- [339] S. Bera, G. De Tomasi, I. M. Khaymovich, and A. Scardicchio, “Return probability for the Anderson model on the random regular graph”, *Phys. Rev. B* **98**, 134205 (2018).
- [340] R. Nandkishore and D. A. Huse, “Many-body localization and thermalization in quantum statistical mechanics”, *Annu. Rev. Condens. Matter Phys.* **6**, 15–38 (2015).
- [341] I. Šuntajs, J. Bonča, T. Prosen, and L. Vidmar, “Quantum chaos challenges many-body localization”, *Phys. Rev. E* **102**, 062144 (2020).
- [342] P. Sierant, D. Delande, and J. Zakrzewski, “Thouless time analysis of Anderson and many-body localization transitions”, *Phys. Rev. Lett.* **124**, 186601 (2020).
- [343] P. Sierant and J. Zakrzewski, “Challenges to observation of many-body localization”, *Phys. Rev. B* **105**, 224203 (2022).
- [344] R. Abou-Chacra, D. Thouless, and P. Anderson, “A selfconsistent theory of localization”, *J. Phys. C* **6**, 1734 (1973).
- [345] Y. Ueoka and K. Slevin, “Dimensional dependence of critical exponent of the Anderson transition in the orthogonal universality class”, *J. Phys. Soc. Jap.* **83**, 084711 (2014).
- [346] S. Hikami, “Localization, nonlinear  $\sigma$  model and string theory”, *Prog. Theo. Phys. Supp.* **107**, 213–227 (1992).
- [347] Y. Ueoka and K. Slevin, “Borel–Padé Re-summation of the  $\beta$ -functions Describing Anderson Localisation in the Wigner–Dyson Symmetry Classes”, *J. Phys. Soc. Jap.* **86**, 094707 (2017).
- [348] N. Mott, “The mobility edge since 1967”, *J. Phys. C* **20**, 3075 (1987).
- [349] J. T. Chalker, “Scaling and eigenfunction correlations near a mobility edge”, *Physica A* **167**, 253 (1990).
- [350] A. De Luca, A. Scardicchio, V. E. Kravtsov, and B. L. Altshuler, “Support set of random wave-functions on the Bethe lattice”, arXiv:1401.0019 (2013).
- [351] V. Kravtsov, B. Altshuler, and L. Ioffe, “Non-ergodic delocalized phase in Anderson model on Bethe lattice and regular graph”, *Ann. Phys.* **389**, 148–191 (2018).
- [352] B. L. Altshuler, V. E. Kravtsov, and I. V. Lerner, “Statistical properties of mesoscopic fluctuations and similarity theory”, *JETP Lett.* **43**, 441 (1986).

- [353] B. L. Altshuler, V. E. Kravtsov, and I. V. Lerner, “Statistics of mesoscopic fluctuations and instability of one-parameter scaling”, *Zh. Eksp. Teor. Fiz.* **91**, 2276 (1986).
- [354] J. T. Chalker, V. E. Kravtsov, and I. V. Lerner, “Spectral rigidity and eigenfunction correlations at the Anderson transition”, *JETP Lett.* **64**, 386–392 (1996).
- [355] E. Bogomolny, O. Giraud, and C. Schmit, “Integrable random matrix ensembles”, *Nonlinearity* **24**, 3179–3213 (2011).
- [356] E. Bogomolny and O. Giraud, “Eigenfunction entropy and spectral compressibility for critical random matrix ensembles”, *Phys. Rev. Lett.* **106**, 044101 (2011).
- [357] V. E. Kravtsov, I. M. Khaymovich, E. Cuevas, and M. Amini, “A random matrix model with localization and ergodic transitions”, *New J. Phys.* **17**, 122002 (2015).
- [358] I. M. Khaymovich, V. E. Kravtsov, B. L. Altshuler, and L. B. Ioffe, “Fragile ergodic phases in logarithmically-normal Rosenzweig-Porter model”, *Phys. Rev. Res.* **2**, 043346 (2020).
- [359] P. A. Lee and T. Ramakrishnan, “Disordered electronic systems”, *Rev. Mod. Phys.* **57**, 287 (1985).
- [360] I. Šuntajs, T. Prosen, and L. Vidmar, “Localization challenges quantum chaos in the finite two-dimensional Anderson model”, *Phys. Rev. B* **107**, 064205 (2023).
- [361] F. Wegner, “Anomalous dimensions for the nonlinear sigma-model in 2+epsilon dimensions”, *Nucl. Phys. B* **280**, 210 (1987).
- [362] F. Wegner, “Four-loop-order beta-function of nonlinear sigma-models in symmetric spaces”, *Nucl. Phys. B* **316**, 663 (1989).
- [363] P. Wölfle and D. Vollhardt, “Self-consistent theory of Anderson localization: General formalism and applications”, *Int. J. Mod. Phys. B* **24**, 1526–1554 (2010).
- [364] J. T. Chalker and G. J. Daniel, “Scaling, diffusion, and the integer quantized Hall effect”, *Phys. Rev. Lett.* **61**, 593 (1988).
- [365] K. Slevin and T. Ohtsuki, “Corrections to scaling at the Anderson transition”, *Phys. Rev. Lett.* **82**, 382–385 (1999).
- [366] A. Rodrigues, L. Vasquez, K. Slevin, and R. A. Roemer, “Multifractal finite-size scaling and universality at the Anderson transition”, *Phys. Rev. B* **84**, 134209 (2011).
- [367] A. M. Garcia-Garcia, “Semiclassical theory of the Anderson transition”, *Phys. Rev. Lett.* **100**, 076404 (2008).
- [368] A. M. Garcia-Garcia and E. Cuevas, “Dimensional dependence of the metal-insulator transition”, *Phys. Rev. B* **75**, 074203 (2007).
- [369] F. Madani, M. Denis, P. Szriftgiser, J. C. Garreau, A. Rancon, and R. Chircireanu, “Exploring quantum criticality in a 4d quantum disordered system”, arXiv:2402.06573 (2024).
- [370] K. Slevin and T. Ohtsuki, “Critical exponent for the Anderson transition in the three-dimensional orthogonal universality class”, *New J. Phys.* **16**, 015012 (2014).
- [371] A. D. Mirlin, Y. V. Fyodorov, F.-M. Dittes, J. Quezada, and T. H. Seligman, “Transition from localized to extended eigenstates in the ensemble of power-law random banded matrices”, *Phys. Rev. E* **54**, 3221 (1996).
- [372] F. Wegner, “The mobility edge problem: continuous symmetry and a conjecture”, *Z. Phys. B* **35**, 207–210 (1979).
- [373] K. B. Efetov, “Supersymmetry and theory of disordered metals”, *Adv. Phys.* **32**, 53 (1983).

- [374] B. L. Altshuler, V. E. Kravtsov, and I. V. Lerner, *Mesoscopic phenomena in solids* (Elsevier, 1991), p. 449.
- [375] E. Kowalski, *An introduction to expander graphs*, Collection SMF / Cours spécialisés (Société Mathématique de France, 2019).
- [376] P. A. Lee, “Real-space scaling studies of localization”, *Phys. Rev. Lett.* **42**, 1492–1494 (1979).
- [377] V. L. Berezinskiĭ, “Destruction of Long-range Order in One-dimensional and Two-dimensional Systems having a Continuous Symmetry Group I. Classical Systems”, *Sov.JETP* **32**, 493 (1971).
- [378] V. L. Berezinskiĭ, “Destruction of long-range order in one-dimensional and two-dimensional systems possessing a continuous symmetry group. ii. quantum systems”, *Sov. JETP* **34**, 610 (1972).
- [379] J. M. Kosterlitz and D. J. Thouless, “Ordering, metastability and phase transitions in two-dimensional systems”, *J. Phys. C* **6**, 1181–1203 (1973).
- [380] R. Vosk, D. A. Huse, and E. Altman, “Theory of the many-body localization transition in one-dimensional systems”, *Phys. Rev. X* **5**, 031032 (2015).
- [381] A. C. Potter, R. Vasseur, and S. A. Parameswaran, “Universal properties of many-body delocalization transitions”, *Phys. Rev. X* **5**, 031033 (2015).
- [382] L. Zhang, B. Zhao, T. Devakul, and D. A. Huse, “Many-body localization phase transition: a simplified strong-randomness approximate renormalization group”, *Phys. Rev. B* **93**, 224201 (2016).
- [383] P. T. Dumitrescu, A. Goremykina, S. A. Parameswaran, M. Serbyn, and R. Vasseur, “Kosterlitz-Thouless scaling at many-body localization phase transitions”, *Phys. Rev. B* **99**, 094205 (2019).
- [384] S.-k. Ma, C. Dasgupta, and C.-k. Hu, “Random antiferromagnetic chain”, *Phys. Rev. Lett.* **43**, 1434–1437 (1979).
- [385] C. Dasgupta and S.-k. Ma, “Low-temperature properties of the random Heisenberg antiferromagnetic chain”, *Phys. Rev. B* **22**, 1305 (1980).
- [386] D. S. Fisher, “Random antiferromagnetic quantum spin chains”, *Phys. Rev. B* **50**, 3799–3821 (1994).
- [387] D. A. Huse, “Strong-randomness renormalization groups”, arXiv:2304.08572 (2023).
- [388] U. Sivan, Y. Imry, and A. Aronov, “Quasi-particle lifetime in a quantum dot”, *Europhys. Lett.* **28**, 115 (1994).
- [389] M. R. Zirnbauer, “Localization transition on the Bethe lattice”, *Phys. Rev. B* **34**, 6394–6408 (1986).
- [390] K. S. Tikhonov and A. D. Mirlin, “Critical behavior at the localization transition on random regular graphs”, *Phys. Rev. B* **99**, 214202 (2019).
- [391] C. Monthus and T. Garel, “Anderson localization on the Cayley tree: multifractal statistics of the transmission at criticality and off criticality”, *J. Phys. A: Math. Theor.* **44**, 145001 (2011).
- [392] I. Khaymovich and V. Kravtsov, “Dynamical phases in a “multifractal” Rosenzweig-Porter model”, *SciPost Physics* **11**, 045 (2021).

- [393] A. Burin and L. Maksimov, “Localization and delocalization of particles in disordered lattice with tunneling amplitude with  $R^{-3}$  decay”, *JETP Lett* **50**, 338 (1989).
- [394] A. G. Kutlin and I. M. Khaymovich, “Renormalization to localization without a small parameter”, *SciPost Phys.* **8**, 049 (2020).
- [395] L. S. Levitov, “Delocalization of vibrational modes caused by electric dipole interaction”, *Phys. Rev. Lett.* **64**, 547–550 (1990).
- [396] L. Levitov, “Absence of localization of vibrational modes due to dipole-dipole interaction”, *Europhysics Letters* **9**, 83 (1989).
- [397] A. L. Burin, “Localization in a random XY model with long-range interactions: Intermediate case between single-particle and many-body problems”, *Phys. Rev. B* **92**, 104428 (2015).
- [398] P. Jacquod and D. L. Shepelyansky, “Emergence of quantum chaos in finite interacting Fermi systems”, *Phys. Rev. Lett.* **79**, 1837–1840 (1997).
- [399] A. Burin, “Localization and chaos in a quantum spin glass model in random longitudinal fields: Mapping to the localization problem in a Bethe lattice with a correlated disorder”, *Ann. Phys.* **529**, 1600292 (2017).
- [400] A. L. Burin, “Many-body delocalization in a strongly disordered system with long-range interactions: finite-size scaling”, *Phys. Rev. B* **91**, 094202 (2015).
- [401] A. L. Burin, “Energy delocalization in strongly disordered systems induced by the long-range many-body interaction”, arXiv:cond-mat/0611387 (2006).
- [402] D. B. Gutman, I. V. Protopopov, A. L. Burin, I. V. Gornyi, R. A. Santos, and A. D. Mirlin, “Energy transport in the Anderson insulator”, *Phys. Rev. B* **93**, 245427 (2016).
- [403] C. Jacobi, “Über ein leichtes Verfahren die in der Theorie der Säcularstörungen vorkommenden Gleichungen numerisch aufzulösen”, *J REINE ANGEW MATH* **1846**, 51–94 (1846).
- [404] J. Z. Imbrie, “Multi-scale Jacobi method for Anderson localization”, *Comm. Math. Phys.* **341**, 491–521 (2015).
- [405] D. M. Long, P. J. D. Crowley, V. Khemani, and A. Chandran, “Phenomenology of the prethermal many-body localized regime”, *Phys. Rev. Lett.* **131**, 106301 (2023).
- [406] D. M. Long, D. Hahn, M. Bukov, and A. Chandran, “Beyond Fermi’s golden rule with the statistical Jacobi approximation”, *SciPost Phys.* **15**, 251 (2023).
- [407] V. Kravtsov, I. Khaymovich, E. Cuevas, and M. Amini, “A random matrix model with localization and ergodic transitions”, *New J. Phys.* **17**, 122002 (2015).
- [408] J. Edwards and D. Thouless, “Numerical studies of localization in disordered systems”, *J. Phys. C* **5**, 807 (1972).
- [409] A. Kutlin and I. M. Khaymovich, “Anatomy of the eigenstates distribution: A quest for a genuine multifractality”, *SciPost Phys.* **16**, 008 (2024).
- [410] F. Evers and A. D. Mirlin, “Anderson transitions”, *Rev. Mod. Phys.* **80**, 1355–1417 (2008).
- [411] E. Bogomolny and M. Sieber, “Eigenfunction distribution for the Rosenzweig-Porter model”, *Phys. Rev. E* **98**, 032139 (2018).
- [412] V. E. Kravtsov, I. M. Khaymovich, B. L. Altshuler, and L. B. Ioffe, “Localization transition on the random regular graph as an unstable tricritical point in a log-normal Rosenzweig-Porter random matrix ensemble”, arXiv:2002.02979 (2020).

- [413] A. D. Mirlin and Y. V. Fyodorov, “Universality of level correlation function of sparse random matrices”, *J. Phys. A: Math. Gen.* **24**, 2273 (1991).
- [414] R. Richardson, “A restricted class of exact eigenstates of the pairing-force Hamiltonian”, *Physics Letters* **3**, 277–279 (1963).
- [415] R. Richardson and N. Sherman, “Exact eigenstates of the pairing-force Hamiltonian”, *Nucl. Phys.* **52**, 221–238 (1964).
- [416] M. Cambiaggio, A. Rivas, and M. Saraceno, “Integrability of the pairing Hamiltonian”, *Nucl. Phys. A* **624**, 157–167 (1997).
- [417] A. Ossipov, “Anderson localization on a simplex”, *J. Phys. A: Math. Theor.* **46**, 105001 (2013).
- [418] R. Modak, S. Mukerjee, E. A. Yuzbashyan, and B. S. Shastry, “Integrals of motion for one-dimensional Anderson localized systems”, *New J. Phys.* **18**, 033010 (2016).
- [419] J. Smith, A. Lee, P. Richerme, B. Neyenhuys, P. W. Hess, P. Hauke, M. Heyl, D. A. Huse, and C. Monroe, “Many-body localization in a quantum simulator with programmable random disorder”, *Nature Phys.* **12**, 907–911 (2016).
- [420] M. Schreiber, S. S. Hodgman, P. Bordia, H. P. Lüschen, M. H. Fischer, R. Vosk, E. Altman, U. Schneider, and I. Bloch, “Observation of many-body localization of interacting fermions in a quasirandom optical lattice”, *Science* **349**, 842–845 (2015).
- [421] O. Shtanko, D. S. Wang, H. Zhang, N. Harle, A. Seif, R. Movassagh, and Z. Mineev, “Uncovering local integrability in quantum many-body dynamics”, [arXiv:2307.07552](https://arxiv.org/abs/2307.07552) (2023).
- [422] D. H. White, T. A. Haase, D. J. Brown, M. D. Hoogerland, M. S. Najafabadi, J. L. Helm, C. Gies, D. Schumayer, and D. A. Hutchinson, “Observation of two-dimensional Anderson localisation of ultracold atoms”, *Nat. Comm.* **11**, 4942 (2020).
- [423] J. Billy, V. Josse, Z. Zuo, A. Bernard, B. Hambrecht, P. Lugan, D. Clément, L. Sanchez-Palencia, P. Bouyer, and A. Aspect, “Direct observation of Anderson localization of matter waves in a controlled disorder”, *Nature* **453**, 891–894 (2008).
- [424] G. Roati, C. D’Errico, L. Fallani, M. Fattori, C. Fort, M. Zaccanti, G. Modugno, M. Modugno, and M. Inguscio, “Anderson localization of a non-interacting Bose–Einstein condensate”, *Nature* **453**, 895–898 (2008).
- [425] S. Wold, K. Esbensen, and P. Geladi, “Principal component analysis”, *Chem. Int. Lab. Sys.* **2**, 37–52 (1987).
- [426] I. T. Jolliffe, *Principal component analysis for special types of data* (Springer, 2002).
- [427] J. Šuntajs, M. Hopjan, W. De Roeck, and L. Vidmar, “Similarity between a many-body quantum avalanche model and the ultrametric random matrix model”, *Phys. Rev. Res.* **6**, 023030 (2024).
- [428] P. Kunkel, M. Prüfer, S. Lannig, R. Rosa-Medina, A. Bonnin, M. Gärttner, H. Strobel, and M. K. Oberthaler, “Simultaneous readout of noncommuting collective spin observables beyond the standard quantum limit”, *Phys. Rev. Lett.* **123**, 063603 (2019).
- [429] T. Brydges, A. Elben, P. Jurcevic, B. Vermersch, C. Maier, B. P. Lanyon, P. Zoller, R. Blatt, and C. F. Roos, “Probing Rényi entanglement entropy via randomized measurements”, *Science* **364**, 260–263 (2019).
- [430] J. C. e. a. Hoke, G. Q. AI, and Collaborators, “Measurement-induced entanglement and teleportation on a noisy quantum processor”, *Nature* **622**, 481–486 (2023).

- [431] V. Vitale, A. Rath, P. Jurcevic, A. Elben, C. Branciard, and B. Vermersch, “Estimation of the quantum fisher information on a quantum processor”, arXiv:2307.16882 (2023).
- [432] S. J. Wetzel, “Unsupervised learning of phase transitions: from principal component analysis to variational autoencoders”, *Phys. Rev. E* **96**, 022140 (2017).
- [433] T. Mendes-Santos, X. Turkeshi, M. Dalmonte, and A. Rodriguez, “Unsupervised learning universal critical behavior via the intrinsic dimension”, *Phys. Rev. X* **11**, 011040 (2021).
- [434] T. Mendes-Santos, A. Angelone, A. Rodriguez, R. Fazio, and M. Dalmonte, “Intrinsic dimension of path integrals: data-mining quantum criticality and emergent simplicity”, *PRX Quantum* **2**, 030332 (2021).
- [435] X. Turkeshi, “Measurement-induced criticality as a data-structure transition”, *Phys. Rev. B* **106**, 144313 (2022).
- [436] R. K. Panda, R. Verdel, A. Rodriguez, H. Sun, G. Bianconi, and M. Dalmonte, “Non-parametric learning critical behavior in Ising partition functions: PCA entropy and intrinsic dimension”, arXiv:2308.13636 (2023).
- [437] V. Vitale, T. Mendes-Santos, A. Rodriguez, and M. Dalmonte, “Topological Kolmogorov complexity and the Berezinskii-Kosterlitz-Thouless mechanism”, arXiv:2305.05396 (2023).
- [438] R. Verdel, V. Vitale, R. K. Panda, E. D. Donkor, A. Rodriguez, S. Lannig, Y. Deller, H. Strobel, M. K. Oberthaler, and M. Dalmonte, “Data-driven discovery of statistically relevant information in quantum simulators”, *Phys. Rev. B* **109**, 075152 (2024).
- [439] T. Mendes-Santos, M. Schmitt, A. Angelone, A. Rodriguez, P. Scholl, H. J. Williams, D. Barredo, T. Lahaye, A. Browaeys, M. Heyl, and M. Dalmonte, “Wave function network description and kolmogorov complexity of quantum many-body systems”, arXiv:2301.13216 (2023).
- [440] C. Muzzi, R. S. Cortes, D. S. Bhakuni, A. Jelić, A. Gambassi, M. Dalmonte, and R. Verdel, “Principal component analysis of absorbing state phase transitions”, arXiv:2405.12863 (2024).
- [441] P. Mehta, M. Bukov, C.-H. Wang, A. G. Day, C. Richardson, C. K. Fisher, and D. J. Schwab, “A high-bias, low-variance introduction to machine learning for physicists”, *Phys. Rep.* **810**, 1–124 (2019).
- [442] J. Carrasquilla, “Machine learning for quantum matter”, *Adv. Phys.: X* **5**, 1797528 (2020).
- [443] G. De Tomasi, S. Bera, A. Scardicchio, and I. M. Khaymovich, “Subdiffusion in the Anderson model on the random regular graph”, *Phys. Rev. B* **101**, 100201 (2020).
- [444] P. Sierant and X. Turkeshi, “Universal behavior beyond multifractality of wave functions at measurement-induced phase transitions”, *Phys. Rev. Lett.* **128**, 130605 (2022).
- [445] B. A. Van Tiggelen, “Localization of waves”, *Diff. Waves Compl. Media*, 1–60 (1999).
- [446] P. Sierant, M. Lewenstein, and J. Zakrzewski, “Polynomially filtered exact diagonalization approach to many-body localization”, *Phys. Rev. Lett.* **125**, 156601 (2020).
- [447] D. J. Luitz, F. Huveneers, and W. De Roeck, “How a small quantum bath can thermalize long localized chains”, *Phys. Rev. Lett.* **119**, 150602 (2017).
- [448] A. Elben, S. T. Flammia, H.-Y. Huang, R. Kueng, J. Preskill, B. Vermersch, and P. Zoller, “The randomized measurement toolbox”, *Nat. Rev. Phys.* **5**, 9–24 (2023).
- [449] P. Cieřliński, S. Imai, J. Dziewior, O. Gühne, L. Knips, W. Laskowski, J. Meinecke, T. Paterek, and T. Vértesi, “Analysing quantum systems with randomised measurements”, arXiv:2307.01251 (2023).